Novel Covalent Organic Frameworks for the Energy Transition

Veldhuizen, H.V.

DOI
10.4233/uuid:06ccff49-3558-4f70-a58a-547e1514af52

Publication date
2023

Document Version
Final published version

Citation (APA)
Veldhuizen, H. V. (2023). *Novel Covalent Organic Frameworks for the Energy Transition*. [Dissertation (TU Delft), Delft University of Technology]. https://doi.org/10.4233/uuid:06ccff49-3558-4f70-a58a-547e1514af52

Novel Covalent Organic Frameworks for the Energy Transition

Novel Covalent Organic Frameworks for the Energy Transition

Proefschrift

ter verkrijging van de graad van doctor
aan de Technische Universiteit Delft,
op gezag van de Rector Magnificus prof. dr. ir. T. H. J. J. van der Hagen
voorzitter van het College voor Promoties,
in het openbaar te verdedigen op vrijdag 15 september 2023 om 10:00 uur

door

Hugo Victor VELDHUIZEN

Master of Science in Chemistry,
Radboud Universiteit, Nijmegen, Nederland,
geboren te ’s-Hertogenbosch, Nederland

Dit proefschrift is goedgekeurd door de

Promotor: Prof. Dr. ir. S. van der Zwaag
Promotor: Dr. ir. M. A. van der Veen

Samenstelling promotiecommissie:

Rector Magnificus	voorzitter
Prof. Dr. ir. S. van der Zwaag	Technische Universiteit Delft
Dr. ir. M. A. van der Veen	Technische Universiteit Delft
Onafhankelijke leden:	
Prof. dr. S. J. Picken	Technische Universiteit Delft
Dr. R. Eelkema	Technische Universiteit Delft
Prof. Dr. S. Calero	Technische Universiteit Eindhoven
Prof Dr. D. E. de Vos	Katholieke Universiteit Leuven
Prof. Dr. ir. L. C P. M. de Smet	Wageningen University & Research
Prof. Dr. J. H. van Esch	Technische Universiteit Delft, reservelid

Keywords: Covalent organic frameworks, synthesis, structure-property relationships, micro- and mesoporosity
Printed by: Ipskamp Printing B.V.
Cover by: Hugo Veldhuizen

ISBN 978-94-6473-201-6

An electronic version of this dissertation is available at

https://repository.tudelft.nl/

CONTENTS

1

INTRODUCTION

1.1 NANOPOROUS MATERIALS

Porosity is a material property that is present in a wide variety of materials that surround our everyday lives: from concrete in structural buildings to bones in animals and humans. The functionality of pores in a material can vary, but they are often used as weight reduction, size exclusion, or to influence mechanical properties or heat capacity. Depending on the material and application, the sizes of pores range from centimetres to subnanometres. Nanopores can be divided in so-called macropores (pore size > 50 nm), mesopores (2 – 50 nm) and micropores (< 2 nm). Both micro- and small mesopores, especially, have drawn material scientists' attention over the last decades, because once implemented into materials they are ideally suited to capture small molecules such as H_2, H_2O, CH_4, CO_2, salts/ions and many others. The capture and separation of these molecules are key challenges within current sustainable development goals: mitigating greenhouse gases (CH_4 and CO_2),[1] alternative green fuels (H_2),[2] clean water/desalination (H_2O and salts),[3] energy storage (ions),[4] and targeted drug release,[5]

Examples of nanoporous materials are: porous carbons,[6] silicas,[7] zeolites,[8] and more recently: metal organic frameworks (MOFs),[9] and covalent organic frameworks (COFs).[10] While MOFs are distinguished by having organic linkers coupled to metal nodes that comprise their framework, COFs are purely organic structures that are synthesized from 2 or more organic monomers. MOFs and COFs have the advantage of the ever-expanding library of building blocks being available to synthesize them, allowing a high degree of synthetic control over functional material properties. With the design and application of novel porous materials,

framework stability and lifetime are important properties. Here, COFs seem to be especially suited as their backbones are exclusively structured through strong covalent bonds.[11]

The main focus of this thesis is on COFs, spanning a wide variety of topics, starting at the design and synthesis, going through detailed characterization, and finally touching on future applications such as CO_2 separation and energy storage. Pioneering work in the development of COF materials and expansion of COF chemistry has been done by, among others, A. Nagai, and this introduction chapter builds further on his recently published comprehensive COF handbook.[11]

1.2 INTRODUCTION TO COVALENT ORGANIC FRAMEWORKS (COFS)

COFs are a subclass among hypercrosslinked polymers, which emphasizes one of their main characteristics; having a structural backbone of covalent bonds. Furthermore, COFs display permanent nanoporosity and contain crystalline domains within their structure. The geometry and chemistry of the COF building blocks are important, since they are indicative of the properties of the final COF. One of the monomers used for COF synthesis has necessarily more than 2 polymerizable groups, while the complementary monomer has 2 or more of these groups. Classical examples include reacting A_3 and B_2 monomers in a stochiometric ratio to form 2D polymer sheets. Although many more topologies are known (including 3D COFs), the ones that are most prevalent in this thesis have been depicted in **Figure 1A**. These topologies provide nanoporosity (typically between 1 – 5 nm) within the material via sheet stacking. Stacked 2D sheets are necessary to provide 1D open channels. These pores are readily accessible for adsorption of external species, as well as the open spaces between the layers (typically between 0.2 – 0.4 nm). Since the inter-layer interactions rely on weak π-π or van der Waals forces, multiple different stacking modes are possible in 2D COF sheets. In early COF literature, eclipsed stacking (known as AA) and unidirectional stacking with an offset of half the unit cell (known as AB) are frequently discussed.[12] Advanced microstructural characterization techniques (*e.g.* total scattering data using synchrotron radiation) introduced a more nuanced look on the different stacking modes and revealed hidden stacking disorder (*i.e.* random stacking) between 2D COF sheets.[13] Disorder can also occur within a single 2D sheet through rotational freedom within the monomers or of the formed polymer bond (**Figure 1B**). High-resolution transmission electron microscopy (HR-TEM) studies revealed in-plane COF defects for both hexagonal and square topologies.[14,15] On the other hand, out-of-plane defects are also often observed, especially when monomers are not highly

rigid.[16] The combination of all three (topology, stacking and defects) influence two main characteristics of the COF; nanoporosity and crystallinity.

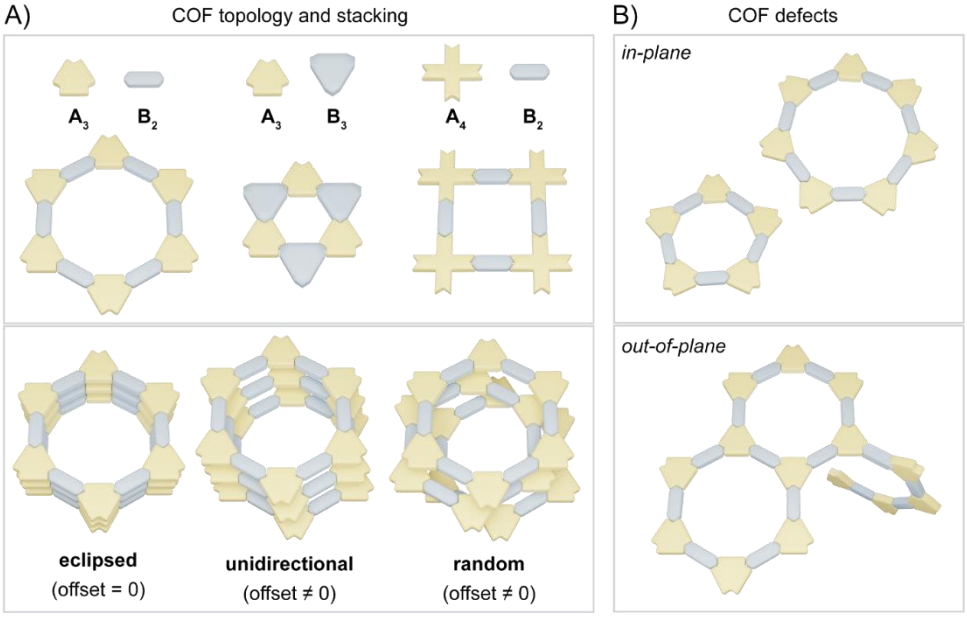

Figure 1 A) Schematic overview of three different COF topologies and three different stacking motives. Eclipsed stacking is often referred to in literature as AA stacking, whereas unidirectional stacking with an offset of half the unit cell dimensions is known as AB stacking. **B)** Schematic overview of different kinds of COF defects due to rotational freedom within the monomers or of the connecting linkage.

1.2.1 COF CHARACTERIZATION

The state of the art characterization method for porosity analysis, *i.e.* a static manometric method, uses the phenomenon of gas sorption (typically N_2 at 77 K). Adsorption isotherms are constructed - point-by-point - through admission of successive charges of gas to the adsorbent with the aid of a dosing technique and application of the appropriate gas laws. In 2015, IUPAC recommendations on the classifications of isotherm shapes have recently been updated and they are adapted here in **Figure 2**.[17] These characteristic shapes are closely related to particular pore structures. Type I isotherms are most relevant to this thesis, since these shapes indicate microporous (Type I(a)) and small mesoporous (Type I(b)) adsorbents. Isotherms of Types II and III often represent non- or microporous adsorbents. On the other hand, Type IV isotherms are observed for mesoporous adsorbents including some MOFs and COFs with larger pore sizes, where the P/P_0 value at the step increase hints at the expected pore size (the larger P/P_0, the larger the pore size). Type V isotherms indicate weak adsorbent-adsorbate interactions

at low P/P_0, after which molecular clustering is followed by pore filling. This behaviour is seen in, for example, water vapor adsorption on hydrophobic adsorbents. Lastly, the step-wise uptake in Type VI presumes layer-by-layer adsorption and is, for example, seen in argon-graphitic carbon interactions.

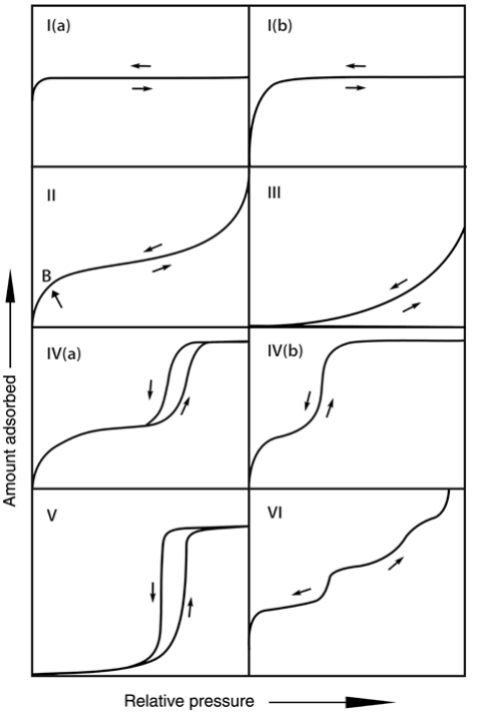

Figure 2 Classification of physisorption isotherms.[17]

Further analysis of such isotherms can be performed by, for example, calculating pore size distributions (PSDs), using the experimental isotherm and correlating it to theoretical isotherms that are developed for certain adsorption systems (e.g. N_2 or Ar on carbons, silicas or zeolites). Interestingly, the PSDs already give hints for (semi)-crystallinity of the COF depending on the broadness of the distributions. Characterization of the crystallinity of COFs is usually done by powder X-ray diffraction (PXRD) in combination with computational structure modelling and refinement. Methods for structure modelling may range from classical force field methods to the more accurate, albeit computationally costly, density functional theory (DFT) models.[18] Irrespective of the method, typically two different stacking modes are simulated: AA and AB stacking (**Figure 1A**). Then, PXRD patterns based on these two stacking modes are predicted within the modelling software. Thereafter, they are compared to the experimental pattern and a qualitative

estimation is made on which simulated stacking mode best describes the experimental one.

1.3 CURRENT CHALLENGES IN COF DEVELOPMENT

1.3.1 CRYSTALLINITY VERSUS STABILITY

The development and synthetic optimization of novel COF materials is primarily focussed on controlling crystallinity and porosity, which are directly linked to each other as has been discussed in 1.1. The first COFs that have been developed by Yaghi and coworkers in 2005 relied upon highly reversible boroxine anhydride or boronate ester linkages between the building blocks.[10] The reversibility of these bonds allowed the growing polymer to undo topological imperfections and yield a highly regular structure, which was previously thought of as near impossible for crosslinked polymers. While not the only prerequisite for the formation of crystalline COFs, reversibility of the connecting bonds has been a leading design principle for early COFs.[19] Synthesis techniques such as the addition of a mono-functional modulating agent build further on this: acting as a nucleation inhibitor and competitive modulator with the multifunctional building units that bear the same functional group as the modulator.[20] However, the transient nature of the chemical bonds that constitute the polymer backbone comes with an immediate dilemma of chemical instability.[21] Therefore, it is not surprising that early boronate ester linked COFs are easily degraded through hydrolysis at ambient conditions.[22] As an alternative, imine chemistry was employed, since aromatic imines are less sensitive to moisture while their bond formation is still relatively reversible. Imine COFs are synthesized from the acid-catalysed reaction of amines with aldehydes (**Scheme 1**).

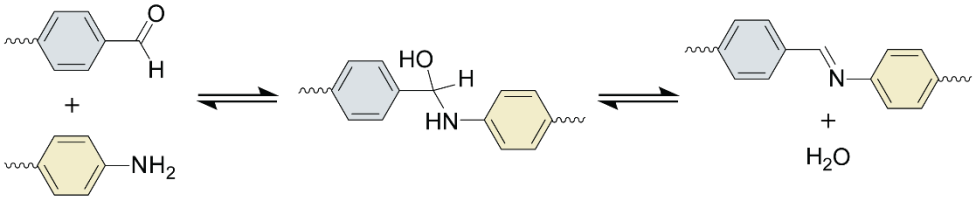

Scheme 1 Reaction pathway of imine formation through addition and elimination.

Careful optimization of catalyst concentration is required to yield crystalline structures, as has been systematically investigated by Dichtel and co-workers.[23] Despite the improvements that imine chemistry brings, they still do not present the long-term stability (hydrolytic, acidic, alkaline) that is required in the aforementioned applications. A promising strategy in tackling this issue is through

'locking'. When, for example, hydroxyl groups are introduced at the 2- and 5-position relative to the aldehyde groups in terephthaldehyde and this compound reacts with primary amines to form imines, intramolecular hydrogen bonding takes place between the hydroxyl-H and the lone pair of the imine-N.[24] As a result, these imine COFs retain their crystallinity after seven days of 3 M HCl treatment, which is fatal for the structural integrity of similar imine COFs where this strategy is not applied. Another 'locking' strategy uses post-synthetic sulphur-assisted modification of an imine COF into a thiazole COF.[14] The latter showed structural robustness even when exposed to concentrated acid and alkaline solutions, hydrazine, and sodium borohydride, which was not the case for the former COF. Lastly, a developing strategy towards more long-term stability leans on the development of COFs with stronger, non-reversible chemical backbones. A promising candidate here is the imide-COF, formed through the polycondensation reaction of anhydrides and primary amines (**Scheme 2**).

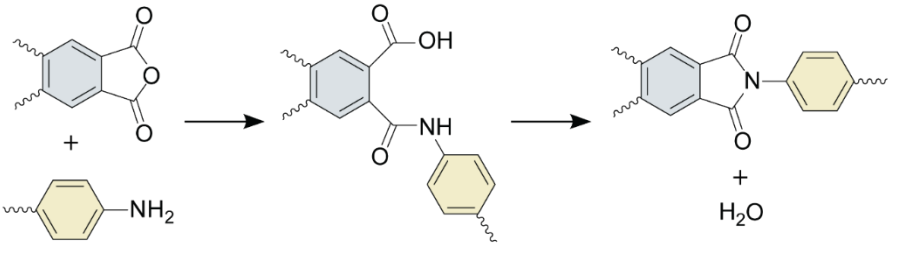

Scheme 2 Reaction pathway of imide formation through addition and elimination.

1D analogues of such polyimide polymers have been commercially implemented in high-temperature applications. Their reaction pathways are, however, not very reversible: the nucleophilic attack of the primary amines on the anhydride carbonyl is much more favored than the backwards reaction and once imide cyclization sets in, the reaction is even less reversible. Yet, owing to the rigidity of the monomers and the cyclic imide bond, implementation of these linkages in COFs led to relatively crystalline materials.[25,26] The challenges lie in expanding the library of polyimide COFs and assessing whether they indeed maintain their stability and functionality when exposed to typical chemical environments of their envisioned application.

1.3.2 COF SYNTHESIS

COFs are often synthesized in highly controlled environments, which is necessary to carefully regulate the experimental conditions (time, temperature, pressure, inert atmosphere). Moreover, COF reaction mixtures are usually left unperturbed,

as it is implicitly accepted that this would help the formation of more regular structures. However, this has not been properly investigated. In addition, regardless whether this assumption is true or not, the amorphous counterparts of COFs (*i.e.* porous organic polymers, or POPs) are known to have a similar performance in applications like gas separation.[27]

In 1D polymer synthesis, mechanical perturbation as an optimization parameter is able to reveal materials with different microstructures and functional properties. Varying the shear rates of mechanical stirrers directly affect particle- and agglomerate size distributions.[28,29] Applying this strategy to the COF field potentially broadens the library of functional COF materials, without the need for complex synthesis routes towards novel monomers. At the same time, this is a vital line of research to assess the scalability of COFs. Liquid assisted grinding during synthesis of β-ketoenamine COFs has been employed and compared to the same COFs prepared through conventional routes.[30] Here, the authors discovered no loss in structural properties by the use of this mechanosynthesis technique, and even noticed improved reaction rates. Thus, unforeseen improvements in COF development strategies could be revealed through the processing-side of the synthesis. Here, the challenge lies in finding COF chemistries that are robust enough for these perturbations, and in the optimization of experimental parameters so that the porosity and other vital properties of the COF are not compromised.

1.3.3 APPLICATION OF COFS

The nanoporosity and chemical structure of the COF are central in designing it for a specific application. In the case of gas capture, the emphasis is often on the porous architecture. CO_2 capture is enhanced when small micropores are present in the framework, since the close pore walls promote adsorption events to occur. The strive towards smaller micropores has been a leading design principle in COFs to improve the CO_2 capacity in highly controlled environments.[31] However, in order for COFs to be feasible candidates for CO_2 separation and capture in, for example, direct air capture or industrial flue gas applications, a large absolute capacity is only one of the many requirements. Selective CO_2 adsorption over other ubiquitous components in flue gas (*e.g.* N_2 and O_2) is of high importance, as well as hydrolytic stability and CO_2 capacity retention in the presence of water vapor.[32] In addition, oxidative stability plays a large role in applications using high O_2 concentrations,[33] such as direct air capture. In order to tackle these challenges, a careful balance between porous architecture and chemical backbone is necessary.

In the field of electrochemical energy storage and catalysis, a key property that COFs might bring is a high availability of active sites due to their large surface areas. Implementing redox- or catalytically active segments in the backbone of the COF could enhance performance while providing structural stability,[34] which pushes the field of organic electrochemical devices forward. In the field of catalysis, porphyrin-based COFs are becoming increasingly popular, since porphyrin ligands can incorporate metal ions that are highly active in the assisted conversion of stable molecules such as CO_2.[35] The tunable nature of COFs allows to construct multivariate structures, which, regarding porphyrin-based COFs, would allow to develop single COF particles with multiple different catalytic centres. In the catalysis of reactions having complex reaction mechanisms with various stable intermediates (*e.g.* CO_2 reduction), multivariate COFs can potentially steer towards desired reaction products. The challenge here is controlling the spatial distribution of the porphyrin units in order to obtain a high product selectivity and conversion efficiency, while maintaining framework stability.

Although recent years have seen a rise in the utilisation of COFs for these applications,[36] structure-property relationships are not often extensive enough to formulate design rules. This is, however, a vital part in order to assess whether COFs can compete with known / commercial gas adsorbents or electrochemically active organic materials. One strategy to do so is by employing a range of chemically similar COFs in the same experimental setup: *e.g.* fixed bed breakthrough setup for gas capture, or membrane electrode assembly for electrocatalysis. Then, correlating the COF's performance to molecular structure and polymer network in order to establish design rules and future optimizations.

1.4 THESIS OUTLINE

Chapter 2 aims to expand the library of thermally and hydrolytically stable polyimide COFs. Although polyimide COFs have already been discovered, their pore sizes mostly range between 2.5 – 3 nm. By utilising a small A_3 monomer called mellitic trianhydride with B_3 triamine monomers, a purely microporous COF could be formed. Microporous polyimide COFs provide a step forward in the design of adsorbents for CO_2 capture, since their porous architecture should allow a high CO_2 capacity, while its polymer backbone should provide structural robustness.

The conventional approach of static COF reaction mixtures is implicitly accepted to be more helpful in the formation of regular, crystalline structures, yet there is little experimental evidence for this. At the same time, in 1D polyimide polymer analogues, mechanical perturbations have been shown to enhance

properties such as their photophysical behaviour. **Chapter 3** examines three different situations: no stirring during synthesis, mild stirring at 4.5 – 190 s^{-1} using a conventional stir bar, or high intensity stirring using a Taylor-Couette reactor at 250 s^{-1}. The COFs' structural changes as a result of these three synthesis methods is then discussed in detail.

The application of COFs in the field of CO_2 separation is largely unexplored, especially using experimental setups and gas compositions that are relevant for industry. **Chapter 4** builds on that gap of knowledge, specifically zooming in on the interplay between a hydrolytically stable COF, CO_2, and H_2O. Water vapour, which is present at various concentrations in flue gas, often competes for adsorption sites with CO_2 and lowers the performance. Through systematic variation of column temperature and humidity, this chapter aims to understand the driving forces for competitive and cooperative adsorption, which could lead to stricter design rules for next-generation adsorbents.

Chapter 5 tackles the challenge of understanding structure-property relationships of polyimide COFs in field of CO_2 capture and energy storage. Using two different triamine monomers and two different dianhydride monomers, four polyimide COFs were synthesized and investigated as CO_2 adsorbents and electrochemically active materials. The focus here lies on the combination of powder X-ray diffraction with density functional theory (DFT) geometry optimizations, to gain deeper insights into the stacking structure of the COFs. Drawing relationships between polyimide COF structures and their specific properties in CO_2 capture or Li-/Na-ion batteries is a central theme in this chapter. Especially since it allows a fair assessment in deciding whether the advantages COFs bring are promising enough to compete with conventional materials.

Chapter 6 follows-up on the electrochemical application of nanoporous polymers, by assessing the performance of a perylene diimide-based nanoporous polymer in supercapacitors. The emphasis of this research lies in the comparison of two different methods for electrode preparation. Typically, porous polymer-based electrochemical devices are prepared via mixing the polymer with binder and conductive agent. However, depositing the porous polymer as a top-layer onto the conductive layer could potentially enhance performance through a better polymer-electrolyte interface.

In a similar approach to chapter 5, **Chapter 7** employs chemically and structurally similar COFs as electrochemical catalyst for CO_2 reduction in order to establish structure-property relationships. Here, Ni- and/or Zn-porphyrin segments form the active sites and they can be implemented as repeating units in

the COF backbone. Rather than chemically altering the porphyrin monomers to influence the material's performance, this chapter assesses the potential synergistic effects that could arise when a mixture of multiple different porphyrin monomers are used in the synthesis. In this specific application where the electrochemical CO_2 conversion is a complex pathway with multiple different intermediates, dual-functional catalyst have shown to provide greater performance than the sum of its parts.

REFERENCES

[1] R. E. Morris, P. S. Wheatley *Angew. Chem. Int. Ed.* **2008**, *47*, 4966–4981. *Gas Storage in Nanoporous Materials*.

[2] L. Zhang, M. D Allendorf, R. Balderas-Xicohténcatl, D. P Broom, G. S Fanourgakis, G. E Froudakis, T. Gennett, K. E Hurst, S. Ling, C. Milanese, P. A Parilla, D. Pontiroli, M. Riccò, S. Shulda, V. Stavila, T. A Steriotis, C. J Webb, M. Witman, M. Hirscher *Prog. Energy* **2022**, *4*, 042013. *Fundamentals of hydrogen storage in nanoporous materials*.

[3] D. M. Stevens, J. Y. Shi, M. Reichert, A. Roy *Ind. Eng. Chem. Res.* **2017**, *56*, 10526–10551. *Next-Generation Nanoporous Materials: Progress and Prospects for Reverse Osmosis and Nanofiltration*.

[4] S. L. Candelaria, Y. Shao, W. Zhou, X. Li, J. Xiao, J.-G. Zhang, Y. Wang, J. Liu, J. Li, G. Cao *Nano Energy* **2012**, *1*, 195–220. *Nanostructured carbon for energy storage and conversion*.

[5] R. Duan, F. Xia, L. Jiang *ACS Nano* **2013**, *7*, 8344–8349. *Constructing Tunable Nanopores and Their Application in Drug Delivery*.

[6] J. Lee, S. Han, T. Hyeon *J. Mater. Chem.* **2004**, *14*, 478–486. *Synthesis of new nanoporous carbon materials using nanostructured silica materials as templates*.

[7] J. S. Beck, J. C. Vartuli, W. J. Roth, M. E. Leonowicz, C. T. Kresge, K. D. Schmitt, C. T-W. Chu, D. H. Olson, E. W. Sheppard, S. B. McCullen, J. B. Higgins, J. L. Schlenker *J. Am. Chem. Soc.* **1992**, *114*, 10834–10843. *A New Family of Mesoporous Molecular Sieves Prepared with Liquid Crystal Templates*.

[8] W. Hölderich, M. Hesse, F. Näumann *Angew. Chem. Int. Ed. Engl.* **1988**, *27*, 226–246. *Zeolites: Catalysts for Organic Syntheses*.

[9] B. F. Hoskins, R. Robson *J. Am. Chem. Soc.* **1989**, *111*, 5964–5965. *Infinite Polymeric Frameworks Consisting of Three Dimensionally Linked Rod-like Segments*.

[10] A. P. Coté, A. I. Benin, N. W. Ockwig, M. O'Keeffe, A. J. Matzger, O. M. Yaghi *Science* **2005**, *310*, 1166–1170. *Porous, Crystalline, Covalent Organic Frameworks*.

[11] A. Nagai, *Covalent Organic Frameworks* (Jenny Stanford Publishing Pte. Ltd., 2020)

[12] K. Geng, T. He, R. Liu, S. Dalapati, K. T. Tan, Z. Li, S. Tao, Y. Gong, Q. Jiang, D. Jiang *Chem. Rev.* **2020**, *120*, 8814–8933. *Covalent Organic Frameworks: Design, Synthesis, and Functions*.

[13] A. M. Pütz, M. W. Terban, S. Bette, F. Haase, R. E. Dinnebier, B. V. Lotsch *Chem. Sci.* **2020**, *11*, 12647–12654. *Total scattering reveals the hidden stacking disorder in a 2D covalent organic framework.*

[14] F. Haase, E. Troschke, G. Savasci, T. Banerjee, V. Duppel, S. Dörfler, M. M. J. Grundei, A. M. Burow, C. Ochsenfeld, S. Kaskel, B. V. Lotsch *Nat. Commun.* **2018**, *9*, 2600. *Topochemical conversion of an imine- into a thiazole-linked covalent organic framework enabling real structure analysis.*

[15] H. Qi, H. Sahabudeen, B. Liang, M. Položij, M. A. Addicoat, T. E. Gorelik, M. Hambsch, M. Mundszinger, S. W. Park, B. V. Lotsch, S. C. B. Mannsfeld, Z. Zheng, R. Dong, T. Heine, X. Feng, U. Kaiser *Sci. Adv.* **2020**, *6*, eabb5976. *Near–atomic-scale observation of grain boundaries in a layer-stacked two-dimensional polymer*.

[16] A. Trewin, D. J. Willock, A. I. Cooper *J. Phys. Chem. C* **2008,** *112*, 20549–20559. *Atomistic Simulation of Micropore Structure, Surface Area, and Gas Sorption Properties for Amorphous Microporous Polymer Networks*.

[17] M. Thommes, K. Kaneko, A. V. Neimark, J. P. Olivier, F. Rodriguez-Reinoso, J. Rouquerol, K. S. W. Sing *Pure Appl. Chem*. **2015**, *87*, 1051–1069. *Physisorption of gases, with special reference to the evaluation of surface area and pore size distribution (IUPAC Technical Report)*.

[18] D. Ongari, A. V. Yakutovich, L. Talirz, B. Smit *ACS Cent. Sci.* **2019**, *5*, 1663–1675. *Building a Consistent and Reproducible Database for Adsorption Evaluation in Covalent–Organic Frameworks*.

[19] S. Kandambeth, A. Mallick, B. Lukose, M. V. Mane, T. Heine, R. Banerjee *J. Am. Chem. Soc.* **2012**, *134*, 19524–19527. *Construction of Crystalline 2D Covalent Organic Frameworks with Remarkable Chemical (Acid/Base) Stability via a Combined Reversible and Irreversible Route*.

[20] T. Ma, E. A. Kapustin, S. X. Yin, L. Liang, Z. Zhou, J. Niu, L.-H. Li, Y. Wang, J. Su, J. Li, X. Wang, W. David Wang, W. Wang, J. Sun, O. M. Yaghi *Science* **2018**, *361*, 48–52. *Single-crystal x-ray diffraction structures of covalent organic frameworks*.

[21] F. Haasse, B. V. Lotsch *Chem. Soc. Rev.* **2020**, *49*, 8469–8500. *Solving the COF trilemma: towards crystalline, stable and functional covalent organic frameworks*.

[22] L. M. Lanni, R. William Tilford, M. Bharathy, J. J. Lavigne *J. Am. Chem. Soc.* **2011**, *133*, 13975–13983. *Enhanced Hydrolytic Stability of Self-Assembling Alkylated Two-Dimensional Covalent Organic Frameworks*.

[23] B. J. Smith, A. C. Overholts, N. Hwang, W. R. Dichtel *Chem. Commun.* **2016**, *52*, 3690–3693. *Insight into the crystallization of amorphous imine-linked polymer networks to 2D covalent organic frameworks*.

[24] S. Kandambeth, D. B. Shinde, M. K. Panda, B. Lukose, T. Heine, R. Banerjee *Angew. Chem. Int. Ed.* **2013**, *52*, 13052–13056. *Enhancement of Chemical Stability and Crystallinity in Porphyrin-Containing Covalent Organic Frameworks by Intramolecular Hydrogen Bonds*.

[25] Q. Fang, Z. Zhuang, S. Gu, R. B. Kaspar, J. Zheng, J. Wang, S. Qiu, Y. Yan *Nat. Commun.* **2014**, *5*, 4503. *Designed synthesis of large-pore crystalline polyimide covalent organic frameworks*.

[26] Q. Fang, J. Wang, S. Gu, R. B. Kaspar, Z. Zhuang, J. Zheng, H. Guo, S. Qiu, Y. Yan *J. Am. Chem. Soc.* **2015**, *137*, 8352–8355. *3D Porous Crystalline Polyimide Covalent Organic Frameworks for Drug Delivery*.

[27] W. Wang, M. Zhou, D. Yuan *J. Mater. Chem. A* **2017**, *5*, 1334–1347. *Carbon dioxide capture in amorphous porous organic polymers*.

[28] G. González, E. Colmenar, G. Diaconu, F. Alarcia, M. Manea, M. Paulis, M. J. Barandiaran, J. R. Leiza, J. C. de la Cal, J. M. Asua *Macromol. React. Eng.* **2009**, *3*, 233–240. *Production of Widely Different Dispersed Polymers in a Continuous Taylor–Couette Reactor*.

[29] L. Guérin, C. Coufort-Saudejaud, A. Liné, C. Frances *J. Colloid Interface Sci.* **2017**, *491*, 167–178. *Dynamics of aggregate size and shape properties under sequenced flocculation in a turbulent Taylor-Couette reactor*.

[30] G. Das, D. B. Shinde, S. Kandambeth, B. P. Biswal, R. Banerjee *Chem. Commun.*, **2014**, *50*, 12615–12618. *Mechanosynthesis of imine, β-ketoenamine, and hydrogen-bonded imine-linked covalent organic frameworks using liquid-assisted grinding*.

[31] Y. Zeng, R. Zou, Y. Zhao *Adv.Mater.* **2016**, *28*, 2855–2873. *Covalent Organic Frameworks for CO_2 Capture*.

[32] Y. Wang, C. Kang, Z. Zhang, A. K. Usadi, D. C. Calabro, L. S. Baugh, Y. D. Yuan, D. Zhao *ACS Sustainable Chem. Eng.* **2022**, *10*, 332–341. *Evaluation of Schiff-Base Covalent Organic Frameworks for CO_2 Capture: Structure–Performance Relationships, Stability, and Performance under Wet Conditions*.

[33] Y. Zhao, Y. Zhao, C. Wu, J. Qiu, H. Wang, Z. Li, Y. Zhao, J. Wang *Chem. Eur. J.* **2021**, *27*, 9391–9397. *An Ultrastable Crystalline Acylhydrazone-Linked Covalent Organic Framework for Efficient Removal of Organic Micropollutants from Water*.

[34] R. Shi, L. Liu, Y. Lu, C. Wang, Y. Li, L. Li, Z. Yan, J. Chen *Nat. Commun.* **2020**, *11*, 178. *Nitrogen-rich covalent organic frameworks with multiple carbonyls for high-performance sodium batteries*.

[35] M. Abdinejad, K. Tang, C. Dao, S. Saedy, T. Burdyny *J. Mater. Chem. A* **2022**, *10*, 7626–7636. *Immobilization strategies for porphyrin-based molecular catalysts for the electroreduction of CO_2*.

[36] H. L. Nguyen, A. Alzamly *ACS Catal.* **2021**, *11*, 9809–9824. *Covalent Organic Frameworks as Emerging Platforms for CO_2 Photoreduction*.

2

Synthesis, Characterization, and CO_2 uptake of Mellitic Triimide-Based Covalent Organic Frameworks

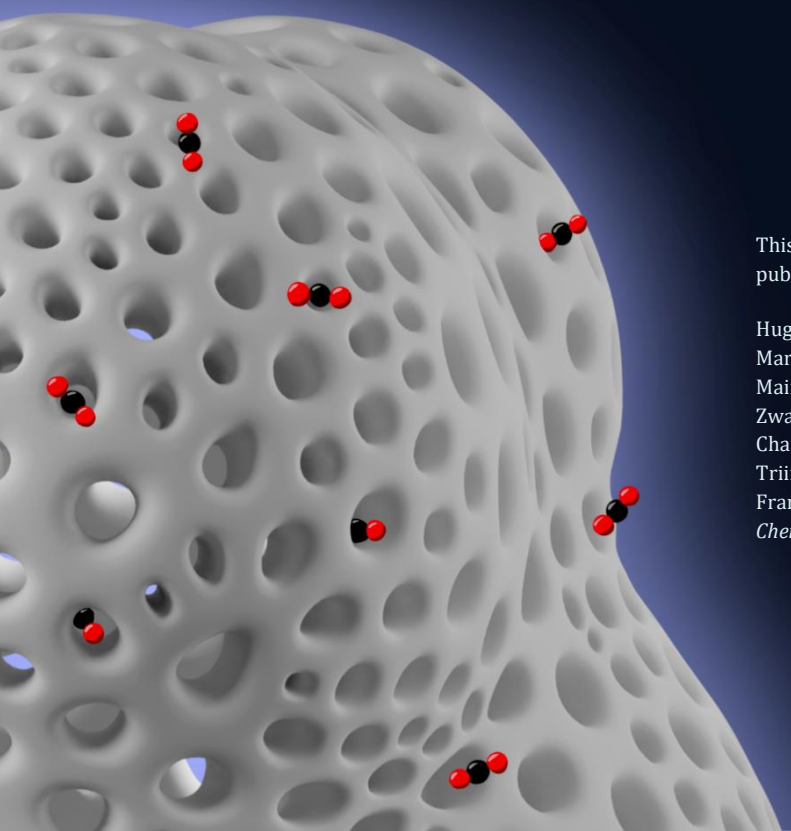

This chapter is based on the following publication:

Hugo Veldhuizen, Alexandros Vasileiadis, Marnix Wagemaker, Tadhg Mahon, Durga P. Mainali, Lishuai Zong, Sybrand van der Zwaag, Atsushi Nagai. Synthesis, Characterization, and CO_2 Uptake of Mellitic Triimide-Based Covalent Organic Frameworks. *J. Polym. Sci. Part A Polym. Chem.* **2019**, *57*, 2373–2377.

Abstract

Polyimide-based covalent organic frameworks (COFs) are a promising class of nanoporous polymers, as they significantly improve upon the thermal and chemical stability of known COFs, which pushes their applicability forward. This work expands the library of high-performance polyimide COFs through the imidization polymerization of mellitic trianhydride with two different triamines. The resulting porous polymers possess microporous structures (< 2 nm pore sizes), exhibit relatively large surface areas (> 300 $m^2 g^{-1}$) and are thermally stable up until 275 °C. Moreover, both COFs show good CO_2 uptake with capacities around 40 $cm^3 g^{-1}$.

2.1 INTRODUCTION

Among the material class of organic porous polymers, covalent organic frameworks (COFs) are a special subclass, because of their crystalline nature.[1] Moreover, depending on the building blocks, COFs can be designed with predictable pore shapes and sizes. The uniform and controlled porosity as a result of their crystallinity makes COFs perfect candidates for separation of gasses,[2] as well as purification of liquids.[3] Furthermore, redox-active COFs with a high surface area have become an increasingly interesting class of material for electrochemical energy storage devices.[4,5] Whatever the application, a high thermal and chemical stability of the structural linkages of COFs is very important and this drove the direction of the research as reported in this paper.

Generally, dynamic covalent chemistry is a requisite for the creation of crystalline COFs, since it allows for error-checking and reparation of amorphous segments in order to form the thermodynamically stable structure (*i.e.* the crystal). For this reason, highly reversible boroxine and boron ester bonds where the first to be employed as connecting linkages in COFs.[6,7] Although these early COFs were not excellent in terms of stability, recent advances were made towards the development of structurally more robust frameworks.[8–11] In particular, polyimide COFs bring a high chemical and thermal stability to this material class,[8,12,13] which will push their applicability forward.

In this research, we designed and synthesized mellitic triimide (MTI)-based COFs derived from mellitic trianhydride (MTA) with 1,3,5-tris(4-aminophenyl)benzene (TAPB) or 1,3,5-tris(4-aminophenyl)amine (TAPA) to yield **MTI-COF-1** or **MTI-COF-2**, respectively. The combination of the small monomer mellitic trianhydride in the polymerization of A_3 with B_3 monomers contributes to the formation of porous (quasi-) crystalline materials with hexagonal micropores (< 2 nm). In addition, MTI-based materials are being studied because of their excellent redox-activity.[14–16] By utilizing MTI in an A_3-B_3 COF, we introduce a large number of active sites with respect to the overall molecular weight of the unit cell. Therefore, we envisage that this material could be interesting in both gas separation (due to its micropores) and energy storage (due to its redox-active groups) applications.

2.2 RESULTS AND DISCUSSION

The synthesis of **MTI-COF-1** and **MTI-COF-2** goes *via* a polycondensation reaction of MTA as trianhydride with TAPB or TAPA as primary triamines respectively,

using solvothermal conditions (Scheme 1). MTA was synthesized from mellitic acid and acetic anhydride (Supporting Information), while TAPB and TAPA were commercially obtained. The monomers were suspended in a mixed solvent of equal amounts of *meta*-cresol and *N*-methyl-2-pyrrolidone, and isoquinoline was used as the catalyst. Degassed reaction mixtures were flame sealed in glass ampules and left for three days in an oven at 150 °C. The resulting polymers were assessed regarding their chemical structure, crystallinity and porosity.

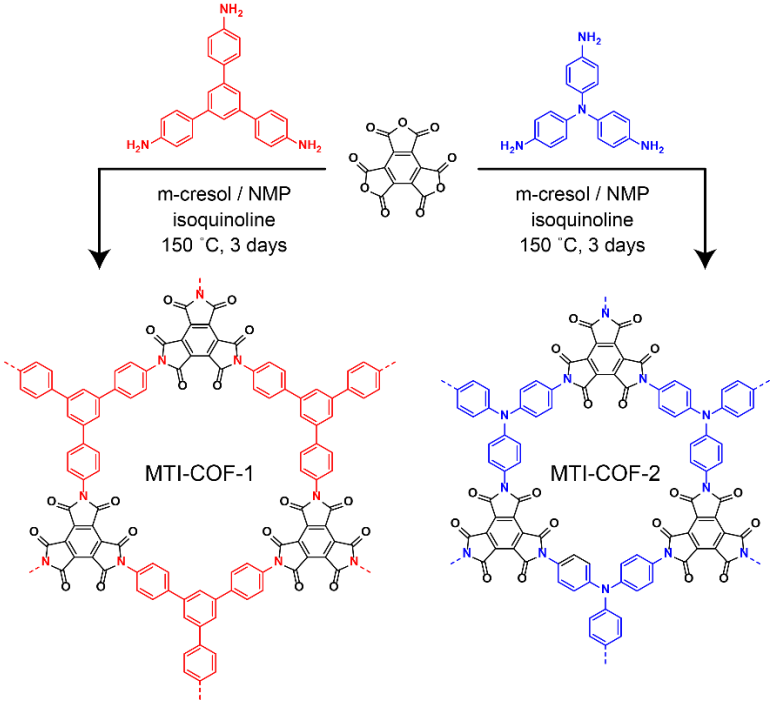

Scheme 1 Polycondensation of MTA with TAPB, or TAPA to yield **MTI-COF-1**, or **MTI-COF-2** respectively.

Imide formation was confirmed with FT-IR spectroscopy (Figures 1A and 1B). For both COFs, the characteristic C=O anhydride peaks at 1791 (symm.) and 1871 (asymm.) cm^{-1} disappeared. Additionally, the N–H amine peaks around 3400 cm^{-1} for TAPB and TAPA were not detected in the obtained COF materials. Characteristic imide carbonyl (C=O) peaks around 1730 (symm.) and around 1780 cm^{-1} (assym.) were observed for both COF materials. Moreover, the broad peaks at 1372 and 1382 cm^{-1} for **MTI-COF-1** and **MTI-COF-2** respectively, were attributed to imide C–N stretching. Thus, polyimide formation was confirmed for both COFs. Furthermore, the thermal properties of the polymers were determined by thermogravimetric analysis (TGA). The 5% weight loss decomposition

temperatures for **MTI-COF-1** and **MTI-COF-2** were 291 and 275 °C, respectively (Supporting Information). Although still moderately thermally stable, these temperatures are lower than reported decomposition temperatures of polyimide COFs (> 400 °C).[8,12,13] This observation may be an indication of an amount of polyamic acid intermediate to be still present in the frameworks (possibly explaining the first decomposition step in Figure S2), but closer investigation is required. Lastly, chemical stability checks in various liquid media were carried out (Supporting Information). Given the synthesis and purification conditions we conclude that the COFs are stable in organic solvents. While the additional stability checks showed good framework retention in pure water and acid solutions. Alkali aqueous solutions, however, significantly affect the framework stability, as is to be expected for polyimide polymers.[17]

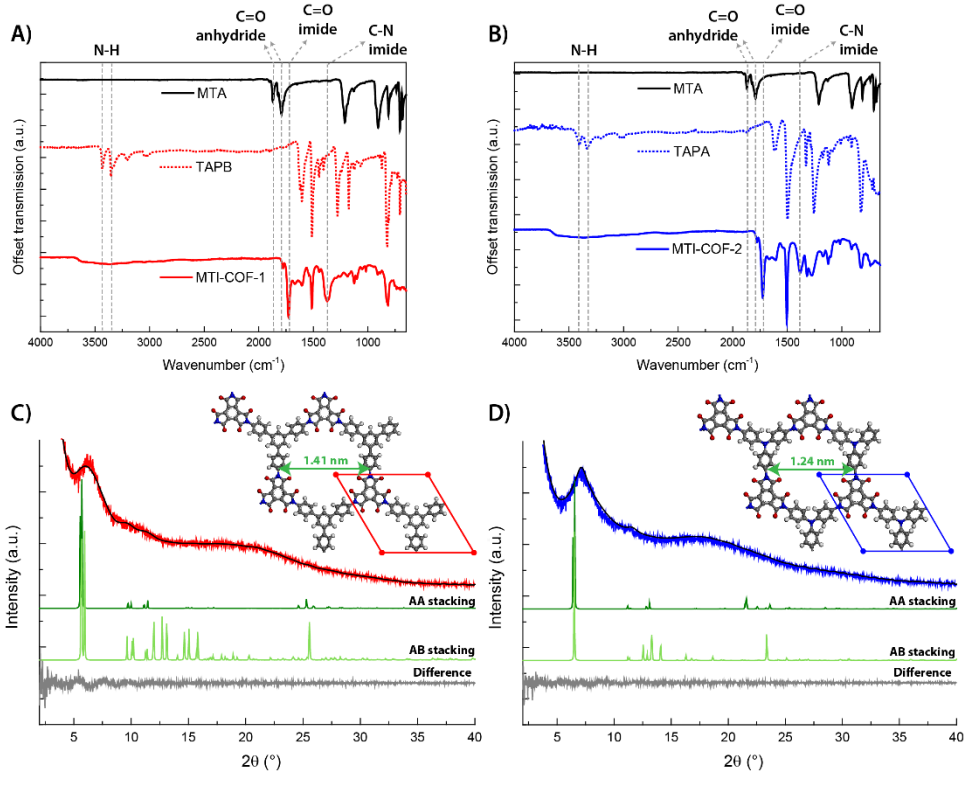

Figure 3 A) FT-IR spectra of monomers MTA and TAPB, and polymer **MTI-COF-1**. **B)** FT-IR spectra of monomers MTA and TAPA, and polymer **MTI-COF-2**. **C) and D)** Experimental (red line for **MTI-COF-1**; blue for **MTI-COF-2**) vs. Pawley refined (black line) vs. their corresponding simulated (dark green for AA; light green for AB stacking) PXRD data. The refinement agreements for **MTI-COF-1** are R_{wp} = 3.77% and R_p = 2.93%, and for **MTI-COF-2** R_{wp} = 3.71% and R_p = 2.83%.

Structural characterization was further carried out by means of powder X-ray diffraction (PXRD) measurements, and the experimental spectra were compared with the computer simulated patterns (Figures 1C and 1D). Although both COFs were found to also contain amorphous segments, a well-defined short-range order was observed, which corresponds to theoretically expected micropore sizes: 1.41 nm for **MTI-COF-1** and 1.24 nm for **MTI-COF-2**. In addition, structural optimizations were performed computationally with a classical force field approach (using Materials Studio v8.0, see Supporting Information). During these simulations, both COFs relaxed from a completely flat 2D sheet to a non-flat configuration, exhibiting torsion within the framework. The main cause was discovered to be a break of 2D symmetry of the triamine linkage molecules TAPB and TAPA. The preferred torsion angles between the outer benzene rings of these segments were calculated to be 33° for **MTI-COF-1** and 36° for **MTI-COF-2**. Similar torsion angles between the MTI segments and the outer benzene rings of TAPB and TAPA were also observed (Supporting Information). Since this transition was self-occurred during the geometry optimization, it indicates that there is no (or small) energy barrier for this transition and that both COFs will naturally obtain a configuration exhibiting torsion. Furthermore, the packing of the 2D polymer sheets was computationally investigated: AA stacking representing adjacent sheets to perfectly overlap and to create straight 1D channels, and AB stacking representing an offset of 1 unit cell between neighboring sheets not leading to continuous 1D channels. The most stable conformation in both COFs was the AA stacking mode. The simulated AA stacking PXRD patterns were then utilized as a basis for Pawley refinement of the experimental diffraction patterns. In both cases, a good agreement was obtained (Figures 1C and 1D), and the crystallographic data of both COFs can be found in the Supporting Information. The simulated PXRD data of the AA stacked COFs matched well with the experimental reflections, and better than for an assumed AB stacking mode.

Scanning electron microscopy (SEM) images of **MTI-COF-1** and **MTI-COF-2** are shown in Figures 2A–2B and 2C–2D, respectively. No clear difference in morphology between the two COFs was observed. Both polymers show aggregation of nanosphere particles with sizes of the order of 100 to 200 nm. In addition, the aggregates reflect the presence of macroporous structures. To quantify the porosity levels more quantitatively, nitrogen gas sorption measurements were performed (Figure 2E). The isotherms of both COFs resemble typical type II isotherms, which confirms the presence of micropores. The surface areas of both COF samples were calculated through the Brunauer–Emmett–Teller (BET) theory. Both COFs exhibited a good porosity level, with BET surface areas of

339 m^2 g^{-1} for **MTI-COF-1** and 397 m^2 g^{-1} for **MTI-COF-2**. Such values are within the range of surface areas of state-of-the-art microporous polymers, and it is expected that further improvement of the polymerization conditions could contribute to an even more porous structure. Additionally, pore size distributions were calculated on the basis of the nitrogen isotherms (Figure S2). Although it was not possible to extract specific micropore sizes from these isotherms, the pore sizes distributions were centered around the lower limit of mesopores (2 nm) and expectedly more so around the micropores.

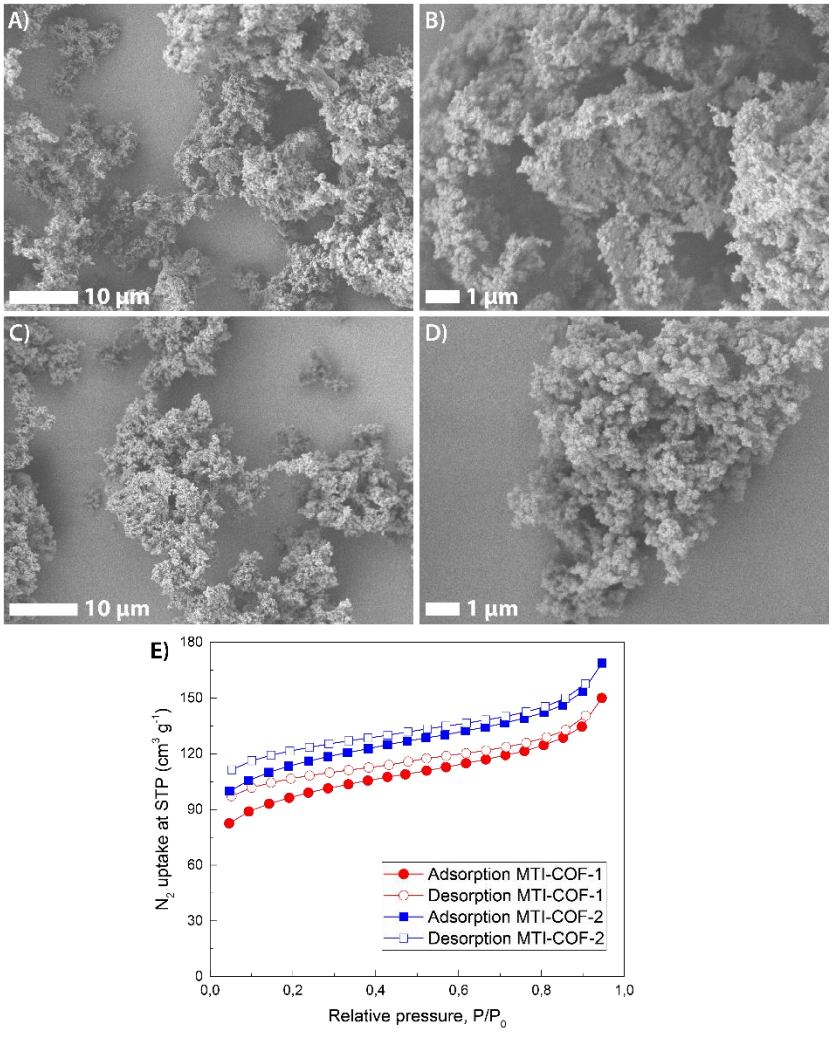

Figure 2 A) and **B)** SEM micrographs of **MTI-COF-1**. **C)** and **D)** SEM micrographs of **MTI-COF-2**. **E)** Nitrogen sorption isotherms of **MTI-COF-1** (red) and **MTI-COF-2** (blue) measured at 77 K.

Additionally, the CO_2 adsorption performance of **MTI-COF-1** and **MTI-COF-2** of was determined. The isotherms were measured at 273 K over a range of 3 to 997 mbar, and the data are shown in Figure 3, using the conventional protocol of plotting CO_2 uptake versus the absolute pressure. CO_2 capacities at 273 K and 1 bar were measured to be 39 and 46 $cm^3\ g^{-1}$ for **MTI-COF-1** and **MTI-COF-2,** respectively. Interestingly, despite having different molecular sizes and physicochemical adsorption mechanisms, both nitrogen and carbon dioxide gas adsorbed better to **MTI-COF-2** than to **MTI-COF-1**. A possible reason for this is the large difference of the *c* lattice parameter between the two porous polymers (as a result of the difference in torsion angles reported earlier), which is 3.7 Å for **MTI-COF-1**, and 4.2 Å for **MTI-COF-2**. A larger c lattice parameter could cause elongation of the 1D COF channels, which exposes a larger accessible area for gas molecules. At the same time, it is likely that such a large interlayer distance allows gas to not only enter the COF *via* the 1D channel ends, but parallel to the layers as well.

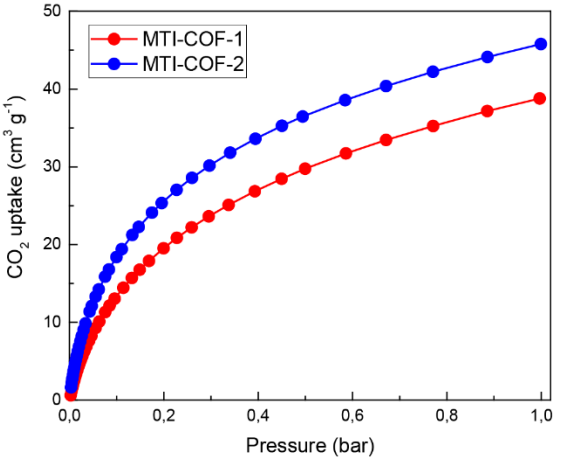

Figure 3 Carbon dioxide adsorption isotherms of **MTI-COF-1** (red) and **MTI-COF-2** (blue) measured at 273 K

Nevertheless, the CO_2 storage capacity values for both polymers are relatively high, considering the fact that no additional pore surface engineering was used to further enhance the capacities.[18] Incorporation of CO_2 fixating groups along the polymer backbone,[19,20] might also be a strategy applicable to COF research in order to increase the CO_2 storage capacity values even further. In addition, these MTI-based porous polymers are among the first polyimide polymers to be employed as CO_2 gas hosts, and their CO_2 uptake is already comparable to that of the widely tested imine, triazine, and boronate COFs.[21] Also, a pressing issue of competing

metal-organic frameworks (MOFs), and boronate COFs is their lack of good performance in CO_2 uptake under humid conditions or in general their hydrolytic stability.[22–24] The porous materials presented in this research, however, are expected to not be affected by humidity because of the general stability of polyimides in aqueous environments. Research to confirm this expectation has been initiated and the results will be reported elsewhere.

2.3 CONCLUSION

In summary, mellitic triimide COFs have been synthesized in high yields through imidization of mellitic trianhydride with two different triamines. Both COFs displayed short-ranged crystalline order, corresponding to expected micropore sizes. Computational studies revealed that the 2D polymer sheets were adopting a non-flat configuration, due to torsions between the linking monomers. Both COFs exhibited porous structures with good surface areas, and affinities towards nitrogen and carbon dioxide gasses. The combination of high surface areas with micropores makes these porous polymers good candidates for separation fields, as well as energy storage applications, considering their expected redox-activities.

ACKNOWLEDGEMENTS

A.N. dedicates this manuscript to Prof. Takeshi Endo in recognition of his inspirational mentorship and ground-breaking achievements in the field of polymer chemistry. The authors also thank Dalian University of Technology for the permission to use their Materials Studio software package.

2.4 SUPPORTING INFORMATION

2.4.1 MATERIALS

All chemicals which are presented in this research (with the exception of mellitic trianhydride shown in section C) were commercially available and were used without further treatment. Chemicals including mellitic acid; 1,3,5-tris(4-aminophenyl)benzene; 1,3,5-tris(4-aminophenyl)amine (TAPA); isoquinoline; and *meta*-cresol were purchased from TCI Europe N.V. Acetic anhydride was purchased from Sigma Aldrich.

2.4.2 Characterization methods

NMR spectra were recorded at 298 K on an Agilent-400 MR DD2 spectrometer (400 MHz) in DMSO-d_6. FT-IR spectra were recorded on a PerkinElmer Spectrum 100 FT-IR Spectrometer with the Universal ATR Accessory over a range of 4000 to 650 cm^{-1}. PXRD data were collected on a Rigaku MiniFlex 600 powder diffractometer using a Cu-Kα source (λ = 1.5418 Å) over the 2θ range of 2° to 60° with a scan rate of 1°/minute. Scanning electron microscopy (SEM) images were recorded with a JEOL JSM-840 SEM: materials were deposited onto a sticky carbon surface on a flat sample holder, vacuum-degassed, and subjected to gold sputtering. Nitrogen isotherms were measured on the NOVAtouch gas sorption analyzer from Quantachrome Instruments with high purity N_2 (99.99%) at 77 K. Non-Local Density Functional Theory (NLDFT) simulations on the basis of the experimental nitrogen adsorption isotherms were performed to calculate the pore size distributions. Carbon dioxide measurements were performed at 273 K on a Quantachrome NOVA gas sorption analyzer. Thermal properties were determined by thermogravimetric analysis (TGA). TGA analyses were performed from room temperature to 860 °C, under nitrogen atmosphere at 10 °C/min heating rate using a Perkin Elmer TGA 4000. Prior to the measurement, the samples were dried at 100 °C for one hour.

Molecular modeling of the COFs was carried out using the Materials Studio (v8.0) suite of programs by Accelrys. The unit cell precursor (without the lattice) was defined as one MTI-unit with either one TAPB or one TAPA unit. Thereafter, lattice parameters a and b were initially set as the measured distance between the outer nitrogen atom of MTI and the outer benzene carbon of TAPB or TAPA in the energy optimized (using the Forcite module) precursor unit cell. Lattice parameter c was arbitrarily set at 4 Å, alpha and beta were set at 90°, and gamma was set at 120°. After geometry optimization using Forcite, the Powder Reflex module was used to calculate expected PXRD patterns. The experimental PXRDs were subjected to Pawley refinement using the Pseudo-Voigt peak shape function and Finger-Cox-Jephcoat asymmetry correction function (up to 20°) to produce the refined profiles.

2.4.3 SYNTHESIS

Mellitic trianhydride was synthesized according to a literature procedure.[1] The reaction was monitored with FT-IR analysis and after four hours the carboxylic acids were fully converted. We altered the work-up procedure as followed: after four hours, the reaction mixture was poured into dry diethyl ether, and subsequently filtered to yield the final product bearing a white color with a 53% yield.

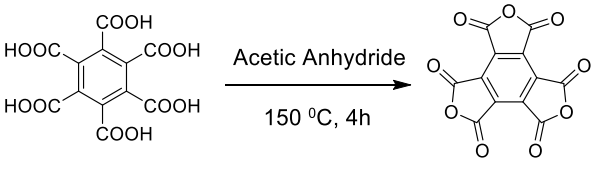

MTA:^{1}H NMR (400 MHz, DMSO-d_6, δ): -; ^{13}C NMR (100 MHz, DMSO-d_6, δ): 164.2, 163.0, 160.0, 157.7, 134.9, 133.7, 129.7; IR (ATR): ν = 1870 (m), 1791 (s), 1212 (s), 906 (s), 812 (s), 707 (s), 683 (s) cm^{-1}.

[1] G. A. Adamson, C. W. Rees, *J. Chem. Soc., Perkin Trans. 1* **1996**, 1535-1543.

Synthesis of MTI-COFs

A 10 mL Pyrex tube was charged with MTA (144.1 mg, 0.5 mmol), and TAPB (175.7 mg, 0.5 mmol) or TAPA (145.2 mg, 0.5 mmol) in a solution of *m*-cresol / NMP (4 mL / 4 mL). The reaction mixture was stirred for 5 minutes and sonicated for 2 minutes. Isoquinoline (0.1 mL) was added, after which the tube was directly degassed via three freeze-pump-thaw cycles at 77K, and subsequently flame sealed. Then, the tube was heated in a 150°C oven for 3 days. The resulting precipitate was washed with methanol (3x 10 mL) and acetone (3x 10 mL) and recovered by centrifugation. The resulting compound was purified by Soxhlet extraction in THF for 16h, and then dried at 60°C under vacuum for 16h to provide **MTI-COF-1** as an ochre powder (275 mg, 94 %) and **MTI-COF-2** as a brown powder (239 mg, 91%).

MTI-COF-1: IR (ATR): *ν* = 1778 (w), 1727 (s), 1669 (m), 1605 (m), 1514 (s), 1372 (bs), 1125 (m), 816 (s) cm^{-1}.

MTI-COF-2: IR (ATR): *ν* = 1778 (w), 1725 (s), 1666 (m), 1606 (m), 1505 (s), 1381 (bm), 1319 (bm), 1275 (bm), 1125 (m), 819 (bm) cm^{-1}.

2.4.4 NITROGEN SORPTION

Figure S1 shows the BET plots of **MTI-COF-1** and **MTI-COF-2**, from which we calculated surface areas of 339 and 397 m^2 g^{-1} respectively for the porous materials.

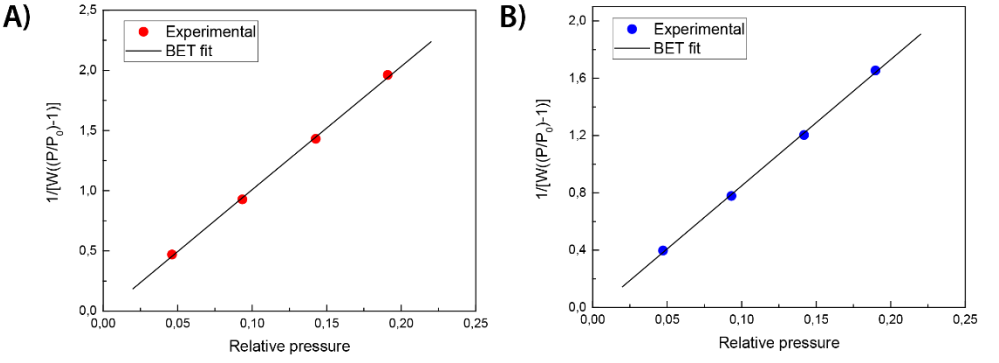

Figure S1 A) BET plot of **MTI-COF-1** calculated from the N_2 adsorption isotherm at 77 K. BET surface area = 339 m^2 g^{-1}. **B)** BET plot of **MTI-COF-2** calculated from the N_2 adsorption isotherm at 77 K. BET surface area = 397 m^2 g^{-1}.

2.4.5 PORE SIZE DISTRIBUTION

Figure S2 shows the pore size distributions (PSDs) of **MTI-COF-1** and **MTI-COF-2**, derived from the N_2 isotherms. Since these were measured with a minimum relative pressure of 0.05 P/P_0, we were not able to extract the exact micropore sizes. However, Figure S2 does indicate the favor of lower region mesopores (and expectedly micropores) over general mesopores.

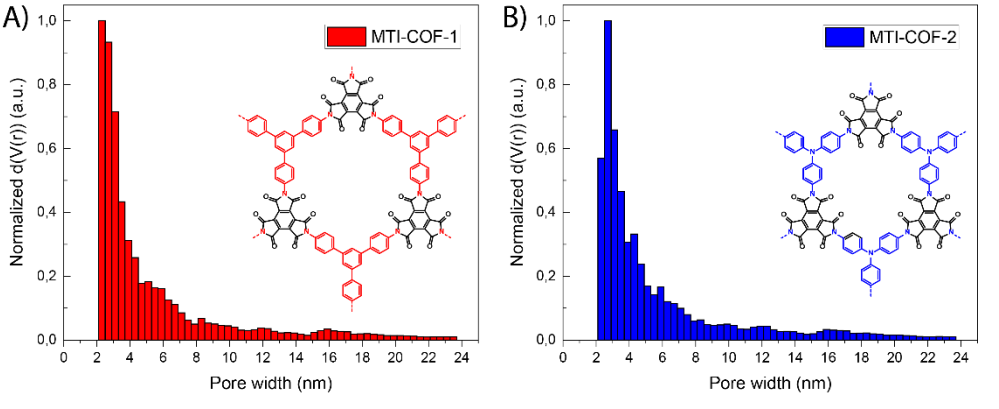

Figure S2 A) PSD of **MTI-COF-1** calculated from the N_2 adsorption isotherm at 77 K. **B)** PSD of **MTI-COF-2** calculated from the N_2 adsorption isotherm at 77 K.

2.4.6 THERMOGRAVIMETRIC ANALYSIS

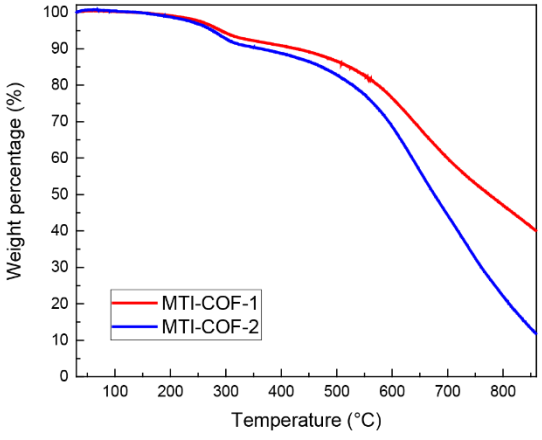

Figure S3 TGA profiles of **MTI-COF-1** (red) and **MTI-COF-2** (blue). The temperatures at 5 and 10 percent weight loss for **MTI-COF-1** were 291 and 427 °C respectively, and those of **MTI-COF-2** were 275 and 363 °C respectively.

2.4.7 STABILITY CHECK WITH PXRD

Stability checks were performed by stirring roughly 80 mg of COF in a 4 mL solution of water, 3 M HCl, or 0.1 M NaOH for 16 hours at room temperature. After stirring, the COFs were washed with water (2 x 10 mL) and acetone (2 x 10 mL), dried for 2 hours under vacuum at 60 °C, after which PXRD measurements were carried out.

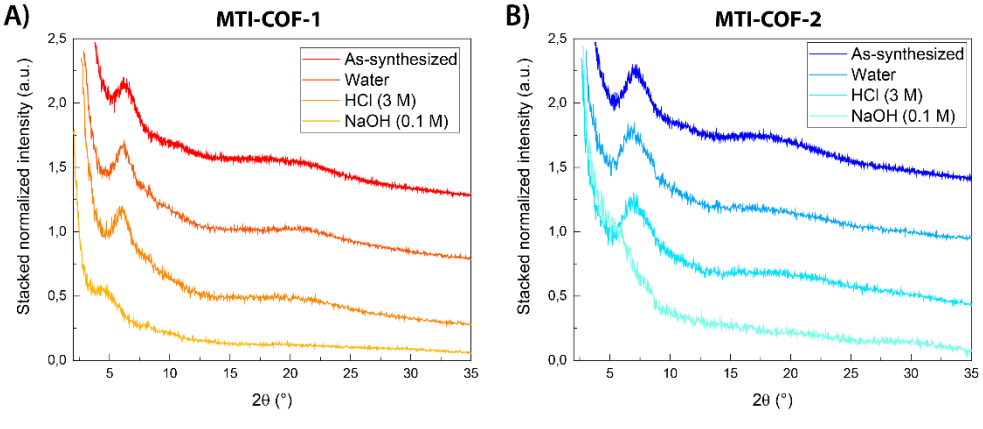

Figure S4 Experimental PXRD data after stability experiments under various conditions of: **A) MTI-COF-1** and **B) MTI-COF-2**.

2.4.8 Crystal structures

Below we present the simulated crystal structures of **MTI-COF-1** and **MTI-COF-2**.

MTI-COF-1 AA stacking

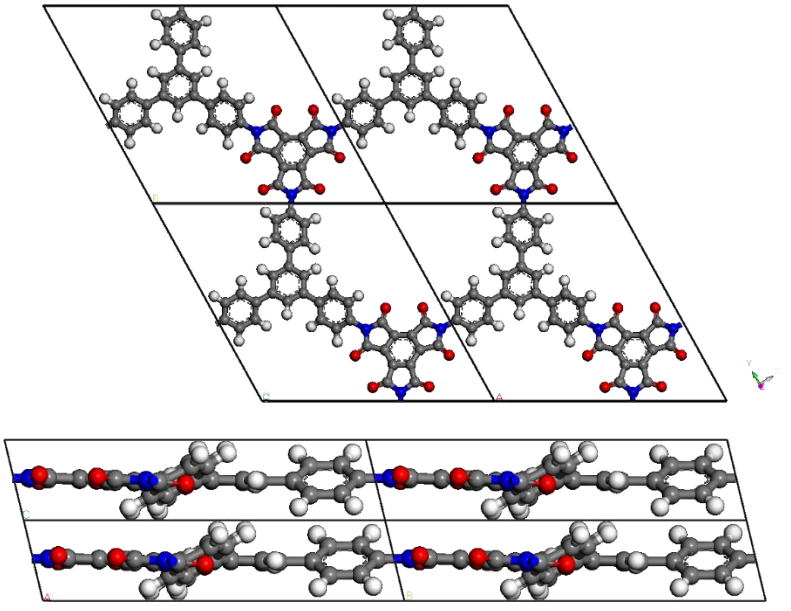

MTI-COF-1 AB stacking

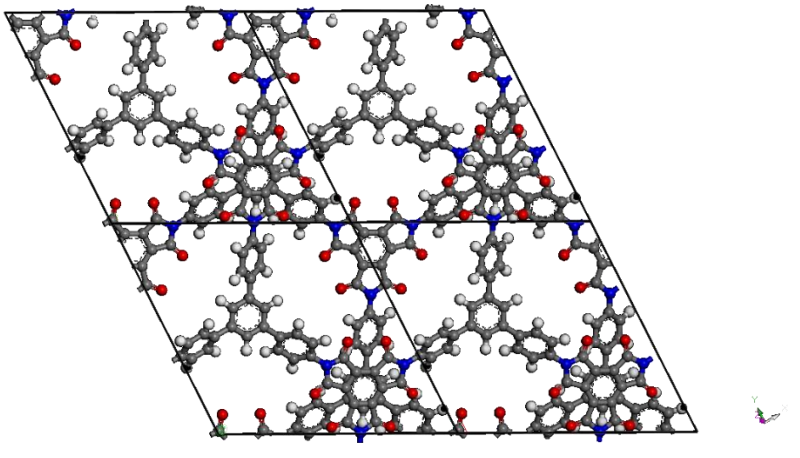

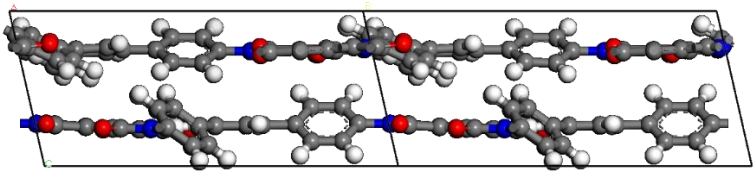

MTI-COF-2 AA stacking

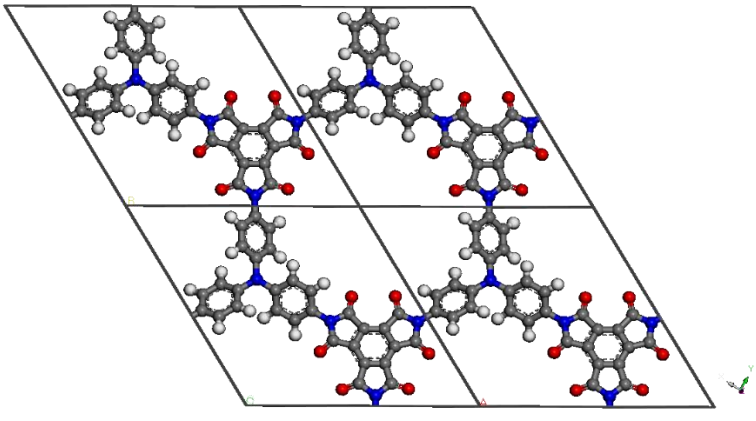

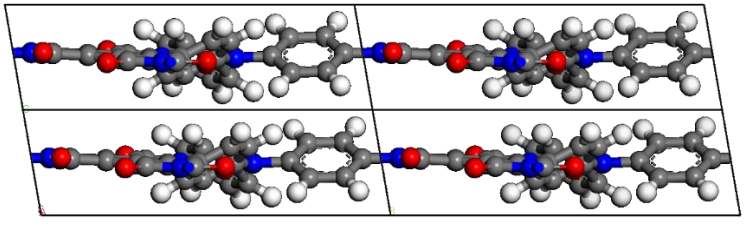

MTI-COF-2 AB stacking

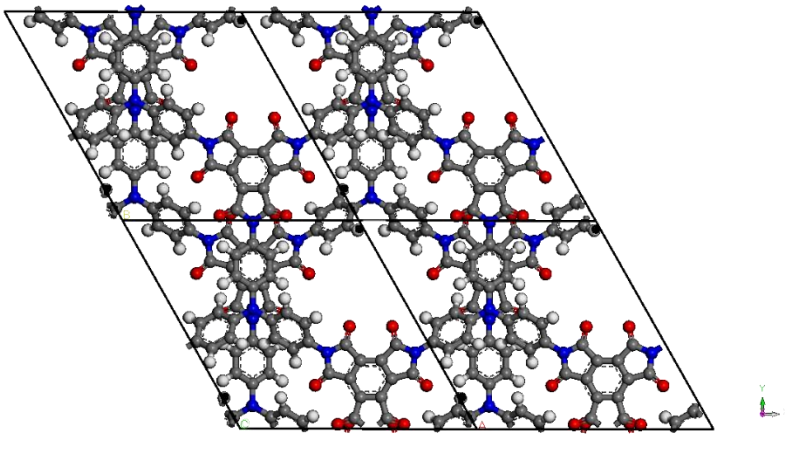

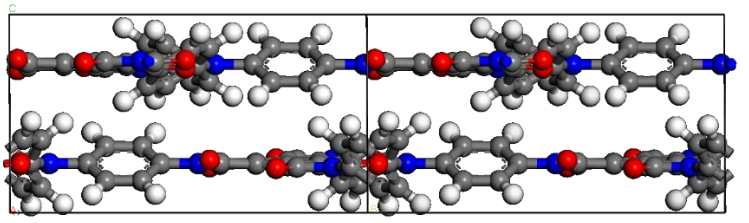

s.g.	MTI-COF-1 AA (P1)	MTI-COF-1 AB (P1)	MTI-COF-1 AA (P1)	MTI-COF-1 AB (P1)
a (Å)	18.337	18.324	16.082	15.798
b (Å)	18.393	18.363	16.266	15.845
c (Å)	3.656	7.451	4.238	7.705
alpha (°)	105.571	71.031	95.428	94.642
beta (°)	82.264	106.392	95.805	81.140
gamma (°)	119.721	119.930	120.702	119.905

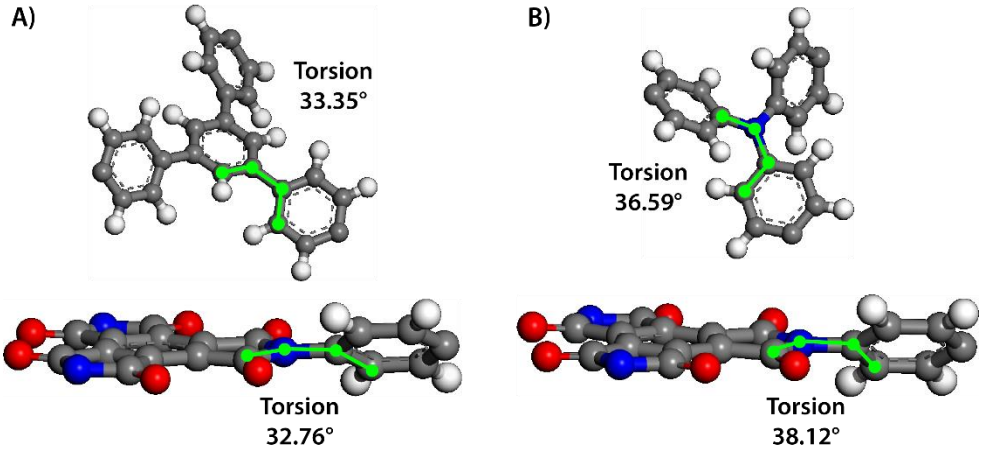

Figure S5 A) Segments within AA stacking crystal structure of **MTI-COF-1** showing the torsions that are responsible for non-flat 2D polymer sheets. **B)** Segments within AA stacking crystal structure of **MTI-COF-2** showing the torsions that are responsible for non-flat 2D polymer sheets.

References

1. X. Feng, X. Ding, D. Jiang, *Chem. Soc. Rev.* **2012**, *41*, 6010–6022.

2. S. S. Han, H. Furukawa, O. M. Yaghi, W. A. Goddard, *J. Am. Chem. Soc.* **2008**, *130*, 11580–11581.

3. H. Fan, J. Gu, H. Meng, A. Knebel, J. Caro, *Angew. Chemie Int. Ed.* **2018**, *57*, 4083–4087.

4. C. R. DeBlase, K. E. Silberstein, T.-T. Truong, H. D. Abruña, W. R. Dichtel, *J. Am. Chem. Soc.* **2013**, *135*, 16821–16824.

5. S. B. Alahakoon, C. M. Thompson, G. Occhialini, R. A. Smaldone, *ChemSusChem* **2017**, *10*, 2116–2129.
6. A. P. Côté, A. I. Benin, N. W. Ockwig, M. O'Keeffe, A. J. Matzger, O. M. Yaghi, *Science* **2005**, *310*, 1166 LP-1170.
7. H. M. El-Kaderi, J. R. Hunt, J. L. Mendoza-Cortés, A. P. Côté, R. E. Taylor, M. O'Keeffe, O. M. Yaghi, *Science* **2007**, *316*, 268 LP-272.
8. Q. Fang, Z. Zhuang, S. Gu, R. B. Kaspar, J. Zheng, J. Wang, S. Qiu, Y. Yan, *Nat. Commun.* **2014**, *5*, 1–8.
9. F. J. Uribe-Romo, C. J. Doonan, H. Furukawa, K. Oisaki, O. M. Yaghi, *J. Am. Chem. Soc.* **2011**, *133*, 11478–11481.
10. C. R. DeBlase, W. R. Dichtel, *Macromolecules* **2016**, *49*, 5297–5305.
11. S. Kandambeth, D. B. Shinde, M. K. Panda, B. Lukose, T. Heine, R. Banerjee, *Angew. Chemie Int. Ed.* **2013**, *52*, 13052–13056.
12. Q. Fang, J. Wang, S. Gu, R. B. Kaspar, Z. Zhuang, J. Zheng, H. Guo, S. Qiu, Y. Yan, *J. Am. Chem. Soc.* **2015**, *137*, 8352–8355.
13. L. Jiang, Y. Tian, T. Sun, Y. Zhu, H. Ren, X. Zou, Y. Ma, K. R. Meihaus, J. R. Long, G. Zhu, *J. Am. Chem. Soc.* **2018**, *140*, 15724–15730.
14. K. A. McMenimen, D. G. Hamilton, *J. Am. Chem. Soc.* **2001**, *123*, 6453–6454.
15. J. B. Carroll, M. Gray, K. A. McMenimen, D. G. Hamilton, V. M. Rotello, *Org. Lett.* **2003**, *5*, 3177–3180.
16. Y. Kofuji, S. Ohkita, Y. Shiraishi, H. Sakamoto, S. Ichikawa, S. Tanaka, T. Hirai, *ACS Sustain. Chem. Eng.* **2017**, *5*, 6478–6485.
17. L. E. Stephans, A. Myles, R. R. Thomas, *Langmuir* **2000**, *16*, 4706–4710.
18. N. Huang, R. Krishna, D. Jiang, *J. Am. Chem. Soc.* **2015**, *137*, 7079–7082.
19. B. Ochiai, K. Yokota, A. Fujii, D. Nagai, T. Endo, *Macromolecules* **2008**, *41*, 1229–1236.
20. M. Sakuragi, N. Aoyagi, Y. Furusho, T. Endo, *J. Polym. Sci. Part A Polym. Chem.* **2014**, *52*, 2025–2031.
21. Y. Zeng, R. Zou, Y. Zhao, *Adv. Mater.* **2016**, *28*, 2855–2873.
22. A. C. Kizzie, A. G. Wong-Foy, A. J. Matzger, *Langmuir* **2011**, *27*, 6368–6373.
23. J. Liu, J. Tian, P. K. Thallapally, B. P. McGrail, *J. Phys. Chem. C* **2012**, *116*, 9575–9581.
24. L. M. Lanni, R. W. Tilford, M. Bharathy, J. J. Lavigne, *J. Am. Chem. Soc.* **2011**, *133*, 13975–13983.

3

Impact of Flow-Induced Disturbances During Synthesis on the Photophysical Properties of Naphthalene Diimide Covalent Organic Frameworks

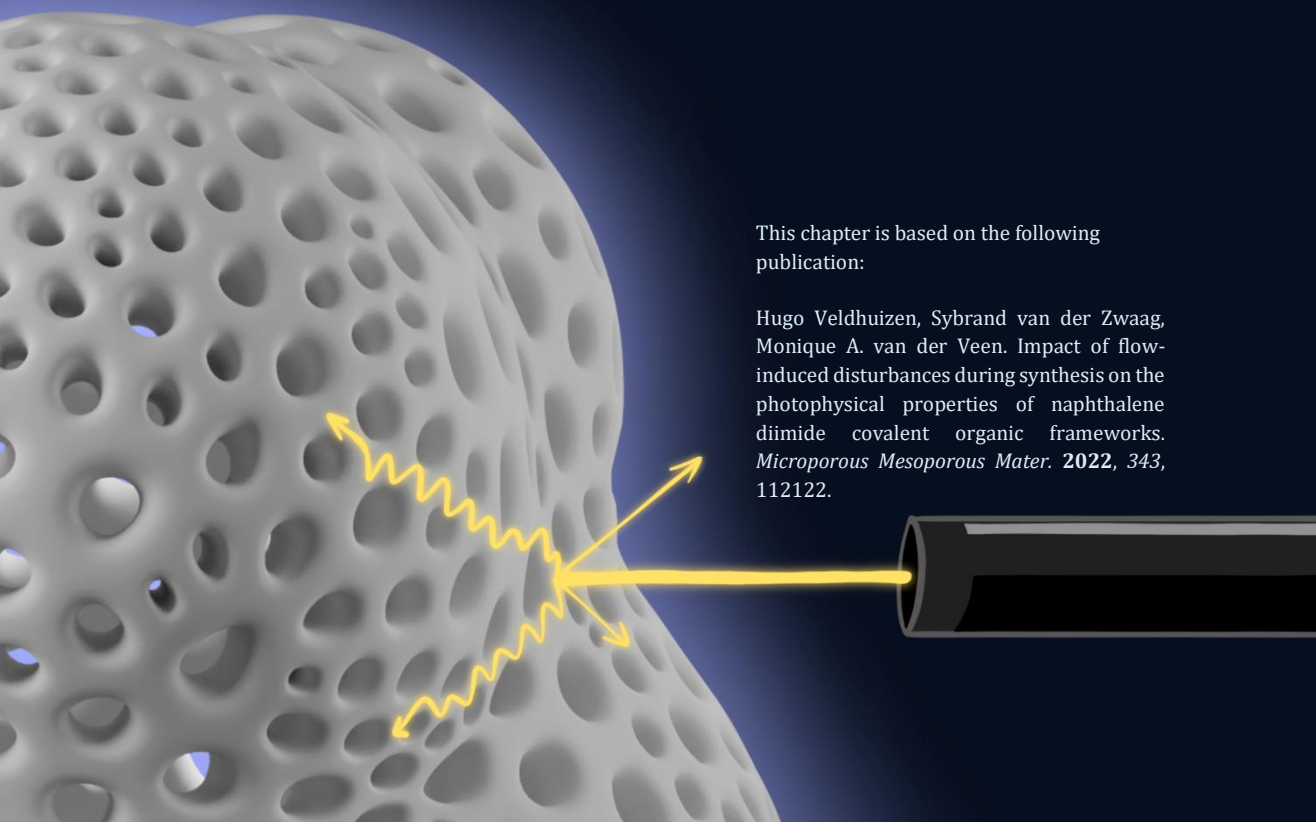

This chapter is based on the following publication:

Hugo Veldhuizen, Sybrand van der Zwaag, Monique A. van der Veen. Impact of flow-induced disturbances during synthesis on the photophysical properties of naphthalene diimide covalent organic frameworks. *Microporous Mesoporous Mater.* **2022**, *343*, 112122.

Abstract

Flow-induced disturbances were applied during the synthesis of a naphthalene diimide covalent organic framework (NDI-COF), which resulted in different COF polymer networks. We discovered that a high intensity of stirring resulted in more aggregated structures on both the micro- and nano-length scale. Subsequently, these structures absorbed light over longer wavelengths due to a relatively higher contribution of intermolecular interactions between the NDI-segments.

3.1 INTRODUCTION

Among the material class of hyper-crosslinked polymers with permanent porosity, there is the subclass of covalent organic frameworks (COFs). These polymers are designed to display a degree of crystallinity, which can range from large single crystals to local crystalline domains of few repeating units in an overall amorphous network [1]. The porous structure of a COF depends for a large part on the chemistry and geometry of the building blocks. Moreover, the COF chemistry and polymer network dictate the functional properties, such as redox- and catalytic-activity [2], photovoltaic effect [3] and greenhouse gas capture capacity [4].

Conventional COF synthesis is typically executed in a highly controlled environment (i.e. glass ampules in an oven), in order to carefully regulate the experimental conditions (uniform temperature over long reaction times, inert atmosphere, controlled pressure). In addition, the reaction mixture is usually static, as it is implicitly accepted to be more helpful in the formation of regular, crystalline structures for systems with reversible chemical bonds which would undo topological imperfections. However, the evidence that optimal functional properties are obtained for the best structured networks is weak. In the field of carbon capture, for example, the amorphous counterparts of COFs (i.e. porous organic polymers, POPs) reach similar levels of CO_2 capacity [5]. As an additional benefit, POPs have a broader library of linking chemistries to their disposal. Similarly, both COFs and POPs have shown to be promising redox-active materials in electrochemical devices (irrespective of their degree of crystallinity) [6,7]. Theoretically, highly conjugated, crystalline COFs should provide additional electron transport pathways; boosting the device performance [8]. In practice, however, both COFs and POPs often still need to be hybridized with conductive agents for electrode fabrication and their performances remain comparable.

In this work, we deliberately applied flow-induced disturbances during the synthesis of a COF to affect the final polymer network. We distinguished three types of agitation: static, mild, and intense stirring. The COF chosen for this work is structured by naphthalene diimide linkages, since the functional properties of the 1D-polymer variants of these systems have a high dependency on polymer architecture [9,10]. In addition, utilizing poorly-reversible imide-connections in the polymer backbone fits this research well, since the flow-induced disturbances should not affect the in-plane crystallinity as much as more reversible COF systems. The molecular and porous structure of the three NDI-COFs presented here are

characterized with FT-IR, PXRD, N_2 sorption, and SEM, while the focus of the functional properties is on the photophysical properties.

3.2 Experimental

3.2.1 Materials

All reagents presented in this report were commercially available and used without further purification or treatment. 1,3,5-Tris(4-aminophenyl)benzene (≥ 93 %), 5'-Phenyl-[1,1':3',1''-terphenyl]-4-amine (≥ 98 %), and isoquinoline were purchased from TCI Europe N.V (Zwijndrecht, Belgium), 1,4,5,8-naphthalenetetracarboxylic dianhydride (≥ 95 %) and ortho-dichlorobenzene from abcr GmbH (Karlsruhe, Germany) and N-methyl-2-pyrrolidone from Acros Organics B.V.B.A (Geel, Belgium).

3.2.2 Covalent organic framework synthesis

Fig. 1 shows a schematic overview of the COF chemistry and different synthesis methods employed in this research. All syntheses were performed in borosilicate glass flat-bottom 100 mL cylindrical reactors, using the monomers 1,3,5-tris(4-aminophenyl)benzene (TAPB), and 1,4,5,8-naphthalenetetracarboxylic dianhydride (NTCDA). COFs named 'static' were not agitated during synthesis, while 'stir bar' COFs were continuously stirred with a conventional stir bar. Lastly, intense stirring was applied by utilizing a cylindrical mechanical stirrer in the reactor, resembling a Taylor-Couette reactor (TCR) [11]. Considering the rotational speed and dimensions of the reactor and stirrer, the continuous and homogeneous shear rate for the TCR method is estimated at 250 s^{-1}. On the other hand, the stir bar method imposes a highly heterogeneous shear rate; ranging from $\dot{\gamma}_{min}$ = 4.5 s^{-1} to a very local maximum at the stir bar tip of $\dot{\gamma}_{max}$ = 190 s^{-1} (Fig. S2). The detailed synthesis protocols of static, stir bar and TCR COFs are documented in the Supporting Information, as well as the details on characterization techniques.

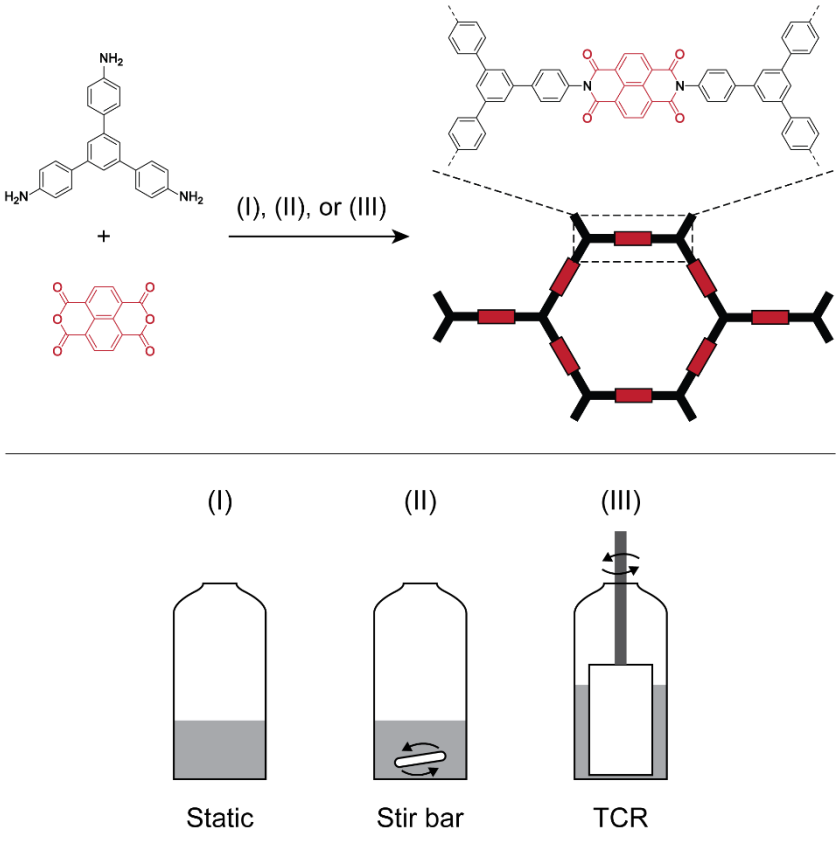

Fig. 1 Schematic overview of COF formation by polycondensation of TAPB and NDA, and the three different synthesis methods : (I) static: no agitation, (II) continuous stirring with a stir bar, and (III) high-intensity stirring in a Taylor-Couette reactor (TCR).

3.3 RESULTS AND DISCUSSION

Completion of the polycondensation reactions of the stir bar-, and TCR-COFs was confirmed by FT-IR (Fig. S4). All three different syntheses yielded polyimide polymers, which was apparent from the appearance of symmetric (1674 cm^{-1}) and asymmetric C=O (1715 cm^{-1}) imide peaks and C-N imide peaks (1339 cm^{-1}), combined with the disappearance of characteristic functional group vibrations of the originating monomers. No significant molecular differences between the differently agitated syntheses were observed. The thermal stabilities of the three COFs are similar as well (Figure S5), with the main decomposition at a maximum around the temperature range of 640 – 660 °C. In addition, a minor weight loss (5 – 10 wt. %) is present in the region of 300 – 500 °C for all COFs. The origin of this

weight loss is yet unclear: it could be trapped solvent species, unreacted monomer, and/or water release due to cyclization reactions of unreacted poly(amic acid).

PXRD measurements revealed that all COFs display similar crystalline order, being only on a short, local length scale (Fig. S6), as is also the case for previously reported COFs with the same polymer chemistry [6,12]. The static-, stir bar-, and TCR-COFs all show (100) and (200) reflections (where the former at 2.8 ° corresponds to the expected hexagonal size of 3.1 nm; previously investigated by our group through molecular modelling) [6]. Agitation during synthesis did influence the porosity of the COFs significantly, which we investigated by measuring nitrogen sorption isotherms (**Fig. 2A**). While the stir bar-COF shows very similar isotherm curves to the static-COF, the TCR-COF's porosity decreased notably: in particular the isotherm knee around 0.25 P/P_0 became less pronounced and the increase in N_2 uptake between 0.05 and 0.25 P/P_0 diminished. These observations indicate a reduction in small mesopore volume and a broader pore size distribution (PSD) of TCR-COFs. The PSDs were calculated based on the adsorption branches of the COFs (**Fig. 2B**), using a quenched solid density functional (QSDFT) model that is based on carbon materials with slit and cylindrical pore geometries [13]. The fitting curves of the PSD calculations are provided in the supplementary Figure S7. Finally, the overall Gurvich pore volume based on the N_2 uptake at 0.9 P/P_0 are 0.49, 0.50 and 0.37 $cm^3\ g^{-1}$ for the static-, stir bar- and TCR-COFs respectively.

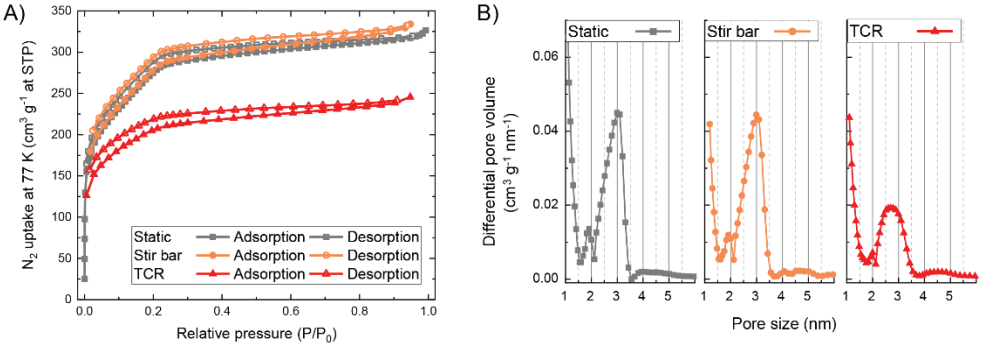

Fig. 2 A) Nitrogen gas sorption isotherms of static-, stir bar- and TCR-COFs. **B)** Pore size distributions of static-, stir bar- and TCR-COFs based on the adsorption branch of the nitrogen isotherms and a QSDFT (slit-cylindrical pore geometry) carbon model.

SEM micrographs of the COFs prepared by the three synthesis methods are shown in **Fig. 3**. First, in the zoomed-out micrographs (**Fig. 3** left), the large agglomerates (ranging from 20 to 200 µm) of the static-COFs stand in stark contrast to the more uniform and smaller particles of the stir bar- and TCR-COFs (sizes between 10 – 20

µm). Secondly, on a smaller length scale (**Fig. 3** right) a clear distinction in morphology is observed when comparing non-agitated to agitated COFs. The 'open', dendritic-like structures of static-COFs are distinguished from the more collapsed, aggregated-spherical structure of the stir bar- and TCR-COFs.

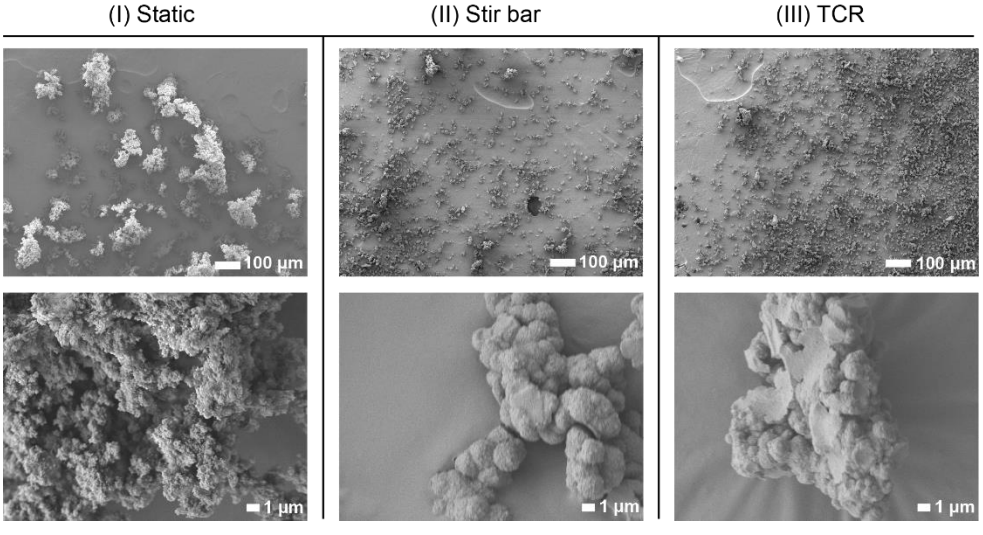

Fig. 3 SEM images of static-, stir bar-, and TCR-COFs. The scale bars are the same for each column: left 100 µm, right 1 µm.

Evidently, the shear rates applied during the synthesis of NDI-COFs have a significant effect on the final polymer network, without affecting the polymer chemistry or in-plane crystallinity. This observation is quite interesting, since the majority of published COF syntheses (where optimization is directed towards the highest degree of crystallinity) invariably involve only static reaction mixtures under solvothermal conditions and only effects of polymer chemistry, temperature and time on morphology are captured.

Regarding the porous structures of the three polymer powders, the mesopore volume derived from the crystalline pores of 3.1 nm as observed by PXRD, likely originates from local areas of stacked hexagonal units within the polymer. The clear maximum in PSDs of static- and stir bar-COFs suggest a relatively uniform stacking mode within these local areas of stacked hexagonal units. In contrast, the stacking mode is more random with larger offsets for TCR-COFs, since this would yield a reduction in mesopore volume and a broader maximum [14]. In addition, the mesopore volume could also be reduced through pore blocking within the polymer aggregates or interpenetration of neighbouring local stacks. In both cases, this decrease in

mesopore volume of TCR-COFs suggests a high degree of aggregation on the nanoscopic scale. Furthermore, SEM images at low magnification show that the static COF has a much larger agglomerate size than the other two powders. This was to be expected, since sufficient stirring intensities break up loosely bound particles while the agglomerates grow [15]. However, when examined at higher magnification the stir bar- and TCR-COFs display larger single particle sizes, while appearing increasingly more aggregated. We expect that the effects of stirring in this regard are two-fold: (1) homogeneously distributed monomers in their stochiometric ratios causing a higher molecular weight and subsequently larger, more uniform particles [16], and (2) additional flow forces acting on the forming particles causing the polymer network to be formed in a more inward facing, collapsed manner [17]. According to these results, we have employed a facile approach towards morphology control in NDI-COF systems.

Structural control on the nanoscale in NDI-based systems may play a large role in controlling their photophysical properties. This phenomenon has been observed in mesoporous silicas containing chemically similar perylene diimide segments [18]. Also in the case of polyimine COFs, Deng and coworkers have recently shown how careful regulation of interlayer packing through COF chemistry can enhance the optical properties [19]. Therefore, we investigated how the observed structural changes in the COFs presented here, affected these properties. We observed stark differences in their UV-Vis spectra (**Fig. 4A**). Each COF has a different λ_{max}, being 393 nm for static, 417 nm for stir bar, and 446 nm for TCR COFs, where red-shifts of these maxima typically indicate longer conjugation lengths. Furthermore, the absorbance intensity of the secondary shoulder peak (in the range of 490 – 510 nm) is much more a distinct peak in the TCR-COFs.

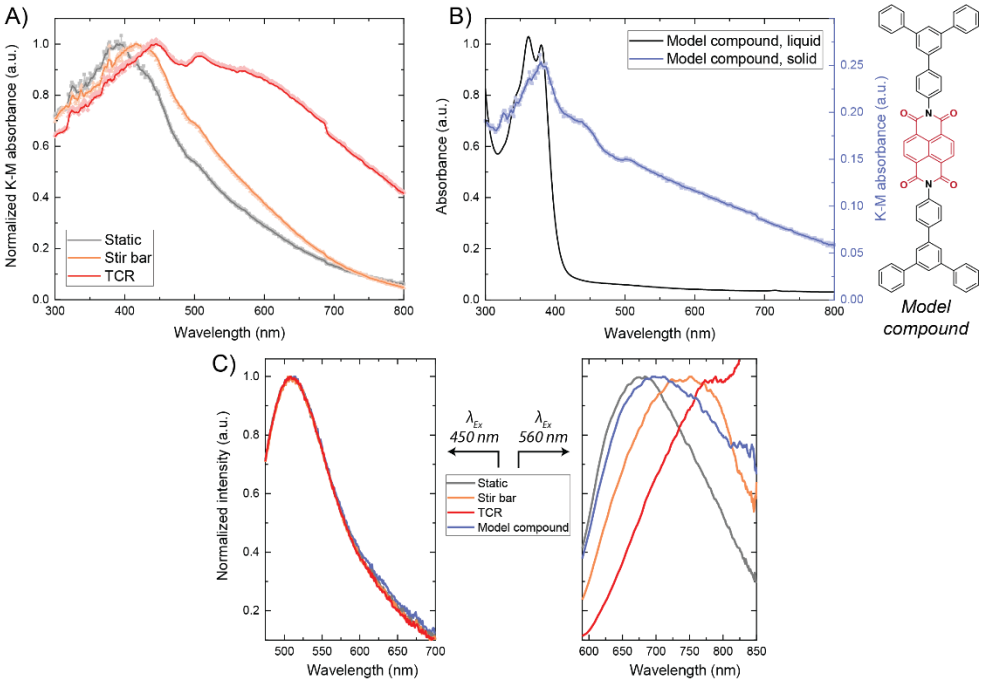

Fig. 4 A) Kubelka-Munk absorbance spectra of static-COF, stir bar-COF and TCR-COF measured by diffuse reflectance spectroscopy. **B)** UV absorbance spectrum of the model compound: dissolved in toluene (black line) and in the solid state (blue line, K-M absorbance). The step-change around 687 nm is an artefact of the measurement. **C)** Photoluminescence spectra of static-COF, stir bar-COF and TCR-COFs and the model compound, at excitation wavelengths of 450 (left) and 560 (right) nm.

In order to attribute the observed changes in spectral features to their chemical and structural origins, we synthesized a model compound that represents an isolated repeating unit of the COF framework (**Fig. 4B**). The 0-2, 0-1, and 0-0 absorption bands of this molecule at λ_{max} of 345, 361, and 380 nm respectively are clearly visible in the liquid state and are in line with characteristic π-π* transitions of other NDI-based materials [20]. The UV spectrum of the same model compound in the solid state, however, shows light absorption over a broad range of wavelengths with distinct spectral features. Next to the NDI π-π* transition at 380 nm, we observed two shoulder peaks between 430 - 450 nm and 496 - 510 nm. These differences in UV absorbance behaviour from the solvated state in NDI-based systems has extensively been studied and are often attributed to self-organization [20]. The presence of two distinct shoulders at longer wavelengths suggests multiple different intermolecular stacking modes [21]. In NDI-based small molecule systems, this has been further explored by combining these molecules with electron-rich aromatic donors (e.g. pyrene or derivatives thereof).

Here, charge transfer (CT) complexes, that are a result of electrons in the HOMO of the donor promoted to the LUMO of the NDI-unit, are observed through the appearance of a characteristic broad absorption band centred around 500 – 550 nm [22,23]. It is possible that the phenyl rings of the triphenylbenzene segments acted as electron donors in the self-organization of the model compound [24], as well as in local areas within the polymer networks of the COFs. The position and intensity of this CT band relies on multiple factors, such as the orbital overlap and solvent effects (chemical environment). Lastly, photoluminescence (PL) measurements were conducted to investigate the effect of differently packed polymer networks on excited-state properties. Excitation at 450 nm triggered the same emission behaviour for all COFs and the model compound (**Fig. 4C**), implying that this is caused by the main absorption bands of NDI segments that are present in all materials. On the other hand, excitation at 560 nm red-shifted the emission spectra of the COFs and model compound in a similar trend to the absorption spectra. This PL behaviour has been observed in NDI-based polymers and is indicative of a large content of inter-polymer NDI aggregates present in TCR-COFs, which would yield red-shifted aggregation-induced emission [9, 25].

The distinct nanostructures of the COFs investigated here lead to distinctly different photophysical properties. The differences in absorption spectra between the static- and stir bar COFs are relatively small compared to their differences with the TCR-COF. These trends are similar to the trends observed when comparing the PSDs and mesopore volume. Thus, we were able to correlate the TCR-synthesis method to a different nanostructure (through observation of a lower mesopore volume), and subsequently to the COF's light absorbance and aggregation-induced emission. While engineering the optical properties in COFs typically relies on chemically altering the building blocks [25-27], we have shown that changing the processing-side of the synthesis may lead to similar changes. In a similar vein, we anticipate that mechanochemical concepts such as ball milling synthesis (that have been applied to other porous materials) [28], are promising for alternative COF preparation routes with enhanced properties as well.

3.4 Conclusion

In summary, COFs prepared via a static method display an outstretched, open polymer network, with a relatively lower contribution of intermolecular NDI-based interactions. On the other hand, a high intensity of stirring during synthesis yields a COF polymer network that is more aggregated in micro- and nano-length scales, which causes an overall higher contribution of intermolecular NDI-based

interactions. We anticipate that utilisation of these synthesis strategies for NDI-COFs will affect their electrochemical device performance, because of its reliance on charge transport between aggregated NDI-based polymer chains [29]. While the effects have been shown for one COF system only, we expect that the route is more generic and can be applied successfully to other COF and COF related systems.

ACKNOWLEDGEMENTS

The authors thank Dr. Lorenzo Botto and Dr. Hugo Perrin for valuable discussions regarding reactor design, experimental parameters, and shear rate estimations. The authors also thank Ing. Bahiya Ibrahim for her assistance during the photoluminescence measurements.

3.5 SUPPORTING INFORMATION

3.5.1 EXPERIMENTAL DETAILS

Reagents

All reagents presented in this report were commercially available and used without further purification or treatment. 1,3,5-Tris(4-aminophenyl)benzene (≥ 93 %), 5'-Phenyl-[1,1':3',1''-terphenyl]-4-amine (≥ 98 %), and isoquinoline were purchased from TCI Europe N.V (Zwijndrecht, Belgium), 1,4,5,8-naphthalenetetracarboxylic dianhydride (≥ 95 %) and *ortho*-dichlorobenzene from abcr GmbH (Karlsruhe, Germany) and *N*-methyl-2-pyrrolidone from Acros Organics B.V.B.A (Geel, Belgium).

Characterization techniques

FT-IR spectra were recorded on a PerkinElmer Spectrum 100 FT-IR Spectrometer with an universal ATR accessory over a range of 4000 to 650 cm^{-1}. TGA analyses were performed from room temperature to 900 °C, under nitrogen atmosphere at a heating rate of 10 °C/min using a Perkin Elmer TGA 4000. Before the measurement, the samples were dried at 130 °C for one hour under a nitrogen atmosphere. Scanning electron microscopy (SEM) images were captured on a JEOL JSM-840 SEM: materials were deposited onto a sticky carbon surface on a flat sample holder, vacuum-degassed, and subjected to gold sputtering. PXRD patterns

were measured on a Rigaku MiniFlex 600 powder diffractometer using a Cu-Kα source (λ = 1.5418 Å) over the 2θ range of 2° to 40° with a scan rate of 1°/minute. Calculated PXRD patterns of the COF crystal model can be found in our previous publication (Chem. Mater 33 (2021) 818–833.). Nitrogen isotherms were measured on the NOVAtouch gas sorption analyzer from Quantachrome Instruments. Before the measurements, all samples were degassed at 130 °C under vacuum for 16 h. The nitrogen uptake at 0.9 P/P_0 (adsorption branch) was used to calculate the Gurvich pore volume. The Quantachrome VersaWin software package was used for calculations of pore size distributions by fitting the nitrogen adsorption isotherms to the quenched solid density functional theory (QSDFT) carbon model (using slit and cylindrical pores). No smoothing factor was applied for the PSD calculation. The corresponding fitting curves are provided here in the SI. The UV-Vis-NIR absorption spectra for solid samples were obtained using a PerkinElmer Lambda 900. Prior to the measurements, we manually (with mortar and pestle) ground the COF powders and through sieving collected the < 200 µm particle fraction to keep the powders as comparable as possible. The solids were then mixed and ground with $BaSO_4$ (1:20 dilution, w/w), and inserted into a powder cell sample holder. Optical measurements for solids were performed in reflection-mode and utilized an integrating sphere unit. Liquid UV-vis spectra were recorded at 298 K on a PerkinElmer Lambda 35 UV-vis spectrometer (quartz cuvette) at a concentration of 0.05 mM in toluene. Photoluminescence (PL) spectra were recorded by using an Edinburgh Instruments FLSP920 luminescence spectrophotometer. For PL measurements, COF powders were directly (without further dilution) spread between two quartz plates and inserted into the sample holder. NMR spectra were recorded at 298 K on an Agilent-400 MR DD2 spectrometer (400 MHz) in toluene-d_8.

3.5.2 COF SYNTHESIS PROCEDURES

The three syntheses with different ways of agitation are schematically depicted in **Figure 1** and are, in this report, all executed with the same triamine (1,3,5-tris(4-aminophenyl)benzene, TAPB) and dianhydride (1,4,5,8-naphthalenetetracarboxylic dianhydride, NTCDA). All syntheses were performed in a borosilicate glass flat-bottom 100 mL cylindrical reactor with a separate borosilicate glass three-neck lid, linked by a steel reactor clamp.

Static-COF synthesis (I)

TAPB (351 mg, 1.0 mmol) and NTCDA (402 mg, 1.5 mmol) were added to a glass cylindrical reactor and subsequently *o*-DCB (10 mL), NMP (10 mL) and

isoquinoline (0.1 mL) were added. Thereafter, the reactor was sealed, vacuum degassed, and placed in an oil bath. Under gently shaking the reactor vessel, it was heated to a temperature of 150 °C. Upon complete dissolution of the monomers, the temperature was step-wise (10 °C per 15 min) increased to 190 °C and kept without agitation at that temperature for 3 days. After the work-up (see 2.3.4), the static-COF was isolated as an ochre-brown, fluffy powder (642 mg, 92 %).

Stir bar-COF synthesis (II)

A stir bar (25 mm radius, 7.3 mm thickness), TAPB (351 mg, 1.0 mmol) and NTCDA (402 mg, 1.5 mmol) were added to a glass cylindrical reactor and subsequently *o*-DCB (10 mL), NMP (10 mL) and isoquinoline (0.1 mL) were added. While stirring continuously at 300 rpm, the reactor was sealed, vacuum degassed, and placed in an oil bath. The reactor vessel was heated to a temperature of 150 °C, which was step-wise (10 °C per 15 min) increased to 190 °C and left stirring at that temperature for 3 days. After the work-up (see 2.3.4), the stir bar-COF was isolated as an orange-brown powder (546 mg, 78 %).

TCR-COF synthesis (III)

TAPB (351 mg, 1.0 mmol) and NTCDA (402 mg, 1.5 mmol) were added to a glass cylindrical reactor. Then, a steel bar fit for a mechanical stirrer was coupled to a Teflon block (with the dimensions shown in Figure S1) and inserted in the reactor vessel. After that, *o*-DCB (10 mL), NMP (10 mL) and isoquinoline (0.1 mL) were added and the Teflon stirrer was allowed to stir at 300 rpm. Then, the reactor was sealed, vacuum degassed, and placed in an oil bath. Under continuous stirring, the temperature was increased to 150 °C, which was then step-wise (10 °C per 15 min) increased to 190 °C and left stirring at that temperature for 3 days. After the work-up (see 2.3.4), the TCR-COF was isolated as an dark-brown powder (588 mg, 84 %).

General work-up procedure

The reaction mixture was cooled to room temperature, suspended in 60 mL methanol, and mixed thoroughly. The solid was separated from the liquid through centrifugation (10 min at 4400 rpm), after which the solid was washed with methanol (3 x 30 mL) and acetone (1 x 30 mL). After drying the solid in a vacuum oven at 60 °C for one hour, it was subjected to Soxhlet extraction with THF for 20 hours. After that, the COF was allowed to dry in a vacuum oven at 60 °C for 20 hours. For all three different syntheses, the same work-up procedure was used.

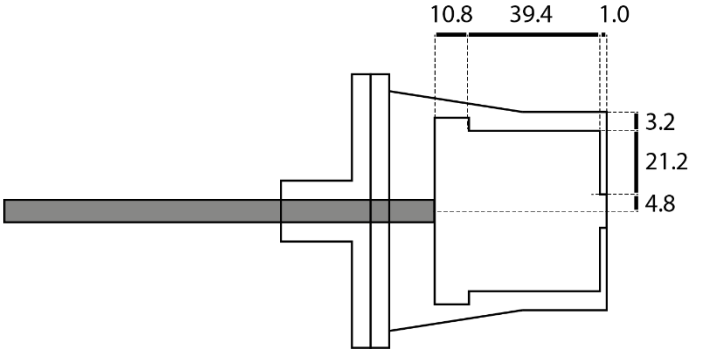

Figure S1 Dimensions (expressed in milimeters) of the Taylor-Couette reactor used for TCR-COF synthesis.

3.5.3 Shear rate estimation

The shear rate ($\dot{\gamma}$) of the Taylor-Couette reactor can be estimated through the following equation:

$$\dot{\gamma} = \frac{r \cdot \omega}{d}$$

with the radius of the inner cylinder r ($26 \cdot 10^{-3}$ m), rotational speed ω (300 rpm = $300 \cdot \frac{2\pi}{60}$ radians per second), and annular gap d ($3.2 \cdot 10^{-3}$ m). This results in $\dot{\gamma}$ = 255 s^{-1}.

The same equation could be used to estimate the minimum and maximum shear rate of the stir bar synthesis (at the tip of the bar), utilizing the dimensions of the stir bar: r ($25 \cdot 10^{-3}$ m); thickness ($7.3 \cdot 10^{-3}$ m) and the radius of the reactor ($29.2 \cdot 10^{-3}$ m). From these parameters we can estimate a minimum and maximum shear rate (as is illustrated in Figures S2): $\dot{\gamma}_{min}$ = 4.5 s^{-1} and $\dot{\gamma}_{max}$ = 190 s^{-1}. This value is a broad generalization, as the shear rate in a process concerning a rotating magnetic stir bar is highly spatially dependent. Nevertheless, it is a valid approximation for the minimum and maximum shear rate.

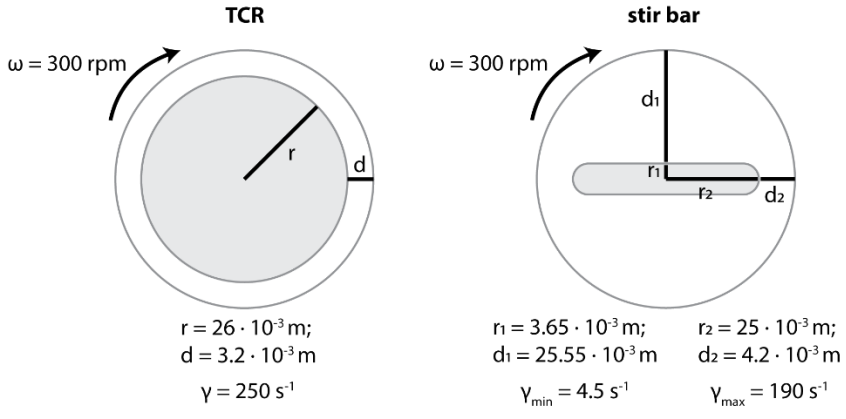

Figure S2 Schematic illustration (top view) of the parameters used for shear rate calculations.

3.5.4 OBSERVATIONS DURING SYNTHESIS

A reaction time of 3 days is typically used for the polyimide COF synthesis, of which the first 60 minutes the reaction mixture visibly changes significantly (colour and consistency). All reaction mixtures (from static, stir bar, and TCR) discussed in this report change from suspended monomers in an olive-green fluid, into a transparent brown fluid, into dark brown precipitates in a brown-black fluid. The intermediate transparent phase typically occurs in the range of 100 – 120 °C in which complete dissolution of the monomers is reached. Interestingly, the static-COF reaction mixture forms a solid, spongey mass after keeping the reactor at 190 °C for 60 min, suggesting the formation of a highly interconnected network. Oppositely, the reaction mixtures of stir bar- and TCR-COFs displayed suspended particles in solution.

Figure S3 highlights the observations of a typical TCR-COF reaction mixture between 0 and 60 minutes of reaction initiation. At certain time intervals, parallel lines were visible, which indicate brief moments of macroscopic laminar flow regimes (although with significant turbulence within these lines). However, these parallel lines became increasingly unstable over time, and more often, TCR-COF reaction mixtures displayed combinations of wavy vortex and turbulent flow. It should also be noted that such parallel-lined flow behaviour was difficult to reproduce from batch to batch, because it is highly dependent on the axial alignment of the mechanical stirrer and the reactor. Nevertheless, TCR-COFs displayed little batch-to-batch variations.

Figure S3 Photographs (projected sideways) of the COF reaction mixture in the Taylor-Couette reactor with increasing reaction time and reaction temperature from left to right.

3.5.5 FT-IR and TGA

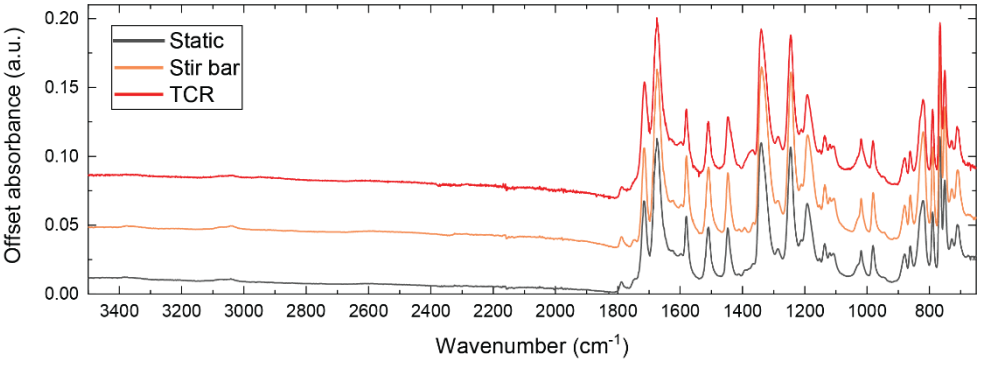

Figure S4 FT-IR absorbance spectra of polyimide static-, stir bar-, and TCR-COFs.

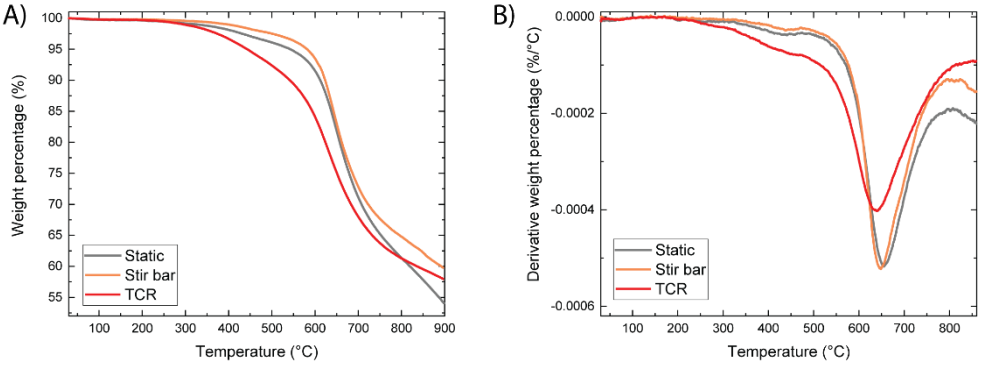

Figure S5 A) TGA curves of polyimide static-, stir bar-, and TCR-COFs at a heating rate of 10 °C/min under a nitrogen atmosphere. **B)** First-order derivatives of the TGA curves.

3.5.6 PXRD AND PSD FITTING CURVES

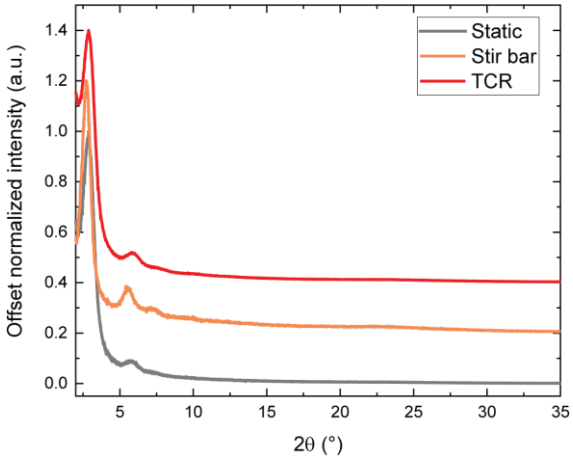

Figure S6 Powder X-ray diffraction patterns of static-, stir bar- and TCR-COFs.

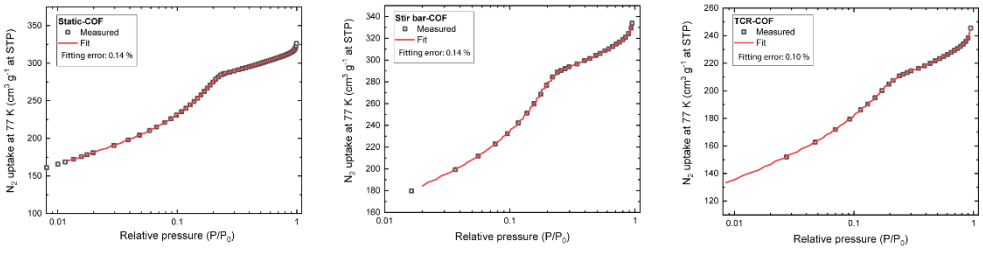

Figure S7 Fitting curves to the pore size distributions of static, stir bar- and TCR-COFs.

3.5.7 MODEL COMPOUND SYNTHESIS AND CHARACTERIZATION

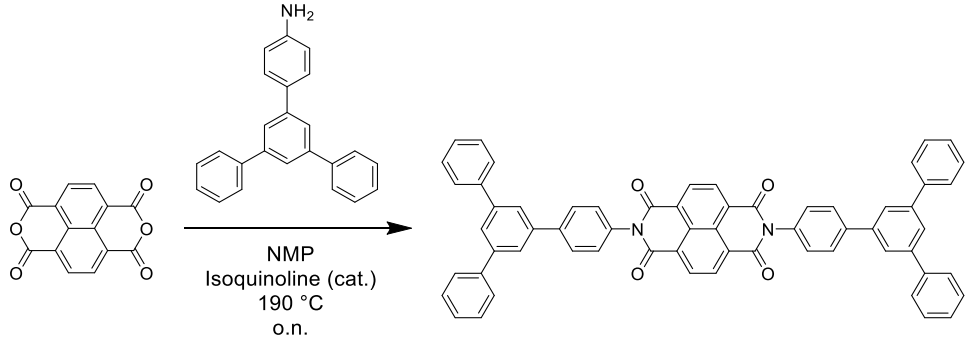

A 2-neck roundbottom flask was charged with 5'-phenyl-[1,1':3',1''-terphenyl]-4-amine (0.5 mmol, 134 mg), 1,4,5,8-naphthalenetetracarboxylic dianhydride (1.25 mmol, 402 mg), a condenser, and a magentic stir bar, and the flask was flushed with N_2 for 15 minutes. Then, 15 mL dry NMP and 0.6 mL isoquinoline were added.

The reaction mixture was heated to 190 °C under continuous stirring and a N_2 atmosphere, and left stirring under the same conditions over night (~ 20 hours). Thereafter, the mixture was allowed to cool to room temperature and further cooled to 0 °C. The suspension was precipitated in cold methanol (100 mL) and the solid was collected through centrifugation (30 minutes at 4400 rpm). The solid was again washed with 3 x 20 mL methanol and collected through centrifugation. Then, the solid was dried over night at 60 °C under vacuum, after which it was washed with acetone (3 x 20 mL). The solid was dried for 3 hours at 60 °C under vacuum, to yield the model compound as a brown powder (249 mg, 57 %). ^{1}H NMR (400 MHz, toluene-d_8): δ 8.45 (s, 4H), 7.86 (s, 2H), 7.81 (s, 4H), 7.71 (d, J = 8.0 Hz, 4H), 7.64 (d, J = 7.9 Hz, 8H), 7.44 (d, J = 8.0 Hz, 4H), 7.38 (t, J = 7.4 Hz, 8H), 7.29 (d, J = 6.9 Hz, 4H).

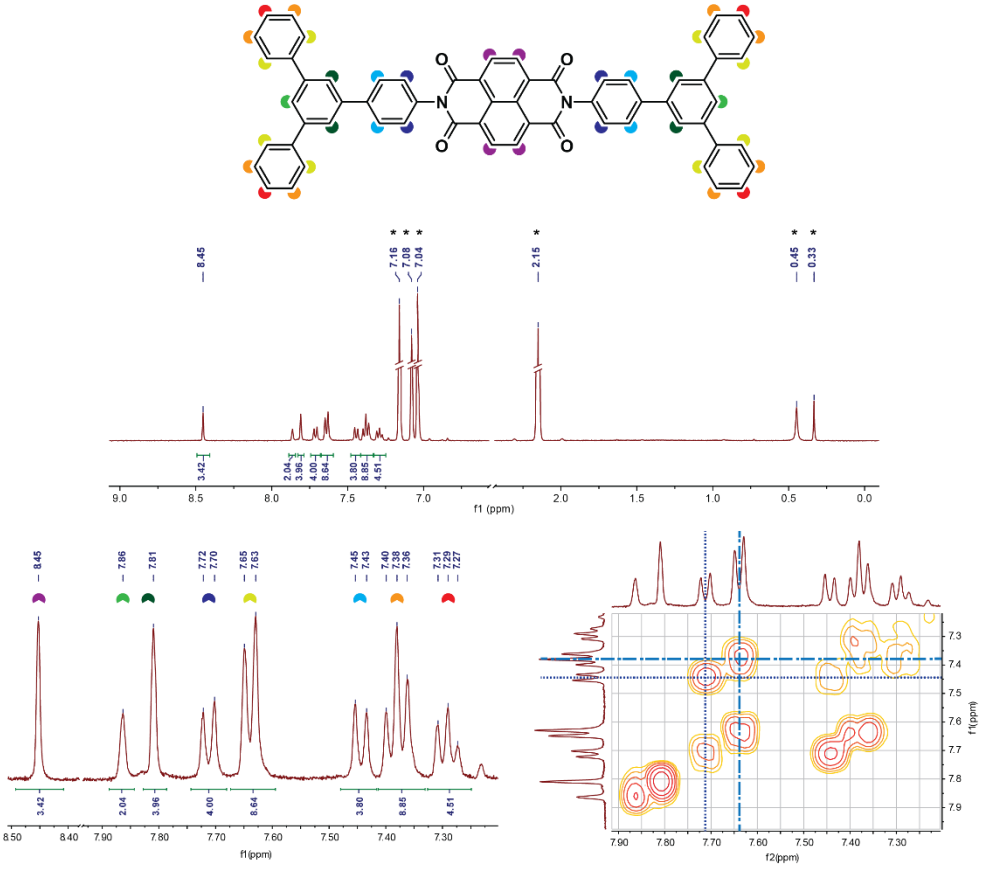

Figure S8 ^{1}H-NMR and 2D-COSY NMR of the model compound in toluene-d_8.

REFERENCES

1 T. Ma, E. A. Kapustin, S. X. Yin, L. Liang, Z. Zhou, J. Niu, L.-H. Li, Y. Wang, J. Su, J. Li, X. Wang, W. D. Wang, W. Wang, J. Sun, O. M. Yaghi, Science 361 (2018) 48–52. https://doi.org/10.1126/science.aat7679

2 K. Zhang, K. O. Kirlikovali, R. S. Varma, Z. Jin, H. W. Jang, O. K. Farha and M. Shokouhimehr, ACS Appl. Mater. Interfaces 12 (2020) 27821–27852. https://doi.org/10.1021/acsami.0c06267

3 M. Calik, F. Auras, L. M. Salonen, K. Bader, I. Grill, M. Handloser, D. D. Medina, M. Dogru, F. Löbermann, D. Trauner, A. Hartschuh and T. Bein, J. Am. Chem. Soc. 136 (2014) 17802–17807. https://doi.org/10.1021/ja509551m

4 H. Furukawa and O. M. Yaghi, J. Am. Chem. Soc. 131 (2009) 8875–8883. https://doi.org/10.1021/ja9015765

5 W. Wang, M. Zhou and D. Yuan, J. Mater. Chem. A 5 (2017) 1334–1347. https://doi.org/10.1039/C6TA09234A

6 R. van der Jagt, A. Vasileiadis, H. Veldhuizen, P. Shao, X. Feng, S. Ganapathy, N. C. Habisreutinger, M. A. van der Veen, C. Wang, M. Wagemaker, S. van der Zwaag and A. Nagai, Chem. Mater 33 (2021) 818–833. https://doi.org/10.1021/acs.chemmater.0c03218

7 N. Fernando, H. Veldhuizen, A. Nagai, S. Van der Zwaag and A. Abdelkader, Materials 15 (2022) 4. https://doi.org/10.3390/ma15010004

8 S. Patwardhan, A. A. Kocherzhenko, F. C. Grozema and L. D. A. Siebbeles, J. Phys. Chem. C 115 (2011) 11768–11772. https://doi.org/10.1021/jp202399u

9 Y. Wu, S. Schneider, C. Walter, A. H. Chowdhury, B. Bahrami, H. C. Wu, Q. Qiao, M. F. Toney and Z. Bao, J. Am. Chem. Soc. 142 (2020) 392–406. https://doi.org/10.1021/jacs.9b10935

10 D. Fazzi and M. Caironi, Phys. Chem. Chem. Phys. 17 (2015) 8573–8590. https://doi.org/10.1039/C5CP00523J

11 M. Schrimpf, J. Esteban, H. Warmeling, T. Färber, A. Behr and A. J. Vorholt, AIChE J. 67 (2021) 1–24. https://doi.org/10.1002/aic.17228

12 Q. Fang, Z. Zhuang, S. Gu, R. B. Kaspar, J. Zheng, J. Wang, S. Qiu and Y. Yan, Nat. Commun. 5 (2014) 4503. https://doi.org/10.1038/ncomms5503

13 A. V. Neimark, Y. Lin, P. I. Ravikovitch and M. Thommes, Carbon 47 (2009) 1617–1628. https://doi.org/10.1016/j.carbon.2009.01.050

14 C. Kessler, R. Schuldt, S. Emmerling, B. V. Lotsch, J. Kästner, J. Gross, N. Hansen, Microporous Mesoporous Mater. 336 (2022) 11796. https://doi.org/10.1016/j.micromeso.2022.111796

15 S. H. Kang, S. G. Lee, W. M. Jung, M. C. Kim, W. S. Kim, C. K. Choi and R. S. Feigelson, J. Cryst. Growth 254 (2003) 196–205. https://doi.org/10.1016/S0022-0248(03)01152-7

16 G. González, E. Colmenar, G. Diaconu, F. Alarcia, M. Manea, M. Paulis, M. J. Barandiaran, J. R. Leiza, J. C. de la Cal and J. M. Asua, Macromol. React. Eng. 3 (2009) 233–240. https://doi.org/10.1002/mren.200900015

17 L. Guérin, C. Coufort-Saudejaud, A. Liné and C. Frances, J. Colloid Interface Sci. 491 (2017) 167–178. https://doi.org/10.1016/j.jcis.2016.12.042

18 F. J. Trindade, G. J. T. Fernandes, A. S..Araújo, V. J. Fernandes Jr., B. P..G. Silva, R. Y. Nagayasu, M. J. Politi, F. L. Castro, S. Brochsztain, Microporous Mesoporous Mater. 113 (2008) 463–471. https://doi.org/10.1016/j.micromeso.2007.12.013

19 L. Zhang, Y. Zhou, M. Jia, Y. He, W. Hu, Q. Liu, J. Li, X. Xu, C. Wang, A. Carlsson, S. Lazar, A. Meingast, Y. Ma, J. Xu, W. Wen, Z. Liu, J. Cheng, H. Deng, Matter 2 (2020) 1049–1063. https://doi.org/10.1016/j.matt.2020.01.019

20 S. Maniam, H. F. Higginbotham, T. D. M. Bell and S. J. Langford, Chem. - A Eur. J. 25 (2019) 7044–7057. https://doi.org/10.1002/chem.201806008

21 M. Pandeeswar, H. Khare, S. Ramakumar and T. Govindaraju, RSC Adv. 4 (2014) 20154–20163. https://doi.org/10.1039/C3RA47257D

22 P. Li, J. M. Maier, J. Hwang, M. D. Smith, J. A. Krause, B. T. Mullis, S. M. S. Strickland and K. D. Shimizu, Chem. Commun. 51 (2015) 14809–14812. https://doi.org/10.1039/C5CC06140G

23 M. D. Gujrati, N. S. S. Kumar, A. S. Brown, B. Captain and J. N. Wilson, Langmuir 27 (2011) 6554–6558. https://doi.org/10.1021/la2012809

24 N. A. Kukhta, D. Volyniuk, J. V. Grazulevicius and G. Sini, J. Mater. Chem. C 6 (2018) 1679–1692. https://doi.org/10.1039/C7TC05798A

25 R. Steyrleuthner, M. Schubert, I. Howard, B. Klaumünzer, K. Schilling, Z. Chen, P. Saalfrank, F. Laquai, A. Facchetti, D. Neher, J. Am. Chem. Soc. 134 (2012) 18303–18317. https://doi.org/10.1021/ja306844f

25 X. Li, Q. Gao, J. Aneesh, H. Sen Xu, Z. Chen, W. Tang, C. Liu, X. Shi, K. V. Adarsh, Y. Lu and K. P. Loh, Chem. Mater. 30 (2018) 5743–5749. https://doi.org/10.1021/acs.chemmater.8b02560

26 Y. Zhao, X. Liu, Y. Li, M. Xia, T. Xia, H. Sun, Z. Sui, X. Hu, Q. Chen, Microporous Mesoporous Mater. 319 (2021) 111046. https://doi.org/10.1016/j.micromeso.2021.111046

27 L. Zhang, L. Yi, Z.-J. Sun, H. Deng, Aggregate 2 (2021) e24. https://doi.org/10.1002/agt2.24

28 B. Szczęśniak, S. Borysiuk, J. Choma, M. Jaroniec, Mater. Horiz. 7 (2020) 1457–1473. https://doi.org/10.1039/d0mh00081g

29 S. Wang, S. Fabiano, S. Himmelberger, S. Puzinas, X. Crispin, A. Salleo and M. Berggren, Proc. Natl. Acad. Sci. U. S. A. 112 (2015) 10599–10604. https://doi.org/10.1073/pnas.1501381112

4

Competitive and Cooperative CO_2–H_2O Adsorption through Humidity Control in a Polyimide Covalent Organic Framework

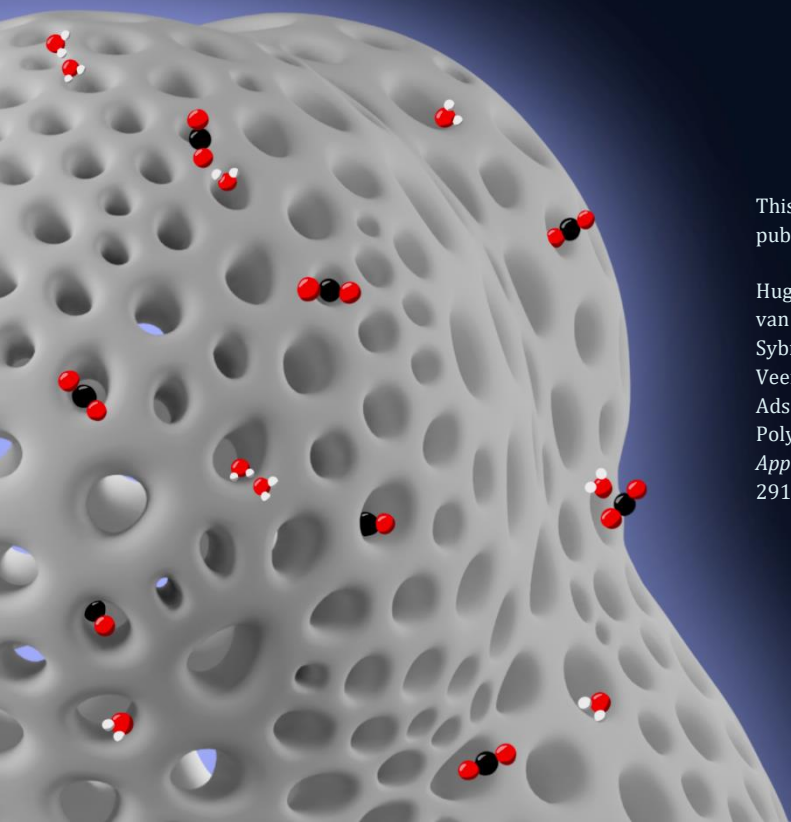

This chapter is based on the following publication:

Hugo Veldhuizen, Saira Alam Butt, Annemiek van Leuken, Bart van der Linden, Willy Rook, Sybrand van der Zwaag, Monique A. van der Veen. Competitive and Cooperative CO_2–H_2O Adsorption through Humidity Control in a Polyimide Covalent Organic Framework. *ACS Appl. Mater. Interfaces* **2023**, *15*, 29186–29194.

Abstract

In order to capture and separate CO_2 from the air or flue gas streams through nanoporous adsorbents, the influence of the humidity in these streams has to be taken into account, as it hampers the capture process in two main ways: (1) water preferentially binds to CO_2 adsorption sites and lowers the overall capacity, and (2) water causes hydrolytic degradation and pore collapse of the porous framework. Here, we have used a water-stable polyimide covalent organic framework (COF) in $N_2/CO_2/H_2O$ breakthrough studies and assessed its performance under varying levels of relative humidity (RH). We discovered that at limited relative humidity, the competitive binding of H_2O over CO_2 is replaced by cooperative adsorption. For some conditions, the CO_2 capacity was significantly higher under humid versus dry conditions (e.g. a 25 % capacity increase at 343 K and 10 % RH). These results in combination with FT-IR studies on equilibrated COFs at controlled RH values allowed us to assign the effect of cooperative adsorption to CO_2 being adsorbed on single-site adsorbed water. Additionally, once water cluster formation sets in, loss of CO_2 capacity is inevitable. Finally, the polyimide COF used in this research retained performance after a total exposure time of > 75 hours and temperatures up to 403 K. This research provides insight in how cooperative CO_2–H_2O can be achieved, and as such provides directions for the development of CO_2 physisorbents that can function in humid streams.

4.1 INTRODUCTION

Physical adsorption of CO_2 on solid adsorbents has been demonstrated to be a promising upcoming technology for CO_2 removal from flue gas. It distinguishes itself form traditional processes such as amine absorption, by being a process with cost- and energy-efficient regeneration of the adsorbent.[1] In addition, the non-corrosive nature of the physical adsorbents, makes storage and maintenance less complicated. Activated carbons, zeolites, metal-organic frameworks (MOFs) and covalent organic frameworks (COFs) have been widely studied as nanoporous physical adsorbents for carbon capture under experimental conditions similar to those in industrial applications (*i.e.* multi-component gas separation in a packed bed).[2] MOFs and COFs, in particular, are promising materials since their frameworks are highly tunable through the vast library of building blocks that can be used to construct them. In this way, MOFs and COFs have been molecularly engineered to display both a high CO_2 capacity and framework robustness.[3-6] Depending on the chemical structure and topology, subclasses of these materials retain a high selectivity towards CO_2 adsorption when they are exposed to mixed gas streams of N_2, H_2 and / or CH_4. The most used experimental setup to verify their potential for post-combustion carbon capture concerns exposing a packed bed of adsorbent to a mixed stream of N_2/CO_2 of ratios ranging from 80/20 to 95/5, as these represent typical N_2/CO_2 ratios in flue gas.[4,7]

Water vapour, an ubiquitous component in flue gas, often lowers the efficiency of these adsorbents through competitive adsorption of water over CO_2.[8] This phenomenon depends firstly on the concentration-dependent affinities (*i.e.* isosteric enthalpy of adsorption) of CO_2 and H_2O towards the adsorbent. Water–adsorbent enthalpies are often higher and adsorbed water provides new adsorption sites for multilayer water sorption (*i.e.* water clusters), which results in complete pore filling at high relative humidity (RH) values. Although CO_2 sorption is often diminished in the presence of water,[6] in some cases it is unaffected or even enhanced, depending on the RH and specific adsorbent.[9,10] Recent examples of unaffected CO_2 adsorption at humid conditions are from the group of Smit and co-workers.[3] In their study, they computationally screened a library of 300,000 MOFs to discover specific structural motifs that enables - once implemented in a framework - high CO_2/N_2 selectivity which persists in wet flue gases. In their study, they discovered (*in silico*) parallel aromatic motifs with a distance of 7 Å as a highly selective CO_2 binding site. Once this segment was experimentally included in a hydrophobic MOF, CO_2 adsorption performance was retained in breakthrough experiments with humidified streams using 85 % RH in the feed flow, throughout

multiple consecutive cycles. However, initially dry adsorbents are used in these experiments, as well as desorption steps at higher temperatures. As a result of such experimental procedure and the inherent slow diffusion of water in nanoporous materials,[11] an overall lower RH level is likely present in the adsorption column. In another study regarding a novel zinc triazolate oxalate framework, a rare phenomenon of competitive binding of CO_2 over H_2O was observed.[4] There, as the result of the specific ultramicroporous architecture, water cluster formation is sterically hindered: the adsorption of CO_2 causes the breaking of H-bonds in the water cluster, while due to space limitations no alternative H-bonds can be formed. This means that until 40 % RH, CO_2 (at 1 bar) is competitively adsorbed, such that it even leads to water expulsion.

Enhanced CO_2 sorption in the presence of water also occurs with specific adsorbents that contain small mesopores at controlled RH values, for example in the MOF MIL-100(Fe) bearing 2.5 and 2.9 nm mesoporous cages.[10,12] Pre-equilibrated water is able to effectively bring the pore walls closer together, and subsequently form microporous pockets which causes the retention of a higher concentration of CO_2 than in the dry state. On the other hand in microporous PCN-250 MOFs, CO_2 adsorption capacities can be enhanced 1.7 times when adsorption is being executed with humified gas streams compared to dry streams.[13] This particular improvement is said to be due to H_2O molecules clamping the CO_2 molecules on the open metal sites, which uses the adsorption sites more effectively than in the dry situation. Also compared to dry conditions, relative humidity values of 20 % are causing a 1.5- and 2.4-fold CO_2 capacity increase in MOFs MIL-53(Al) and NOTT-400, respectively.[14,15] In these cases, the bridging hydroxo-groups within the MOF are providing water adsorption sites. In the case of MIL-101, water can coordinate to the otherwise exposed Cr-sites, and these terminal water molecules act as additional interaction sites to enhance CO_2 uptake, particularly at low pressures.[16] Pre-adsorbed water at low RH values provide more favourable CO_2 binding sites than the dry variants of these structures. Although COFs seem to be equally suited for CO_2 separation from humid gas streams, there is a lack of detailed COF studies with systematic RH variations to investigate potentially similar water-enhanced effects as have been observed for MOFs. Among few of these examples in the COF field,[17] there are fewer experimental studies that attempt to relate COF chemistry and structure to CO_2 separation performance under humid environments as encountered in industrially relevant setups. An extensive study involving imine-COFs assessed the performance of NUS-2 and TpPa-1 (promising COFs in terms of high CO_2 capacity and stability) in N_2/CO_2 breakthrough experiments where the adsorbents are pre-saturated with water.[6]

This study showed that at 17 % RH, NUS-2 and TpPa-1 retained about 70 % of their dry CO_2 adsorption capacities over prolonged periods of time. Nevertheless, CO_2 breakthrough studies in the presence of water using COF adsorbents always report a negative effect of water.[6,7] Expanding on these studies with different COF structures at various RH values would allow for a fair assessment of the potential of COFs for industrial CO_2 separation from humid streams. In addition, these studies unravel the possibility of water-enhanced CO_2 adsorption as has been found in specific MOFs.

Here, we systematically controlled the RH values to which the adsorbent is exposed in $N_2/CO_2/H_2O$ breakthrough studies, to assess the material and experimental requirements for control over the competitive or cooperative binding of CO_2 and H_2O. We chose a polyimide COF as a model COF system for this particular study, synthesized from 1,3,5-tris(4-aminophenyl)benzene (TAPB) and 1,4,5,8-naphthalenetetracarboxylic dianhydride (NDA). The reason being the overall hydrolytic and mechanical stability of polyimide COFs, the relative ease of preparation and their commercially available building blocks. Furthermore, the TAPB-NDA COF contains a significant supermicropore and mesopore volume, which seems to be beneficial in achieving water assisted CO_2 adsorption. The large degree of aromatic planes could potentially also promote the presence of the aromatic motifs that Smit *et al.* identified as capable of competitively adsorbing CO_2 over water.

4.2 RESULTS AND DISCUSSION

The solvothermal polycondensation of 1,3,5-tris(4-aminophenyl)benzene (TAPB) and 1,4,5,8-naphthalenetetracarboxylic dianhydride (NDA) was executed in a sealed glass flat-bottom 100 mL cylindrical reactor, and yielded the nanoporous polyimide polymer named TAPB-NDA-COF (**Figure 1A**). The powder was then subjected to pelletization (hydraulic press, 30 MPa) and sieving (fractions of 300 – 425 µm), after which these COF pellets were characterized. The completion of the polymerization was confirmed by FT-IR analysis (Figure S1) and the TGA profile of the TAPB-NDA-COF (Figure S2); revealed a 5 % weight loss temperature of 535 °C at a heating rate of 10 °C·min^{-1} under N_2 atmosphere, which is expected behaviour for polyimides confirming their thermal stability. The nanoporous polymer network was further characterized by PXRD and N_2 sorption. The former technique was used to classify this TAPB-NDA-COF as semi-crystalline, since there are noticeable reflections at (100) (from 2.8 ° 2θ, corresponding to the expected hexagonal size of 3.1 nm) and (200), but no peaks indicative of long-range order

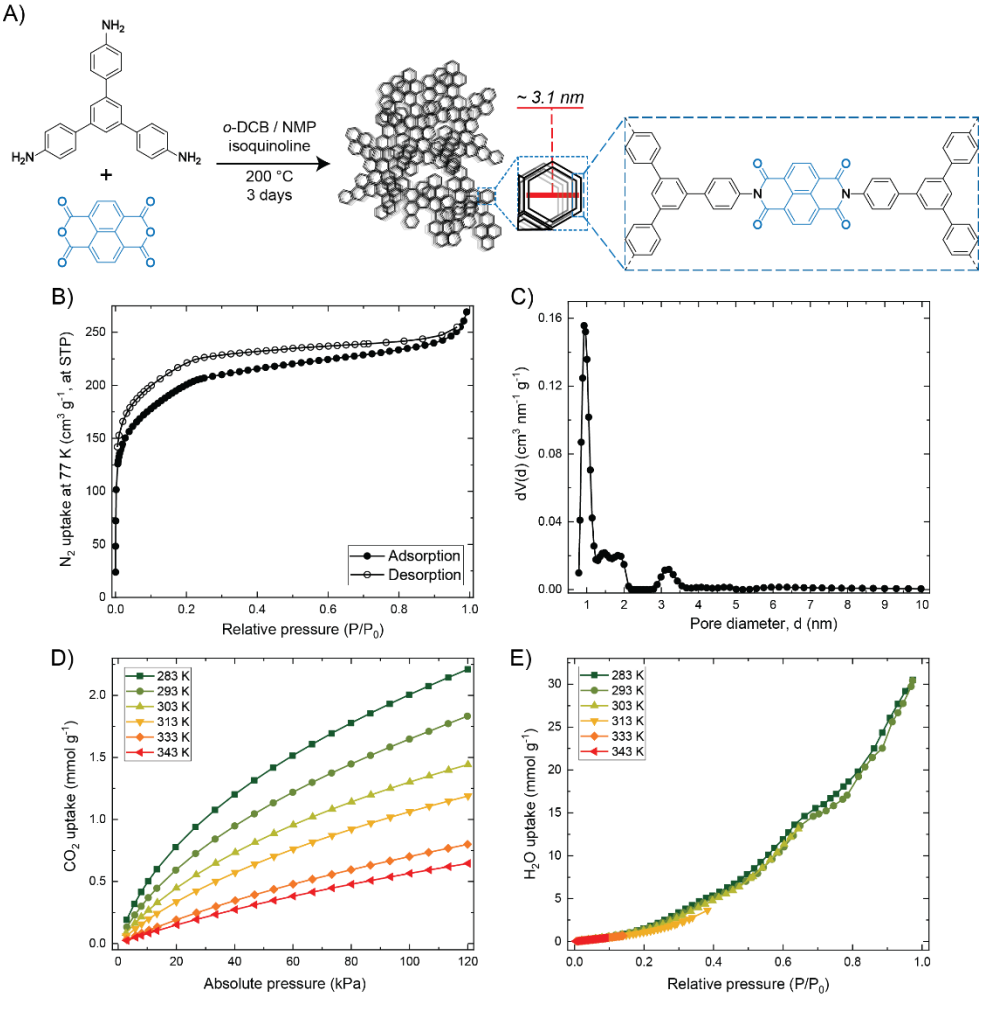

Figure 1. A) TAPB-NDA-COF synthesis conditions and representation of its chemical and porous structure. **B)** Nitrogen sorption isotherms of TAPB-NDA-COF at 77 K. **C)** Pore size distribution based on the adsorption branch of the nitrogen isotherm and a QSDFT carbon model. **D)** CO_2 adsorption isotherms of TAPB-NDA-COF at 283, 293, 303, 313, 333 and 343 K. **E)** H_2O vapour adsorption isotherms (relative pressure) of TAPB-NDA-COF at 283, 293, 303, 313, 333 and 343 K.

(Figure S3). Lastly, the nitrogen sorption isotherms provided insights into the porous architecture of the COF (**Figure 1B**). The BET surface area of the TAPB-NDA-COF calculated from the adsorption isotherm is 722 $m^2 \cdot g^{-1}$, of which analysis details are provided in the supporting information (Figure S4). The adsorption branch shows a steep N_2 uptake until 0.02 P/P_0 and a more gradual N_2 uptake between 0.02 and 0.3 P/P_0, after which the curve plateaus. Such features are indicative of a distribution of micro- and mesopores being present in the

framework, which prompted us to calculate a pore size distribution (PSD) based on the experimental data of this adsorption branch (further specified in supplementary information, Figure S5 and S6). The PSD of the TAPB-NDA-COF is depicted in **Figure 1C**, showing distinct supermicropore volume (1 – 2 nm, ~ 0.27 $cm^3 \cdot g^{-1}$) and a relatively small mesopore volume (at 3.1 nm, ~ 0.03 $cm^3 \cdot g^{-1}$). Thus, the accessible pore volume originates not exclusively from the expected pore size of 3.1 nm based on molecular simulations.[18] This prominent supermicropore volume plays an important role in the CO_2 capacity of the COF.

The functional gas sorption properties of the COF were first studied in a controlled, single-component environment in order to later compare the capacities with values obtained from breakthrough experiments. The CO_2 uptake at 1 bar varied from 2.0 to 0.5 $mmol \cdot g^{-1}$ at adsorption temperatures from 283 to 343 K (**Figure 1D**).[19] In addition, serving as benchmark values for the experimental data of the breakthrough studies using 20/80 CO_2/N_2 mixtures at 3 bar, the CO_2 uptake at 0.6 bar varied from 1.5 to 0.3 $mmol \cdot g^{-1}$ at adsorption temperatures from 283 to 343 K. Although seemingly the absolute H_2O uptake drops at higher adsorption temperatures, plotting the water uptake as a function of relative pressure (*i.e.* relative humidity) shows overlapping isotherms for all temperatures (**Figure 1E**). The COF's water vapour capacity at RH 90 % of 30 $mmol \cdot g^{-1}$ (> 50 wt. %) is comparatively high.[20] The small, yet significant water uptake even at low RH values (e.g. 1.5 $mmol \cdot g^{-1}$ at 20 % RH) suggests some hydrophilicity within the COF. The polymer backbone is largely structured by hydrophobic benzene rings, but hydrophilicity may originate from the imide bonds, where the high electron density around the oxygen atoms can result in hydrogen bonding with water. Finally, the isosteric enthalpy of adsorption (ΔH_{ads}) of CO_2 is calculated based on its isotherms at multiple temperatures. The ΔH_{ads} of CO_2 adsorbed on TAPB-NDA-COF varies from -35 to -28 $kJ \cdot mol^{-1}$ at 0.1 and 0.8 $mmol \cdot g^{-1}$ loading respectively (Figure S7).

A series of breakthrough studies on TAPB-NDA-COF was executed to assess the COF's CO_2 separation performance under dry and humid conditions. The COF was always first equilibrated with a humid helium stream at the same temperature and water vapour pressure as that of the ensuing CO_2/N_2 breakthrough experiment. 20/80 CO_2/N_2 feed mixtures were used at 3.1 bar and various temperatures: 298, 313, 333, 343 and 353 K (for detailed experimental methods see supplementary information, Figure S8 – S12). For the humid streams the inlet stream was humidified through a saturator at room temperature leading to a constant partial water vapour pressure of 2.9 kPa. The temperature of the

column would then determine the effective relative humidity. Thus, RH values of 6, 9, 15, 39 and 90 % were imposed for column temperatures of 353, 343, 333, 313 and 298 K respectively. **Figure 2A** and **2B** display the CO_2 breakthrough curves (as a ratio of estimated exit flow rate over the feed flow rate) of these experiments for dry and humid gas streams respectively. In both cases, t = 0 s represents the first detection of non-adsorbing N_2 gas. The breakthrough time and curve slope dictate the CO_2 capacity of the adsorbent, as it can be quantified as the area above the curve. Each experiment contained 3 to 4 consecutive cycles of ad- and desorption, of which the CO_2 breakthrough times and capacities have been calculated (Table 1). In the case of dry gas streams, CO_2 has shorter breakthrough times and smaller CO_2 adsorption capacity as the temperature increases (see Table 1), in line with the expectations based on the CO_2 adsorption isotherms at different temperatures. Inversely, for the humid CO_2/N_2 gas streams, CO_2 breakthrough times and CO_2 adsorption capacity (see Table 1) initially increase with temperature, with a maximum at 343K. Under humid conditions the CO_2 breakthrough curves become less steep at higher temperatures, indicative of more dispersion.

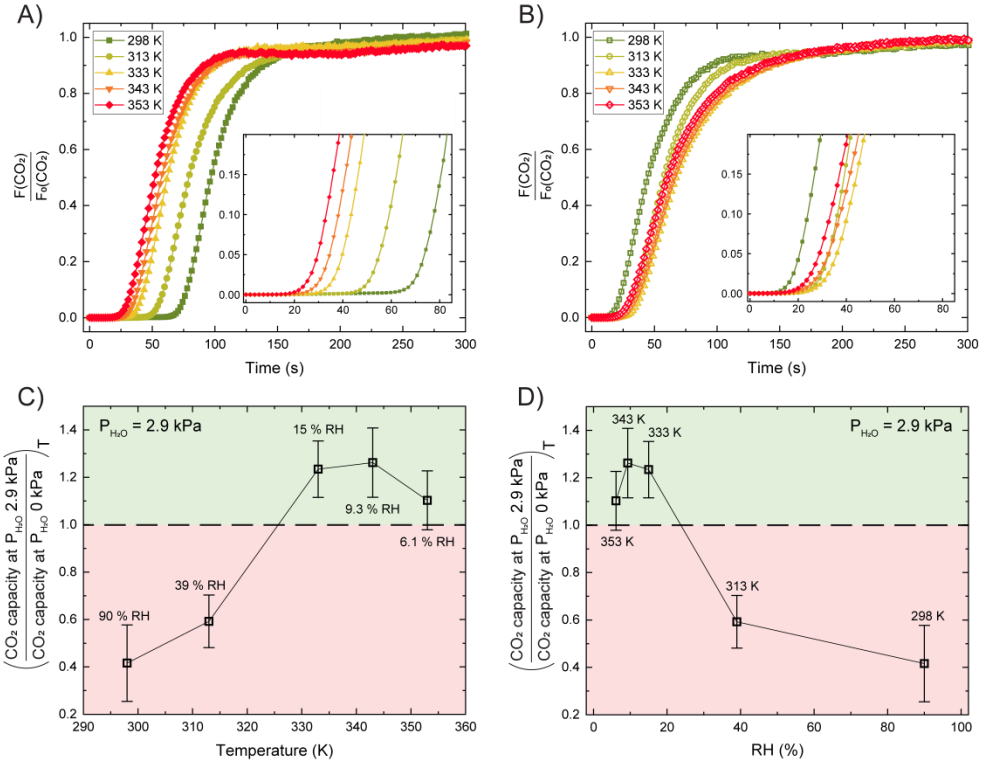

Figure 2. A) CO_2 breakthrough curves from dry 20/80 CO_2/N_2 mixed gas over a packed bed of TAPB-NDA-COF at 298, 313, 333, 343 or 353 K, all at 3.1 bar total pressure (all cycle 2). **B)** CO_2

breakthrough curves from humid ($P(H_2O)$ = 2.9 kPa) 20/80 CO_2/N_2 mixed gas over a packed bed of TAPB-NDA-COF at 298, 313, 333, 343 or 353 K, all at 3.1 bar (all cycle 2). **C)** Ratio of the CO_2 capacity at $P(H_2O)$ = 2.9 kPa over the CO_2 capacity at $P(H_2O)$ = 0 kPa, plotted as a function of temperature. Error bars are calculated based on 3 to 4 consecutive breakthrough cycles. **D)** The same data as figure C), plotted now as a function of relative humidity.

Table 1. Resulting CO_2 breakthrough times and CO_2 capacities from experiments of 20/80 CO_2/N_2 mixed gas over a packed bed of TAPB-NDA-COF at 298, 313, 333, 343 or 353 K, all at 3.1 bar, either at dry or humid conditions ($P(H_2O)$ = 2.9 kPa). The values and errors originate from 3-4 consecutive cycles for each experiment.

Adsorption temperature (K)	**$P(H_2O)$ (kPa) dry // humid**	**CO_2 breakthrough time (s) dry // humid**	**CO_2 capacity ($mmol \cdot g^{-1}$)**
298	0 // 2.9	63 ± 1.0 // 9.1 ± 1.5	1.3 ± 0.029 // 0.56 ± 0.20
313	0 // 2.9	45 ± 3.6 // 21 ± 2.7	1.1 ± 0.052 // 0.64 ± 0.089
333	0 // 2.9	28 ± 4.3 // 22 ± 0.91	0.71 ± 0.036 // 0.88 ± 0.041
343	0 // 2.9	22 ± 1.0 // 18 ± 1.0	0.66 ± 0.027 // 0.83 ± 0.063
353	0 // 2.9	19 ± 1.0 // 15 ± 0.91	0.65 ± 0.045 // 0.72 ± 0.032

The maximum capacity at RH 0 % was 1.3 $mmol \cdot g^{-1}$ (298 K) and the minimum capacity at RH 0 % was 0.65 $mmol \cdot g^{-1}$ (353 K). With increasing adsorption temperatures under dry conditions, the CO_2 breakthrough curves shifted more towards those of N_2 (Figure S10), indicating a diminishing CO_2/N_2 selectivity. Furthermore, the experiments with humidified gas streams yielded a maximum capacity of 0.88 $mmol \cdot g^{-1}$ (RH 15 %; 333 K) and a minimum of 0.56 $mmol \cdot g^{-1}$ (RH 90 %; 298 K). The ratio of the CO_2 capacity at $P(H_2O)$ = 2.9 kPa over the CO_2 capacity at $P(H_2O)$ = 0 kPa is plotted in **Figure 2C** and **2D**. The horizontal dashed line at 1.0 represents the dividing line below which water negatively affects CO_2 adsorption and above which water-enhanced CO_2 adsorption is observed. At 298 K at 90 % RH only 42 % of the original CO_2 capacity under dry conditions is retained. It is clear that from a certain relative humidity onwards (between RH 39 %, T = 313 K and RH 15 %, T = 333 K), water strongly competes with CO_2. This transition coincides with the onset of water cluster formation at ~ 30 % RH in the water vapour sorption isotherms. In addition, we observed that RH values of 6, 9

and 15 % at adsorption temperatures of 353, 343 and 333 K respectively increased the CO_2 adsorption capacity of TAPB-NDA-COF up to ~ 1.3 times. The CO_2/N_2 selectivity is increased going from 298 K at 90 % RH where the CO_2 and N_2 breakthrough curves nearly overlap, to lower RH values / higher temperatures where a clear shift between the curves is again noticeable. Finally, although a detailed study concerning the hydrolytic stability of COFs as adsorbents is not the main focus of this research, we duplicated the breakthrough experiment at 298 K and RH 0 % after all breakthrough experiments (involving a total exposure time of > 75 hours and temperatures up to 403 K) presented here had been executed. We overlapped these curves in Figure S13 and noticed no considerable change in CO_2 separation performance.

To also understand the CO_2 adsorption at constant temperature and pressure (298 K, atm. pressure) for varying amounts of adsorbed water, we opted for a small-scale laboratory test based on a protocol developed by Llewellyn and co-workers,[9] where a pre-humidified COF sample was subjected to CO_2 ad- and desorption cycles in a thermogravimetric analysis (TGA) instrument. Between the cycles, small amounts of water were successively desorbed, in order to monitor the CO_2 capacity of the material at various water loadings (see supplementary information and Figure S14 for the complete protocol and data analysis). The results are summarized in **Figure 3**, where the data was normalized over the specific CO_2 capacity at dry conditions. The relative humidity corresponding in equilibrium with the different amounts of adsorbed water (determined from the water adsorption isotherm at T = 298 K) is also indicated. The measurable range of adsorbed water content with this method is restricted, since the weakly adsorbed water is desorbed quickly by the dry passive nitrogen flow. We see the CO_2 capacity increasing with the adsorbed water content, up to the highest measurable content, which corresponds with ~ 9 % RH. Likely the relative humidity corresponding to the maximum amount of CO_2 adsorbed is even higher. These data indicate a synergistic effect of pre-adsorbed water enhancing the CO_2 capacity of the COF compared to the 'dry' state at a constant temperature, strengthening the notion that the key parameter for enhanced CO_2 uptake is relative humidity. Similar effects have been noticed by Ibarra and co-workers,[14,15] among others, and a comparison between the CO_2 capture performance (dry and humid) of TAPB-NDA-COF and other adsorbents under similar experimental conditions has been provided in Table S2. Here, mainly MOFs with μ-OH segments in their structure were compared, as these MOFs show enhanced CO_2 uptake at comparable low amounts of pre-adsorbed water. The performance of another MOF, HKUST-1 bearing open metal sites that are occupied by water at low

humidity levels, is also compared. The common structural feature that causes enhanced CO_2 adsorption seems to be hydrophilic groups (be it μ-OH or open metal sites), which – once bound to water molecules – favor CO_2 binding more than the dry structures themselves.

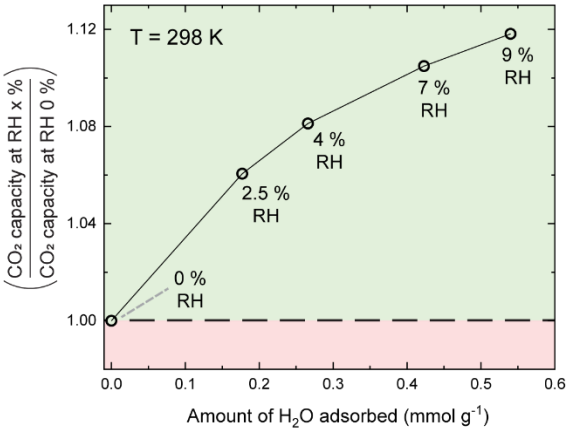

Figure 3. Ratio at 298 K of the CO_2 capacity at specific RH values over the CO_2 capacity at RH 0 %, plotted as a function of the amount of H_2O adsorbed at 298 K and atmospheric pressure. Capacity values are extracted from CO_2 and H_2O sorption TGA experiments based on a protocol proposed by Llewellyn and co-workers.[9] The shown % RH are those that correspond in equilibrium with the amount of adsorbed water as determined from the water adsorption isotherm at 298 K.

To relate these findings to the structure and chemistry of the COF, we performed *ex situ* FT-IR experiments at controlled RH values. **Figure 4A** represents the FT-IR spectra for various COF aliquots equilibrated at 298 K and specific RH values. The spectra were normalized over the symmetric imide carbonyl stretching vibrations at maximum absorbance in the region of 1640 – 1700 cm^{-1}. We varied the RH from ~ 0 % to 80 % and we performed a control experiment where the COF exposed to RH 80 % was vacuum degassed again (to RH ~ 0 %) and subjected to the FT-IR measurement. The spectra of prior to- and after-water equilibration overlapped (Figure S15), indicating that the changes observed here are reversible. It should be noted, however, that the samples denoted as RH 0 % are briefly exposed to the humidity of the lab during transfer to the ATR crystal and the FT-IR spectrometer.

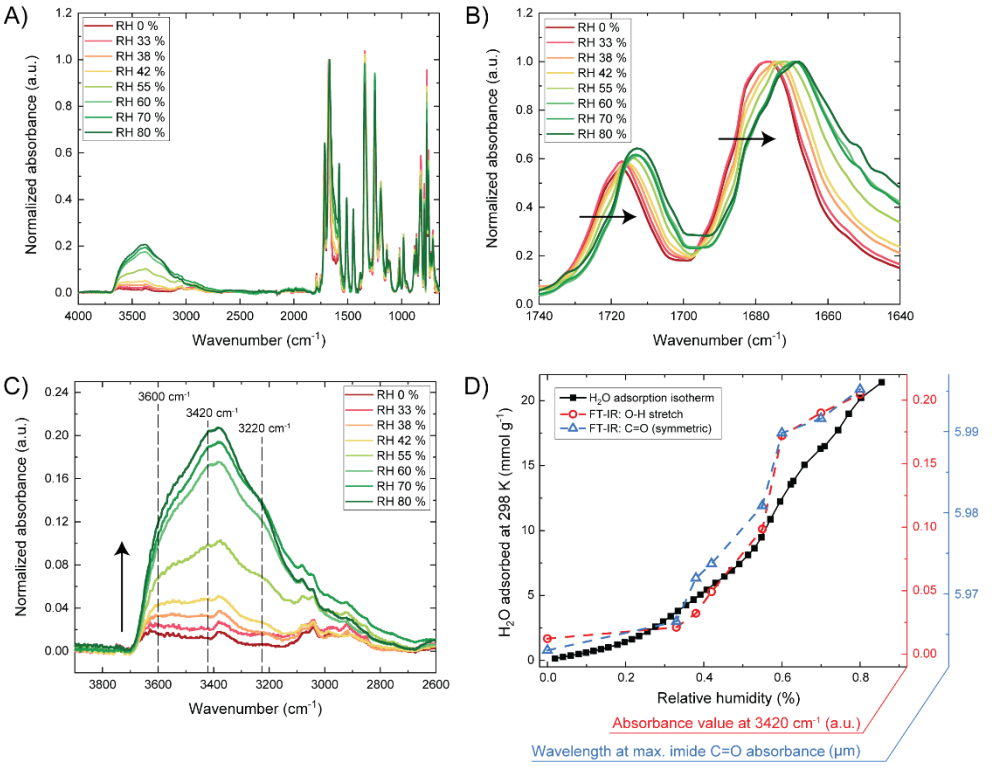

Figure 4. A) FT-IR spectra of TAPB-NDA-COF equilibrated at 298 K and various RH values. **B)** Zoom-in on the (a)symmetric C=O stretch vibrations of the imide bond. **C)** Zoom-in on the region of O-H stretch vibrations. **D)** Overlap of water vapor sorption isotherm at 298 K, a plot of the inverse of the imide carbonyl peak maxima (1677 – 1668 cm^{-1}, extracted from B)) as a function of the RH and a plot of RH versus the absorbance values at 3420 cm^{-1}, extracted from C).

The imide peaks that we investigated are presented in **Figure 4B**, since these signals changed (red-shifted) most drastically as a result of increasing RH values, which suggests that these groups are actively involved in the water uptake. This shift (even at low water loadings: 3 cm^{-1} from 0 to 38 % RH) is significant, considering that within a COF unit cell there is a large amount of active sites: ~ 8.6 mmol carbonyl O-atoms per gram of COF. Both the symmetric (~ 1680 cm^{-1}) and asymmetric (~ 1720 cm^{-1}) carbonyl stretching vibrations of the imide bonds are red-shifted as a result of increasing RH values. Focussing on the symmetric vibrational mode, the maximum absorbance shifts significantly from 1677 cm^{-1} at RH 0 % to 1668 cm^{-1} at RH 80 %. Although the effect was less pronounced on the C-N stretch vibration of the imide bond (Figure S16), the increasing RH values caused a noticeable blue-shift from 1340 cm^{-1} at RH 0 % to 1344 cm^{-1} at RH 80 %. The lone pair of the imide nitrogen is delocalized through resonance with the imide

carbonyls, making the nitrogen less likely to participate in hydrogen bonding, in line with the observation here that the C-N bond strength increases upon water adsorption. Secondly, the absorbance intensity of the O-H stretching vibrations increases significantly with larger RH values (**Figure 4C**). While this region is a complex accumulation of different vibrational modes, we focussed on three main signals: ~ 3600, 3420, and 3220 cm^{-1}. All three signals are RH-dependent, but the onset of their increase seem to differ. The signal at ~ 3600 cm^{-1} is already present at ~ 0 % RH and seems to be dominating at low RH values. The signals at 3420 and 3220 cm^{-1} develop into a clear peak and shoulder peak, respectively, at higher RH values (around 38 – 42 %). Overall the ratio of the peak at ~ 3600 cm^{-1} compared to the one at 3220 cm^{-1} is much higher at RH up to 42 %, versus at higher values. In **Figure 4D**, we plotted both the increasing absorbance of the O-H stretching vibration at 3420 cm^{-1} and the inverse of the imide carbonyl peak maxima (1677 – 1668 cm^{-1}) as functions of the RH. In the same plot we display the water isotherm of the COF at 298 K (also following a water signal over a RH range, albeit manometrically) as complementary data to the FT-IR data.

Solid-state NMR studies on hydrated polyimide films by Waters *et al.* support the claim of imide-carbonyl groups being the main active sites for water adsorption.[21] Moreover, the detailed work of Musto *et al.* on the interaction of water with polyimides studied by 2D-FT-IR correlation spectra noticed the imide carbonyl red-shift as well,[22] and distinguished first- and second-shell hydration layers through deconvolution of the complex O-H stretch region. The first hydration event generates single site adsorbed water of which the free O-H bond vibrates at a relatively high wavenumbers. Indeed, the shoulder peak at 3600 cm^{-1} is more prominent at low RH values, compared to the signals at 3420 and 3220 cm^{-1} (**Figure 4C**). These latter two signals could represent multiple-bound water in the form of water clusters and such clusters seem to become more significant around 38 – 42 % RH. Furthermore, the imide-carbonyls signals red-shift continuously over the whole RH range (following a similar trend to the water vapour isotherm; **Figure 4D**). So, while they are the main adsorption sites for water (~ 8.6 mmol per gram of COF), they are not completely saturated upon the first hydration events. This stands in contrast to, for example, MOFs with hydrophilic open metal-sites. There, a clear 2-step mechanism can be observed of: (1) coordination of water on active sites and subsequent saturation of these sites, and (2) pore filling through water network formation.[23] In the case of TAPB-NDA-COF, however, it seems more likely that at 38 – 42 % RH water-water interactions are roughly equally favoured as water-framework interactions, *i.e.* isolated water-carbonyl interactions in one pore occur simultaneously with water clustering and

centre pore filling in the other pore.[24] Such a pore filling mechanism allows rationalization of the breakthrough results. The RH values where single-site adsorbed water is a dominant feature namely coincides with the RH values where water-enhanced CO_2 adsorption was observed. Therefore, it is likely that the ΔH_{ads} for CO_2 on single site adsorbed water is greater than the ΔH_{ads} for CO_2 on the adsorption sites of the dry COF. Recent computational studies using many-body potential energy functions for simple $(H_2O)_m(CO_2)_n$ systems revealed that the interaction energies of clusters with $m \geq 1$ are always greater than for clusters where $m = 0$ (*e.g.* $(CO_2)_2 \sim -6.3$ kJ·mol^{-1} while $(H_2O)(CO_2) \sim 12.4$ kJ·mol^{-1}).[25] These absolute values cannot be fully translated to our system (partly due to the inclusion of a complex adsorbent), yet the relative trends of our study and these computational results coincide and strengthen the hypothesis of water-enhanced CO_2 adsorption being attributed to single-site adsorbed water. The interaction between this single site adsorbed water and CO_2 can occur via two modes: between the partially negatively charged oxygen of H_2O and the partially positively charged carbon of CO_2 or between the partially positively charged hydrogen of H_2O and the partially negatively charged oxygen of CO_2.[26,27] This particular interaction is likely to be energetically more favourable than the interaction between the dry COF and CO_2. As such, we expect that CO_2 uptake could be enhanced by pre-confining other molecules as well,[28] especially those with similar hydrogen bonding capabilities.

Lastly, the rate of the CO_2 – COF mass transfer is slower in the breakthrough experiments that showed water-assisted CO_2 adsorption, *i.e.* slower diffusion through the porous network. The slower CO_2 diffusion in sub-nanoporous channels created at similar water concentrations has also been observed in MOF UiO-66.[11] As is also mentioned in their research, water-enhanced effects at equilibrium can come at the cost of slow kinetics, which shows the importance of fundamentally understanding these processes for rapid separation processes.

4.3 Conclusion

In summary, the extensive breakthrough studies allowed us to couple material characteristics to the COF's performance of CO_2 separation from humid CO_2/N_2 streams. The relative humidity throughout these experiments was varied at *constant water vapour pressure* around 2.9 kPa in the gas stream by changing the adsorbent column temperature. By doing so we discovered that the CO_2 adsorption capacity increases ~ 25 % in comparison with the dry stream at 333 K (RH = 15 %) and 343 K (RH = 9.3 %), when – in the case of TAPB-NDA-COF – the gas stream

is humidified. Via measuring the CO_2 adsorption capacity for varying amounts of adsorbed water at a *constant temperature* (298 K) using a thermogravimetric protocol, we corroborated the water-enhanced CO_2 adsorption effect. These results show that this phenomenon for the TAPB-NDA-COF is robust (independent on the experimental setup).

Via infrared spectroscopy, we could correlate the enhanced CO_2 adsorption at low relative humidity values with single site adsorbed water on the imide carbonyl groups. The ΔH_{ads} for CO_2 adsorbed on such a water adsorbate is likely greater (more negative) than the ΔH_{ads} determined for the CO_2 interaction with dry the COF (~ -35 $kJ \cdot mol^{-1}$), resulting in water-enhanced CO_2 adsorption. At 38 – 42 % RH, water clustering and centre pore filling becomes dominant. Here, CO_2 binding would mean the interruption of multiple hydrogen bonds (a large energy penalty), and thus CO_2 adsorption is inhibited. Percolation of the water network at these higher RH values drastically lowers the CO_2 capacity of the COF.

Although there are many examples displaying the water tolerance of COFs, few place this in the context of how adsorbed water affects CO_2 capture and separation,[29,30] and fewer still systematically varied RH values in industrially relevant breakthrough setups (where mostly a negative effect of water is observed).[6,7] The results presented here are among the first to show cooperative CO_2–H_2O adsorption in COFs. The overall CO_2 adsorption capacity of this COF is rather modest (~ 1.3 $mmol \cdot g^{-1}$ at 0.6 bar CO_2). Yet, we trust that the understanding of water-enhanced CO_2 adsorption we uncovered here, can be exploited via the tuneable nature of COFs, specifically focussing on COFs that show a high CO_2 adsorption capacity.

ACKNOWLEDGEMENTS

The authors acknowledge Prof. Dr. Freek Kapteijn, Prof. Dr. Atsushi Urakawa, Dr. José Palomo Jiménez, and Dr. Eduardo Andres-Garcia for valuable discussion throughout the project. The authors are also grateful for the initial high-temperature humid breakthrough experiments performed by Marie-Claire Rekkers.

4.4 Supporting Information

4.4.1 Experimental Method Details

Reagents

All reagents presented in this report were commercially available and used without further purification or treatment. 1,3,5-Tris(4-aminophenyl)benzene (≥ 93 %) and isoquinoline were purchased from TCI Europe N.V (Zwijndrecht, Belgium), 1,4,5,8-naphthalenetetracarboxylic dianhydride (≥ 95 %) and ortho-dichlorobenzene from abcr GmbH (Karlsruhe, Germany) and N-methyl-2-pyrrolidone from Acros Organics B.V.B.A (Geel, Belgium).

Characterization techniques

FT-IR spectra were recorded on a PerkinElmer Spectrum 100 FT-IR Spectrometer with an universal ATR accessory over a range of 4000 to 650 cm^{-1}. TGA analyses were performed from 30 to 860 °C, under a nitrogen atmosphere at a heating rate of 10 °C·min^{-1} using a Perkin Elmer TGA 4000. Before the measurement, the samples were degassed at 130 °C for one hour under a nitrogen atmosphere. PXRD patterns were measured on a Rigaku MiniFlex 600 powder diffractometer using a Cu-Kα source (λ = 1.5418 Å) over the 2θ range of 2 ° to 40 ° with a scan rate of 1 °·$minute^{-1}$. Nitrogen and carbon dioxide isotherms were measured on the Micromeritics TriStar II porosity analyser. Water vapour isotherms were measured on the Micromeritics 3Flex adsorption analyser. Prior to the sorption measurements, all samples were degassed at 130 °C under vacuum for 16 h. The Quantachrome VersaWin software package was used for calculations of pore size distributions by fitting the nitrogen adsorption isotherms to the quenched solid density functional theory (QSDFT) carbon model (using slit/cylindrical/spherical pores). No smoothing factor was applied for the PSD calculation.

Synthesis of TAPB-NDA COF

TAPB (351 mg, 1.0 mmol) and NDA (402 mg, 1.5 mmol) were added to a glass cylindrical reactor and subsequently o-DCB (10 mL), NMP (10 mL) and isoquinoline (0.1 mL) were added. Thereafter, the reactor was sealed, vacuum degassed, and placed in an oil bath. Under gently shaking the reactor vessel, it was heated to a temperature of 150 °C. Upon complete dissolution of the monomers, the temperature was step-wise (10 °C per 15 min) increased to 190 °C and kept without agitation at that temperature for 3 days. The reaction mixture was cooled to room temperature, suspended in 60 mL methanol, and mixed thoroughly. The solid was separated from the liquid through centrifugation (10 min at 4400 rpm),

after which the solid was washed with methanol (3 x 30 mL) and acetone (1 x 30 mL). After drying the solid in a vacuum oven at 60 °C for one hour, it was subjected to Soxhlet extraction with THF for 20 hours. After that, the COF was allowed to dry in a vacuum oven at 60 °C for 20 hours. The TAPB-NDA-COF was isolated as an ochre-brown, fluffy powder (610 mg, 87 %).

Post-synthetic processing

The COF powder was pelletized in batches of ~ 100 mg, using a pellet die with a diameter of 20 mm. For each batch, a hydraulic press was used to apply a pressure of 31 MPa for 60 seconds. After that, the pellets were crushed and then, through sieving, we collected COF pellets in the particle size range between 300 and 425 µm. These pellets were used without further treatment for characterization and breakthrough studies.

Isosteric enthalpy of adsorption,

The common Freundlich–Langmuir fit/Clausius–Clapeyron approach for the calculation of ΔH_{ads} was executed according to the procedure described by Alexander Nuhnen and Christoph Janiak (DOI: 10.1039/D0DT01784A) and applied to all CO_2 adsorption isotherms. The corresponding Freundlich–Langmuir fitting parameters are presented in Table S1.

Water-COF FT-IR binding studies

Around 5 mg of pelletized COF was transferred to an open vial. This vial was placed in a 250 mL glass jar that also contained a vial of ~ 10 mL of salt solutions / suspensions. A relative humidity sensor was added to the system, which was subsequently sealed with Parafilm. The COFs were allowed to equilibrate for 16 hours at room temperature. Thereafter, they were immediately subjected to standard FT-IR analysis. The following RH values were monitored for the specific salt solutions: calcium chloride for 33 %, magnesium chloride for 38 %, sodium iodide for 42 %, sodium bromide for 55 %, magnesium bromide for 60 %, sodium chloride for 70 % and distilled water for 80 % relative humidity. The latter value is relatively low compared to other systems with distilled water, but this is likely a kinetic effect (*i.e.* insufficient equilibration time). On the other hand, the lower RH values agree with literature values. RH values of ~ 0 % are obtained by directly retrieving the COF vial from a vacuum oven set at 130 °C. Those vials were directly sealed when retrieved from the oven and utilized directly for FT-IR analysis.

Breakthrough studies

Setup

The breakthrough setup for multicomponent breakthrough studies is an in-house built setup (see Fig. S7), extensively used in the doctoral thesis *Gas Adsorptive Separation through Microporous Materials*, by Andres Garcia, Eduardo, 2019 (https://doi.org/10.4233/uuid:cfbabbfc-b66c-4279-b717-df9e73ed921f). It primarily consists of He, N_2 and CO_2 feed flows (regulated by mass flow controllers, Brooks 5850 series), water saturators and a packed bed column within which temperature and pressure can be regulated. The bed height of the COF (95 mg) in the stainless steel column (length 79 mm, inner diameter 4 mm) is 39 mm, and the bed is sandwiched between two layers of quartz wool. A four-way switching valve allows the operator to switch between N_2 (at 8 mL·min^{-1}) / CO_2 (at 2 mL·min^{-1}) mixture (feed 1) and He (feed 2) gas streams and back-pressure regulators ensure a constant pressure when switching. The second He flow (at 10 mL·min^{-1}) is added after the column to prevent flow disruptions and securing a constant flow to the analysis instruments. The breakthrough response is monitored by a mass spectrometer (MS, LPM T100 Gas Analyzer) and a relative humidity sensor (PosiTector Dew Point Meter, DeFelsko). A complete overview of the setup is displayed in Figure S7.

Experiments

Prior to every experiment (set of 4 cycles per experimental parameter set), the system is flushed overnight (~ 16 h) with 10 mL·min^{-1} He and the oven is set to 130 °C. Then, the column is allowed to reach the specific temperature necessary for the experiment. An additional pre-treatment step is used for humid experiments, where the column is exposed to a humid He stream with a controlled RH value and temperature, and equilibrated overnight (~ 16 h). Typically, 60 minutes are used for the adsorption and desorption cycles unless stated otherwise. Dead volume measurements were performed by replacing the COF with non-adsorbent silicon carbide (350 μm) using a similar bed height.

Analysis of breakthrough data

MS signal to flow rate

The conversion of MS signal to estimated flow rates from the exit are based on the following equations. For every component x, a normalized component fraction y is calculated (eq. 1) based on the MS signal, noise and final steady state (ss) values

(i.e. when breakthrough of all components has occurred and the signals stabilized). The *noise* signal is the background MS signal.

$$y_x(t) = \frac{signal_x(t) - noise_x}{signal_x(ss) - noise_x} \quad \text{eq. 1}$$

At steady state, the calculated exit flow rates are directly proportional to $y_x(t)$:

$$F_x(ss) = y_x(t) \cdot F_x^{feed} \quad \text{eq. 2}$$

With F_x^{feed} being the feed flow rates of components x.

But, to have an expression for $F_x(t)$ we have to use a correction factor: there is a constant flow going into the MS, but the total flow rate that exits the adsorption column changes over time (due to adsorption / desorption of different components). So, the time-dependent correction factor $C(t)$ should correct for the fact that the total flow rate at steady state can be different than the total flow rate during adsorption:

$$F_x(t) = y_x(t) \cdot F_x^{feed} \cdot C(t) \quad \text{eq. 3}$$

$$F_x(t) = y_x(t) \cdot F_x^{feed} \cdot \frac{F_{N_2}(t) + F_{CO_2}(t) + F_{He}(t)}{F_{total}(ss)} \quad \text{eq. 4}$$

While eq. 4 can be written as three separate equations for all components, these three equations are not independent and thus cannot be solved in order to get an expression for $F_x(t)$ that is defined by only known values. We also cannot assume $F_{He}(t)$ to be constant (which would help solving the equations), as it is used both as a flush and a sweep gas. Instead, we found that the equation 5, using only known values, where the term $F_{N2}(t) + F_{CO2}(t) + F_{He}(t)$ is approximated as $\left(y_{N2}(t) \cdot F_{N2}^{feed}\right) + \left(y_{CO2}(t) \cdot F_{CO2}^{feed}\right) + \left(y_{He}(t) \cdot F_{He}^{feed}\right)$ yields corrected breakthrough curves. In this case, features such as the roll-up effect on the nitrogen curves are visible and calculating capacities based on eq. 5 yields comparable capacity values to the ones based on the TGA experiments.

$$F_x(t) = y_x(t) \cdot F_x^{feed} \cdot \frac{\left(y_{N_2}(t) \cdot F_{N_2}^{feed}\right) + \left(y_{CO_2}(t) \cdot F_{CO_2}^{feed}\right) + \left(y_{He}(t) \cdot F_{He}^{feed}\right)}{F_{total}(ss)} \quad \text{eq. 5}$$

The normalized corrected flow for component x is defined as $\frac{F_x(t)}{F_x^{feed}}$, otherwise written as $\left(\frac{\mathrm{F}(x)}{F_0(x)}\right)$ in the main manuscript.

<u>CO_2 breakthrough time and capacity</u>

The CO_2 breakthrough time is classified as the breakthrough time difference between N_2 and CO_2 breakthrough. In this research, we identify the exact point of

breakthrough when there is a significant difference in the slope of the curve (see Figure S11). CO_2 capacities were calculated from their breakthrough curves (time vs $F(CO_2)$), by integrating the area above this curve. Areas were always integrated using:

- the x-axis range: time t = 0 (defined as N_2 breakthrough) to t = 1200 seconds (chosen as here typically all curves have plateaued, see Figure S11), and
- the y-axis range: $F(CO_2) = 0$ to $F(CO_2) = 2$.

Then, this area is subtracted by the integrated area above the CO_2 breakthrough curve from the silicon carbide experiments (dead volume). The dry-silicon carbide area was used for the dry COF experiments, and the humid-silicon carbide area for the humid COF experiments. The value of the final integrated area is divided by the weight of the COF in the column (95 mg) to obtain the CO_2 capacity in $cm^3 \cdot g^{-1}$ (at STP) or $mmol \cdot g^{-1}$ (Table 1).

TGA measurements of COFs with pre-adsorbed water

The protocol for TGA measurements of COFs with pre-adsorbed water was adopted from Llewellyn and co-workers with minor changes (https://doi.org/10.1002/cssc.201601816). First, COFs were equilibrated in a closed vessel in the presence of water at 80 % RH. Then, ~ 7 - 10 mg of this powder was transferred to the TGA crucible and submitted to the following program:

1. 100 $mL \cdot min^{-1}$ N_2 flow, 298 K, 60 minutes
   (equilibration, desorption of weakly bound water)
2. 100 $mL \cdot min^{-1}$ CO_2 flow, 298 K, 30 minutes (adsorption)
3. 100 $mL \cdot min^{-1}$ N_2 flow, 298 K, 30 minutes (desorption)
4. 100 $mL \cdot min^{-1}$ N_2 flow, heating to desired temperature at 10 $K \cdot min^{-1}$
   (controlled water desorption)
5. 100 $mL \cdot min^{-1}$ N_2 flow, cooling to 298 K at 10 $K \cdot min^{-1}$
6. 100 $mL \cdot min^{-1}$ N_2 flow, 298 K, 15 minutes
   (ensure temperature stabilization)
7. 100 $mL \cdot min^{-1}$ CO_2 flow, 298 K, 30 minutes (adsorption)
8. 100 $mL \cdot min^{-1}$ N_2 flow, 298 K, 30 minutes (desorption)

We used water desorption temperatures of 333, 363, 393 and 423 K at step 4. All weights from the TGA measurements were corrected with the weight of the empty crucible following the same protocol. After the four measurement cycles of step 1.-

8., the weight of the COF with 0 mmol·g^{-1} H_2O adsorbed was obtained by first drying the COF powder under 100 mL·min^{-1} N_2 flow at 423 K for three hours, cooling to 298 K and stabilizing at that temperature for 60 minutes, after which the monitored weight was taken as the dry-COF weight. Then, the dry COF was again subjected to a final CO_2 ad- and desorption cycle (replicate step 7 and 8). The supplementary data to the main figure (Figure 3) are presented in supplementary Figure S13. The data were analysed as is listed in the supplementary protocol of Llewellyn and co-workers. Similar to the issues with their data analysis, we calculated 2 CO_2 and 2 H_2O capacities (including and excluding the unaccounted weight increase, step 4 in Figure S13A) which were averaged for the final data.

4.4.2 SUPPLEMENTARY EXPERIMENTAL DATA

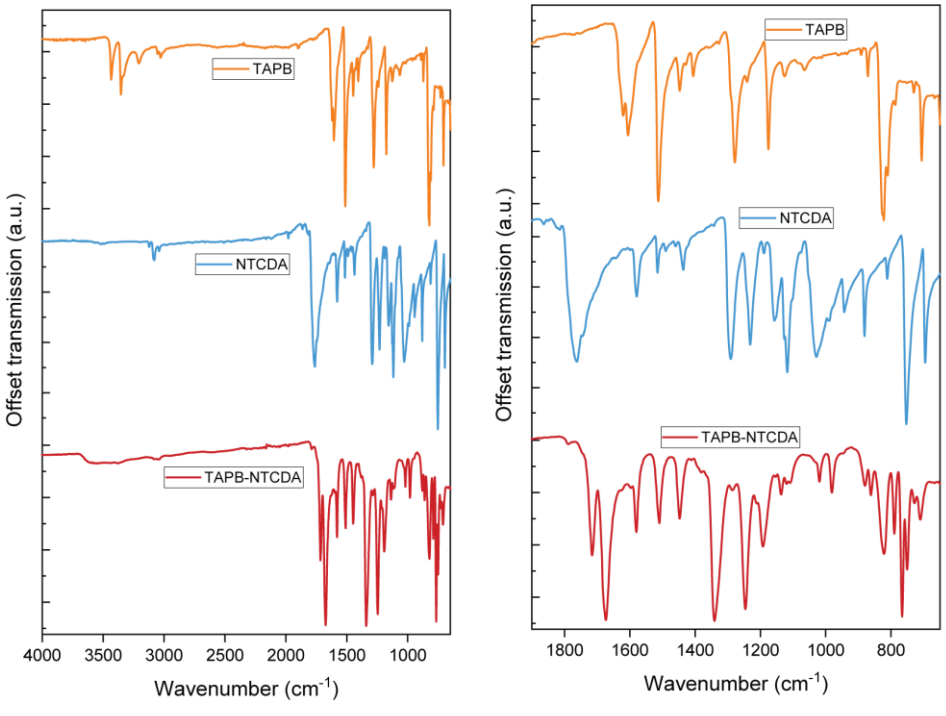

Figure S1. FT-IR spectra of TAPB-NDA-COF and its originating monomers TAPB and NDA. The right graph is a zoom-in of the left graph.

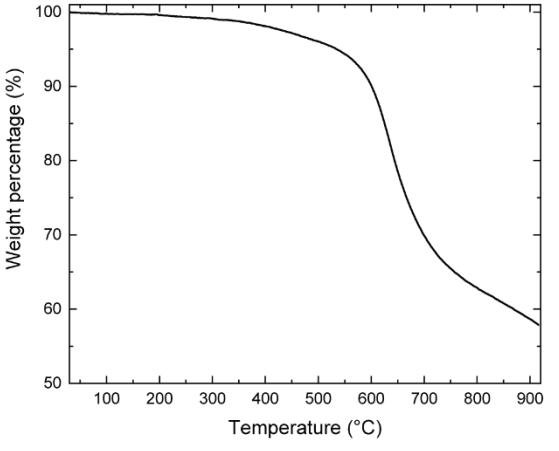

Figure S2. Standard TGA curve of TAPB-NDA-COF. Heating rate of 10 °C/min was used under a constant nitrogen flow at 100 mL/min.

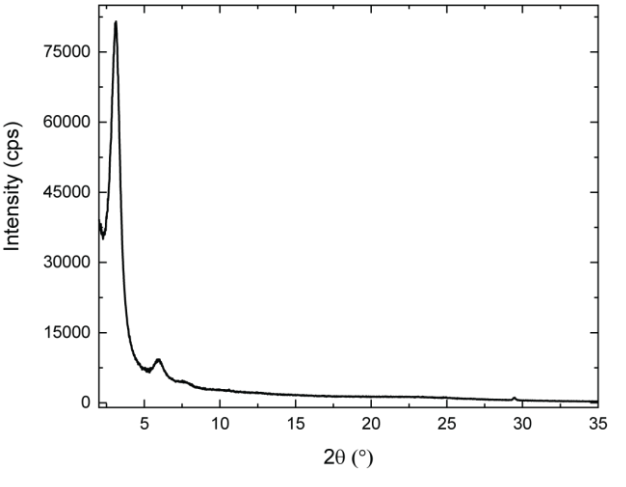

Figure S3. PXRD pattern of TAPB-NDA-COF.

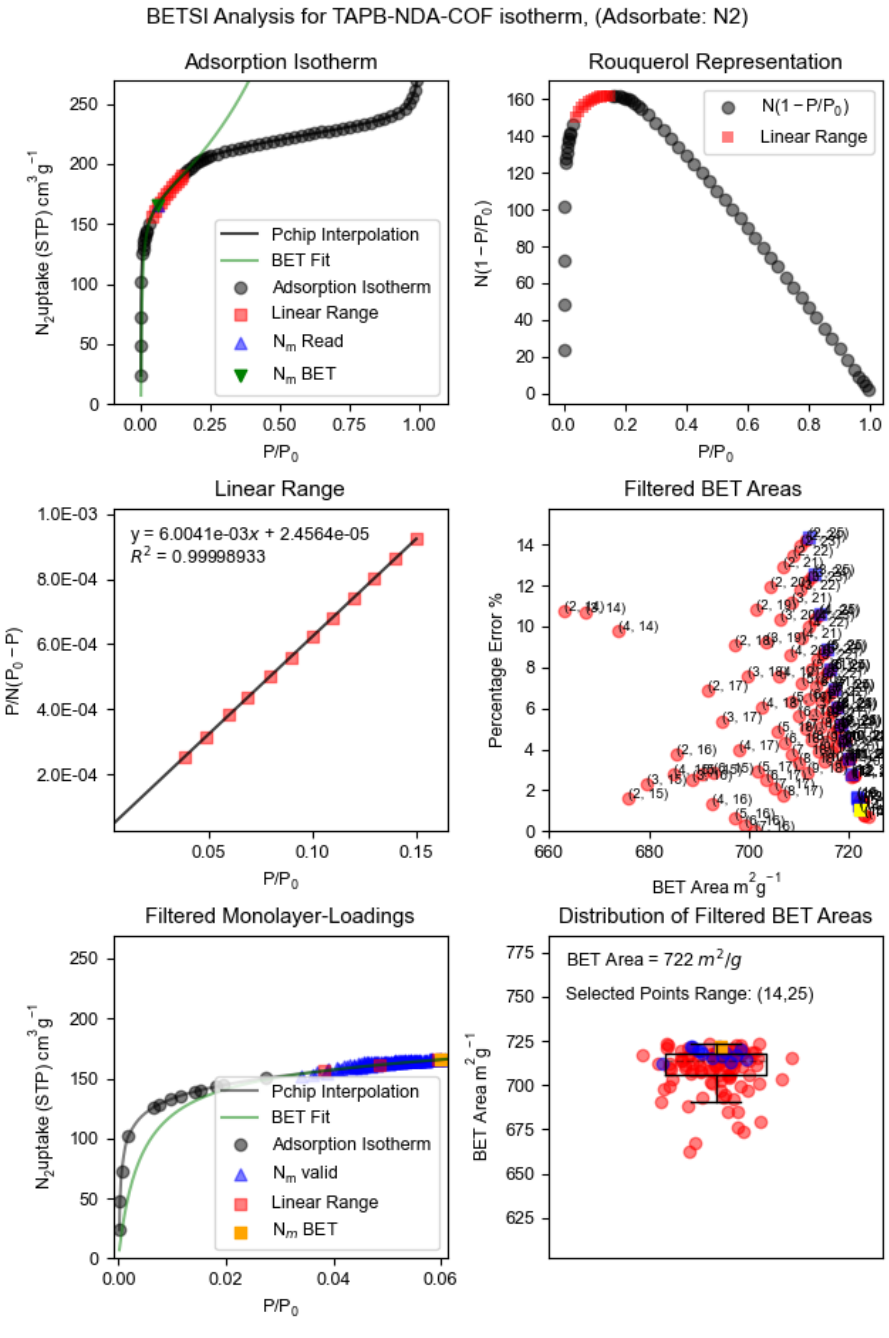

Figure S4. BETSI analysis report for the adsorption isotherm of TAPB-NDA-COF.[S1]

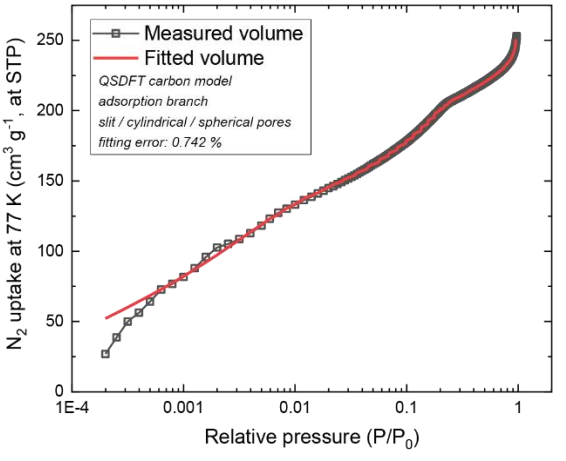

Figure S5. Fitting curve of the PSD of TAPB-NDA-COF, using the adsorption branch of the nitrogen isotherm and a QSDFT carbon model.

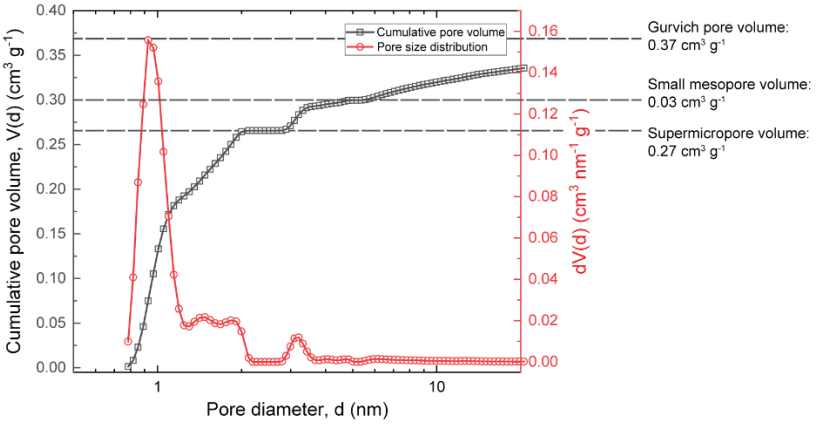

Figure S6. Cumulative pore volume and pore size distribution of TAPB-NDA-COF with indicated supermicropore, small mesopore, and Gurvich pore volume.

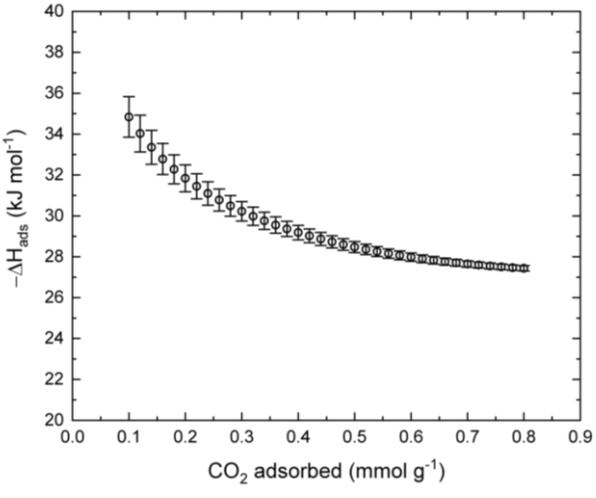

Figure S7. Iosteric enthalpy of adsorption based on the CO_2 adsorption curves and calculated via the Freundlich-Langmuir / Clausius-Clapeyron approach.

Table S1. Fitting parameters for the Freundlich–Langmuir fits applied to CO_2 adsorption isotherms. The equation used for the fit is B = (a*b*p^c)/(1+b*p^c), with p being the absolute pressure (kPa) and B the CO_2 uptake (mmol g^{-1}).

Temperature (K)	**a**	**b**	**c**	**Reduced χ^2**	**R^2**
283	6.89 ± 0.33	0.01424 ± 4E-4	0.730 ± 0.009	4.80E-5	0.9999
293	5.85 ± 0.28	0.0109 ± 3E-4	0.779 ± 0.009	3.15E-5	0.99991
303	3.92 ± 0.09	0.0102 ± 1.2E-4	0.845 ± 0.006	7.72E-6	0.99996
313	3.59 ± 0.08	0.00745 ± 9E-5	0.876 ± 0.005	3.76E-6	0.99998
333	2.99 ± 0.08	0.00414 ± 6E-5	0.936 ± 0.005	1.29E-6	0.99998

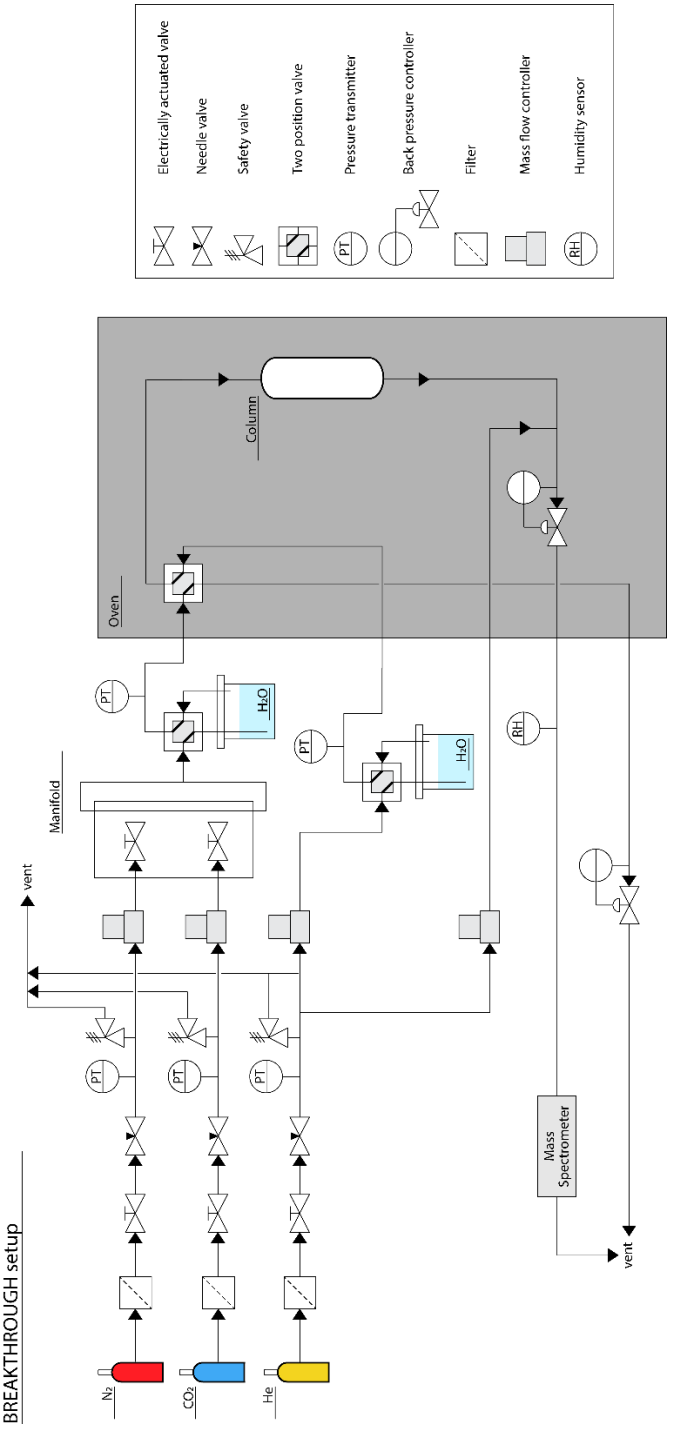

Figure S8. Schematic representation of breakthrough setup.

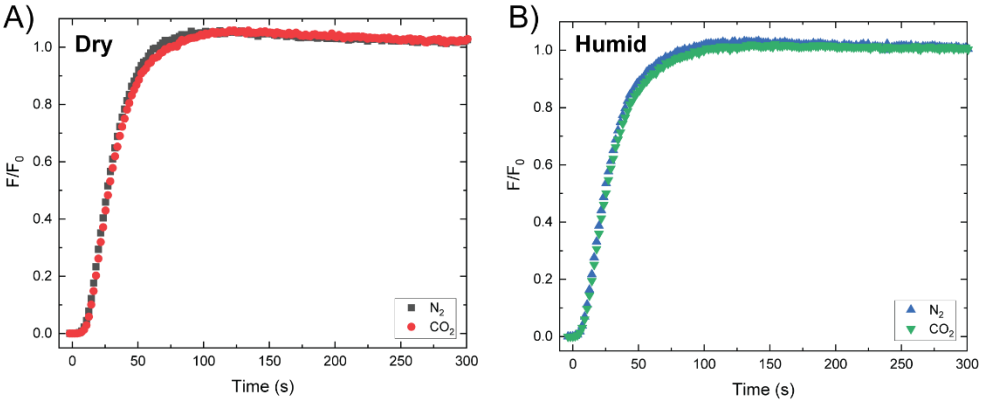

Figure S9. Normalized N_2 (8 mL/min) and CO_2 (2 mL/min) silicon carbide breakthrough curves at 3.1 bar and 298 K under **A)** dry, and **B)** humid conditions.

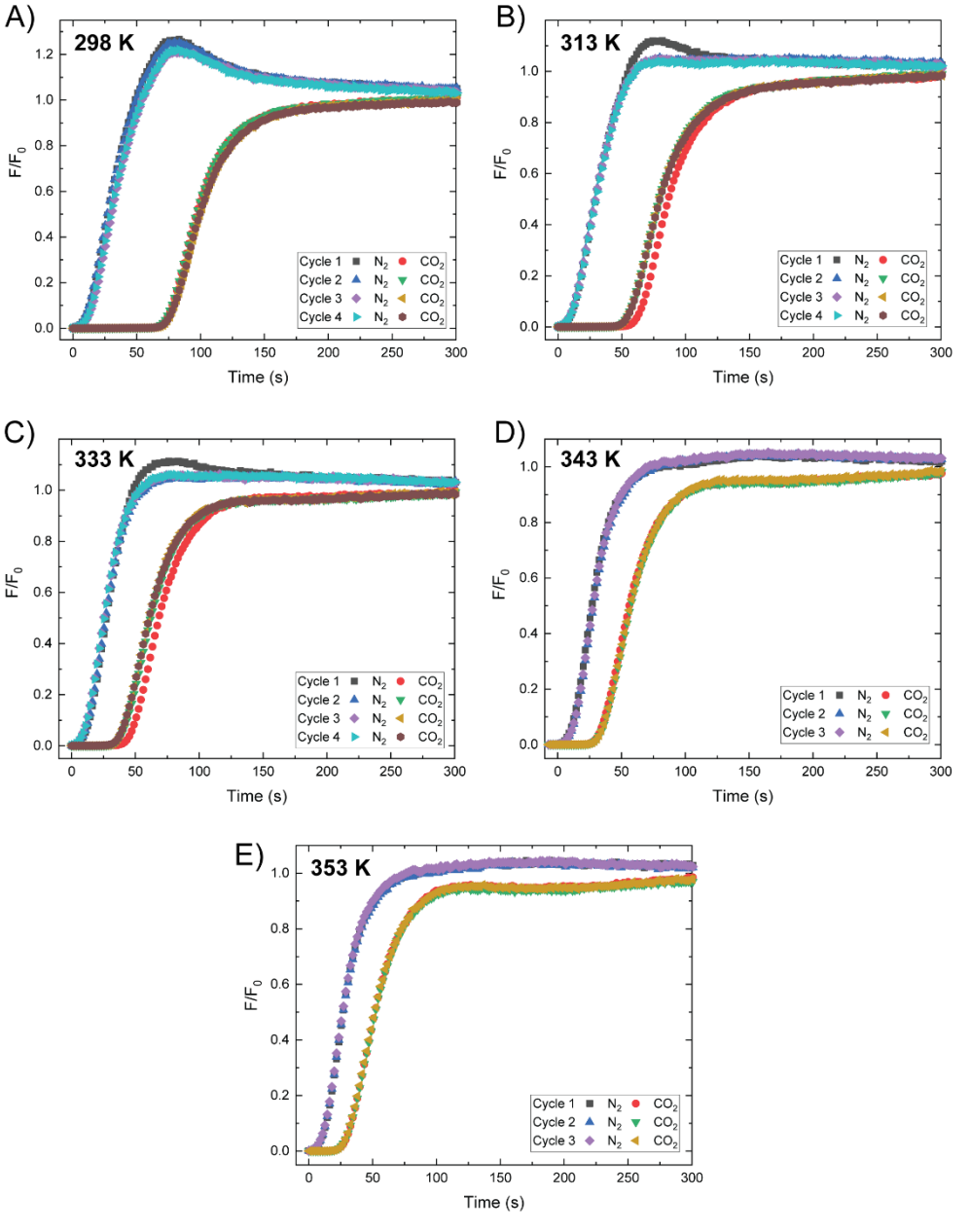

Figure S10. Normalized N_2 (8 mL/min) and CO_2 (2 mL/min) TAPB-NDA-COF breakthrough curves under dry conditions at 3.1 bar and **A)** 298, **B)** 313, **C)** 333, **D)** 343 and **E)** 353 K.

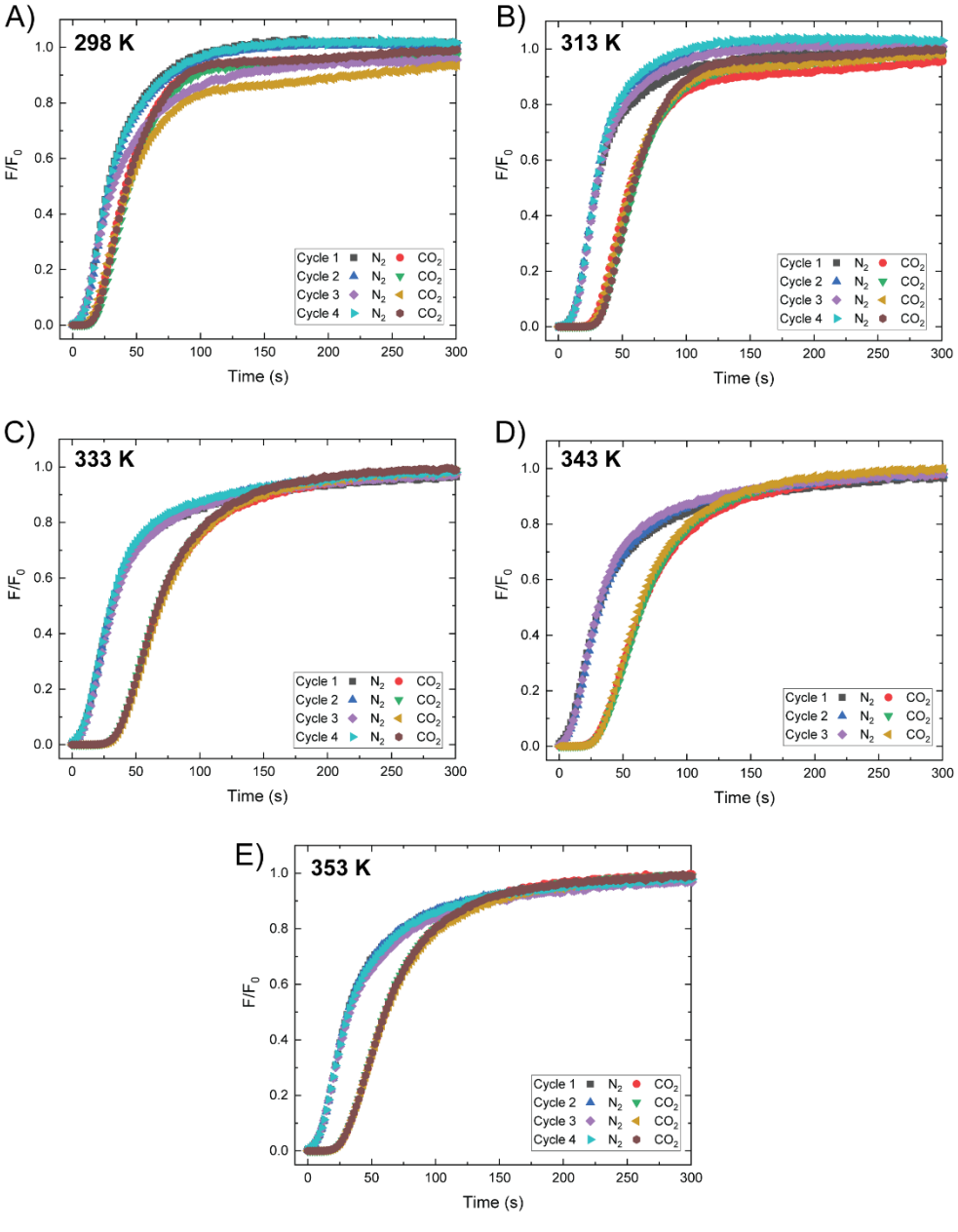

Figure S11. Normalized N_2 (8 mL/min) and CO_2 (2 mL/min) TAPB-NDA-COF breakthrough curves under humid (P_{H2O} = 2.9 kPa) conditions at 3.1 bar and **A)** 298, **B)** 313, **C)** 333, **D)** 343 and **E)** 353 K.

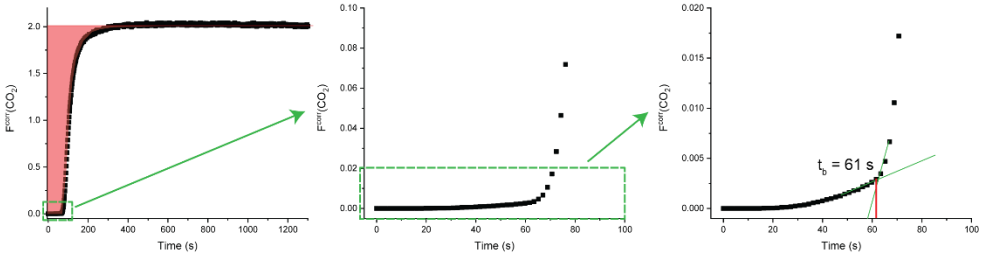

Figure S12. Example CO_2 breakthrough curve (dry experiment, cycle 1) for illustration of how analysis was conducted. Left: light-red area indicates integrated area to determine capacity. Right: the last data point before the slope of the curve starts to significantly increase is taken as the point at breakthrough.

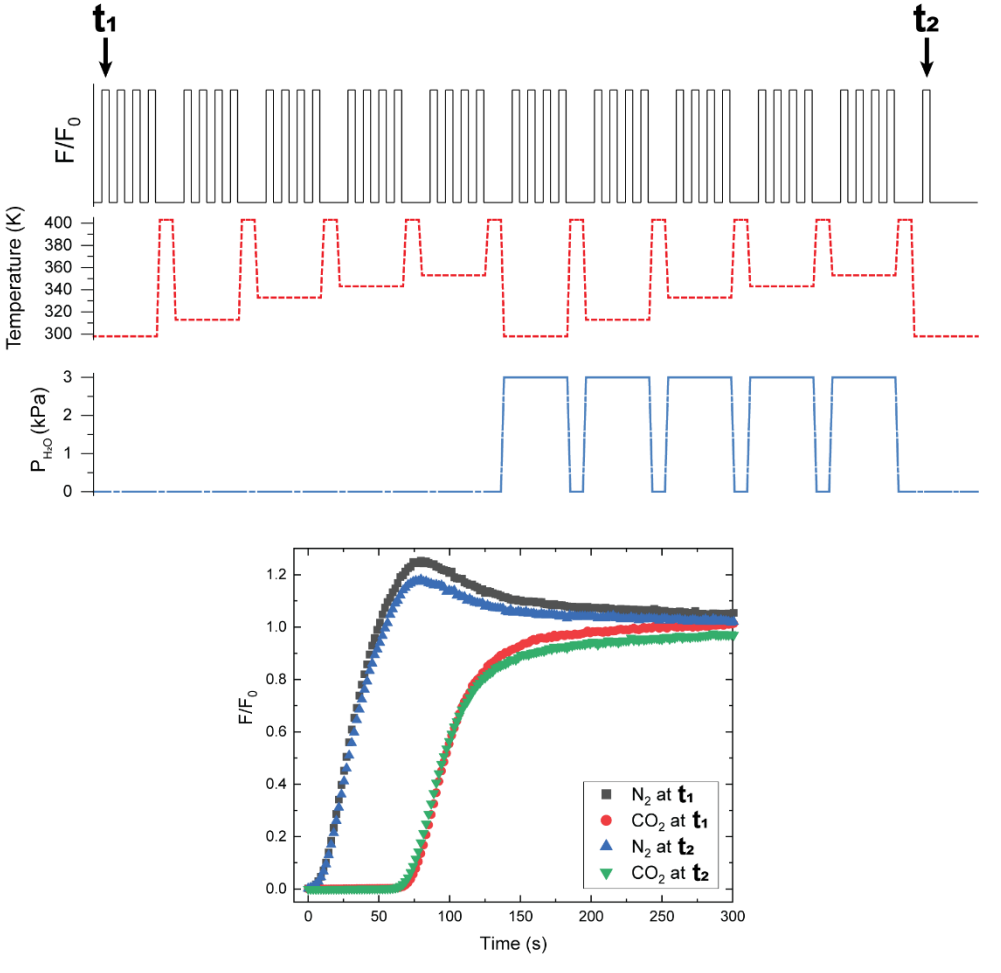

Figure S13. Top: Breakthrough conditions to which a single batch of TAPB-NDA-COF was exposed over time. Bottom: Normalized N_2 (8 mL/min) and CO_2 (2 mL/min) TAPB-NDA-COF

breakthrough curves under dry conditions at 3.1 bar and 298 K, comparing t1 and t2 as indicated by the top figure.

TGA measurements of COFs with pre-adsorbed water

Temperatures of 333, 363, 393 and 423 K were chosen to step-wise desorb water and observe how the CO_2 capacity of the material changed as a result of that (Figure S13A). This trend has been visualised in Figure S13B. After all 4 runs had been executed, the COF powder was dried completely by flowing N_2 at 423 K for three hours. Then the powder was cooled to 298 K and stabilized, and its weight was taken as the weight at 0 mmol·g^{-1} H_2O adsorbed. A final CO_2 ad- and desorption cycle was performed to get the CO_2 capacity of the dry powder.

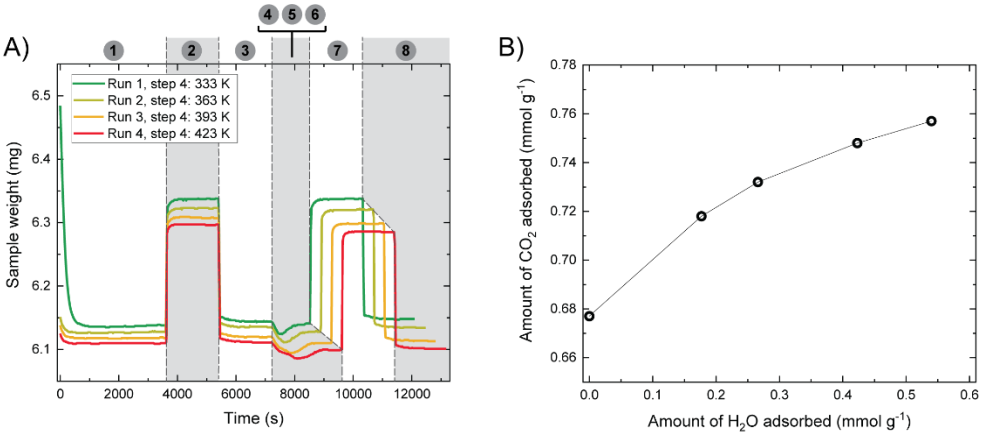

Figure S14. A) TGA curves of water-equilibrated TAPB-NDA-COF, using for every consecutive run the same steps: N_2 flow at 298 K (1), CO_2 flow at 298 K (2), N_2 flow at 298 K (3), heating to indicated temperature and cooling to 298 K under N_2 flow and both rates 10 K min^{-1} (4), CO_2 flow at 298 K (5), N_2 flow at 298 K (6). Flow rates of N_2 and CO_2 were 100 mL·min^{-1}. **B)** Evolution of CO_2 uptake as a function of the amount of pre-adsorbed water of TAPB-NDA-COF. The line between the data points functions to guide the eye.

Table S2. Comparison of CO_2 capture performance (dry and humid) of TAPB-NDA-COF with other adsorbents, all at 1 bar CO_2 partial pressure.

Adsorbent	**BET surface area (m^2 g^{-1})**	**CO_2 capacity at dry conditions (wt. %)**	**CO_2 capacity at humid conditions (wt. %)**	**Reference**
TAPB-NDA-COF	722	3.0 at 298 K	3.4 at 298 K and 9 % RH	This work
InOF-1 [$In_2(OH)_2$(BPTC)]	1060	5.4 at 303 K	11 at 303 K and 20 % RH	S2

Adsorbent	BET surface area ($m^2 g^{-1}$)	CO_2 capacity at dry conditions (wt. %)	CO_2 capacity at humid conditions (wt. %)	Reference
NOTT-400 $[Sc_2(OH)_2(BPTC)]$	1356	4.2 at 303 K	10.2 at 303 K and 20% RH	S3
NOTT-401 [Sc(OH)(TDA)]	1504	1.2 at 303 K	3.9 at 303 K and 5 % RH	S4
MIL-53(Al) [Al(OH)(BDC)]	1096	3.5 at 303 K	5.2 at 303 K and 20 % RH	S5
MIL-53(Al) [Al(OH)(BDC)]	1096	3.5 at 303 K	6.0 at 303 K and 5 % RH	S6
NH_2-MIL-53(Al) $[Al(OH)(NH_2\text{-BDC})]$	780	4.9 at 303 K	4.6 at 303 K and 5 % RH	S6
PCN-250(Fe_3)	1470	5.2 at 298 K	8.0 at 298 K and 50 % RH	S7
PCN-250(Fe_2Co)	1653	5.8 at 298 K	9.8 at 298 K and 50 % RH	S7
Cu-BTC (HKUST-1)	Not mentioned (Langmuir surface area of 1492 m^2/g)	22 at 298 K	36 at 298 K and 4 wt% hydrated	S8

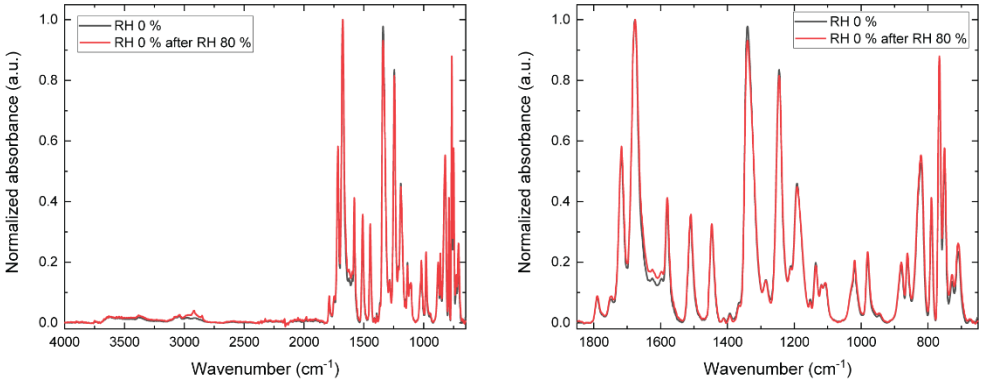

Figure S15. FT-IR spectra of dry TAPB-NDA-COF (black) and dried (degas in vacuum oven at 130 °C overnight) TAPB-NDA-COF after being equilibrated at 298 K and 80 % RH for 16 hours (red). The right graph is a zoom-in of the left graph.

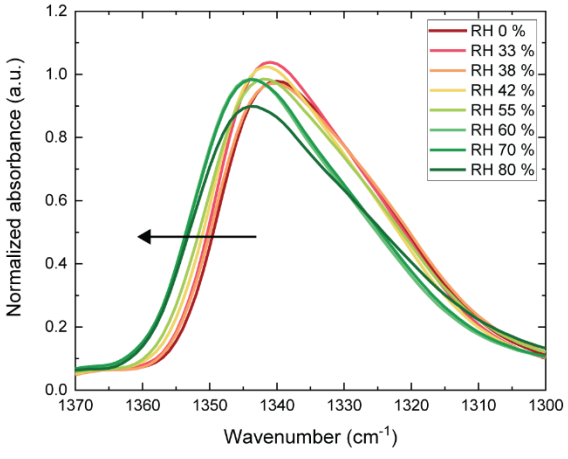

Figure S16. FT-IR spectra of TAPB-NDA-COF equilibrated at 298 K and various RH values, zoom-in on the imide C-N stretch vibration.

REFERENCES

[1] Pardakhti, M.; Jafari, T.; Tobin, Z.; Dutta, B.; Moharreri, E.; Shemshaki, N. S.; Suib, S.; Srivastava, R. Trends in Solid Adsorbent Materials Development for CO_2 Capture. *ACS Appl. Mater. Interfaces* **2019**, *11*, 34533–34559.

[2] Siegelman, R. L.; Kim, E. J.; Long, J. R. Porous materials for carbon dioxide separations. *Nat. Mater.* **2021**, *20*, 1060–1072.

[3] Boyd, P. G.; Chidambaram, A.; García-Díez, E.; Ireland, C. P.; Daff, T. D.; Bounds, R.; Gładysiak, A.; Schouwink, P.; Moosavi, S. M.; Maroto-Valer, M. M.; Reimer, J. A.; Navarro, J. A. R.; Woo, T. K.; Garcia, S.; Stylianou, K. C., Smit, B. Data-driven design of metal–organic frameworks for wet flue gas CO_2 capture. *Nature*, **2019**, *576*, 253–256.

[4] Lin, J.-B.; Nguyen, T. T. T.; Vaidhyanathan, R.; Burner, J.; Taylor, J. M.; Durekova, H.; Akhtar, F.; Mah, R. K.; Ghaffari-Nik, O.; Marx, S.; Fylstra, N.; Iremonger, S. S.; Dawson, K. W.; Sarkar, P.; Hovington, P.; Rajendran, A.; Woo, T. K.; Shimizu, G. K. H. A scalable metal-organic framework as a durable physisorbent for carbon dioxide capture. *Science*, **2021**, *374*, 1464–1469.

[5] Patel, H. A.; Je, S. H.; Park, J.; Chen, D. P.; Jung, Y.; Yavuz, C. T.; Coskun, A. Unprecedented high-temperature CO_2 selectivity in N_2-phobic nanoporous covalent organic polymers. *Nat. Commun.* **2013**, *4*, 1357.

[6] Wang, Y.; Kang, C.; Zhang, Z.; Usadi, A. K.; Calabro, D. C.; Baugh, L. S.; Yuan, Y. D.; Zhao, D. Evaluation of Schiff-Base Covalent Organic Frameworks for CO_2 Capture: Structure–Performance Relationships, Stability, and Performance under Wet Conditions. *ACS Sustainable Chem. Eng.* **2022**, *10*, 332–341.

[7] Zhao, Y.; Yao, K. X.; Teng, B.; Zhang, T.; Han, Y. A perfluorinated covalent triazine-based framework for highly selective and water–tolerant CO_2 capture. *Energy Environ. Sci.* **2013**, *6*, 3684–3692.

[8] Kolle, J. M.; Fayaz, M.; Sayari, A. Understanding the Effect of Water on CO_2 Adsorption. Chem. Rev. **2021**, *121*, 7280−7345.

[9] Chanut, N.; Bourrelly, S.; Kuchta, B.; Serre, C.; Chang, J.-S.; Wright, P. A.; Llewellyn, P. L. Screening the Effect of Water Vapour on Gas Adsorption Performance: Application to CO_2 Capture from Flue Gas in Metal–Organic Frameworks. *ChemSusChem* **2017**, *10*, 1543−1553.

[10] Soubeyrand-Lenoir, E.; Vagner, C.; Yoon, J. W.; Bazin, P.; Ragon, F.; Hwang, Y. K.; Serre, C.; Chang, J.-S.; Llewellyn, P. L. How Water Fosters a Remarkable 5-Fold Increase in Low-Pressure CO_2 Uptake within Mesoporous MIL-100(Fe). *J. Am. Chem. Soc.* **2012**, *134*, 10174−10181.

[11] Magnin, Y.; Dirand, E.; Orsikowsky, A.; Plainchault, M.; Pugnet, V.; Cordier, P.; Llewellyn, P. L. A Step in Carbon Capture from Wet Gases: Understanding the Effect of Water on CO_2 Adsorption and Diffusion in UiO-66. *J. Phys. Chem. C* **2022**, *126*, 3211−3220.

[12] Wang, J.; Wang, S.; Xin, Q.; Li, Y. Perspectives on water-facilitated CO_2 capture materials. *J. Mater. Chem. A* **2017**, *5*, 6794–6816.

[13] Chen, Y.; Qiao, Z.; Huang, J.; Wu, H.; Xiao, J.; Xia, Q.; Xi, H.; Hu, J.; Zhou, J.; Li, Z. Unusual Moisture-Enhanced CO_2 Capture within Microporous PCN-250 Frameworks. *ACS Appl. Mater. Interfaces* **2018**, *10*, 38638–38647.

[14] Sánchez-Serratos, M.; Bayliss, P. A.; Peralta, R. A.; González-Zamora, E.; Lima, E.; Ibarra, I. A. CO_2 capture in the presence of water vapour in MIL-53(Al). *New J. Chem.* **2016**, *40*, 68–72.

[15] Álvarez, J. R.; Peralta, R. A.; Balmaseda, J.; González-Zamora, E.; Ibarra, I. A Water adsorption properties of a Sc(III) porous coordination polymer for CO_2 capture applications. *Inorg. Chem. Front.* **2015**, *2*, 1080−1084.

[16] Chen, Y. F.; Babarao, R.; Sandler, S. I.; Jiang, J. W. Metal−Organic Framework MIL-101 for Adsorption and Effect of Terminal Water Molecules: From Quantum Mechanics to Molecular Simulation. *Langmuir* **2010**, *26*, 8743−8750.

[17] Ge, Y.; Zhou, H.; Ji, Y.; Ding, L.; Cheng, Y.; Wang, R.; Yang, S.; Liu, Y.; Wu, X.; Li, Y. Understanding Water Adsorption and the Impact on CO_2 Capture in Chemically Stable Covalent Organic Frameworks. *J. Phys. Chem. C* **2018**, *122*, 27495−27506.

[18] Van der Jagt, R.; Vasileiadis, A.; Veldhuizen, H.; Shao, P.; Feng, X.; Ganapathy, S.; Habisreutinger, N. C.; Van der Veen, M. A.; Wang, Chao, Wagemaker, M.; Van der Zwaag, S.; Nagai, A. Synthesis and Structure–Property Relationships of Polyimide Covalent Organic Frameworks for Carbon Dioxide Capture and (Aqueous) Sodium-Ion Batteries. *Chem. Mater.* **2021**, *33*, 818−833.

[19] Zeng, Y.; Zou, R.; Zhao, Y. Covalent Organic Frameworks for CO_2 Capture. *Adv. Mater.* **2016**, *28*, 2855–2873.

[20] Byun, Y.; Je, S. H.; Talapaneni, S. N.; Coskun, A. Advances in Porous Organic Polymers for Efficient Water Capture. *Chem. Eur. J.* **2019**, *25*, 10262–10283.

[21] Waters, J. F.; Likavec, W. R.; Ritchey, W. M. ^{13}C CP-MAS NMR Study of Absorbed Water in Polyimide Film. *J. Appl. Polym. Sci.* **1994**, *53*, 59–70.

[22] Musto, P.; Mensitieri, G.; Lavorgna, M.; Scarinzi, G.; Scherillo, G. Combining Gravimetric and Vibrational Spectroscopy Measurements to Quantify First- and Second-Shell Hydration Layers in Polyimides with Different Molecular Architectures. *J. Phys. Chem. B* **2012**, *116*, 1209–1220.

[23] Rieth, A. J.; Hunter, K. M.; Dincă, M.; Paesani, F. Hydrogen bonding structure of confined water templated by a metal-organic framework with open metal sites. *Nat. Commun.* **2019**, *10*, 4771.

[24] Wagner, J. C.; Hunter, K. M.; Paesani, F.; Xiong, W. Water Capture Mechanisms at Zeolitic Imidazolate Framework Interfaces. *J. Am. Chem. Soc.* **2021**, *143*, 21189–21194.

[25] Riera, M.; Yeh, E. P., Paesani, F. Data-Driven Many-Body Models for Molecular Fluids: CO_2/H_2O Mixtures as a Case Study. *J. Chem. Theory Comput.* **2020**, *16*, 2246–2257.

[26] Wang, B.; Cao, Z. How Water Molecules Modulate the Hydration of CO_2 in Water Solution: Insight from the Cluster-Continuum Model Calculations. *J. Comput. Chem.* **2013**, *34*, 372–378.

[27] Gallet, G. A.; Pietrucci, F.; Andreoni, W. Bridging Static and Dynamical Descriptions of Chemical Reactions: An ab Initio Study of CO_2 Interacting with Water Molecules. *J. Chem. Theory Comput.* **2012**, *8*, 4029–4039.

[28] Cotlame-Salinas, V. C.; López-Olvera, A.; Islas-Jácome, A.; González-Zamora, E.; Ibarra, I. A. CO_2 Capture Enhancement in MOFs *via* the Confinement of Molecules. *React. Chem. Eng.* **2021**, *6*, 441–453.

[29] Gottschling, K.; Stegbauer, L.; Savasci, G.; Prisco, N. A.; Berkson, Z. J.;Ochsenfeld, C.; Chmelka, B. F.; Lotsch, B. V. Molecular Insights into Carbon Dioxide Sorption in Hydrazone Based Covalent Organic Frameworks with Tertiary Amine Moieties. *Chem. Mater.* **2019**, *31*, 1946–1955.

[30] Nandi, S.; Werner-Zwanziger, U.; Vaidhyanathan, R. A triazine–resorcinol based porous polymer with polar pores and exceptional surface hydrophobicity showing CO_2 uptake under humid conditions. *J. Mater. Chem. A* **2015**, *3*, 21116–21122.

Ref S1 J. W. M. Osterrieth et al. *Adv.Mater.* **2022**, *34*, 2201502.

Ref S2 R. A. Peralta, B. Alcántar-Vázquez, M. Sánchez-Serratos, E. González-Zamora and I. A. Ibarra, *Inorg. Chem. Front.*, **2015**, *2*, 898–903.

Ref S3 J. R. Álvarez, R. A. Peralta, J. Balmaseda, E. González-Zamora and I. A. Ibarra, *Inorg. Chem. Front.*, **2015**, *2*, 1080–1084.

Ref S4 E. Sánchez-González, J. R. Álvarez, R. A. Peralta, A. Campos-Reales-Pineda, A. Tejeda-Cruz, E. Lima, J. Balmaseda, E. González-Zamora and I. A. Ibarra, *ACS Omega*, **2016**, *1*, 305–310.

Ref S5 M. Sánchez-Serratos, P. A. Bayliss, R. A. Peralta, E. González-Zamora, E. Lima and I. A. Ibarra, *New J. Chem.*, **2016**, *40*, 68–72.

Ref S6 A. Zárate, R. A. Peralta, P. A. Bayliss, R. Howie, M. Sánchez-Serratos, P. Carmona-Monroy, D. Solis-Ibarra, E. González-Zamora and I. A. Ibarra, *RSC Adv.*, **2016**, *6*, 9978–9983.

Ref S7 Chen, Y.; Qiao, Z.; Huang, J.; Wu, H.; Xiao, J.; Xia, Q.; Xi, H.; Hu, J.; Zhou, J.; Li, Z. *ACS Appl. Mater. Interfaces* **2018**, *10*, 38638–38647.

Ref S8 Yazaydin, A. Ö.; Benin, A. I.; Faheem, S. A.; Jakubczak, P.; Low, J. J.; Willis, R. R.; Snurr, R. Q. *Chem. Mater.* **2009**, *21*, 1425–1430.

5

Synthesis and Structure–Property Relationships of Polyimide Covalent Organic Frameworks for CO_2 Capture and (Aqueous) Sodium-Ion Batteries

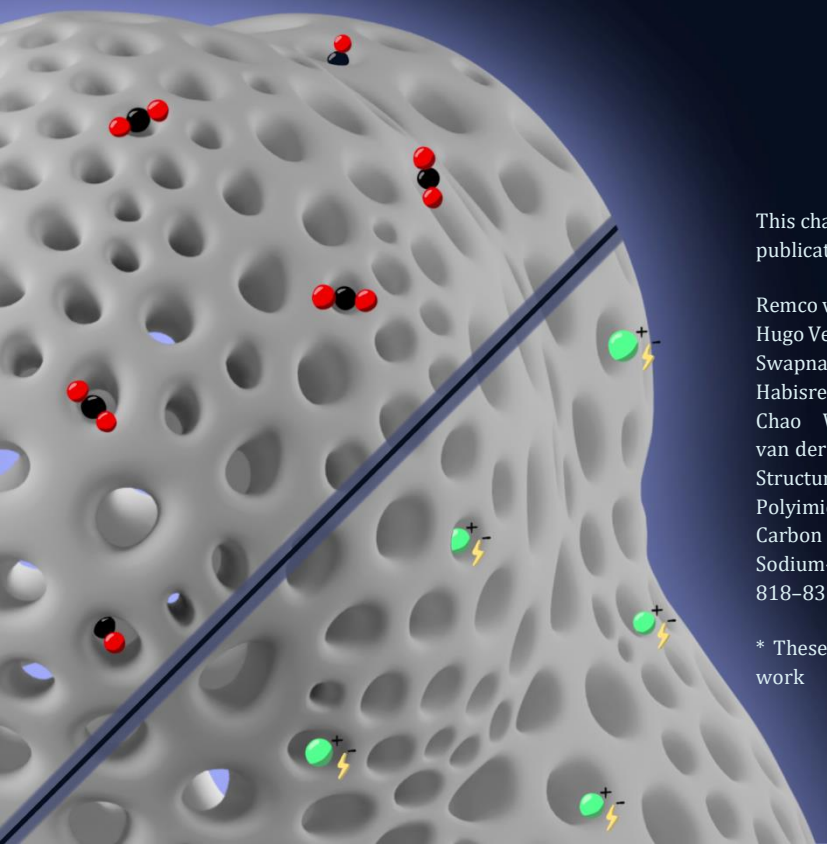

This chapter is based on the following publication:

Remco van der Jagt,* Alexandros Vasileiadis,* Hugo Veldhuizen,* Pengpeng Shao, Xiao Feng, Swapna Ganapathy, Nicolas C. Habisreutinger, Monique A. van der Veen, Chao Wang, Marnix Wagemaker, Sybrand van der Zwaag, Atsushi Nagai. Synthesis and Structure–Property Relationships of Polyimide Covalent Organic Frameworks for Carbon Dioxide Capture and (Aqueous) Sodium-Ion Batteries. *Chem. Mater.* **2021**, *33*, 818–833.

* These authors contributed equally to this work

Abstract

Covalent organic frameworks (COFs) are an emerging material family having several potential applications. Their porous framework and redox-active centers enable gas/ion adsorption, allowing them to function as safe, cheap, and tunable electrode materials in next-generation batteries, as well as CO_2 adsorption materials for carbon-capture applications. Herein, we develop four polyimide COFs by combining aromatic triamines with aromatic dianhydrides and provide detailed structural and electrochemical characterization. Through density functional theory (DFT) calculations and powder X-ray diffraction, we achieve a detailed structural characterization, where DFT calculations reveal that the imide bonds prefer to form at an angle with one another, breaking the 2D symmetry, which shrinks the pore width and elongates the pore walls. The eclipsed perpendicular stacking is preferable, while sliding of the COF sheets is energetically accessible in a relatively flat energy landscape with a few metastable regions. We investigate the potential use of these COFs in CO_2 adsorption and electrochemical applications. The adsorption and electrochemical properties are related to the structural and chemical characteristics of each COF, giving new insights for advanced material designs. For CO_2 adsorption specifically, the two best performing COFs originated from the same triamine building block, which - in combination with forcefield calculations - revealed unexpected structure–property relationships. Specific geometries provide a useful framework for Na-ion intercalation with retainable capacities and stable cycle life at a relatively high working potential (>1.5 V vs Na/Na+). Although this capacity is low compared to conventional inorganic Li-ion materials, we show as a proof of principle that these COFs are especially promising for sustainable, safe, and stable Na-aqueous batteries due to the combination of their working potentials and their insoluble nature in water.

5.1 INTRODUCTION

Modern society is challenged by the necessity of a rapid energy transition toward renewable energy and electric transport while facing the continuous increasing effects of greenhouse gases. The usage of renewable sources, primarily based on solar and wind, is highly intermittent,[1–8] and demands daily electrical energy storage for which stationary batteries appear to be a promising technology. Furthermore, the increasing importance of mobile technologies calls for new cheap and sustainable approaches, which motivates the search for organic electrode materials.[9–15] Also, limiting the carbon dioxide (CO_2) concentration in air is currently one of the key issues on the climate control agenda. In this framework, novel material investigations for electrochemical storage and CO_2-capture applications are performed toward a sustainable future. Currently, Li-ion batteries are the most widely employed technology for reversible electrochemical energy storage systems[1] having the highest energy density, in particular suitable for mobile applications. Lately, Na-ion batteries are suggested to cooperate and even compete with Li-ion batteries in the energy transition due to the greater abundance of Na, albeit at the cost of a lower energy density.[10] In particular, aqueous batteries are considered to be promising for stationary storage,[11] based on their intrinsically lower costs and higher safety. Typical electrodes in batteries are based on transition metals (providing the redox center) for which mining and syntheses are energy-consuming and costly, motivating the search for organic alternatives. In 50 years, the world of organic electrodes has grown and contains now small organic compounds,[3,5] conductive polymers,[12] polycarbonyls,[6,13] polyradicals,[7] and more.[14,15] These can be designed to fit multiple applications and can be used for a diversity of batteries such as Li-ion, Na-ion, dual-ion, and multivalent-ion batteries. However, organic electrodes have (still) many drawbacks such as (a) poor stability and durability due to easy dissolution of small redox-active molecules in the electrolyte, (b) low energy efficiency due to the poor diffusion of ions through the electrode, and (c) a low electronic conductivity, demanding the addition of a large weight fraction of an electronic conducting agent, reducing the amount of active materials and thus the specific capacity of the electrode. As a result, the synthesis of two- or three-dimensional porous conductive polymers can be considered an important strategy. However, the complexity of designing such structures, while maintaining a low price and a sustainable process for the device, is a great challenge.

Covalent organic frameworks (COFs) are a class of two- or three-dimensional crystalline porous polymers composed of lightweight molecules

linked by covalent bonds.[16–39] The periodicity of the structure results in a predictable porous polymer where the two-dimensional polymeric sheets stack on top of each other in the aim to create one-dimensional channels. Usually, the building blocks are linked by boroxines,[16] boronate esters,[23] imines,[40] triazines,[41] hydrazones,[42] azines,[43] or squaraines.[44] The development of new linkages to synthesize such covalent frameworks is essential to exploit the technological potential of this emerging class of materials. Polyimides are known for their high thermal stability[45–48] and excellent chemical resistance and are widely used as thermoplastics as well as in the electronic industry. In addition, polyimides can facilitate redox reactions,[13] making these promising electrode materials in batteries. Recently, imide-based COFs were reported,[45,47,48] introducing a new material family with high porosity, stability, and high availability from biomass. These properties may provide opportunities that answer the typical drawbacks of state-ofthe-art organic electrodes and thus potentially may lead to the development of new redox-active polymers for cheap transition metal-free next-generation batteries. Several COFs have shown very promising electrochemical performances by obtaining high capacities and reliable cycling for Li-ion batteries.[49–53] Na-ion chemistries are also explored in the context of cheaper chemistry for large scale storage applications.[54–56] COFs are additionally expected to play a central role in the sequestration of CO_2 from the atmosphere.[57] Carbon capture has become a well-known term over the last decades to indicate the need for efficient storage solutions of carbon-based greenhouse gases. In this context, nanoporous materials with well-defined pores are attracting increasing attention since their porous nature allows the efficient adsorption of gases, such as carbon dioxide.[58] Among such materials, COFs present a unique advantage by combining strong covalent bonds with a crystalline, porous architecture.[57] Their crystallinity facilitates directed research toward improved gas adsorption because of the precise control over pore sizes and shapes. In addition, the concept of pore structure engineering has been utilized to systematically investigate the effect of chemically or physically different pores on gas adsorption properties.[25,59] Although this concept has been extensively studied for boronate ester and imine-based COFs, such studies for more stable, highperformance COFs are scarce.[60,61] However, in order to utilize nanoporous adsorbents in industry applications, a thermally and chemically stable polymer backbone is often required. As such, polyimide-based COFs are expected to be promising candidates,[45,47,48] and systematically studying their gas sorption properties pushes the field forward. In this work, we report the development of four mesoporous, redox-active polyimide COFs. One of the leading experimental

challenges in the chemistry of the COFs for achieving complete structural characterization is crystallinity. Solving and refining crystal structures with atomic precision require the growth of single crystals, which has been scarcely reported.[62] For this reason, structure simulations are performed based on density functional theory (DFT), which brings forward an accurate description of their structural characteristics consistent with X-ray diffraction (XRD) measurements, shedding light on atomistic configurational preferences and providing insights for functional COFs. The developed COFs are evaluated as CO_2 sequestering and electrode materials by exploring their CO_2 adsorption and electrochemical properties. The operating redox potentials of the presented polyimide-based COFs and their insolubility in water make them suitable anode materials for aqueous batteries. Hence, we open up a new research direction for COFs by demonstrating the proof of principle of the (sodium) aqueous battery concept.

5.2 RESULTS AND DISCUSSION

5.2.1 COF SYNTHESIS AND CHARACTERIZATION

The polyimide COFs presented in this research were prepared by the imidization of aromatic triamines: tris(4-aminophenyl)amine (TAPA) or 1,3,5-tris(4-aminophenyl)benzene (TAPB) with aromatic dianhydrides: pyromellitic dianhydride (PMDA) or 1,4,5,8-naphthalenetetracarboxylic dianhydride (NTCDA). These four building blocks are commercially available. The solvothermal synthesis approach was applied for the imidization reactions using a solvent mixture of *N*-methyl-2-pyrrolidone (NMP) and *meta*-cresol and isoquinoline as the catalyst (detailed synthesis in the Supporting Information). The four different combinations of monomers allowed the formation of a set of four different polyimide polymers that are chemically relatively similar (**Figure 1**), but differ, for example, in pore size. Furthermore, the two aromatic dianhydride molecules (PMDA, NTCDA) can serve as redox-active sites for the reversible interaction with Li- and Na-ions, as will be discussed in the electrochemical characterization.

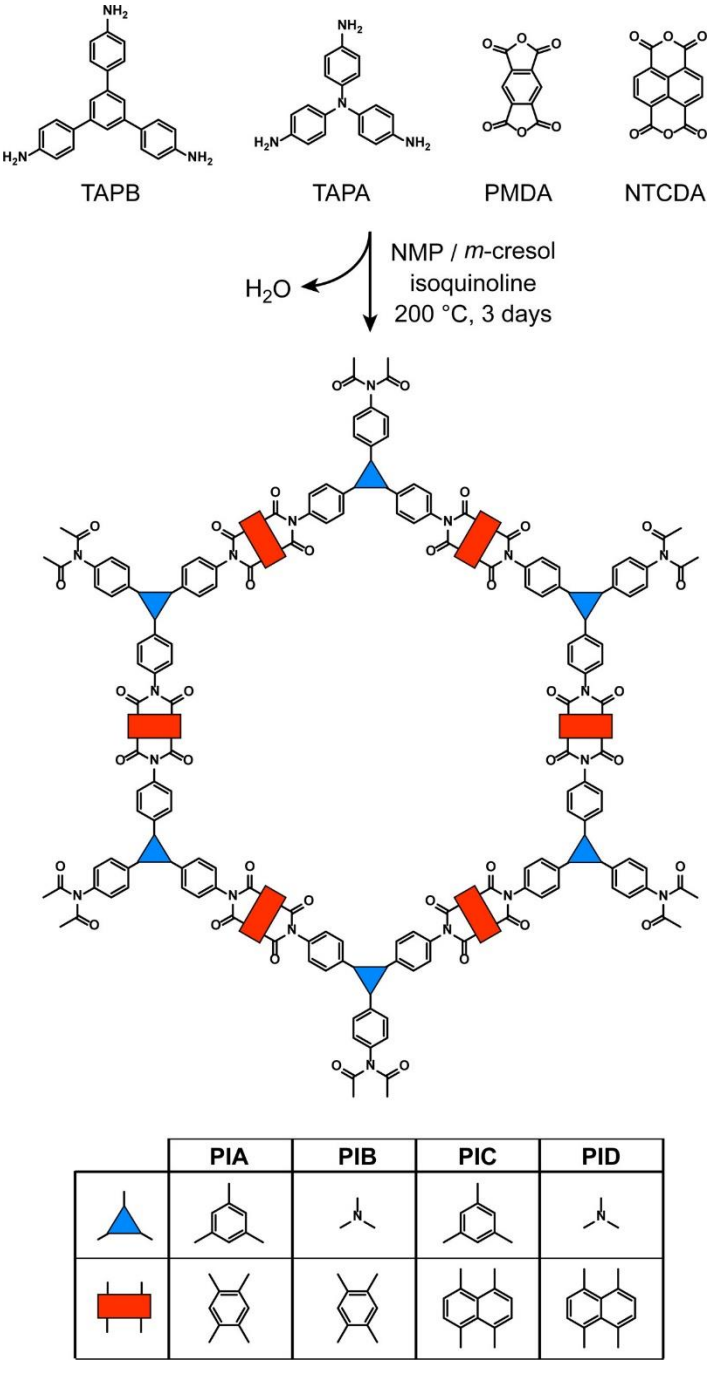

Figure 1. Synthesis scheme and the tags of the four polyimide COFs prepared from TAPB, TAPA, PMDA, and NTCDA.

Fourier transformed infrared (FT-IR) confirmed the formation of polyimides by the presence of three primary specific imide vibrations (Figures S3 – S6). First, we observed vibrational signals for the asymmetric and symmetric vibrations of the imide carbonyl C═O at 1720 and 1775 cm^{-1} for PIA, 1726, and 1778 cm^{-1} for PIB, 1674 and 1715 cm^{-1} for PIC, and 1672 and 1716 cm^{-1} for PID. The third absorption confirmed the presence of C–N–C stretching vibration at 1356 cm^{-1} for PIA, 1375 cm^{-1} for PIB, 1340 cm^{-1} for PIC, and 1344 cm^{-1} for PID. Final confirmation of the synthesis was supported by the disappearance of the characteristic starting material vibrations (around 3340 cm^{-1} for the amines and around 1765 cm^{-1} for the anhydride carbonyls). Additionally, solid-state nuclear magnetic resonance (NMR) measurements were performed on the four COFs (Figures S7 – S12). The precursors TAPA (linker of PIB and PID) and NTCDA (the active part of PIC and PID) are not traceable in the NMR spectra of PIA–PID, confirming the successful synthesis.

Polyimides are well known to be thermally and chemically stable polymers, which is apparent from their usage in high-performance applications. Here, we demonstrated that similar stability is retained when imides are employed as the connecting linkages in COFs. The four PI–COFs show high thermal stability as determined by thermogravimetric analysis (TGA): up to 535 °C for PIA and PIC, 525 °C for PIB, and 520 °C for PID (Figures S13 – S16). In addition, the chemical stability was investigated by storing PIC and PID for 14 days in organic [1 M $NaClO_4$ in ethylene carbonate (EC)/dimethyl carbonate (DMC)] and aqueous electrolyte (1 M Na_2SO_4 in neutral water), after which newly measured powder XRD (PXRD) spectra of the COFs were compared to the spectra of the as-synthesized materials (Figure S17). No significant changes were observed while comparing the spectra: even the secondary crystalline peaks are retained after these tests, reinforcing the suggested chemical stability of polyimide COFs.

The morphologies of the herein prepared COFs were determined *via* scanning electron microscopy (SEM) (Figure S18). In general, the microstructures of these polymers resemble large (radii of >1 μm) semi-spherical particles, which are highly aggregated. Furthermore, a zoom-in of such a particle revealed a sponge-like morphology with macropores in the order of 100 nm. To investigate the micro and mesopores, however, nitrogen gas sorption measurements provided a more quantitative insight for the porous structures of the four COFs.

The curves of the nitrogen sorption isotherms (at 77 K) of the four porous polymers (Figures S19 – S22) all show a steep increase in N_2 uptake in the low

relative pressure region ($P/P_0 < 0.2$). This behavior typically indicates the presence of both micropores and small mesopores. Interestingly, there seems to be a distinction between PMDA-derived polymers (PIA and PIB) and NDA-derived polymers (PIC and PID), where the latter polymers display a significant shoulder in their nitrogen isotherms. This observation indicates that the presence of mesopores is more pronounced in PIC and PID than in PIA and PIB. To verify this conclusion, the isotherms were fitted to a quenched-solid DFT model to calculate pore size distributions (PSDs, Figure S23). These PSDs indeed reveal the presence of a large number of micropores with respect to the expected mesopores, which is most notable for PIA and PIB. While PXRD results later indicate distinct repeating pore sizes for all four polymers, it is essential to realize that these gas sorption experiments reveal broad distributions of pore sizes originating from both crystalline and amorphous segments. Finally, the Brunauer–Emmett–Teller (BET) theory was applied to the nitrogen isotherms to calculate the BET surface area. Coincidentally, the BET surface area values for the polymers were in ascending order: 580 $m^2 g^{-1}$ for PIA, 760 $m^2 g^{-1}$ for PIB, 990 $m^2 g^{-1}$ for PIC, and 1430 $m^2 g^{-1}$ for PID (Figures S24 – S27).

5.2.2 DFT Simulations for Accurate Material Characterization

In order to elucidate the structural characteristics of the COF structures, DFT calculations were performed. The quantum-mechanical treatment of the DFT method can predict configurational preferences more accurately as compared to classical force field approaches.[29] A detailed description of the computations is given in the Experimental Section.

Models for the PIA and PIB structures have been previously reported in the literature where several unit cell descriptions, optimized with the universal force field, were considered, namely, the AA eclipsed ($P6_3/mmm$), the serrated ($Cmcm$) where adjacent sheets are slipped by 1/4 of the unit cell distance, and the AB staggered ($P6_3/mmc$) stackings.[45] Both the eclipsed and serrated simulated PXRD patterns matched the experimental data. However, the serrated description was considered more probable based on the high gas uptake observed.[45] The PID structure has been recently reported to acquire a 2D hexagonal layered configuration based on TEM imaging.[47] The packing on the perpendicular direction remains uncertain due to the broadness of the PXRD peaks; however, the eclipsed AA stacking was put forward as it compared well with simulated PXRD patterns.[47]

Herein, we perform structural optimizations of a variety of possible hexagonal unit cell configurations. Our investigation also includes possibilities regarding intra-molecular configurations, such as the presence of torsion between the components of the COFs. The simulations reveal that it is energetically favorable for the benzene rings of both the TAPA and TAPB linkage molecules to break the 2D symmetry by exhibiting torsion, tilting to form equal angles with one another. The preferable torsion is demonstrated in **Figure 2**, where the energy landscape as a function of the torsion angle in the linkage molecules is presented. Simulations with initial torsion angles between the carbon rings of the linkage molecules of 10, 20, 30, 40, and 50° were performed for the four COFs. Irrespectively of the initial angle, during geometry optimization, all the structures relaxed toward a preferable angle (minimum energy points in **Figure 2**), which is characteristic for each COF. This indicates that there is no barrier present for this transformation. When initializing the simulations in the perfectly 2D eclipsed configuration, all structures retained zero torsion angle configurations obtaining, however, much higher energies. Thus, the flat 2D configuration, which has dominantly brought forward as the best description in the literature, appears to be unstable (or marginally metastable) and is expected to transform naturally to a non-flat configuration exhibiting torsion. Macroscopically, the sheets will still appear as 2D structures due to the large size of the ab-plane. The observed trends in **Figure 2** reveal that the torsion is much more stable for the COFs acquiring the TAPA linkage molecule (PIB and PID). The above observation seems reasonable as the single N atom in the center allows more rotational freedom than the center benzene ring of the TAPB linkage. This is also reflected in the slightly higher torsion angles of the TAPA linkage-containing configurations PIB and PID. A weaker effect is caused by the presence of the active molecule, with the NTCDA being more stable when combined with the tilted linkages than the PMDA. The torsion angle between the active molecules and the adjacent benzene ring of the linkages stabilized in all calculations at 25° for PIA, 36° for PIB, 56° for PIC, and 47° for PID.

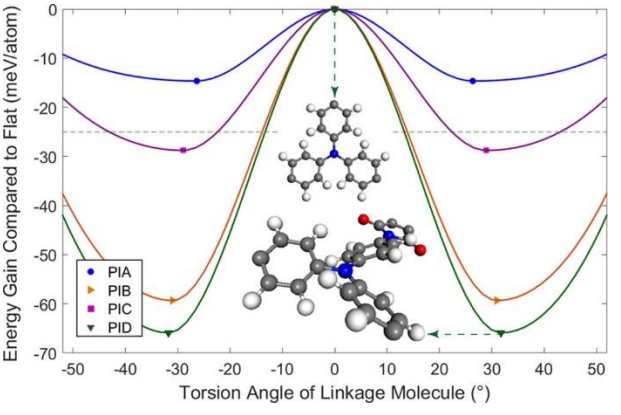

Figure 2. Energy gain as a function of the torsion angle between the benzene rings of the linkage molecules. All calculations per COF, initialized with an initial torsion of 10, 20, 30, 40, and 50°, relaxed toward the same configuration.

These structural aspects have a significant impact on the lattice of the COF structures. Torsion in the linkage molecules shrinks and elongates the ab-plane and *c* lattice parameter, respectively, when compared to the flat structure (**Figure 3a**). A larger torsion angle in the linkages for the PIB and PID dictates greater elongation of the *c* lattice parameter and allows a more compact packing in the ab-plane, explaining why the TAPA-containing COF structures are affected the strongest. In absolute values, the PIB and PID structures obtain larger *c* lattice parameters (**Figure 3a**). The PMDA active molecule is rather small so that its rotation does not have an impact on the lattice (PIA and PIB), but the larger NTCDA molecule that tilted 56° in PIC does contribute.

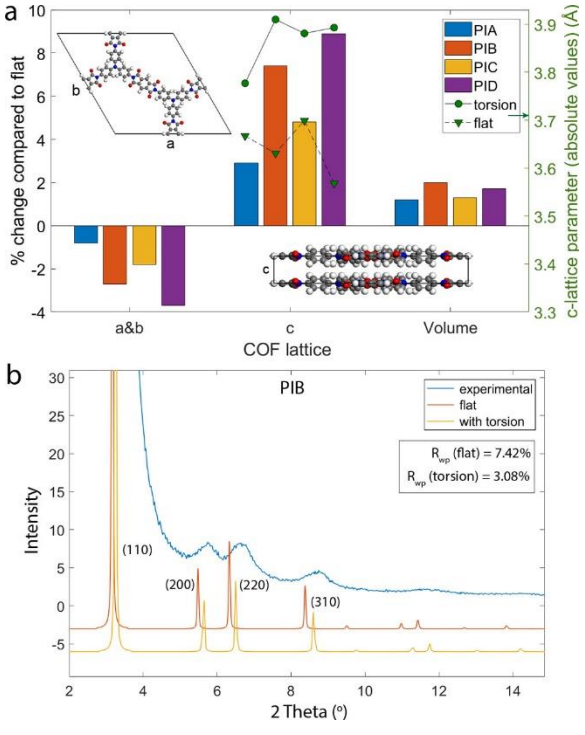

Figure 3. (a) Comparison between the flat and tilted COF configurations. The absolute values of the obtained *c*-lattice parameters are also provided (green scatter plot, right axis). **(b)** Effect of the presence of torsion in the crystal lattice of PIB on the PXRD simulated reflections, in comparison with the experimental pattern. Pawley refinement with the flat symmetry resulted in poorer agreement factors consistent with the torsion predicted by the DFT simulations.

The structural characteristics mentioned above are expected to have an impact on the properties of the COF structures. Torsion provides longer pore-walls since the *c* lattice parameter runs along the channels of the porous structure, enabling more space for gas molecules or charge carrier ions to be attached, as the same pore depth can be achieved with fewer stacks. Elongation of the pore walls due to torsion is likely to have an additional effect, enabling gas molecules and charge carrier ions to access from the outside, which creates an otherwise inaccessible pore due to morphological aspects (such as miss-orientation of one COF ring blocking the pathway). However, validating this proposition requires further calculations outside the scope of this study.

The next step is to investigate the packing in the perpendicular direction. For COFs, there are two extreme options, namely, the AA eclipsed, where adjacent sheets fall precisely on top of each other, and the AB staggered stacking, where adjacent sheets are slipped by 1 unit cell. In between, there is a wide variety of

serrated configurations where adjacent sheets are slipped, creating an offset (**Figure 4a**). The relative stability of the AA eclipsed and AB staggered stacking for the 4 COFs was evaluated. The AA eclipsed stacking was the most stable configuration in all COFs and is set as the 0 energy reference. Recently, a DFT study revealed that 2D layered COFs based on 2,3,6,7,10,11-hexahydroxytriphenylene and 4,4′-diphenyl-1-butadiynebis have a strong preference for slight offsets in the range of 1.7 Å rather than a true eclipsed AA structure.[29] Herein, we investigate if there is a similar trend in the polyimide COFs, calculating configurations with a variety of offsets for the PIA and PID (**Figure 4b**,**c**). The truly eclipsed AA stacking remains the most stable configuration in both cases. The PID configuration with an offset of 1.5 Å even relaxed back during the simulation to the eclipsed configuration.

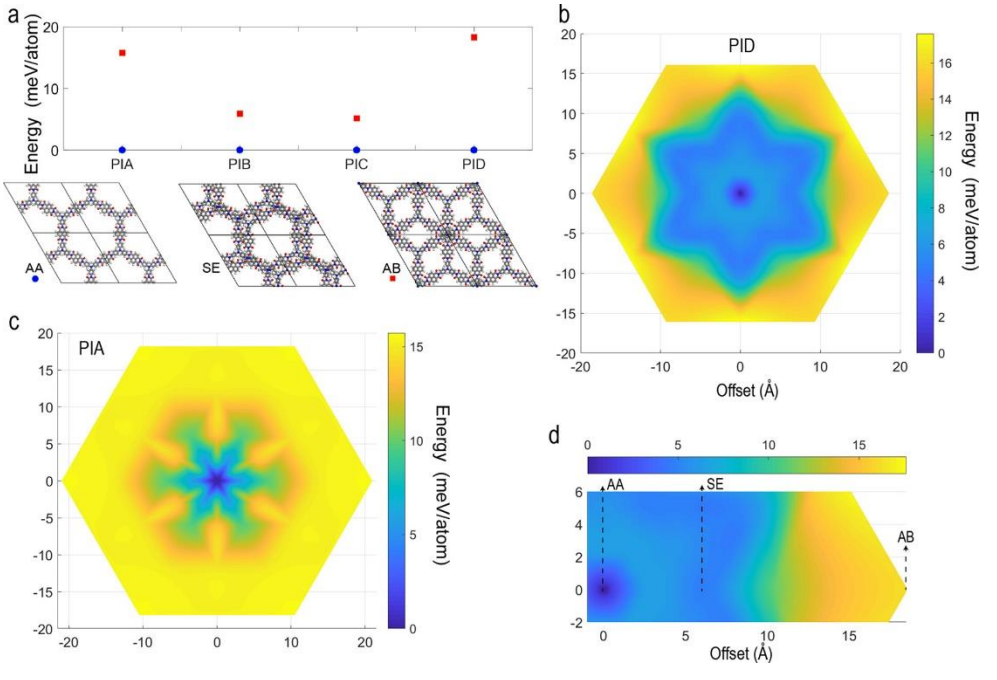

Figure 4. (a) Energy difference between the AA eclipsed, AB staggered stacking for the 4 COFs, an illustration of the AA eclipsed, AB staggered and an example of serrated stacking (SE), **(b)** energy landscape of PID, **(c)** energy landscape of PIA, and **(d)** zoom-in in the energy landscape of PID along the direction toward the AB stacking where the metastable SE at an offset of 6.6 Å is visible. Note that the orientation of the unit cell illustration in (a) is not the same as the orientation of the energy maps. In the energy maps, the corners of the hexagons represent the AB staggered configuration.

The energy landscape, however, does not monotonously increase as we move away from the eclipsed configuration, as a metastable serrated-stacking region is found

with a local minimum where the sheets are slipped 6.6 Å (~1/3 of the distance between the AA and AB stacking, **Figure 4d**). The small energy penalty for offsets indicates that the metastable phase might be stabilized but is likely to fall back toward the eclipsed configuration under thermal energy and stresses caused, for example, by Li or Na insertion. For large offsets, where adjacent sheets are slipped more than 1/2 the unit cell distance, the energy penalty rises to reach the unstable AB configuration in both PIA and PID. This is best demonstrated for the PIA, where the energy landscape is monotonously increasing as the sheets move away from the eclipsed configuration, reaching the unstable AB staggered configuration. The PIA energy map (**Figure 4c**) also suggests that the offsets are more likely to occur in the direction toward the AB staggered stacking (*i.e.*, represented by the corners of the hexagonal energy maps). The energy difference in favor of the AA stacking is likely to originate from the greater molecular overlap leading to more significant van der Waals attraction forces. The above is in agreement with the eclipsed stacking put forward for PID based on TEM and PXRD experiments.[47] Based on the measured BET surface, PIA and PIB were previously reported in serrated configurations.[45] This seems, however, not a strong argument since the measured surfaces are dominated by morphological features rather than the crystal lattice. Our simulations indicate that the relatively flat energy landscape, especially for small offsets, might allow the sheets to slide on one another temporarily; however, the thermodynamically favorable phase is the eclipsed AA stacking. Due to computational cost, energy maps for the PIB and PIC were not constructed. Nevertheless, it is likely that they follow similar behavior. Interestingly, according to **Figure 4a**, the ab-staggered configuration of these structures has a much smaller energy penalty.

Measured PXRD patterns of the 4 COFs were subjected to Pawley refinement based on the optimized DFT structures (hexagonal eclipsed AA stacking, presence of torsion), resulting in good agreement, as shown in **Figure 5**. The predicted torsion breaks the 2D symmetry in the $P6_3/mmm$ space group, resulting in unit cells that can be described by the $C222$ (21) or $C222_1$ (20) symmetries and in the hexagonal unit cell by the $P622$ (177) or $P\bar{3}1m$ (162) symmetries. Crystallographic data for the 4 COF structures in a variety of unit cell descriptions can be found in the Supporting Information. The simulated PXRD data of the eclipsed AA stacking match well with the experimental reflections, consistent with the DFT results presented above, that predict the AA stacking to be the most stable configuration. The obtained lattice parameters in the hexagonal description were $a = b = 36.38$ Å and $c = 3.79$ Å for the PIA ($P\bar{3}1m$), $a = b = 31.37$ Å and $c = 3.91$ Å for the PIB ($P622$), $a = b = 37.07$ Å and $c = 3.89$ Å for the PIC ($P\bar{3}1m$),

and $a = b = 31.94$ Å and $c = 3.90$ Å for the PID (*P*622). The calculated pore sizes presented in **Figure 5** match exceptionally well with the ones determined with XRD.

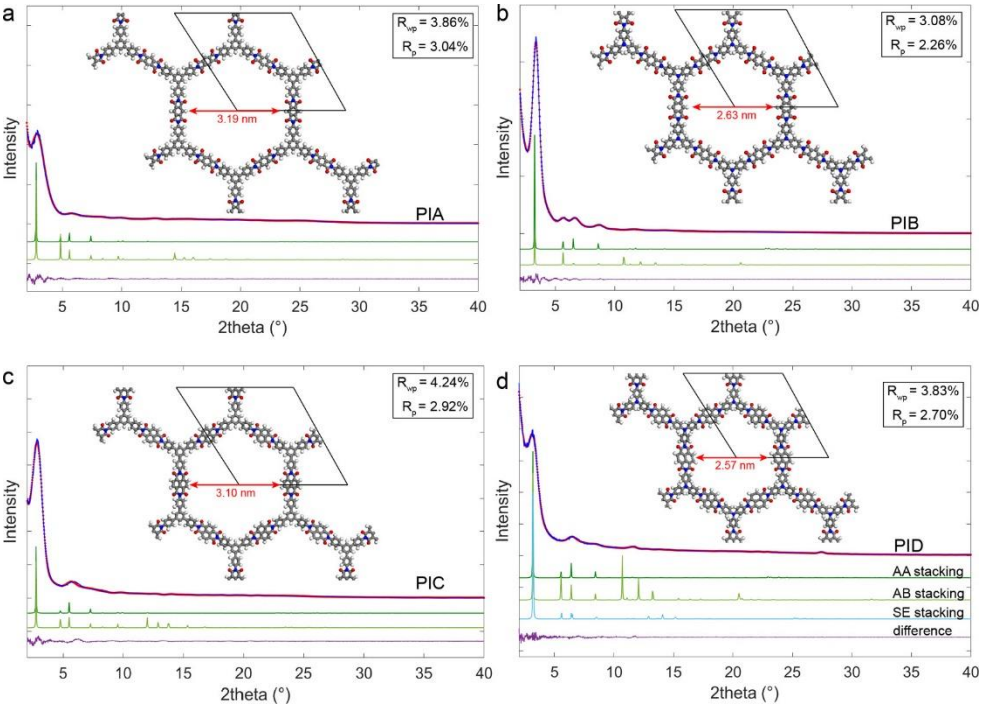

Figure 5. Experimental (blue line) *vs* Pawley refined (red scatter) *vs* simulated (dark green line for AA and light green line for the AB stacking) PXRD data for the **(a)** PIA, **(b)** PIB, **(c)** PIC, and **(d)** PID COFs.

The *c*-lattice parameter quantifies the distance between the sheets in these COF structures. The model found in the literature for the polyimide PID–COF predicted a *c*-lattice parameter of 4.37 Å.[47] The DFT calculations, based on the DFT-DF3 method of Grimme to account for the van der Waals forces (see Experimental Section), reveal that the *c*-lattice parameter is significantly smaller amounting 3.90 Å, similar to the distance predicted for PIB at 3.91 Å. The sensitivity of our result on the choice of the DFT method is investigated by performing calculations on the PIB structure implementing a variety of van der Waals corrections on the PBE functional as well as the vdW-DF functionals of Langreth and Lundqvist *et al.*,[63,64] the results of which are presented in Figure S28. Without the van der Waals corrections (PBE method), we obtain a *c*-lattice parameter of 4.45 Å, a 14% overestimation of the *c*-lattice parameter (12% in volume), an error with the same magnitude as commonly observed in the literature.[65] By including van der Waals

interactions, however, the *c*-lattice parameter is predicted to be on average (all methods) 3.88 ± 0.11 Å, larger than the 3.43 Å presented in a previous study assuming a perfectly flat structure.[45] Due to the lack and/or broadness of the PXRD reflections from these materials, it is possible to obtain acceptable agreement factors with the use of Pawley refinement for a wide range of lattice parameters. Consistent with our description that includes torsion, Pawley refinement based on the perfectly flat hexagonal unit cell ($P6_3/mmm$) resulted in worse agreement factors than when refined with the proposed configurations, including torsion. A more valid check is the comparison of the predicted reflections of the two cases (presence torsion and flat). This is a tough task considering the quality of the reflections; however, it was possible to isolate this behavior in the PIB PXRD pattern. In **Figure 3b**, we observe that the presence of torsion shifts the ab-plane reflections to higher angles. The above observation is a clear indication of the plane-shrinkage due to torsion, leading to significantly better agreement with the experimental XRD results. In addition, a different approach was attempted by performing simulations on the flat, SE, unit cell (*Cmcm*) for the PIB COF reported in the literature.[45] The offset created the conditions to break the 2D symmetry during relaxation, and the structure relaxed to exhibit torsion (~32°) in the linkage molecules ($C222_1$ symmetry) consistent with the hexagonal description. When sliding the sheets to an eclipsed configuration, we obtained lower energies, in agreement with the results obtained for the hexagonal unit cell. These new insights, the role of torsion in the COF structures, are crucial to understand and tailor the functional properties of these materials.

5.2.3 CO_2 Adsorption Properties

The porosity of the four polyimide COFs was further analyzed by CO_2 gas sorption. The efficient storage of greenhouse gases such as CO_2 in COFs has gained increasing attention in recent years because their pore sizes approach the physical size of the gasses (allowing high uptake) and have even shown to be selective when exposed to gas mixtures.[57] Polyimides are particularly interesting since their high thermal and chemical stability make them attractive surfaces for CO_2 capture under industrially realistic conditions.

Figure 6a shows the CO_2 adsorption isotherms of PIA, PIB, PIC, and PID from 0.02 to 1.2 bar at 273 K. Generally, the best CO_2 adsorbents in terms of storage capacity are the ones that contain mostly micropores.[57] Despite the fact that the four COFs discussed here contain a significant amount of mesopores, their CO_2 capacities (at 1 bar) are relatively high: 51 $cm^3\ g^{-1}$ for PIA, 64 for PIB, 56 for

PIC, and 66 for PID. While these capacity values allowed us to benchmark the performance of the four new systems against other COFs, the shape of the CO_2 isotherms revealed additional information about the porous architecture. Similar to the results for N_2 sorption, PIA and PIB have a significantly different CO_2 adsorption behavior than PIC and PID. The slope in the low-pressure (<0.2 bar) region is for all polymers higher than that in the higher-pressure (>0.6 bar) region, but the curves of PIA and PIB tail off more rapidly than those of PIC and PID. This behavior is directly correlated with the difference in PSD (Figure S23) described earlier. Furthermore, **Figure 6b** shows the CO_2 capacities (1 bar, 273 K) and BET surface areas of the four polyimide COFs. These two material properties do not seem to be completely correlated with each other for all polymers, which emphasizes again that the pore size effect seems to be the dominant but not the sole feature responsible for the observed CO_2 capacities.

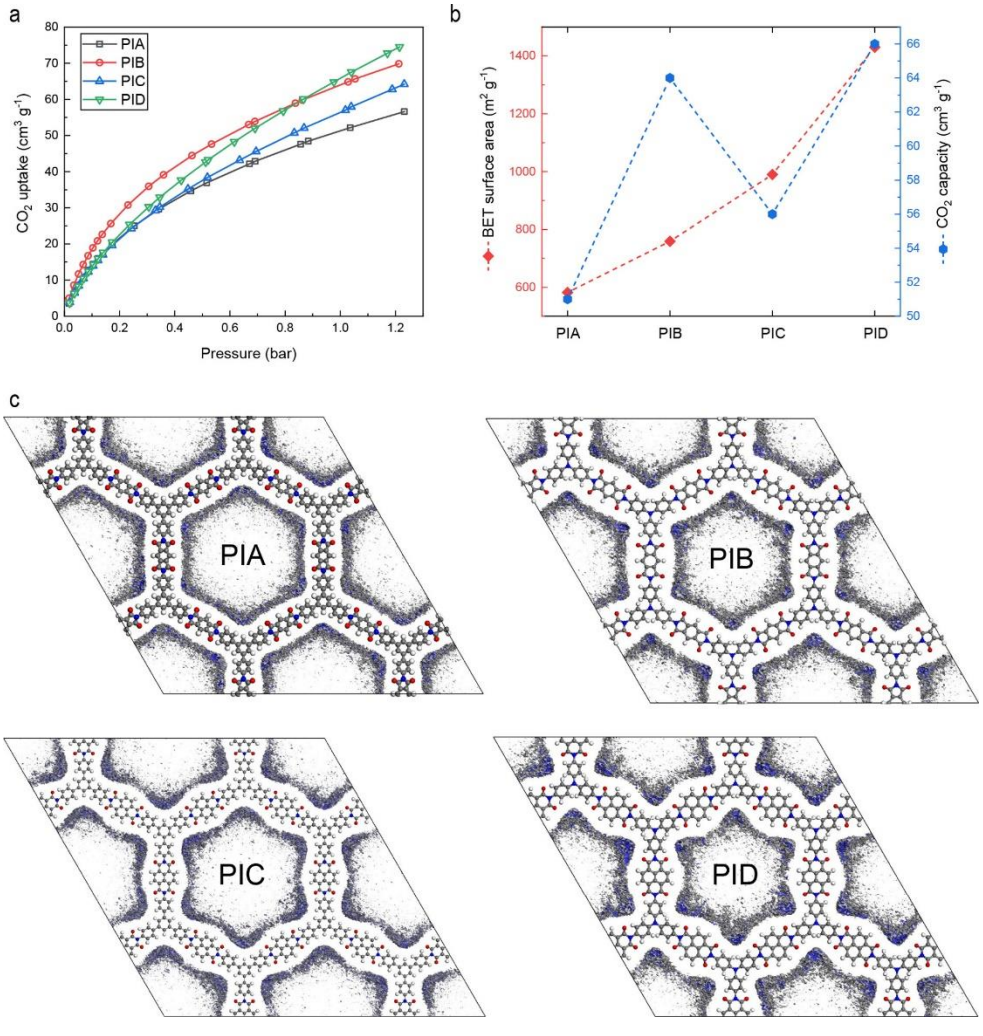

Figure 6. (a) Carbon dioxide adsorption isotherms of PIA, PIB, PIC, and PID measured at 273 K. **(b)** Surface areas of PIA, PIB, PIC, and PID measured by nitrogen gas adsorption *vs* their CO_2 capacities measured by CO_2 gas adsorption. **(c)** Force-field simulation of CO_2 adsorption at 273 K and 1 bar for the four COFs. The figure combines the adsorbed CO_2 density distribution and the potential energy surface, where darker blue areas indicate stronger binding compared to the gray ones.

To gain further insights into the sorption of CO_2 molecules into the COF host structures, we performed force-field calculations. Results are presented in **Figure 6c** for the adsorption of CO_2 at 273 K and pressure of 1 bar. We observe that adsorption in the inner pore surface of PIA forms a hexagonal CO_2 density with relatively homogeneous binding energies. However, for PIB and PID, we observe that the density distribution resembles more of a star-like dissipation, where the

more significant rotation of the TAPA molecule results in the formation of favorable potential wells (blue areas of the distribution). Interestingly, we have previously observed similar CO_2 capacity differences for other TAPB-/TAPA-based COFs,[48] which suggests that the TAPA linkage segments may play a bigger role than originally expected. For all COFs, we observe that adsorption is more favorable near the linkage molecules where the amount of hydrogen exposed to the oxygen atoms of the CO_2 is higher.

The CO_2 adsorption study presented here shows that small molecular changes in the framework of polyimide-based COFs lead to significantly different CO_2 capacities. A review about the effect of COF pore sizes on their CO_2 capacity has been presented by Zeng *et al.*,[57] and we adapted its key figure by adding the results of the polyimide-based COFs described here (**Figure 7**). Only PIC and PID were added for this comparison since their PSDs calculated from N_2 adsorption showed the highest presence of the mesopore sizes observed by PXRD (*i.e.*, the observed crystalline pore size is also the main pore size in gas sorption experiments). While the larger presence of small mesopores over micropores creates an inherent disadvantage for CO_2 capacity, the performances are still comparable with most state-of-the-art microporous COFs. Finally, unlike the other microporous COFs, we expect that the chemical nature of these imide-based COFs provides stable frameworks for CO_2 sorption under industrially realistic (*i.e.,* humid) conditions, which is to be verified in our future research.

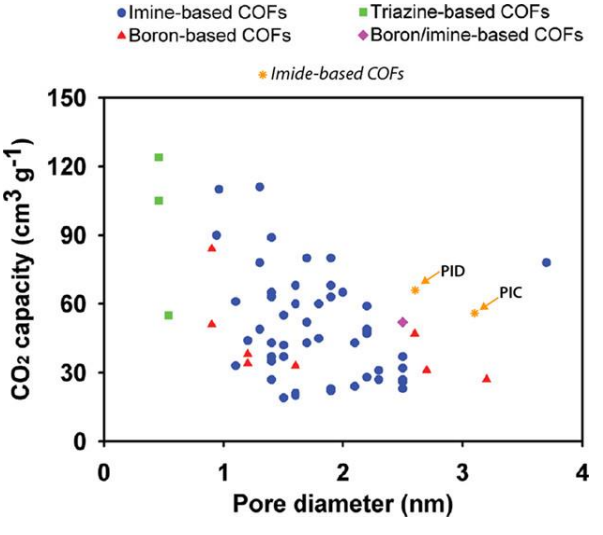

Figure 7. Plot of low-pressure CO_2 uptake against pore diameter for the selected COFs at 273 K and 1 bar. Figure adapted from Zeng *et al.*[57] with the addition of the results presented here. Adapted with permission from ref [57]. Copyright 2016, Wiley-VCH.

5.2.4 ELECTROCHEMICAL PROPERTIES

Each of the four COFs contain active molecules (PMDA or NTCDA), which can undergo redox reactions. The actual redox sites on these organic molecules are at the carbonyl groups. In theory, it is thus possible to reversibly host four alkali metal atoms per active molecule (based on the number of carbonyl groups). This is likely to happen *via* two two-electron transfers, see **Figure 8d**. However, achieving both transfers requires significantly low discharge potentials and leads to irreversible redox reactions, possibly due to destructive reactions or inactivation of the organic materials. The first two-electron transfer is well known to be (completely) reversible.[13,66-68,71] Hence, the theoretical capacities are calculated based on a two-electron transfer mechanism per active molecule (step 1, **Figure 8d**).

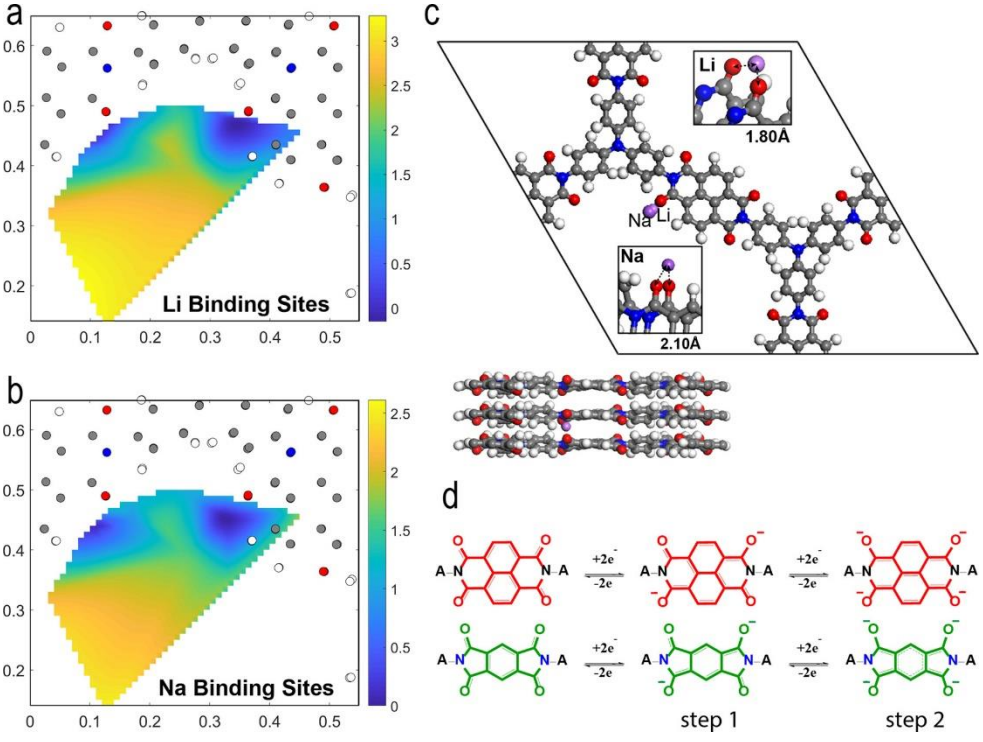

Figure 8. (a) Li and **(b)** Na insertion in PID *via* DFT calculations; the dark blue areas indicate the most favorable adsorption sites for Li and Na, respectively, and are set as the 0 point reference (scale in eV). **(c)** Preferable configurational geometry of the intercalated Li and Na. **(d)** 2-step electron transfer mechanism for the lithiation and sodiation of the COFs.

DFT calculations provide a clear indication that the observed redox reactions correspond to Li and Na binding to the active carbonyl groups of the COF structure.

Scanning through the plane of the PID–COF for favorable Li and Na active sites resulted in the energy bonding landscape maps shown in **Figure 8a,b**. The most favorable positions (indicated by the dark blue color) are located in the proximity of the oxygen atoms. For both ions, a sharp energy increase is observed as we move away from the carbonyl groups. For Na, the energy landscape is relatively more diffuse, as compared to Li, which strongly prefers to stick near the pore walls. Full relaxation of the most favorable positions for both ions reveals the exact insertion geometry. Li is stabilized at a distance of ~1.8 Å, being shared between two oxygen atoms of adjacent sheets at a calculated redox voltage of ~2.51 V versus Li/Li^+, in good agreement with the experimental results (2.49 V).

Similarly, Na-ions are bonded to the same position at slightly larger distances ~2.1 Å due to their larger ionic radius (**Figure 8c**). These positions are in line with the expected electrochemical reaction mechanism of polyimides based on PMDA or NTCDA,[13] which is shown in **Figure 8d**, where ideally four electrons can be transferred in the indicated 2-step scheme. In general, for these materials, step 2 in the redox mechanism results in severe structural damage and irreversible decomposition.[71]

The electrochemical performances of all four COF-materials were determined for lithium- and sodium-ion batteries (LIBs and SIBs) *via* cyclic voltammetry (CV), electrochemical impedance spectroscopy, and galvanostatic cycling (applying a constant current). All COFs are tested in a potential window of 1.5–3.5 V versus Li/Li^+ or Na/Na^+ due to the above reversibility reasons. Each COF, together with a standard electronic conductor (carbon black) and binder (polyvinyl difluoride), was processed in standard non-optimized electrodes and tested as a working electrode against metallic lithium or sodium. The alkali metals acted as the counter and reference electrode. The COF electrodes were not enhanced (*e.g.*, pressed, the addition of nanotubes), and therefore, the electrodes can be considered far from optimized, as the presented focus is the initial evaluation of the electrochemical activity of these materials toward Na (for the aqueous battery). We want to show the first evidence where imide-based COFs can be used for the sodium aqueous battery, and therefore, we only present our most promising electrochemical results regarding Na insertion, which is for the PID system. The electrochemical results for both Na and Li insertion in the four COFs can be found in the Supporting Information.

The CV of Na insertion in PID shows two clear reversible pairs of oxidation and reduction peaks, see **Figure 9a**. This most likely reflects the sodiation of the first and second carbonyl group, in which the second sodiated group is oppositely

located to the first where it experiences the least steric hindrance.[13,69] The presence of two distinct redox pairs has not been observed for other COF electrodes nor for NTCDA electrodes,[13,51,70] which is potentially related to the observed torsion creating more space between adjacent carbonyl groups. Only positive shifts in the potentials of the first reduction (2.16 V *vs* Na/Na^+ to 2.18 V) and oxidation peaks (1.97–2.01 V) differ from the first to the second scan, and the potentials of the other two peaks are not affected. The polarization is small compared to that in the literature.[13,51,69] The complete potential range of the CV of PID in SIB can be found in Figure S31. The large oxidation currents obtained above 2.5 V are irreversible and occur only during the initial five cycles and are induced by the decomposition of the electrolyte, see Figure S32. The presence of the two oxidation and reduction pairs is not noticeable in the charge–discharge profiles, **Figure 9b**. Only a single sloped potential plateau is observed during cycling, similar to that of the other COF electrodes. There is a substantial potential difference (0.19 V) between the initial and sequential five discharge plateaus. This difference decreases over time. The reversible capacity of PID in the SIBs is much higher and more stable than that in the LIB. A significant loss in capacity (25 mA h g^{-1}) occurs during the initial six cycles, after which it stabilizes, and some capacity is even recovered during long-term cycling. After 130 cycles, it still has a decent capacity of 81 mA h g^{-1} (**figure 9c**).

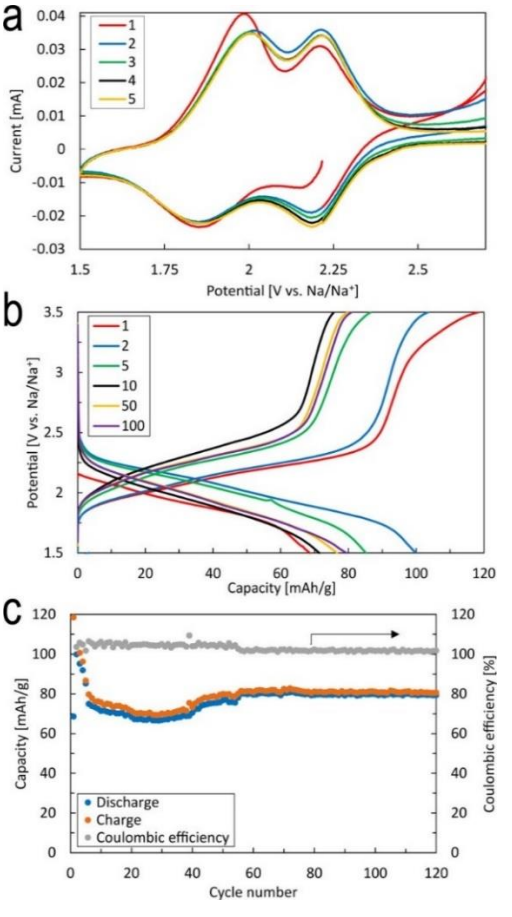

Figure 9. (a) CV curves at a scan rate of 0.1 mV s^{-1}. **(b)** Charge–discharge profiles and **(c)** cycling performance at a rate of 0.1 C (15 mA g^{-1}) for PID in SIB.

The redox potentials of all COFS, extracted from the CVs, are very comparable with those obtained for PMDA/NTCDA containing diimides in linear polymer electrodes[13] (**Table 1**). Na insertion occurs at ~0.27 V below that of the Li-ion insertion, close to the difference of Li/Li^+ and Na/Na^+ standard potentials. This indicates that the larger radius of the Na-ion does not induce a significant additional energy penalty for insertion into COF structures, rationalized by the large COF pores and flexibility. From the four reported COFs in this paper, the most promising material for the application in SIBs appears to be PID, which retains a decent reversible capacity of 81 mA h g^{-1}. Although this capacity stabilizes over more than 100 cycles, it is still significantly lower than its theoretical value (126 mA h g^{-1}). A possible explanation for this is the use of a non-optimized standard electrolyte (1 M $NaClO_4$ in EC/DMC) and non-optimized electrodes.

Table 1. Reduction Potentials of Our NTCDA/PMDA-Based COFs and Linear Polymers from the Literature.

Material	***vs* Li/Li$^+$ (V)**	***vs* Na/Na$^+$ (V)**
NTCDA (COF) (PIC)	2.51	2.25
NTCDA (COF) (PID)	2.49	2.18
NTCDA (polymer)[13]	2.47	
PMDA (COF) (PIA)	1.93	1.51
PMDA (COF) (PIB)	1.95	1.45
PMDA (polymer)[13]	2.08	

Electrochemical impedance measurements were performed on the non-optimized electrodes to obtain insights in the kinetics, Figure S33. All the COF electrodes show poor kinetics, where the Nyquist plots indicate large Ohmic resistances, indicating slow charge transfer reactions at the electrode surfaces and poor diffusion of the ions. The poor ion transport may be improved by optimization of the morphology, for instance, as achieved by Gu *et al.*,[54] clearly demonstrating the importance of particle sizes in COF materials. DAAQ–COFs with different stacking thicknesses were prepared ranging from 4–12 up to 100–250 nm particles. The smallest thicknesses outperformed their counterparts by providing more than 4 times the capacity at high rates. Even at low currents, larger capacities are achieved for the smaller particles, indicating the presence of inactive parts due to buried, poorly accessible material for larger COF particles. Another kinetic aspect of primary importance is the electronic conductivity. This is underlined by the work of Luo *et al.*[49] and Wang *et al.*,[72] who improved the electronic conductivity of their COFs by the addition of graphene (PIBN-G) or carbon nanotubes during synthesis. Lower charge-transfer resistance was reported *via* impedance spectroscopy measurements along with superior rate-capability performance (3 times more capacity at 10 C).[48]

Kim *et al.*[73] investigated the electrochemical properties of the PMDA molecule in macrocycle organic arrangements for Li-ion batteries. This group's results point out that the same active material can experience a wide variety of redox environments depending on the geometry of its arrangement, affecting its electrochemical performance. The poor performance of our PMDA-containing COFs can be attributed to a non-favorable arrangement of the redox unit in the COF arrangement compared to its NTCDA counterpart. It is suggested that the two

conjugated rings of NTCDA offer a better electrochemical environment to host the donated electron than the single conjugated ring of PMDA. Regarding the linkage molecules, the TAPA-containing COFs are likely to offer superior pore accessibility, as is discussed in Section 5.2.2.

The high molecular weight of the electrochemically inactive linkage molecules (TAPA and TAPB) limits the (theoretical) capacities of the investigated COFs instantly to relatively low values: 129, 143, 115, and 126 mA h g^{-1} for PIA, PIB, PIC, and PID, respectively, assuming a two-electron transfer mechanism per active molecule. The obtained capacities are lower than COFs that are able to "store" alkali-ions on their C═N groups and benzene rings at low potentials (≪1.5 V).[50,52,55,74] To increase the specific capacity, future designs of COF-related polyimides should be directed to lighter linkage molecules. For example, usage of 2,4,6-triamino-1,3,5-triazine or 1,3,5-triaminobenzene as the linker instead of TAPA or TAPB. This will raise the theoretical capacities of the PMDA COFs to 199 and 201 mA h g^{-1} and the NTCDA COFs to 168 and 169 mA h g^{-1}.

5.2.5 Aqueous Performance

Several COFs in organic electrolytes that are reported appear to have an extremely low operation potential (0–1.5 V *vs* Li/Li^+ [50,52,55,74] and 0–1 V *vs* Na/Na^+ [55,56,75]) and, thus, from this perspective appear to be quite suitable as anode materials for organic electrolyte containing Li-ion and Na-ion batteries. In contrast, the polyimides tested herein have an operating potential above 1.5 V, which seem very suitable for aqueous electrolytes because it is within the stability window of water over a semi wide pH-range. The thermodynamic potential of the hydrogen evolution reaction (HER) at neutral pH is 2.297 versus Na/Na^+, while the practical HER will be even lower due to a substantial polarization of the HER (depending on the electrode materials), suggesting that our NTCDA-containing COFs may be a potential anode material for Na-aqueous batteries. The high abundancy and easier harvest conditions of sodium, as compared to lithium, in combination with an aqueous electrolyte and organic electrodes, make these combinations in potential a cheap, safe, and environmentally friendly battery which is in particular promising for stationary storage applications, where energy density has less priority.[76,77]

Since PID had the best performances in the SIB with organic electrolyte, it was selected to be tested in an aqueous sodium-ion battery. PID was used as the negative electrode and $Na_{0.44}MnO_2$ as the positive electrode in combination with an Ag/AgCl reference electrode. The electrolyte was a 0.5 M Na_2SO_4 aqueous

electrolyte with a pH of 7. The CV of PID in the aqueous SIB, **Figure 10a**, is similar to the one in the organic SIB. Both redox peaks are present during oxidation and reduction, albeit less sharp and have potential shifts of +0.2 to 0.3 V, most likely caused by the different chemical and kinetic environment of the electrolyte. During the galvanostatic cycling test, **Figure 10b**, the lower cutoff potential of the anode was set at −0.9 V versus Ag/AgCl to be sure to prevent hydrogen evolution. This greatly limits the capacities in these tests, but optimization of the electrolyte (lowering the HER and thus the cutoff) is expected to result in higher capacities. This can be achieved by lowering the pH or by using high Na-salt concentrations,[78,79] but this is out of scope of this paper. The average aqueous operating potential (−0.6 V *vs* Ag/AgCl or 2.31 V *vs* Na/Na^+) is higher (+0.30 to 0.38 V) than that of the average potentials in the organic electrolyte batteries which is consistent with the observed shifts in the CV.

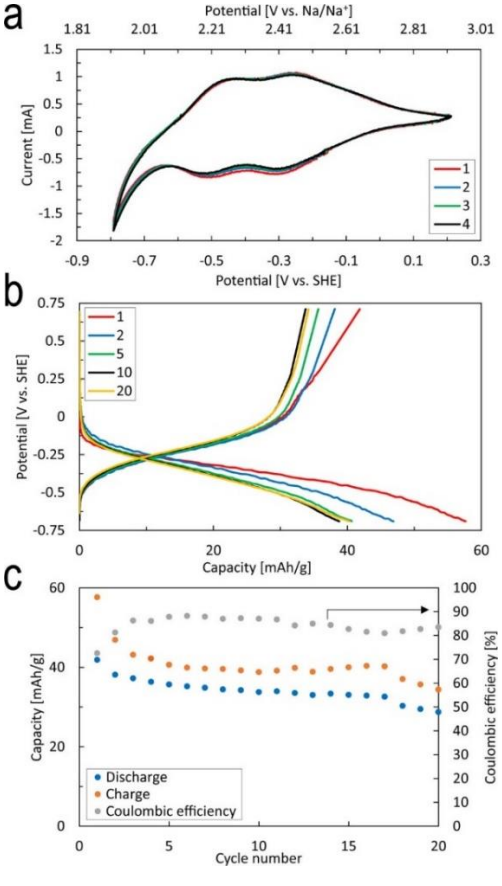

Figure 10. Electrochemical performances of PID in the $Na_{0.44}MnO_2$/PID aqueous sodium-ion battery. **(a)** CV with a scan rate of 0.1 mV s^{-1}. **(b)** Charge–discharge profiles of cycle 1, 2, 5, 10, and 20 at a C-rate of 0.1 C (15 mA g^{-1}). **(c)** Cycling performance at a rate of 0.1 C (16 mA g^{-1}).

The capacity decreases in the initial five cycles before it stabilizes, see **Figure 10c**. However, the shape of the voltage profile is identical, indicating reversible Na-ion insertion and extraction from PID. The difference between the charge and discharge capacities can be explained by the fact that the aqueous electrolyte was not purged to get rid of the oxygen. It is well known that dissolved oxygen in the aqueous electrolytes will react with "bonded" sodium at the anode side, which results in considerable loss in discharge capacities.[66,80,81] Above observed results demonstrate that PID (and probably PIC) can function well as negative electrodes in a Na-aqueous battery. The optimization of the performances is the subject of future studies.

In the same context, **Figure 11** and **Table 2** present an overview of the COF materials reported in the literature for SIBs along with sister materials such as metal organic frameworks (MOFs) and covalent organic nanosheets (CONs). The potential for sodium insertion into these materials is compared to the theoretical HER potential as a function of pH, indicating the feasibility of these materials in aqueous batteries. In particular, of interest is the work of Zhang and Gao [75] who used the TAPB linkage in combination with the light molecule terephthalaldehyde. Due to its high capacity and the plateau-like region, the material can reach 150 mA h/g at a relatively high voltage and might be relevant for alkaline (pH ≫ 7) aqueous systems; however, stability in water remains to be demonstrated. An interesting direction is to combine the TAPA linkage with terephthalaldehyde which, based on the torsion analysis in Section 5.2.2, is expected to stabilize the structure even further by allowing a more rotational freedom. The presence of a nitrogen functional group and also in the linkage molecule will further increase the capacity, compared to a benzene counterpart, and is additionally expected to increase the conductivity and wettability of the material.[75]

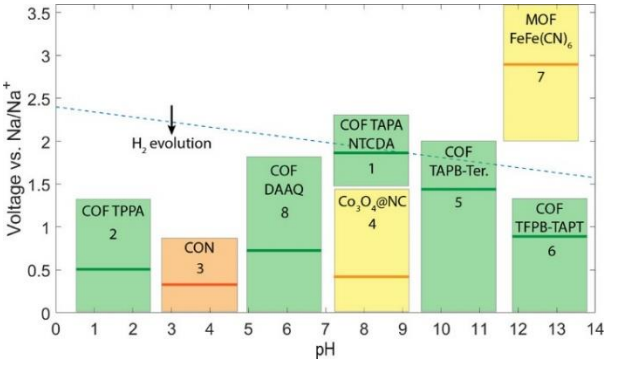

Figure 11. Review of the presented COF material and reported COFs, CON and MOF materials (2–8). The dotted blue line reflects the thermodynamic HER potential as a function of pH. The

vertical length of the boxes reflect their tested operational voltage range and the bold line within the boxes correspond to the voltage where half of the reported capacity is reached. The numbering of the boxes refers to the numbers listed in **Table 2**.

Table 2. Numbers in the First Column Correspond to the Numbering in **Figure 11**.[a]

#	group	system	specific capacity (mAh/g) // current density (mA/g)
1	This work	(COF) TAPA + NTCDA	81 // 15
2	Zhang *et al.*[55]	(COF) TPPA	238 // 50; 89 // 2500
3	Kim *et al.*[82]	Covalent organic nanosheets	190 // 200; 80 // 1000
4	Wang *et al.*[83]	Co_3O_4 on nitrogen-doped carbon	506 // 100; 263 ///1000
5	Zhang and Gao[75]	(COF) TAPB-terephthaldehyde	303 ///100; 170 // 1000
6	Patra *et al.*[56]	(COF) TFPB-TAPT	250 ///30; 160 ///200
7	Nie *et al.*[84]	(MOF) $FeFe(CN)_6$/carbon	82 ///24
8	Gu *et al.*[54]	(COF) DAAQ	420 // 100; 200 ///5000

[a]TFPB stands for 1,3,5-tris(4-formyl phenyl) benzene, TAPT stands for 1,3,5-tris(4 amino phenyl)-triazine, and TPPA for triformylphloroglucin-*p*-phenylenediamine.

5.3 CONCLUSIONS

In summary, we report a synthesis route for producing COFs composed of PMDA or NTCDA with TAPA or TAPB linkage molecules. Computational characterization by DFT reveals the stability and preferred orientation of the molecular components in the COF crystal. The preferential torsion between the benzene rings of the linkage molecules is around 32° introducing longer stacking distances and reducing the pore size compared to their flat (2D) counterparts. Torsion in COF configurations with the TAPA linkage molecule is much more stable due to the presence of the nitrogen atom that allows extra rotational freedom. The stacking of the sheets in the perpendicular direction has AA eclipsed orientations with possible reversible offsets due to metastable phases. These insights guide selecting the right components for advanced nano-architectures for next-generation batteries and other applications.

A brief study on CO_2 uptake of the four COFs was performed and showed clear correlations between CO_2 capacity, surface area, and pore size. In addition, molecular modeling revealed that PIB and PID contain preferred CO_2 binding sites, which emphasized that these COFs were best suited for CO_2 uptake. By combining

these computational results with the fact that the best performing COFs (PIB and PID) contain TAPA building blocks, we identified a valuable new structure–property relationship that enables directed research toward novel high-performing CO_2 adsorbents.

Non-optimized NTCDA-related COFs provide reversible capacities tested in LIBs and SIBs. PID in SIBs showed for the first time two clear pairs of redox peaks and also performed the best overall with a capacity of 81 mA h g^{-1} after 130 cycles. The superior performance of the PID (NTCDA–TAPA) compared to that of the PIC (NTCDA–TAPB) material can be attributed to the structural characteristics explored computationally.

The superior stability of the TAPA linkage results in more cohesive particles ensuring the presence of accessible pores. In addition, the longer pore walls might allow ion accessibility in an otherwise inactive pore from the outside. An overview of COFs and similar organic structures evaluated for SIBs brings forward the promises and directions of future material design. The relatively high redox potential of the presented polyimides, combined with the structural stability when utilized in COF configurations, is put in perspective as potential anode materials for aqueous sodium-ion batteries. Usage of COFs in these batteries, in this paper demonstrated with PID, appears to be quite promising. This will open up new directions for the development and utilization of diimide-related configurations as versatile electrode materials in (aqueous) batteries.

5.4 Experimental Section

5.4.1 General COF Synthesis

A detailed description of the synthesis of the individual polymers is described in the Supporting Information. In general, a 10 mL Pyrex tube was charged with 0.44 mmol of dianhydride monomer (PMDA or NTCDA) and 0.29 mmol of triamine monomer (TAPB or TAPA) in a solution of 1 mL of *m*-cresol/1 mL of NMP in the presence of 0.06 mL of isoquinoline. The tube was degassed *via* three freeze–pump–thaw cycles at 77 K and flame sealed. The tube was then heated at 200 °C for 3 days. The resulting precipitate was washed with methanol (3×) and acetone (3×) and recovered by centrifugation. The resulting compound was purified by Soxhlet extraction in THF for 24 h and then dried at 60 °C under vacuum for 12 h to provide the COF powder.

5.4.2 ELECTRODE PREPARATION

Electrodes were fabricated by casting electrode slurries onto current collectors. First, a mixture of one of the active materials (COF or $Na_{0.44}MnO_2$), an electronic conducting agent (Super P, Timcal) and a binder (polyvinylidene fluoride, Solef) in a mass ratio of 8:1:1 was thoroughly ground. NMP (Sigma-Aldrich) was added to the mixture to form a homogeneous viscous slurry. The slurry was cast with a doctor blade on the current collectors, carbon-coated copper foil for organic electrolyte LIBs, and carbon-coated aluminum foil for organic electrolyte SIBs. Carbon-coated foils were used to improve the adhesion of the coating with the current collector. The electrodes for the aqueous SIB were made by casting the slurry on stainless steel. The coatings were dried in a vacuum oven at 80 °C overnight, and circular discs were cut out with an average mass loading of 2.1 mg cm^{-2}.

5.4.3 ELECTROCHEMICAL TESTING

The organic electrolyte LIBs and SIBs were assembled in an Argon-filled glovebox (MBraun). COF-electrodes were placed as working electrodes in self-made Swagelok cells. Lithium or sodium metal discs (Sigma-Aldrich) were used as both counter and reference electrode. Glass fiber discs (Whatman) were used as separators. Standard 1 M $LiPF_6$ (for LIBs) and 1 M $NaClO_4$ (for SIBs) in EC and DMC battery grade solutions (1:1 vol, Sigma-Aldrich) were used as electrolytes. Three electrode cells were used for testing the electrochemical performances of PID as the working electrode in the aqueous sodium-ion battery. $Na_{0.44}MnO_2$ acted as the counter electrode, and an Ag/AgCl electrode (0.197 V *vs* NHE) was used as the reference electrode. A 0.5 M Na_2SO_4 aqueous solution (pH = 7–8) was used as the electrolyte. CV measurements were performed on a potentiostat/galvanostat (PGSTAT302N, Metrohm). CVs were obtained at a scan rate of 0.1 mV s^{-1} with a voltage window of 1.5–3.5 V versus Li/Li^+ or Na/Na^+ for the organic electrolyte batteries and −1.0 to 0 V versus Ag/AgCl for the aqueous battery. Electrochemical cycling of the batteries was conducted on a M4000 Maccor battery tester at a 0.1 C-rate based on the theoretical capacities of the COF-based electrodes.

5.4.4 COMPUTATIONAL TESTING

DFT calculations, as implemented in the plane-wave Vienna ab initio simulation package,[85] were performed. The generalized gradient approximation of Perdew–Burke–Ernzerhof [86,87] was selected, while the core-electron interactions were

probed with the projector augmented wave method.[88] In order to account for dispersion forces in these large molecules, the zero damping DFT-D3 method of Grimme was implemented. For the geometry optimization of hexagonal unit-cell configurations (AA eclipsed, AB staggered and serrated), a high cutoff energy of 520 eV was selected to ensure accurate calculations. The energy maps are constructed by relaxing configurations with offsets of 0 1.5, 3, 7, 11, and 18.6 Å for the PID and 0, 3, 7, 14, and 21 Å in the direction toward the staggered configurations and configurations with an offset in the respective distances to form hexagons in the diagonal direction (Figure S30). The data points were symmetrically rotated to form the hexagon. Insertion simulations required a 1 × 1 × 3 COF supercell to ensure sufficient Li/Na screening along the tunnel direction. For these relaxations, the cutoff was reduced to 400 eV. The Monkhorst–Pack, *k*-point mesh was set to 3 3 7 and 1 1 3 for the unit and supercell configurations, respectively. In all cases, total energies were obtained from subsequent, self-consistent calculations with a cutoff energy of 520 eV. The simulated PXRD patterns were obtained using the Materials Studio Software package in combination with the Reflex Materials Studio module. The results were based on the DFT-optimized unit cells of the COF materials in several possible configurations. The experimental PXRDs were subjected to Pawley refinement using the pseudo-Voigt peak shape function and Finger–Cox–Jephcoat asymmetry correction function (up to 20°) to produce the refined profile.

Acknowledgements

The authors thank Kees Goubitz, Michel Steenvoorden, and Frans Ooms (Delft University of Technology, faculty of Applied Sciences) for their assistance with experiments. The authors thank Willy Rook (Delft University of Technology, faculty of Applied Sciences) for her support with gas uptake measurements and interpretation of the data. The authors also thank Dalian University of Technology for the permission to use their Materials Studio software package. Financial support is greatly acknowledged from the Netherlands Organization for Scientific Research (NWO) under the OTP grant no. 15785 and the VICI grant no. 16122.

5.5 SUPPORTING INFORMATION

5.5.1 INSTRUMENTATION

Fourier transform infrared spectra were recorded on a PerkinElmer precisely Spectrum 100 FT-IR Spectrometer. TGA was carried out under nitrogen atmosphere on a TGA/DSC 1 thermal analyzer from PerkinElmer TGA 4000. The nitrogen (at 77 K) and carbon dioxide (at 273 K) sorption isotherms were measured on a Tristar II 3020 Micromeritics instrument. All samples were degassed before the measurement at 403 K under vacuum for 16 h. Solid state NMR measurements were performed using a Bruker Ascend 500 WB spectrometer (11.7 T) operating at a 13C frequency of 125.76 MHz and equipped with a two channel 4 mm MAS probe head (Bruker) at a 10 kHz spinning speed. One dimensional 13C CP-MAS spectra were recorded with proton π/2 pulse lengths of 3 – 4 μs and cross polarization periods of 4 ms. Between 4000 - 40000 scans were accumulated depending on the individual s/n obtained from each of the samples, with a recycle delay of 1.5 s between scans. An exponential apodization function corresponding to a line broadening of 20 Hz was applied prior to Fourier transformation. The morphology of the COFs was examined with a JEOL JSM-6010LA scanning electron microscope, operating at an acceleration voltage of 2kV and 10kV. Cyclic voltammetry (CV) measurements were performed on a Metrohm potentiostat/galvanostat (PGSTAT302N) and electrochemical cycling of the batteries were conducted on a M4000 Maccor battery tester. Powder Xray Diffraction (PXRD) data were collected on a Rigaku MiniFlex 600 powder diffractometer using a Cu K(α) -source (λ=1.5418 Å) over the range of 2θ = 2 - 45.0 with a step size of 0.02o and 1s per step.

5.5.2 SYNTHESIS

All building blocks and chemicals are commercially bought.

Synthesis of PIA

A 10 mL Pyrex tube was charged with PMDA (95.9 mg, 0.44 mmol) and TAPB (101.9 mg, 0.29 mmol) in a solution of 1 ml m-cresol/1 ml *N*-methyl-2-pyrrolidone (NMP) in the presence of isoquinoline 0.06 ml The tube was degassed via three-freeze-pump-thaw cycles at 77K and flame sealed. The tube is then heat at 200°C for 3 days. The resulting precipitate was washed with methanol (3x) and acetone (3x) and recovered by centrifugation. The resulting compound is purified by

Soxhlet extraction in THF for 24h and then dried at 60°C under vacuum for 12h to provide PIA as a light brown solid in 82% isolated yield.

Synthesis of PIB

In a similar manner as PIA, PIB has been prepared in a Pyrex tube measuring. It was charged with PMDA (95.9 mg, 0.44 mmol) and TAPA (84.1 mg, 0.29 mmol) in a solution of 1 ml m-cresol/1 ml NMP in the presence of isoquinoline 0.06 ml The tube was degassed via threefreeze-pump-thaw cycles at 77K and flame sealed. The tube is then heat at 200°C for 3 days. The resulting precipitate was washed with methanol (3x) and acetone (3x) and recovered by centrifugation. The resulting compound is purified by Soxhlet extraction in THF for 24h and then dried at 60°C under vacuum for 12h to provide PIB as a light brown solid in 85% isolated yield.

Synthesis of PIC

In a similar manner as PIA, PIC has been prepared in a Pyrex tube measuring. It was charged with NTDA (118 mg, 0.44 mmol) and TAPB (101.9 mg, 0.29 mmol) in a solution of 1 ml dichlorobenzene (PhCl2) / 1 ml NMP in the presence of isoquinoline 0.06 ml The tube was degassed via three-freeze-pump-thaw cycles at 77K and flame sealed. The tube is then heat at 200°C for 3 days. The resulting precipitate was washed with methanol (3x) and acetone (3x) and recovered by centrifugation. The resulting compound is purified by Soxhlet extraction in THF for 24h and then dried at 60°C under vacuum for 12h to provide PIC as a light brown solid in 79% isolated yield.

Synthesis of PID

In a similar manner as PIA, PID has been prepared in a Pyrex tube measuring. It was charged with NTDA (118 mg, 0.44 mmol) and TAPA (84.1 mg, 0.29 mmol) in a solution of 1 ml m-cresol / 1 ml NMP in the presence of isoquinoline 0.06 ml. The tube was degassed via three-freeze-pump-thaw cycles at 77K and flame sealed. The tube is then heat at 200°C for 3 days. The resulting precipitate was washed with methanol (3x) and acetone (3x) and recovered by centrifugation. The resulting compound is purified by Soxhlet extraction in THF for 24h and then dried at 60°C under vacuum for 12h to provide PID as a light brown solid in 91% isolated yield.

Synthesis of $Na_{0.44}MnO_2$

$Na_{0.44}MnO_2$ was prepared via a high temperature calcination of Na_2CO_3 (Sigma-Aldrich) and Mn_2O_3 (Sigma-Aldrich). A 0.55:1 molar ratio was heated up to 300°C

and hold it for 2 hours before it was heated up to 800°C for 12 hours and cooled down to room temperature to obtain $Na_{0.44}MnO_2$.[S1]

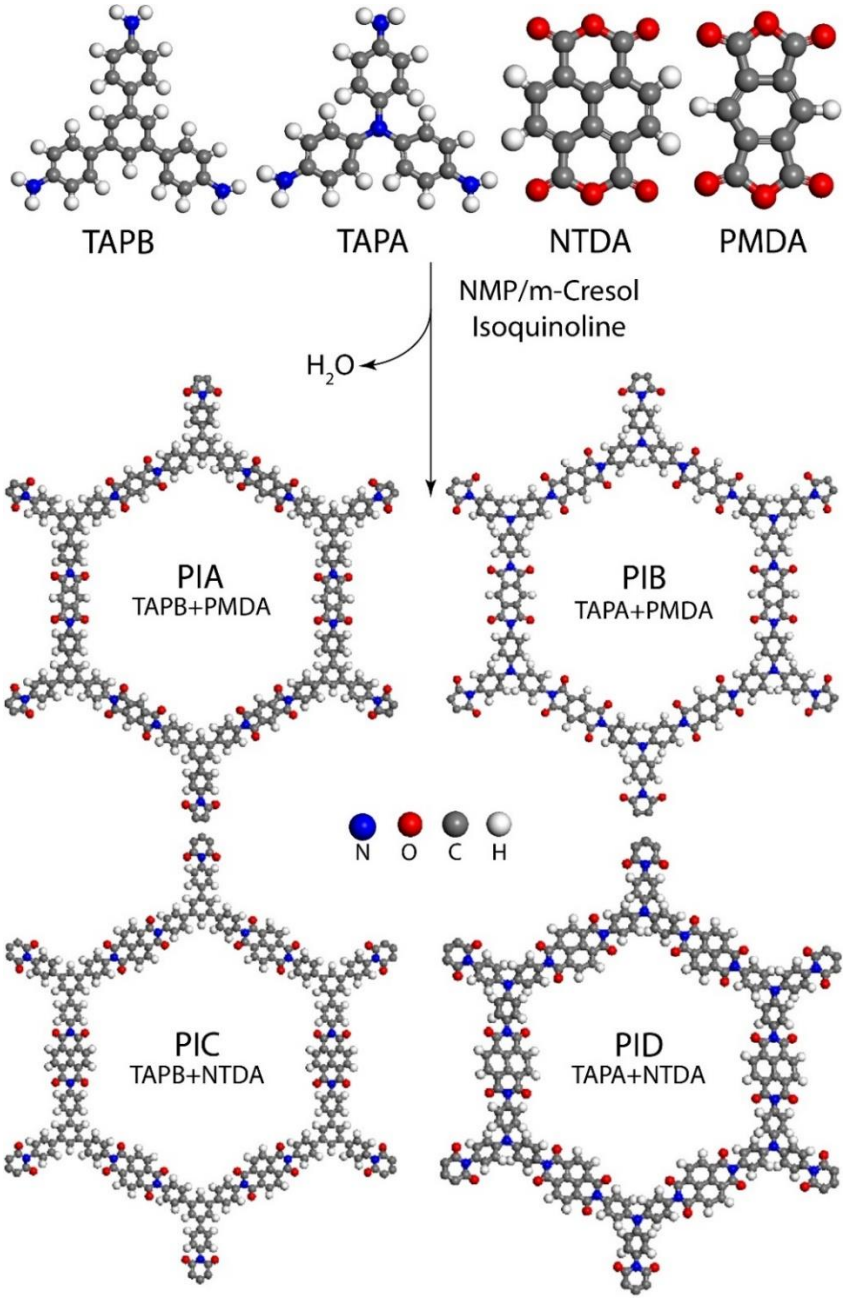

Figure S1: Synthesis of the four polyimide COFs from TAPB, TAPA, NTDA and PMDA to give PIA, PIB, PIC and PID. The imidization is done in NMP (or $PhCl_2$) and m-Cresol (1:1, v/v) in presence of isoquinoline. This reaction releases water.

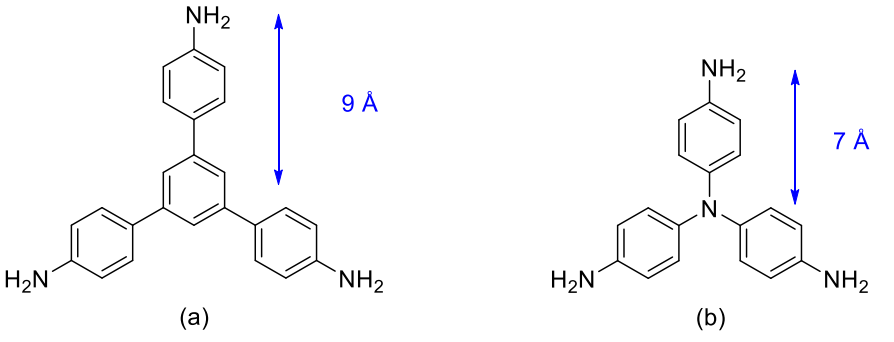

Figure S2: Two extended tritopic amine with various size. The measurements have been taken from the centre of the molecule to the nitrogen atom. **(a)** TAPB: 9 Å. **(b)** TAPA: 7 Å.

5.5.3 FTIR Spectra

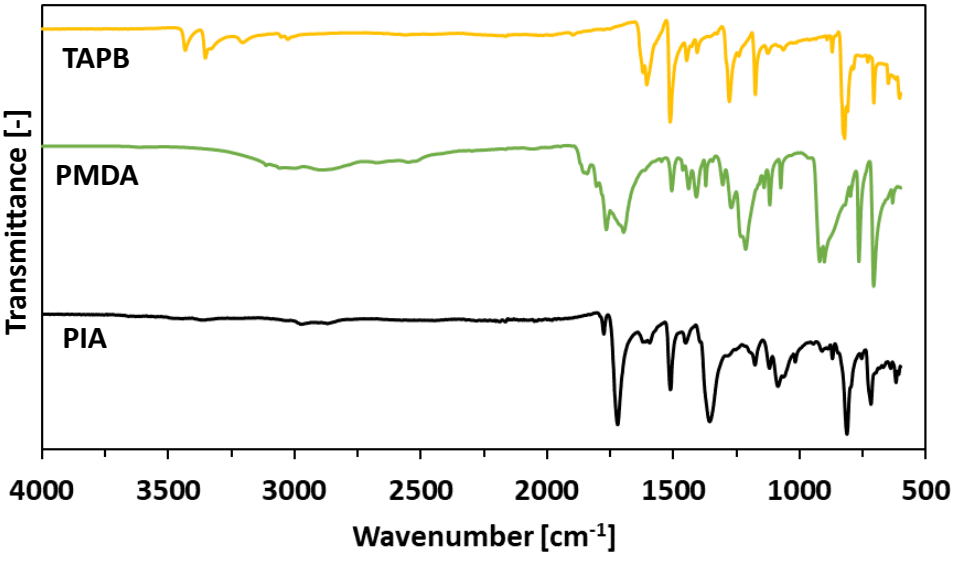

Figure S3: FT-IR spectra of PIA, TAPB, and PMDA.

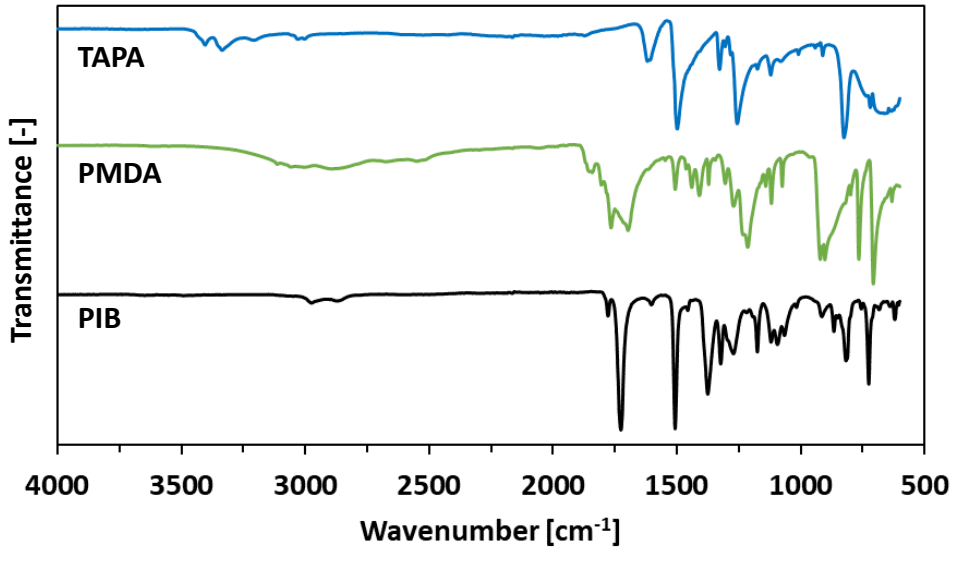

Figure S4: FT-IR spectra of PIB, TAPA, and PMDA.

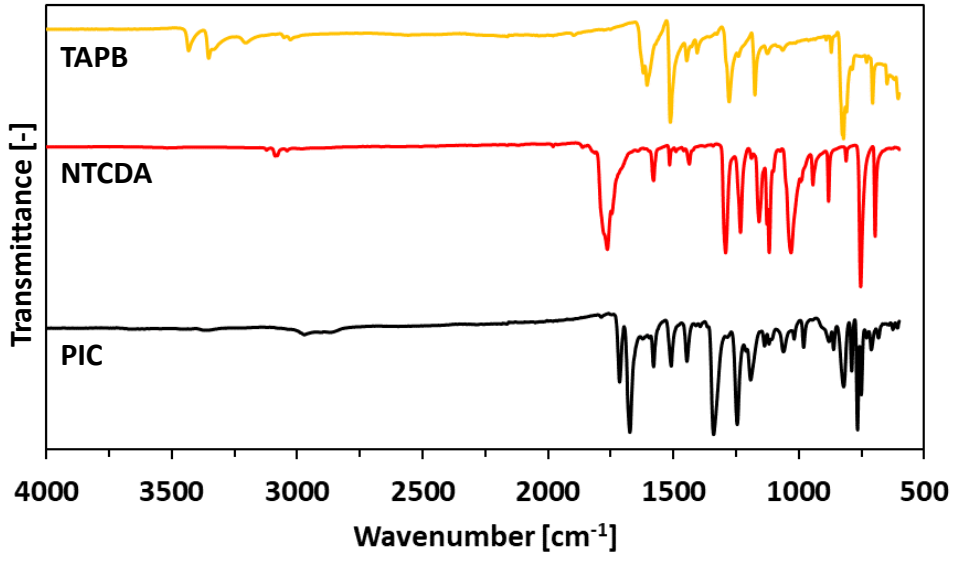

Figure S5: FT-IR spectra of PIC, TAPB, and NTDA.

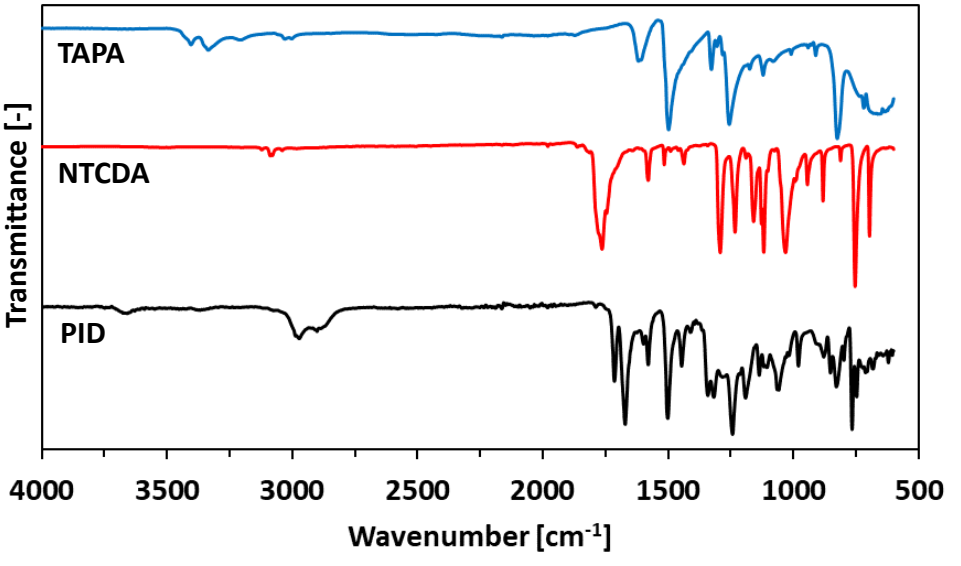

Figure S6: FT-IR spectra of PIA, TAPA, and NTDA.

5.5.4 Solid state ^{13}C and ^{1}H NMR

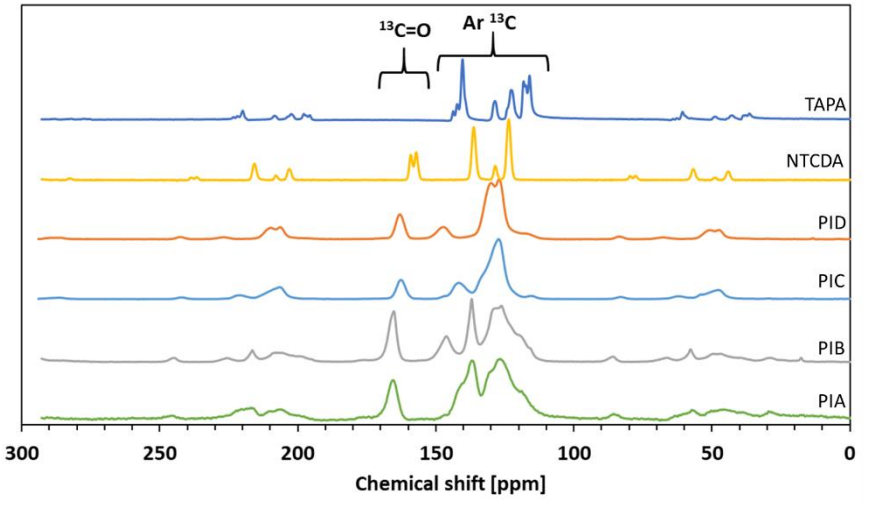

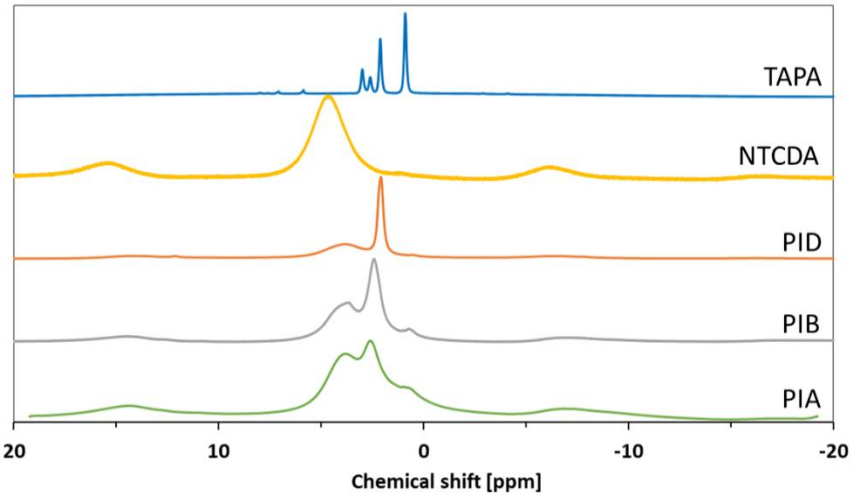

Figure S7: (top, previous page) Solid 13C NMR spectra of PIA, PIB, PIC, PID, NTCDA and TAPA **(bottom)** Solid 1H NMR spectra of PIA, PIB, PID, NTCDA and TAPA.

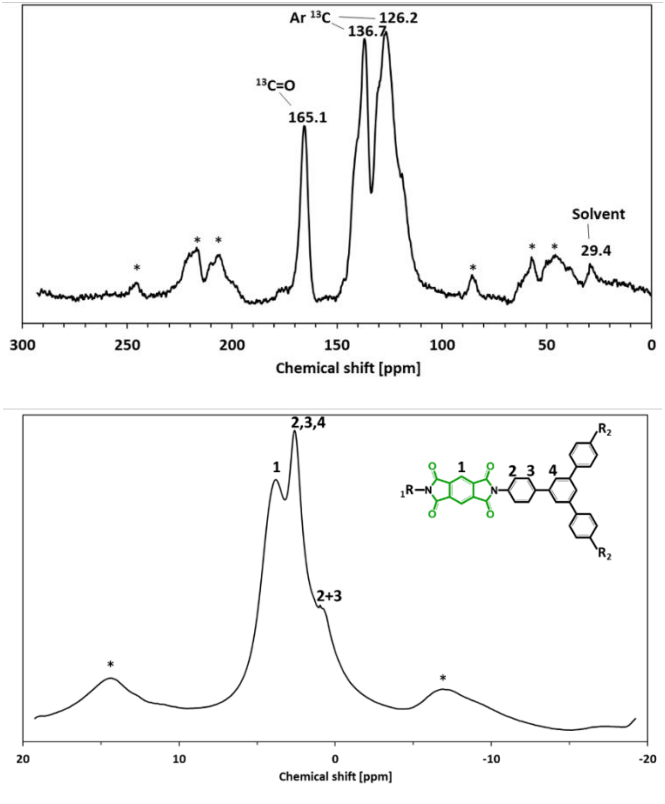

Figure S8: (top) Individual solid 13C NMR spectra of PIA. **(bottom)** Individual solid 1H NMR spectra of PIA. The asterisks represent spinning sidebands.

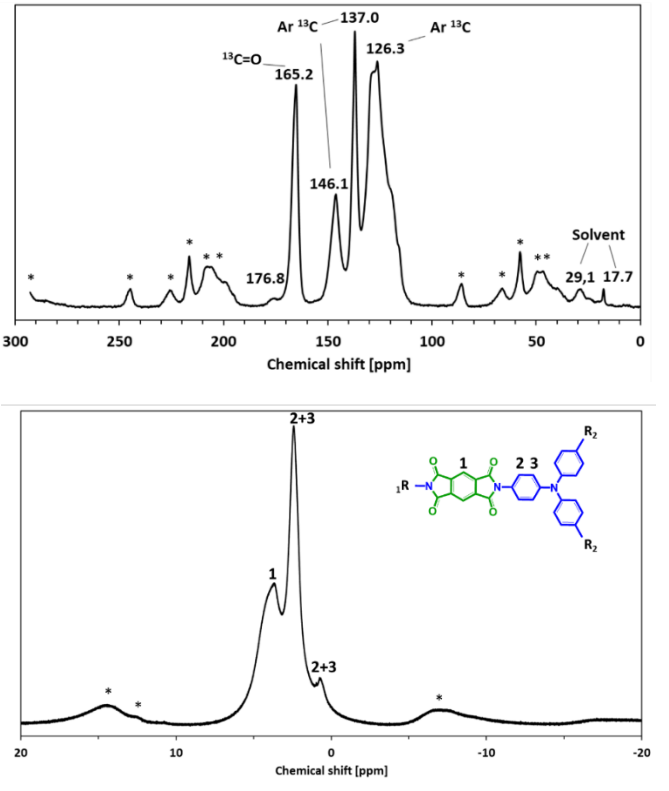

Figure S9: (top) Individual solid 13C NMR spectra of PIB. **(bottom)** Individual solid 1H NMR spectra of PIB. The asterisks represent spinning sidebands.

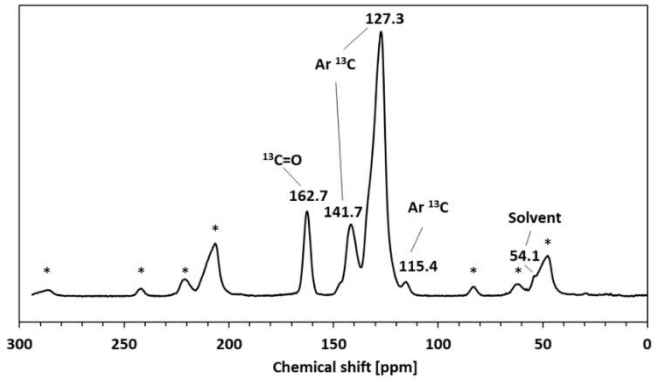

Figure S10: Individual solid 13C NMR spectra of PIC. The asterisks represent spinning sidebands.

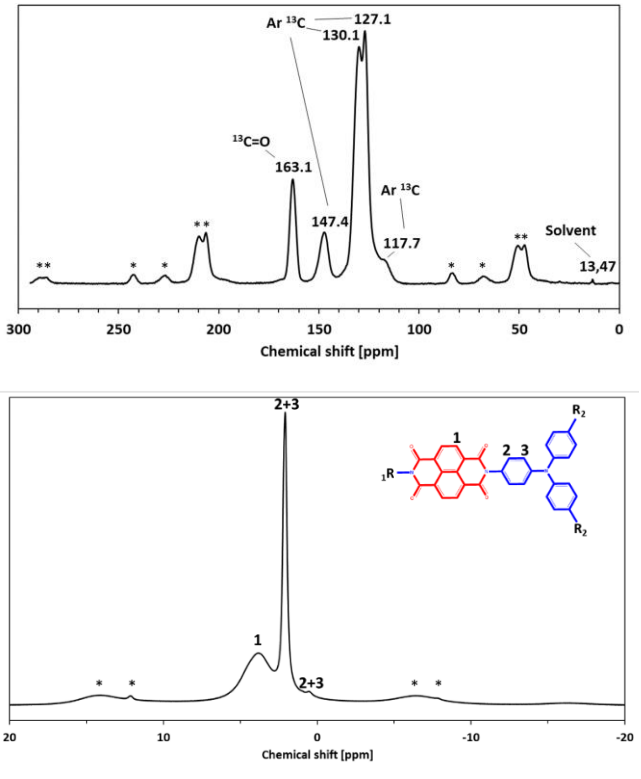

Figure S11: (top) Individual solid 13C NMR spectra of PID. **(bottom)** Individual solid 1H NMR spectra of PID. The asterisks represent spinning sidebands.

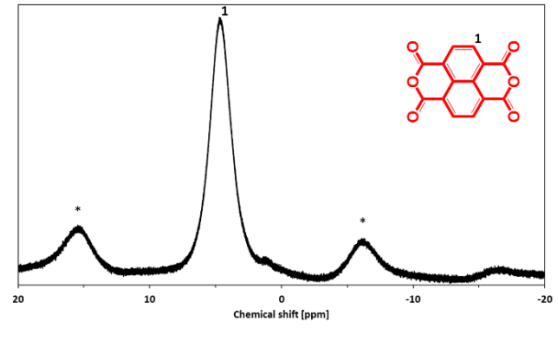

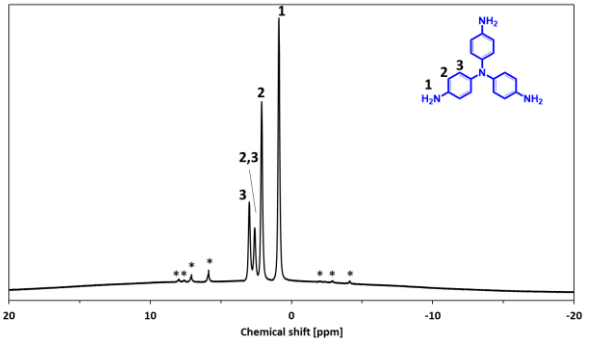

Figure S12: (top, previous page) Individual solid 1H NMR spectra of NTCDA. **(bottom)** Individual solid 1H NMR spectra of TAPA. The asterisks represent spinning sidebands.

5.5.5 Thermogravimetric Analysis

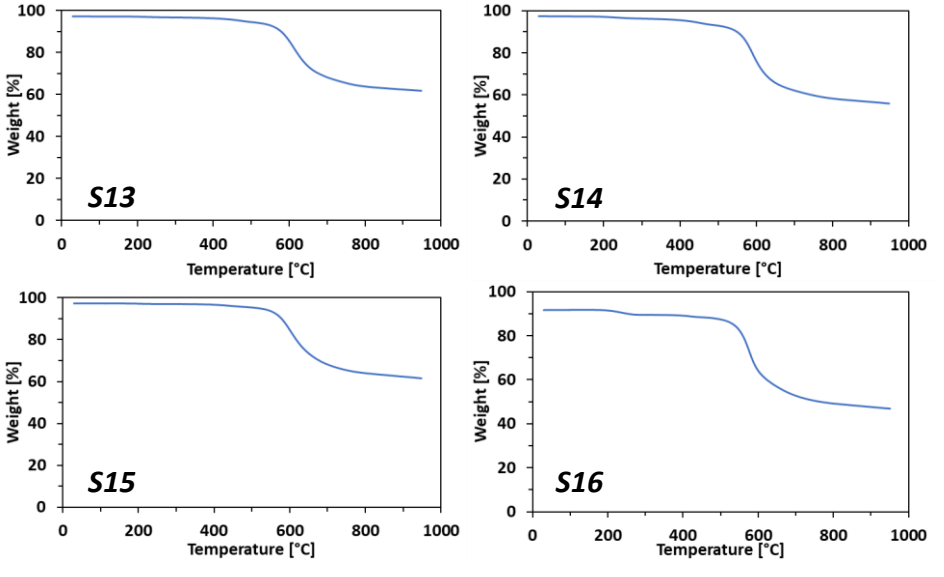

Figure S13: TGA of PIA. **Figure S14:** TGA of PIB. **Figure S15:** TGA of PIC. **Figure S16:** TGA of PID.

5.5.6 Stability Tests

Stability Tests

The stability of the COFs PIC and PID was investigated by performing solubility tests in the sodium electrolytes; 1M NaClO4 in EC/DMC (organic electrolyte) and 1M Na2SO4 in neutral water (aqueous electrolyte). 180 mg of PIC/PID was stored with 20 ml electrolyte for 14 days. Mixtures were shaken every day, where after

the powders were thoroughly washed with DMC or demi water before a XRD spectra was obtained.

Table S1: Masses (mg) of PIC and PID before and after the stability test.

	Organic electrolyte		Aqueous electrolyte	
	Before	After	Before	After
PIC	179.7	175.2	180.3	168.8
PID	181.1	172.4	180.2	175.4

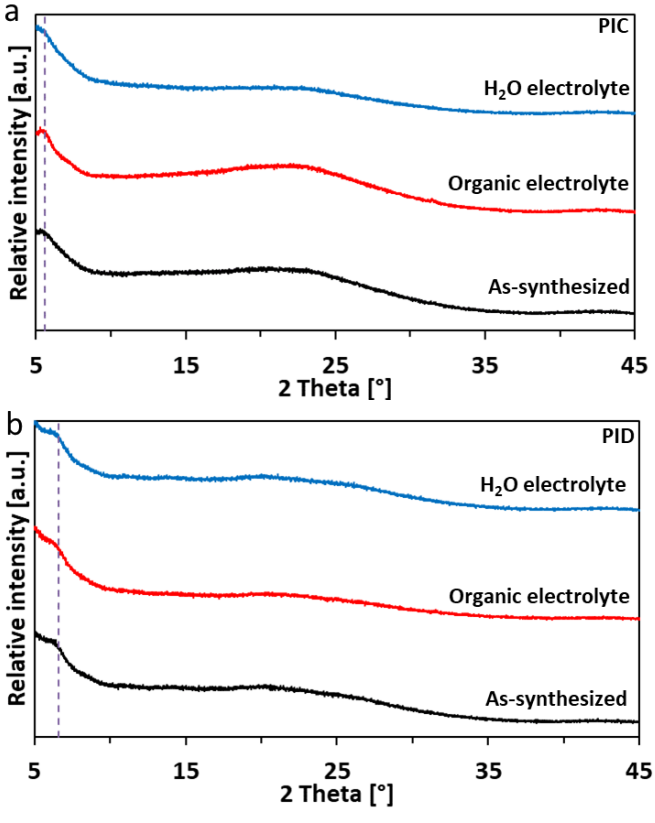

Figure S17: Powder X-ray diffraction spectra (including background) of as-synthesized PIC **(a)** and PID **(b)** as well as after two weeks soaked in organic (1M $NaClO_4$ EC/DMC) and aqueous (0.5M Na_2SO_4) electrolyte.

5.5.7 Scanning Electron Microscopy

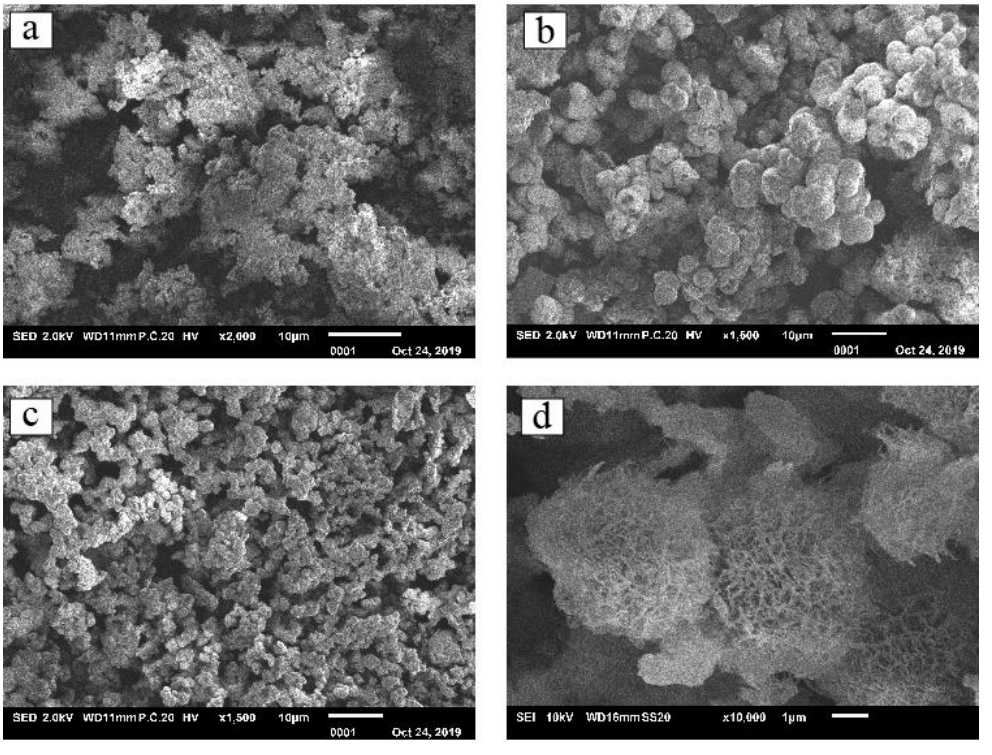

Figure S18: SEM images of **(a)** PIB **(b)** PIC **(c)** PID **(d)** zoomed-in PID.

5.5.8 GAS ADSORPTION

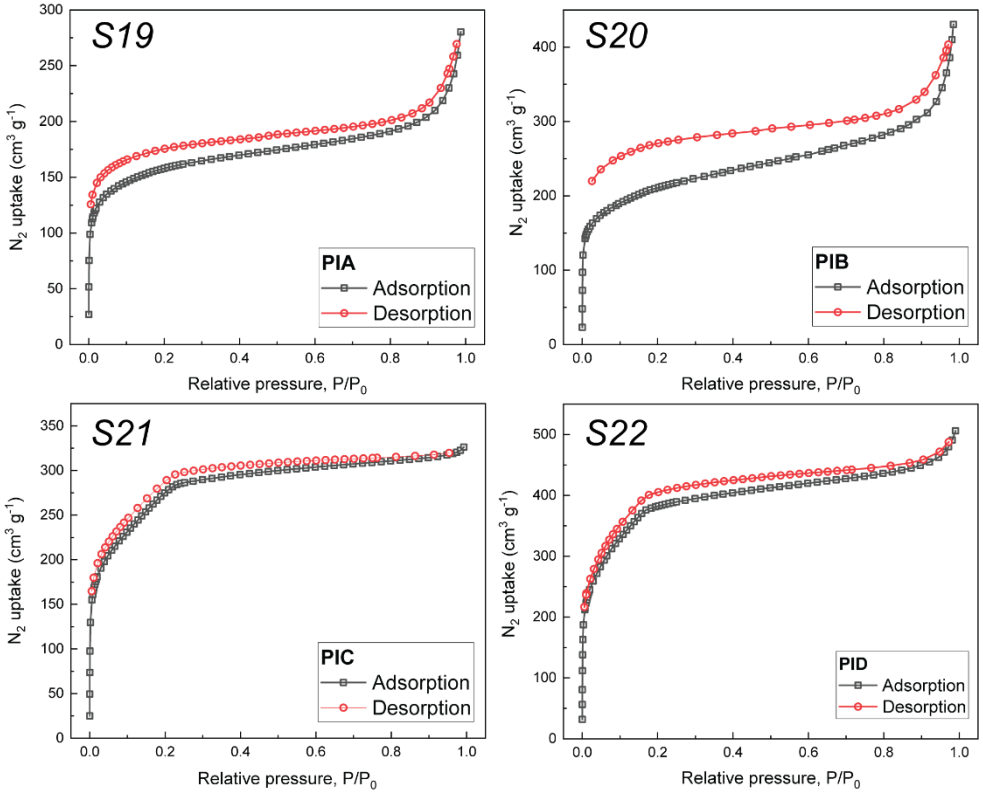

Figure S19 N_2 adsorption and desorption isotherms of PIA measured at 77 K. **Figure S20:** N_2 adsorption and desorption isotherms of PIB measured at 77 K. **Figure S21:** N_2 adsorption and desorption isotherms of PIC measured at 77 K. **Figure S22:** N_2 adsorption and desorption isotherms of PID measured at 77 K.

Pore size distributions (PSDs) were calculated by fitting the nitrogen sorption isotherms of the COFs to a standardized DFT model within the software of the Quantachrome NOVATouch sorption machine. Specifically, the quenched solid density functional theory (QSDFT) carbon model (N2 @ 77 K) on the adsorption branch was chosen for the PSD calculations, and the model takes slit, spherical and cylindrical pore geometries into account.

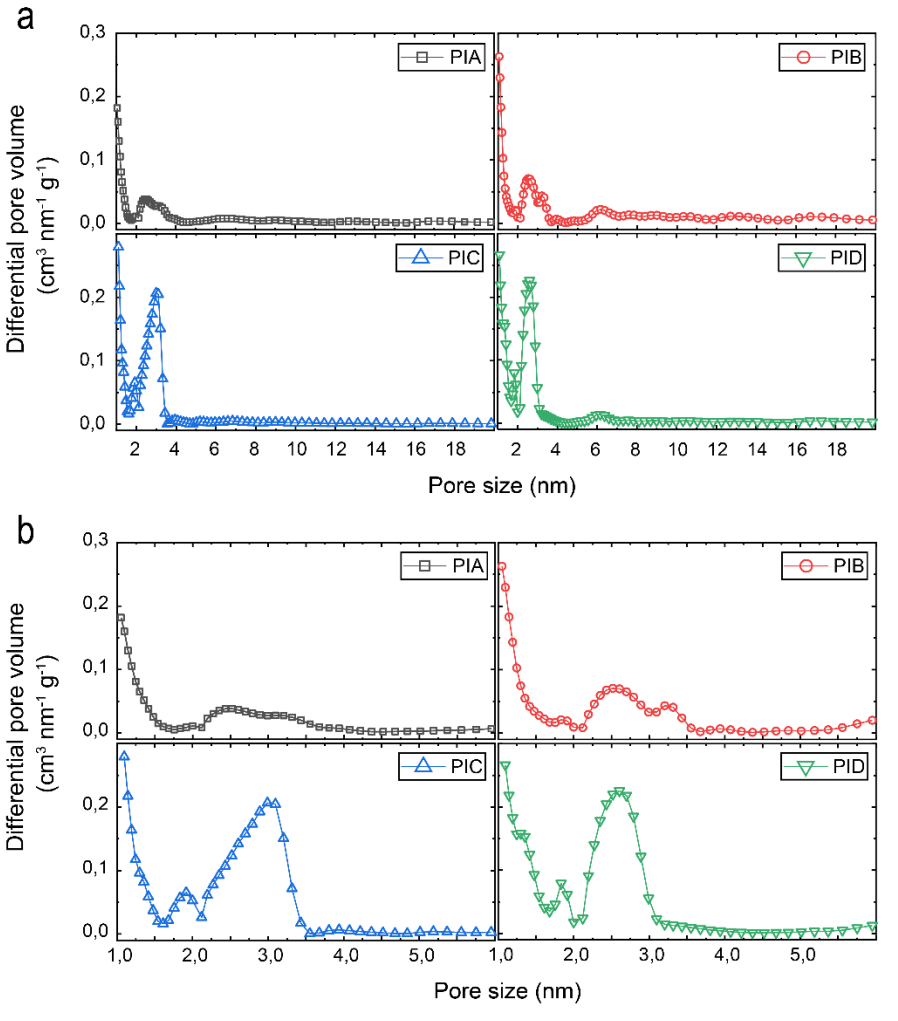

Figure S23 a) Pore size distributions of PIA, PIB, PIC, and PID calculated from the nitrogen adsorption isotherms at 77 K. **b)** Zoom-in on the micro- and small mesopore region.

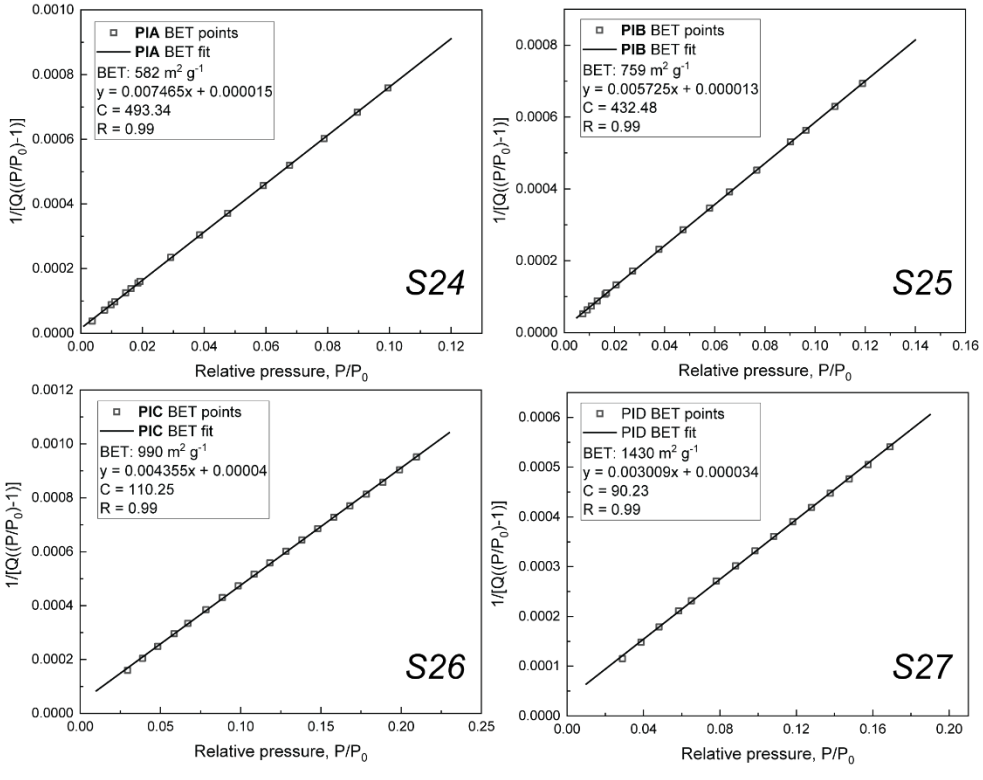

Figure S24: BET plot calculated from the N_2 adsorption isotherm of PIA at 77 K. **Figure S25:** BET plot calculated from the N_2 adsorption isotherm of PIB at 77 K**. Figure S26:** BET plot calculated from the N_2 adsorption isotherm of PIC at 77 K. **Figure S27:** BET plot calculated from the N_2 adsorption isotherm of PID at 77 K.

5.5.9 COMPUTATIONAL METHODS

Below we address some quality indicators regarding DFT simulations.

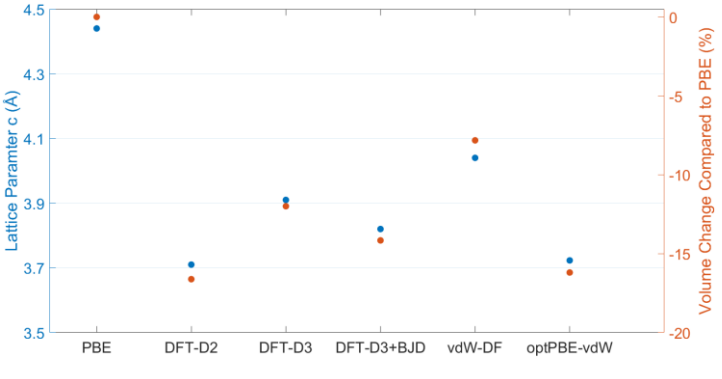

Figure S28: The effect of various DFT methods on the c lattice parameter and volume of PIB. All the results in the main text are reported for the DFT-D3 approximation.

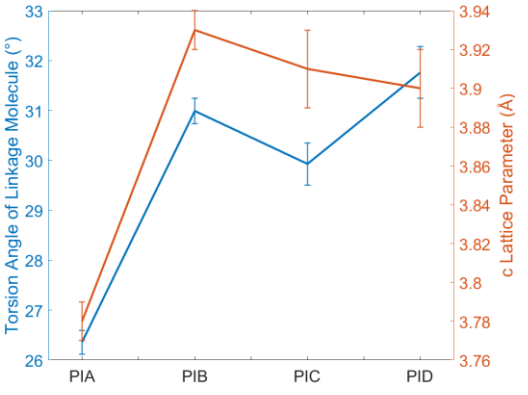

Figure S29: Qualitative correlation between the obtained c lattice parameter and the torsion angles of between the carbon rings of the linkage molecules of the 4 COFs.

In the following table we present the effect of the DFT method on the relative energy between different configurations. Example of stability between the AA eclipsed and AB staggered PID configuration.

DFT-D3	AA is 0.79 eV/FormulaUnit more stable than AB, (17.6 meV/atom)
DFT-D3-BJ	AA is 0.82 eV/ FormulaUnit more stable than AB, (18.3 meV/atom)

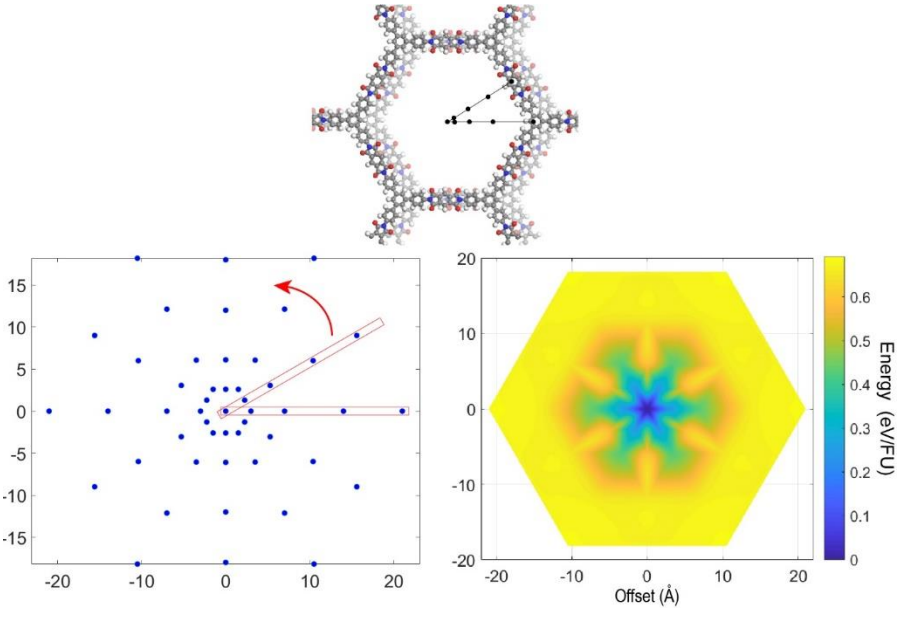

Figure S30: Sampling points of the PIA energy map side by side with the PIA energy map. The points in the red box are the calculated structures that we rotated symmetrically to form the hexagonal space.

5.5.10 CRYSTAL STRUCTURES

Below we present the crystal structures of the 4 COFs.

PIA-AA stacking-eclipsed-torsion

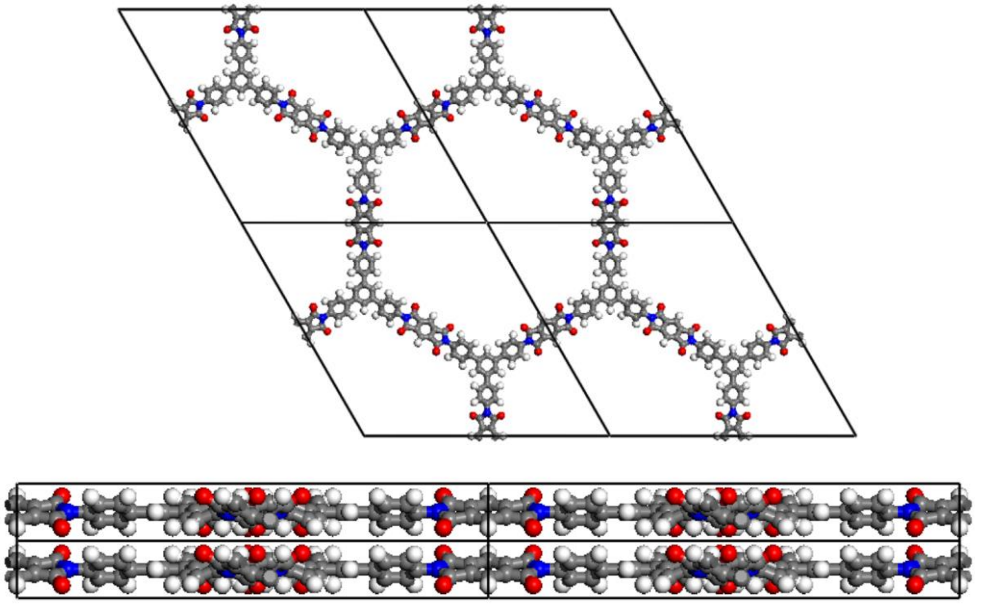

PIA-AB stacking-staggered-torsion

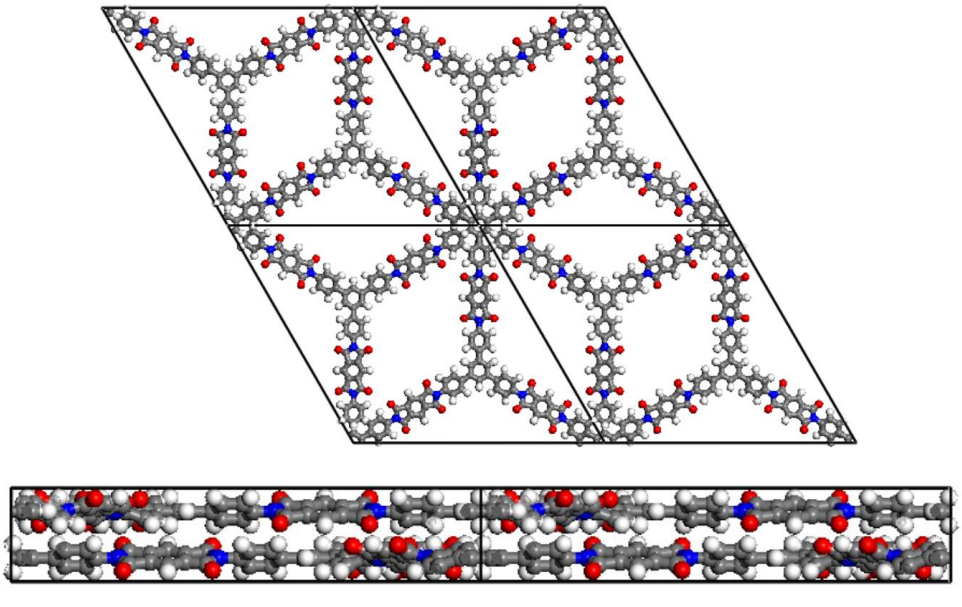

PIB-AA stacking-eclipsed-torsion

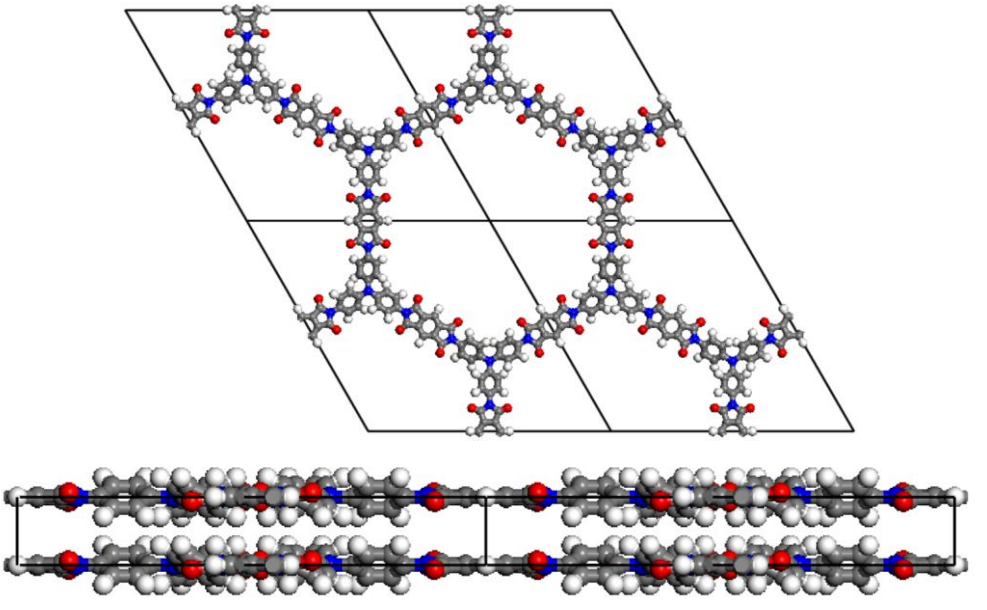

PIB-AB stacking-staggered-torsion

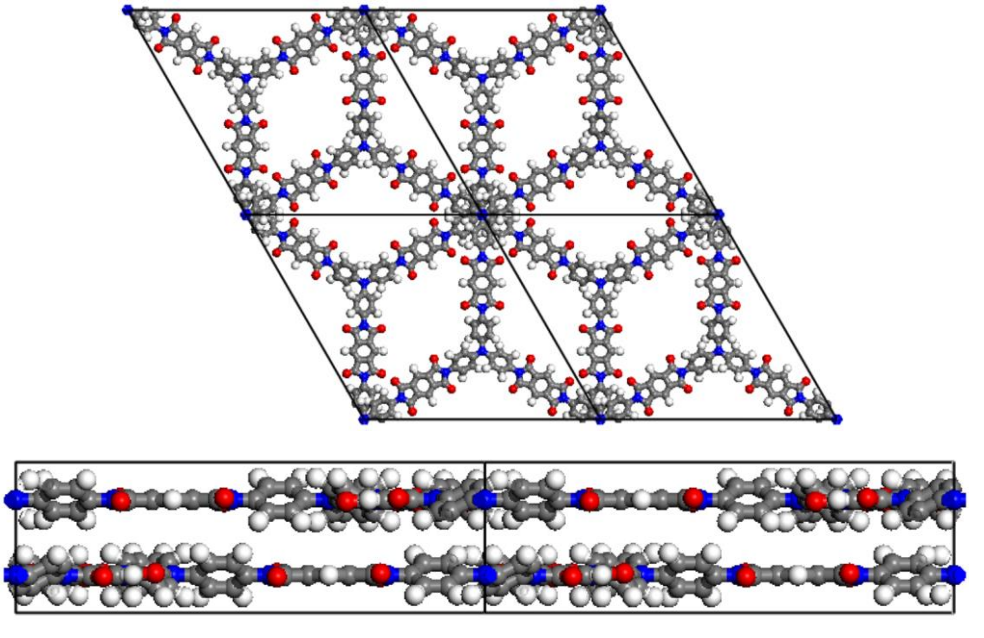

PIC-AA stacking-eclipsed-torsion

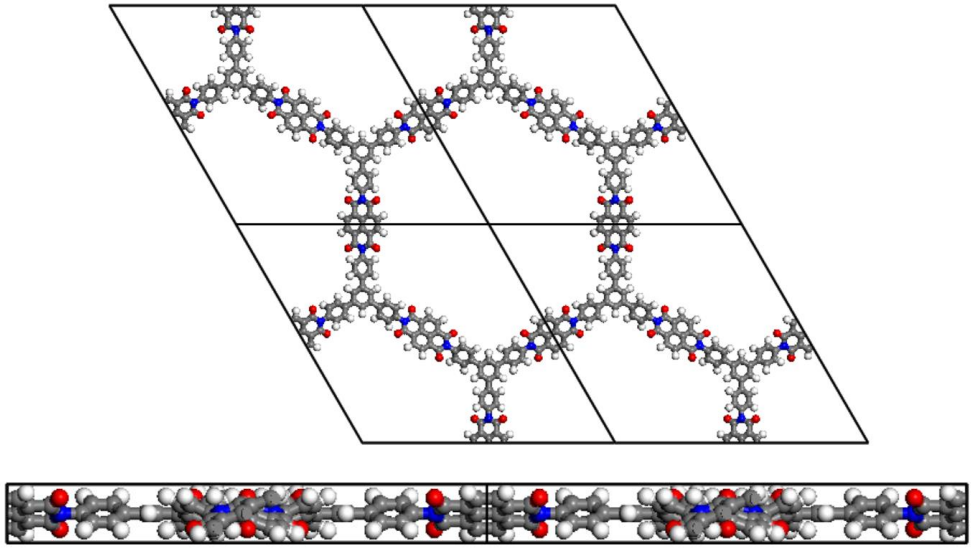

PIC-AB stacking-staggered-torsion

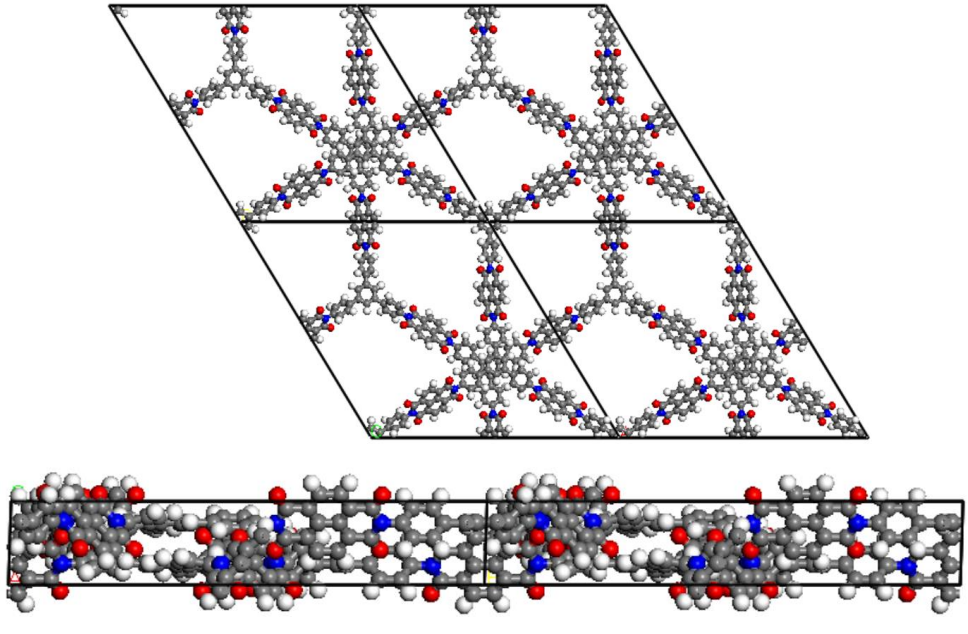

Symmetry after relaxation was reduced to P1. Symmetry searching even with tolerance of 0.5 Å resulted in the P1 symmetry. The atomic positions of the 300 atoms can be found in the .cif file provided.

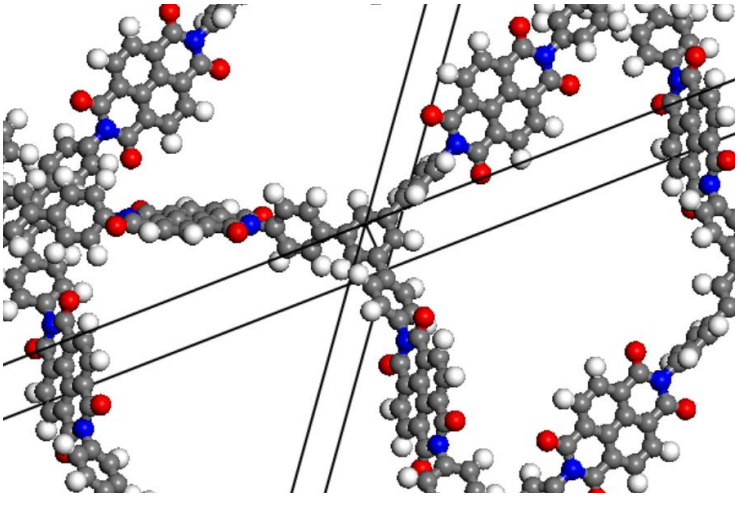

PID-AA stacking-eclipsed-torsion

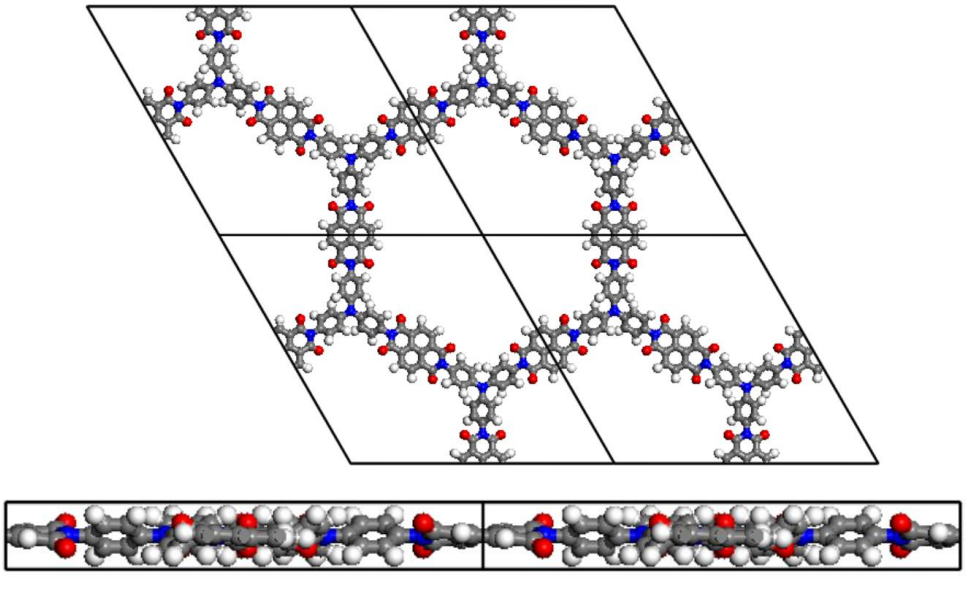

PID-AB stacking-staggered-torsion

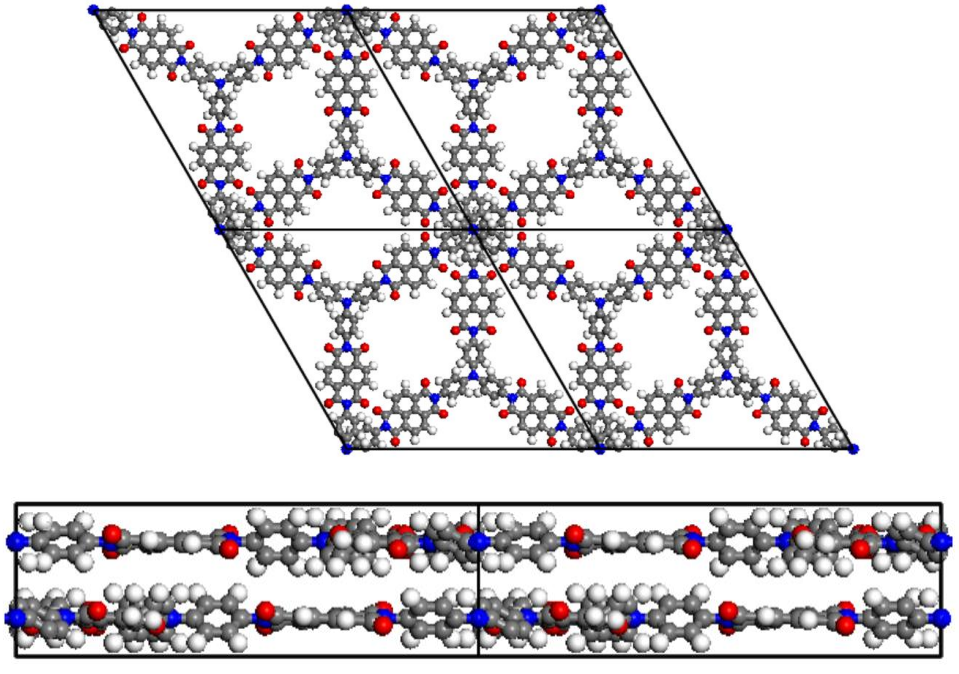

PID-serrated stacking-sheets are slipped by 6.6 Å –torsion

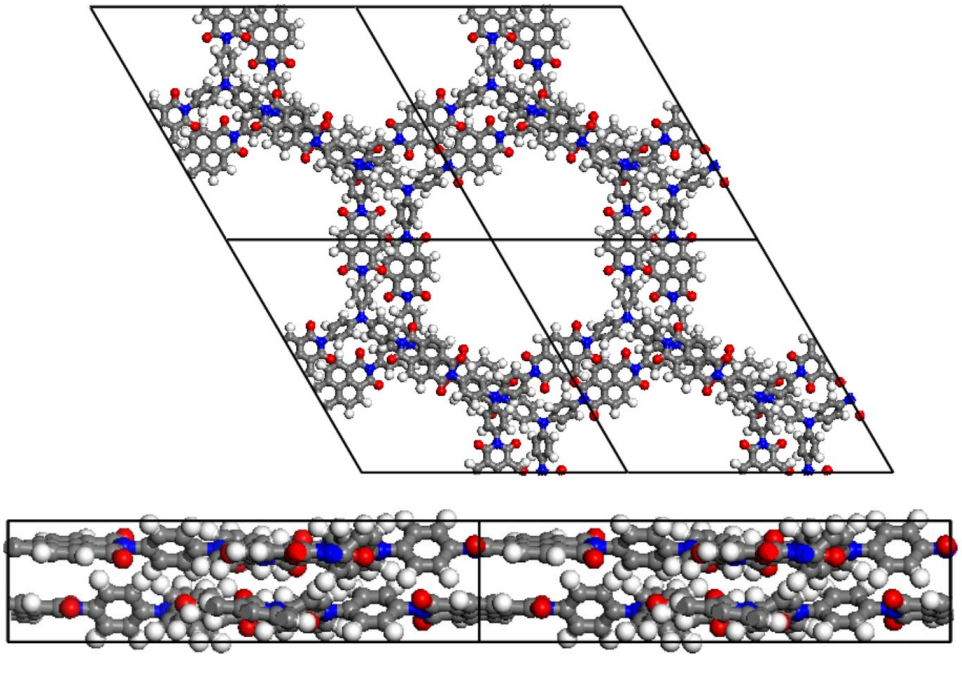

Symmetry after relaxation was reduced to P1. Symmetry searching even with tolerance of 0.5 Å resulted in the P4 symmetry. The atomic positions of the atoms can be found in the PID_AB_tor.cif file provided.

	PIA-AA	**PIA-AB**	**PIB-AA**	**PIB-AB**	**PIC-AA**	**PIC-AB**	**PID-AA**	**PID-AB**	**PID-serrated**
s.g.	P-31M (162)	P-31C (163)	P622 (177)	P6322 (182)	P31-M (162)	P1	P622 (177)	P6322 (182)	P21 (4)
a (Å)	36.5283	36.418	31.369	31.289	37.07	36.6920	31.9450	31.9390	31.9510
b (Å)	36.5283	36.418	31.369	31.289	37.07	37.3260	31.9450	31.939	7.0710
c (Å)	3.8065	6.247	3.910	8.617	3.89	5.5700	3.901	9.069	31.51
alpha (°)	90.00	90.00	90.00	90.00	90.00	88.14	90.00	90.00	90.00
beta (°)	90.00	90.00	90.00	90.00	90.00	90.50	90.00	90.00	120.26
gamma (°)	120.00	120.00	120.00	120.00	120.00	121.20	120.00	120.00	90.00

5.5.11 Electrochemistry

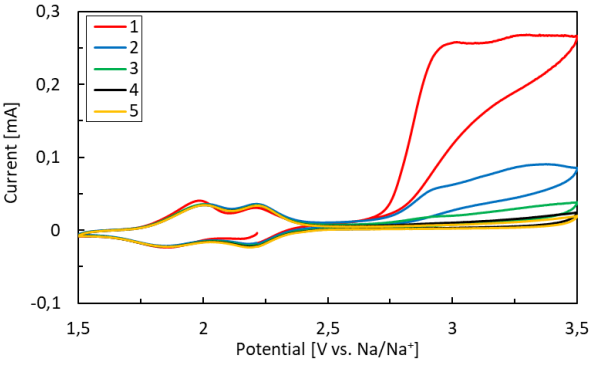

Figure S31: Cyclic voltammetry of PID in a SIB at a scan rate of 0.1 mV s^{-1}.

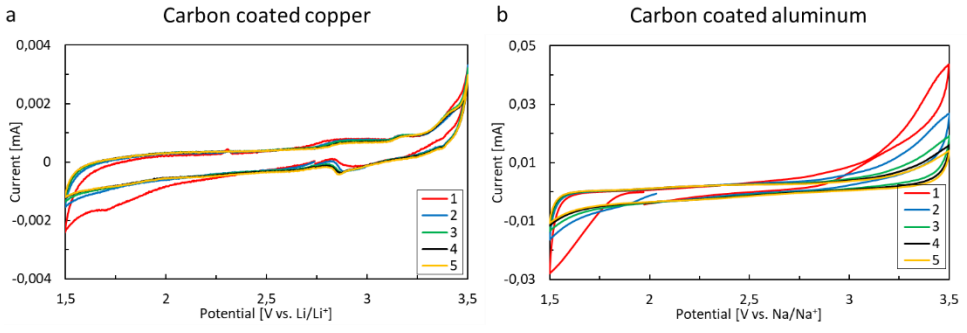

Figure S32: Cyclic voltammetry at a scan rate of 0.1 mV s-1 of **a)** carbon coated copper in a LIB **b)** carbon coated aluminium in SIB.

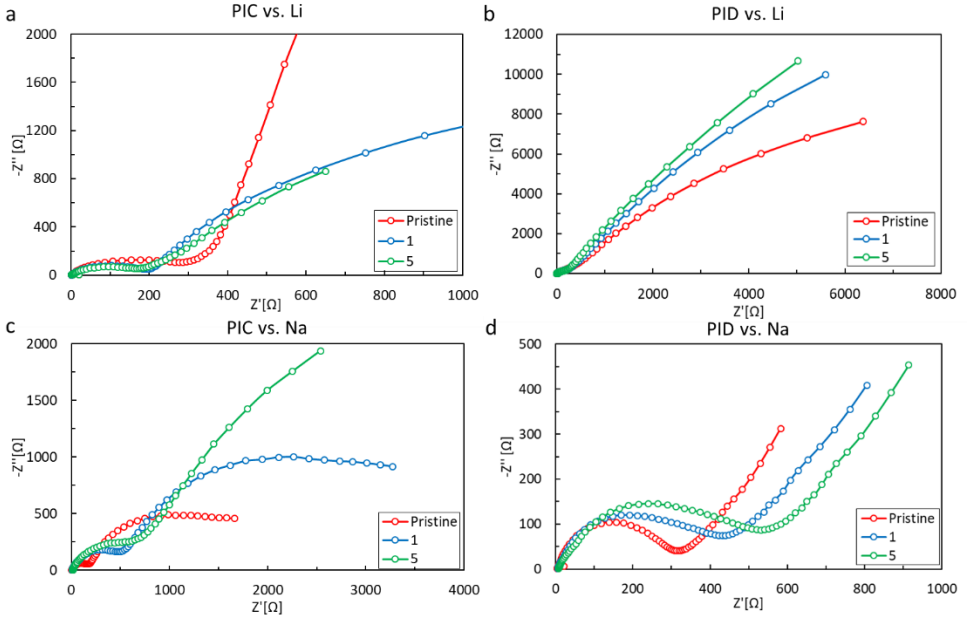

Figure S33: The electrochemical impedance spectra (plotted in Nyquist plots) of the pristine electrode, after its first and fifth CV scan of PIC in a LIB **a)** PID in a LIB **b)** PIC in a SIB **c)** and PID in a SIB **d)**.

PIA and PIB vs Li and Na

The battery tests with PMDA-containing COF materials, PIA and PIB, resulted in unsatisfying performances with specific capacities below 30 mAh g^{-1} and poor capacity retention upon cycling, see Figure S34. It can be clearly seen from the CVs that there is little reduction and oxidation activity after several CV scans. Tian et al. also observed this behaviour for their PMDA-COF (identical to our PIA) in a LIB, despite the larger initial capacity of 62 mAh g^{-1} .[S2] This could be explained by the

lack of stabilization by the single conjugated ring in the centre of the PMDA, where a larger conjugated centre would contribute to more stabilization upon lithiation and sodiation of the reactive carbonyl groups. Wang et al. share a similar explanation, however they achieved better cyclability by synthesizing their PMDA-COF (identical to our PIB) in the presence of CNTs.[S3] The improvement in electrochemical performances cannot be (totally) ascribed to the addition of CNTs because the absence of their COF characterization (isotherms and pore-size distribution) makes it hard to draw concrete conclusions from it. Yang et al. showed that the degree of mesopores can have a significant effect on the performance.[S4]

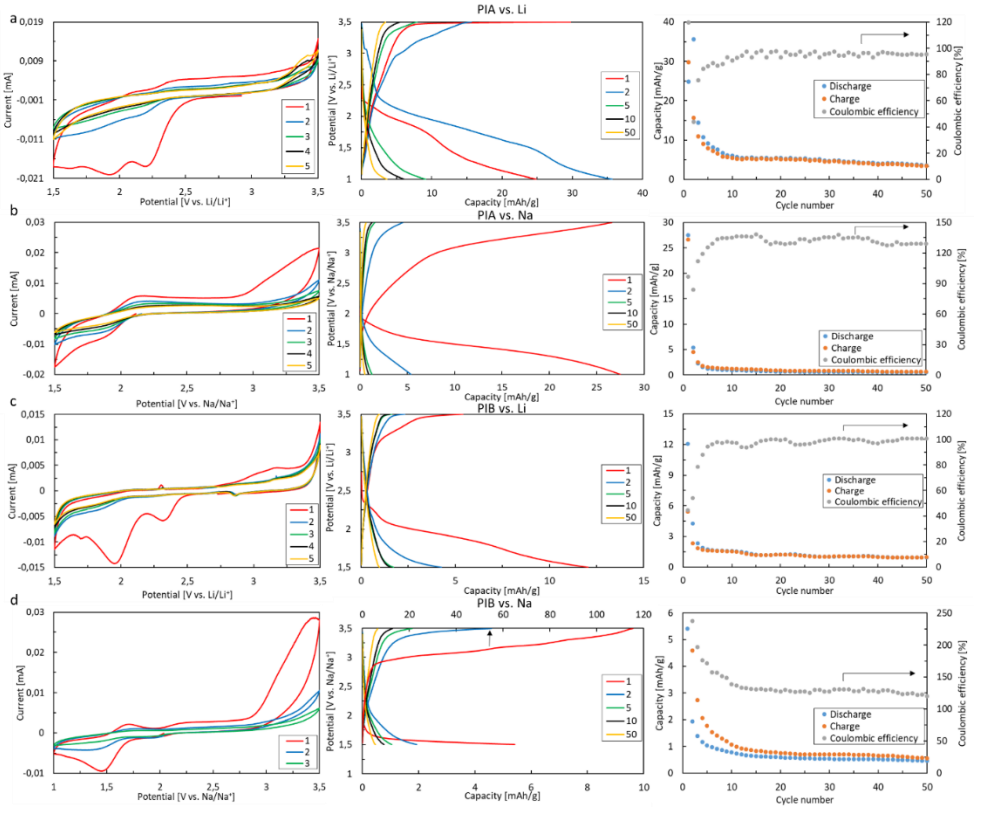

Figure S34: (from left to right) CV curves at a scan rate of 0.1 mV s-1 , discharge-charge profiles, and cycling performance at a rate of 0.1 C (13 mA g-1) for **a)** PIA in LIB **b)** PIA in SIB **c)** PIB in LIB **d)** PIB in SIB.

PIC vs. Li

Figure 35a shows the CV profile of PIC in a LIB for the first initial five scans in the potential range 1.5-3.5 V vs. Li/Li+ . There is only one clear reduction and oxidation

peak visible, which are similar but sharper than those in the CVs of other NTCDA-related (COF-) materials.[S5-S7] The reduction potential peak during the first scan (2.40 V) is different than those of the sequential four scans (2.34 V), whereas the oxidation peak remains constant (2.51 V). This difference in potential could be due to an increased internal resistance originating from the irreversible reduction below 2.15 V, which only occurred during the first scan. The difference between the reduction and oxidation peak (polarization) is smaller (0.17 V) compared to that of other reported NTCDA (-related COFs) (0.2-0.35 V)[S5-S7]. The observed redox peaks are reflected back into relatively flat voltage plateaus in the initial five galvanostatic discharge and charge profiles in Figure 35a. The capacity of the voltage plateau decreases over time from 30 mAh g-1 for the second cycle to 18 mAh g-1 for the 20th cycle. Remarkably, a second reversible plateau forms (during discharge at 1.71 V and during charge at 3.2 V) from the 30th cycle onwards, which keeps growing in capacity until it eventually has merged with the first plateau, resulting in an increasing capacity over time. The origin of this recovering capacity may indicate a structural conversion upon cycling, but the nature of this is unclear at this stage and will be subject of future investigations. The irreversible oxidation peak above 3.2 V is not electrochemical related to PIC but is caused by electrolyte decomposition, as it is similar to that in the CV of an electrode without active material, see Figure S32. Impedance spectra of a pristine PIC-electrode, after the 1st and 5th CV-cycle can be found in Figure S33.

PIC vs. Na

The CV of PIC in the SIB, Figure 35b, also contains one clear reduction and oxidation peak. However, both peaks shift to a more positive potential after the first scan. The reduction peak shifts from 2.07 V vs. Na/Na+ to 2.11 V and the oxidation peak from 2.28 to 2.30 V. A possible explanation is a change in the stacking of the COF-sheets in the perpendicular direction. The DFT calculations in Figure 4 indicate a low energy penalty for changing the stacking. Na-ion induced alteration of the stacking into a more preferred electrochemical active stacking could thus be possible and will result in a more positive redox potential. The polarization is identical to that of the lithium based battery, suggesting that the structure of PIC expands, due to the larger sodium ion, without an additional energy penalty. PIC cycling in a sodium battery, Figure 35b, results in a reasonable initial capacity (58 mAh g-1) which decreases rapidly over time towards 30 mAh g-1 and does not show the capacity recovery as observed for the LIB. The oxidative behaviour above 3 V is again related to the electrolyte decomposition and not by PIC decomposition, see Figure S32. This only occurs substantially during the initial

3 cycles, after which it diminishes, which is the explanation for the difference between the charge and discharge capacities at that stage.

PID vs. Li

Similar to PIC, the CV of PID in a LIB, Figure 35c, displays a single clear reduction and oxidation peak unlike what has been reported previously.[S5,S7,S8] The potential of the reduction peak shifts from 2.28 V vs. Li/Li+ during the first scan to 2.31 V during the sequential scans, whereas the oxidation peak (2.49 V) remains fixed. Although the polarization (0.18 V) is slightly higher than for PIC, it is still lower than reported in literature (0.2-0.35 V) at an identical scan speed (0.1 mV s-1). [S5,S7,S8]. Besides the mentioned peaks, also two small irreversible redox peaks are present during the first scan cycle, during reduction at 1.66 V and during oxidation at 2.81 V. Electrochemical cycling of PID in LIB revealed a single charge and discharge plateau with voltages around 2.42 and 2.33 V. The obtained reversible capacity is still quite low, 40-50 mAh g-1 during the initial twenty cycles. However, the capacity increases during sequential cycles due to the formation of a second discharge plateau (1.75 V) and multiple smaller charge plateaus at 2.89, 3.07 and 3.20 V. Also in this case the origin of the second plateau and the resulting increase in capacity and subsequent battery failure after cycle 37 is unclear at this stage.

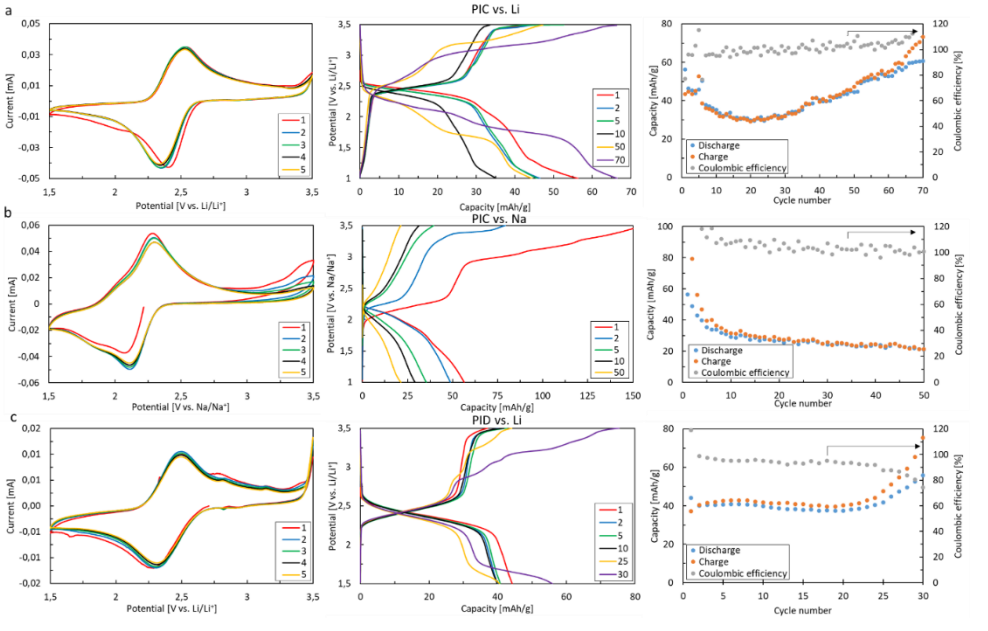

Figure S35:(from left to right) CV curves at a scan rate of 0.1 mV s-1 , discharge-charge profiles, and cycling performance at a rate of 0.1 C (15 mA g-1) for **a)** PIC in LIB **b)** PIC in SIB **c)** PID in LIB.

REFERENCES

(1) Schon, T. B.; McAllister, B. T.; Li, P. F.; Seferos, D. S. The rise of organic electrode materials for energy storage. *Chem. Soc. Rev.* **2016**, *45*, 6405–6406.

(2) Arico, A. S.; Bruce, P.; Scrosati, B.; Tarascon, J. M.; Van Schalkwijk, W. Nanostructured materials for advanced energy conversion and storage devices. *Nat. Mater.* **2005**, *4*, 366–377.

(3) Liang, Y. L.; Tao, Z. L.; Chen, J. Organic electrode materials for rechargeable lithium batteries. *Adv. Energy Mater*. **2012**, *2*, 742–769.

(4) Song, Z. P.; Zhou, H. S. Towards sustainable and versatile energy storage devices: an overview of organic electrode materials. *Energy Environ. Sci.* **2013**, *6*, 2280–2301.

(5) Morita, Y.; Nishida, S.; Murata, T.; Moriguchi, M.; Ueda, A.; Satoh, M.; Arifuku, K.; Sato, K.; Takui, T. Organic tailored batteries materials using stable open-shell molecules with degenerate frontier orbitals. *Nat. Mater.* **2011**, *10*, 947–951.

(6) Wu, H. P.; Shevlin, S. A.; Meng, Q. H.; Guo, W.; Meng, Y. N.; Lu, K.; Wei, Z. X.; Guo, Z. X. Flexible and Binder-Free Organic Cathode for High-Performance Lithium-Ion Batteries. *Adv. Mater*. **2014**, *26*, 3338–3343.

(7) Nishide, H.; Oyaizu, K. Toward flexible batteries. *Science* **2008**, *319*, 737–738.

(8) Williams, D. L.; Byrne, J. J.; Driscoll, J. S. A High Energy Density Lithium/Dichloroisocyanuric Acid Battery System. *J. Electrochem. Soc.* **1969**, *116*, 2–4.

(9) Tarascon, J. M. Key challenges in future Li-battery research. *Philos. Trans. Royal Soc. A* **2010**, *368*, 3227–3241.

(10) Palomares, V.; Casas–Cabanas, M.; Castillo–Martinez, E.; Han, M. H.; Rojo, T. Update on Na-based battery materials. A growing research path. *Energy Environ. Sci*. **2013**, *6*, 2312–2337.

(11) Zhong, L.; Lu, Y.; Li, H. X.; Tao, Z. L.; Chen, J. High-performance aqueous sodium-ion batteries with hydrogel electrolyte and alloxazine/CMK-3 anode. *ACS Sustain. Chem. Eng*. **2018**, *6*, 7761–7768.

(12) Yang, Y.; Wang, C. Y.; Yue, B. B.; Gambhir, S.; Too, C. O.; Wallace, G. G. Electrochemically synthesized polypyrrole/graphene composite film for lithium batteries. *Adv. Energy Mater*. **2012**, *2*, 266–272.

(13) Song, Z. P.; Zhan, H.; Zhou, Y. H. Polyimides: promising energy-storage materials. *Angew. Chem. Int. Edit.* **2010**, *49*, 8444–8448.

(14) Xie, J.; Zhang, Q. C. Recent progress in rechargeable lithium batteries with organic materials as promising electrodes. *J. Mater. Chem. A* **2016**, *4,* 7091–7106.

(15) Xu, Y.; Zhou, M.; Lei, Y. Organic materials for rechargeable sodium-ion batteries. *Mater. Today* **2018**, *21*, 60–78.

(16) Côté, A. P.; Benin, A. I.; Ockwig, N. W.; O'Keeffe, M.; Matzger, A. J.; Yaghi, O. M. Porous, crystalline, covalent organic frameworks. *Science* **2005**, *310*, 1166–1170.

(17) El–Kaderi, H. M.; Hunt, J. R.; Mendoza–Cortés, J. L.; Côté, A. P.; Taylor, R. E.; O'Keeffe, M.; Yaghi, O. M. Designed synthesis of 3D covalent organic frameworks, *Science* **2007**, *316*, 268–272.

(18) Feng, X.; Ding, X. S.; Jiang, D. L. Covalent organic frameworks. *Chem. Soc. Rev*. **2012**, *41*, 6010–6022.

(19) Hunt, J. R.; Doonan, C. J.; LeVangie, J. D.; Côté, A. P.; Yaghi, O. M. Reticular synthesis of covalent organic borosilicate frameworks. *J. Am. Chem. Soc*. **2008**, *130*, 11872–11873.

(20) Tilford, R. W.; Gemmill, W. R.; zur Loye, H. C.; Lavigne, J. J. Facile synthesis of a highly crystalline, covalently linked porous boronate network. *Chem. Mater*. **2006**, *18*, 5296–5301.

(21) Spitler, E. L.; Dichtel W. R. Lewis acid-catalysed formation of two-dimensional phthalocyanine covalent organic frameworks. *Nat. Chem*. **2010**, *2*, 672–677.

(22) Doonan, C. J.; Tranchemontagne, D. J.; Glover, T. G.; Hunt, J. R.; Yaghi, O. M. Exceptional ammonia uptake by a covalent organic framework. *Nat. Chem.* **2010**, *2*, 235–238.

(23) Côté, A. P; El–Kaderi, H. M.; Furukawa, H.; Hunt, J. R.; Yaghi, O. M. Reticular synthesis of microporous and mesoporous 2D covalent organic frameworks. *J. Am. Chem. Soc*. **2007**, *129*, 12914–12915.

(24) Tilford, R. W.; Mugavero, S. J.; Pellechia, P. J.; Lavigne, J. J. Tailoring microporosity in covalent organic frameworks. *Adv. Mater*. **2008**, *20*, 2741–2746.

(25) Nagai, A.; Guo, Z. Q.; Feng, X.; Jin, S. B.; Chen, X.; Ding, X. P.; Jiang, D. L. Pore surface engineering in covalent organic frameworks. *Nat. Commun*. **2011**, *2*, No. 536.

(26) Feng, X. A.; Chen, L.; Dong, Y. P.; Jiang, D. L. Porphyrin-based two-dimensional covalent organic frameworks: synchronized synthetic control of macroscopic structures and pore parameters. *Chem. Commun*. **2011**, *47*, 1979–1981.

(27) Chen, X.; Gao, J.; Jiang, D. L. Designed synthesis of porphyrin-based two-dimensional covalent organic frameworks with highly ordered structures. *Chem. Lett*. **2015**, *44*, 1257–1259.

(28) Bojdys, M. J.; Jeromenok, J.; Thomas, A.; Antonietti, M. Rational extension of the family of layered, covalent, triazine-based frameworks with regular porosity. *Adv. Mater*. **2010**, *22*, 2202–2205.

(29) Spitler, E. L.; Koo, B. T.; Novotney, J. L.; Colson, J. W.; Uribe–Romo, F. J.; Gutierrez, G. D.; Clancy, P.; Dichtel, W. R. A 2D covalent organic framework with 4.7-nm pores and insight into its interlayer stacking. *J. Am. Chem. Soc*. **2011**, *133*, 19416–19421.

(30) Wan, S.; Gandara, F.; Asano, A.; Furukawa, H.; Saeki, A.; Dey, S. K.; Liao, L.; Ambrogio, M. W.; Botros, Y. Y.; Duan, X. F.; Seki, S.; Stoddart, J. F.; Yaghi, O. M. Covalent organic frameworks with high charge carrier mobility. *Chem. Mater*. **2011**, *23*, 4094–4097.

(31) Wan, S.; Guo, J.; Kim, J.; Ihee, H.; Jiang, D. L. A belt-shaped, blue luminescent, and semiconducting covalent organic framework. *Angew. Chem. Int. Edit.* **2008**, *47*, 8826–8830.

(32) Wan, S.; Guo, J.; Kim, J.; Ihee, H.; Jiang, D. L. A photoconductive covalent organic framework: self-condensed arene cubes composed of eclipsed 2D polypyrene sheets for photocurrent generation. *Angew. Chem. Int. Edit.* **2009**, *48*, 5439–5442.

(33) Ding, X. S.; Guo, J.; Feng, X. A.; Honsho, Y.; Guo, J. D.; Seki, S.; Maitarad, P.; Saeki, A.; Nagase, S.; Jiang, D. L. Synthesis of metallophthalocyanine covalent organic frameworks that exhibit high carrier mobility and photoconductivity. *Angew. Chem. Int. Edit*. **2011**, *50*, 1289–1293.

(34) Ding, X. S.; Chen, L.; Honsho, Y.; Feng, X.; Saenpawang, O.; Guo, J. D.; Saeki, A.; Seki, S.; Irle, S.; Nagase, S.; Parasuk, V.; Jiang, D. L. An n-Channel Two-Dimensional Covalent Organic Framework. *J. Am. Chem. Soc*. **2011**, *133*, 14510–14513.

(35) Feng, X.; Liu, L. L.; Honsho, Y.; Saeki, A.; Seki, S.; Irle, S.; Dong, Y. P.; Nagai, A.; Jiang, D. L. High-Rate Charge-Carrier Transport in Porphyrin Covalent Organic Frameworks: Switching from Hole to Electron to Ambipolar Conduction. *Angew. Chem. Int. Edit.* **2012**, *51*, 2618–2622.

(36) Feng, X.; Chen, L.; Honsho, Y.; Saengsawang, O.; Liu, L. L.; Wang, L.; Saeki, A.; Irle, S.; Seki, S.; Dong, Y. P.; Jiang, D. L. *Adv. Mater.* **2012**, *24*, 3026–3031.

(37) Patwardhan, S.; Kocherzhenko, A. A.; Grozema, F. C.; Siebbeles, L. D. A. Delocalization and mobility of charge carriers in covalent organic frameworks. *J. Phys. Chem. C* **2011**, *115*, 11768–11772.

(38) Lanni, L. M.; Tilford, R. W.; Bharathy, M.; Lavigne, J. J. Enhanced hydrolytic stability of self-assembling alkylated two-dimensional covalent organic frameworks. *J. Am. Chem. Soc*. **2011**, *133*, 13975–13983.

(39) Campbell, N. L.; Clowes, R.; Ritchie, L. K.; Cooper, A. I. Rapid microwave synthesis and purification of porous covalent organic frameworks. *Chem. Mater.* **2009**, *21*, 204–206.

(40) Kandambeth, S.; Venkatesh, V.; Shinde, D. B.; Kumari, S.; Halder, A.; Verma, S.; Banerjee, R. Self-templated chemically stable hollow spherical covalent organic framework. *Nat. Commun*. **2015**, *6*, No. 6786.

(41) Lin, L. C.; Choi, J. W.; Grossman, J. C. Two-dimensional covalent triazine framework as an ultrathin-film nanoporous membrane for desalination. *Chem. Commun*. **2015**, *51*, 14921–14924.

(42) Uribe–Romo, F. J.; Doonan, C. J.; Furukawa, H.; Oisaki, K.; Yaghi, O. M. Crystalline covalent organic frameworks with hydrazone linkages. *J. Am. Chem. Soc*. **2011**, *133*, 11478–11481.

(43) Dalapati, S.; Jin, S. B.; Gao, J.; Xu, Y. H.; Nagai, A.; Jiang, D. L. An azine-linked covalent organic framework. *J. Am. Chem. Soc*. **2013**, *135*, 17310–17313.

(44) Nagai, A.; Chen, X.; Feng, X.; Ding, X. S.; Guo, Z. Q.; Jiang, D. L. A Squaraine-Linked Mesoporous Covalent Organic Framework. *Angew. Chem. Int. Edit.* **2013**, *52*, 3770–3774.

(45) Fang, Q. R.; Zhuang, Z. B.; Gu, S.; Kaspar, R. B.; Zheng, J.; Wang, J. H.; Qiu, S. L.; Yan, Y. S. Designed synthesis of large-pore crystalline polyimide covalent organic frameworks. *Nat. Commun*. **2014**, *5*, No. 4503.

(46) Johnston, J. C.; Meador, M. A. B.; Alston, W. B. A mechanistic study of polyimide formation from diester-diacids. *J. Polym. Sci. Pol. Chem.* **1987**, *25*, 2175–2183.

(47) Jiang, L.; Tian, Y.; Sun T.; Zhu Y.; Ren H.; Zou X.; Ma Y.; Meihaus K. R.; Long J. R.; Zhu G. A crystalline polyimide porous organic framework for selective adsorption of acetylene over ethylene. *J. Am. Chem. Soc.* **2018**, *140*, 15724–15730.

(48) Veldhuizen, H.; Vasileiadis, A.; Wagemaker, M.; Mahon, T.; Mainali, D. P.; Zong, L.; Van der Zwaag, S.; Nagai, A. Synthesis, characterization, and CO_2 uptake of mellitic triimide-based covalent organic frameworks. *J. Polym. Sci. Part A: Polym. Chem.* **2019**, *57*, 2373–2377.

(49) Luo, Z. Q.; Liu, L. J.; Ning, J. X.; Lei, K. X.; Lu, Y.; Li, F. J.; Chen, J. A microporous covalent–organic framework with abundant accessible carbonyl groups for lithium-ion batteries. *Angew. Chem. Int. Edit.* **2018**, *57*, 9443–9446.

(50) Yang, H.; Zhang, S. L.; Han, L. H.; Zhang, Z.; Xue, Z.; Gao, J.; Li, Y.; Huang, C. S.; Yi, Y. P.; Liu, H. B.; Li, Y. L. High conductive two-dimensional covalent organic framework for lithium storage with large capacity. *ACS Appl. Mater. Inter.* **2016**, *8*, 5366–5375.

(51) Yang, D. H.; Yao, Z. Q.; Wu, D. H.; Zhang, Y. H.; Zhou, Z.; Bu, X. H. Structure-modulated crystalline covalent organic frameworks as high-rate cathodes for Li-ion batteries. *J. Mater. Chem. A* **2016**, *4*, 18621–18627.

(52) Bai, L. Y.; Gao, Q.; Zhao, Y. L. Two fully conjugated covalent organic frameworks as anode materials for lithium ion batteries. *J. Mater. Chem. A* **2016**, *4*, 14106–14110.

(53) Wang, S.; Wang, Q. Y.; Shao, P. P.; Han, Y. Z.; Gao, X.; Ma, L.; Yuan, S.; Ma, X. J.; Zhou, J. W.; Feng, X.; Wang, B. Exfoliation of covalent organic frameworks into few-layer redox-active nanosheets as cathode materials for lithium-ion batteries. *J. Am. Chem. Soc*. **2017**, *139*, 4258–4261.

(54) Gu, S.; Wu, S. F.; Cao, L. J.; Li, M. C.; Qin, N.; Zhu, J.; Wang, Z. Q.; Li, Y. Z.; Li, Z. Q.; Chen, J J.; Lu, Z. G. Tunable redox chemistry and stability of radical intermediates in 2D covalent organic frameworks for high performance sodium ion batteries. *J. Am. Chem. Soc*. **2019**, *141*, 9623–9628.

(55) Zhang, X. J.; Zhu, G.; Wang, M.; Li, J. B.; Lu, T.; Pan, L. K. Covalent-organic-frameworks derived N-doped porous carbon materials as anode for superior long-life cycling lithium and sodium ion batteries. *Carbon* **2007**, *116*, 686–694.

(56) Patra, B. C.; Das, S. K.; Ghosh, A.; Raj, K. A.; Moitra, P.; Addicoat, M.; Mitra, S.; Bhaumik, A.; Bhattacharya, S.; Pradhan, A. Covalent organic framework based microspheres as an anode material for rechargeable sodium batteries. *J. Mater. Chem. A* **2018**, *6*, 16655–16663.

(57) Zeng, Y.; Zou, R.; Zhao, Y. Covalent Organic Frameworks for CO_2 capture. *Adv. Mater.* **2016**, *28*, 2855–2873.

(58) Dawson, R.; Stöckel, E.; Holst, J. R.; Adams, D. J.; Cooper, A. I. Microporous organic polymers for carbon dioxide capture. *Energy Environ. Sci.* **2011**, *4*, 4239–4245.

(59) Huang, N.; Chen, X.; Krishna, R.; Jiang, D. L. Two–Dimensional Covalent Organic Frameworks for Carbon Dioxide Capture through Channel–Wall Functionalization. *Angew. Chem.* **2015**, *127*, 3029 –3033.

(60) Lee, G.-Y.; Lee, J.; Vo, H. T.; Kim, S.; Lee, H.; Park, T. Amine–Functionalized Covalent Organic Framework for Efficient SO_2 Capture with High Reversibility. *Sci. Rep.* **2017**, *7*, No. 557.

(61) Wu, S.; Gu, S.; Zhang, A.; Yu, G.; Wang, Z.; Jian, J.; Pan, C. A rational construction of microporous imide–bridged covalent–organic polytriazines for high–enthalpy small gas absorption. *J. Mater. Chem. A* **2015**, *3*, 878–885.

(62) Ma, T.; Kapustin, E. A.; Shawn, S. X.; Liang, Y. L.; Zhou, Z.; Niu, J.; Li, L.; Wang, Y.; Su, J.; Li, J.; Wang, X.; Wang, W. D.; Wang, W.; Sun, J.; Yaghi, O. M. Single-crystal x-ray diffraction structures of covalent organic frameworks. *Science*. **2018**, *361*, 48–52.

(63) Klimes, J.; Bowler, D. R.; Michaelides, A. Van der Waals density functionals applied to solids. *Phys. Rev. B* **2011**, *83*, 195131.

(64) Dion, M.; Rydberg, H.; Schroder, E.; Langreth, D. C.; Lundqvist, B. I. Van der Waals density functional for general geometries. *Phys. Rev. Lett*. **2004**, *92*, 246401.

(65) Nazarian, D.; Ganesh, P.; Sholl, D. S. Benchmarking density functional theory predictions of framework structures and properties in a chemically diverse test set of metal–organic frameworks. *J. Mater. Chem. A* **2015**, *3*, 22432–22440.

(66) Deng, W. W.; Shen, Y. F.; Qian, J. F.; Yang, H. X. A polyimide anode with high capacity and superior cyclability for aqueous Na-ion batteries. *Chem. Commun*. **2015**, *51*, 5097–5099.

(67) Han, X. Y.; Chang, C. X.; Yuan, L. J.; Sun, T. L.; Sun, J .T. Aromatic carbonyl derivative polymers as high-performance Li-ion storage materials. *Adv. Mater*. **2007**, *19*, 1616–1621.

(68) Tian, D.; Zhang, H. Z.; Zhang, D. S.; Chang, Z.; Han, J.; Gao, X. P.; Bu, X. H. Li-ion storage and gas adsorption properties of porous polyimides (PIs). *RCS Adv*. **2014**, *4,* 7506–7510.

(69) Banda, H.; Damien, D.; Nagarajan, K.; Hariharan, M.; Shaijumon, M. M. A polyimide based all-organic sodium ion battery. *J. Mater. Chem. A* **2015**, *3*, 10453–10458.

(70) Xu, F.; Jin, S. B.; Zhong, H.; Wu, D.C.; Yang, X. Q.; Chen, X.; Wei, H.; Fu, R.; Jiang, D. L. Electrochemically active, crystalline, mesoporous covalent organic frameworks on carbon nanotubes for synergistic lithium-ion battery energy storage. *Sci. Rep*. **2015**, *5*, No. 8225.

(71) Shi, Y.; Tang, H. M.; Jiang, S. L.; Kayser, L. V.; Li, M. Q.; Liu, F.; Ji, F.; Lipomi, D. J.; Ong, S. P.; Chen, Z. Understanding the electrochemical properties of naphthalene diimide: implication for stable and high-rate lithium-ion battery electrodes. *Chem. Mater.* **2018**, *30*, 3508–3517.

(72) Wang, G.; Chandrasekhar, N.; Biswal, B. P.; Becker, D.; Paasch S.; Brunner, E.; Addicoat, M.; Yu M.; Berger, R.; Feng, X. A crystalline, 2D polyarylimide cathode for ultrastable and ultrafast Li storage. *Adv. Mater.* **2019**, *31*, 1901478.

(73) Kim, D. J.; Hermann, K. R.; Prokofjevs, A.; Otley, M. T.; Pezzato, C.; Owczarek, M.; Stoddart, J. F. Redox-active macrocycles for organic rechargeable batteries. *J. Am. Chem. Soc*. **2017**, *139*, 6635–6643.

(74) Lei, Z. D.; Yang, Q. S.; Xu, Y.; Guo, S. Y.; Sun, W. W.; Liu, H.; Lv, L. P.; Zhang, Y.; Wang, Y. Boosting lithium storage in covalent organic framework via activation of 14-electron redox chemistry. *Nat. Commun*. **2018**, *9*, No. 576.

(75) Zhang, Y.; Gao, Z. Q. High performance anode material for sodium-ion batteries derived from covalent-organic frameworks. *Electrochem. Acta* **2019**, *301*, 23–28.

(76) Posada, J. O. G.; Rennie, A. J. R.; Villar, S. P.; Martins, V. L.; Marinaccio, J.; Barnes, A.; Glover, C. F.; Worsley, D. A.; Hall, P. J. Aqueous batteries as grid scale energy storage solutions. *Renew. Sust. Energ. Rev.* **2017**, *68*, 1174–1182.

(77) Kim, H.; Hong, J.; Park, K. Y.; Kim, H.; Kim, S. W.; Kang, K. Aqueous rechargeable Li and Na ion batteries. *Chem. Rev*. **2014**, *114*, 11788–11827.

(78) Suo, L. M.; Borodin, O.; Wang, Y. S.; Rong, X. H.; Sun, W.; Fan, X. L.; Xu, S. Y.; Schroeder, M. A.; Cresce, A. V.; Wang, F.; Yang, C. Y.; Hu, Y. S.; Xu, K.; Wang, C. S. "Water-in-salt" electrolyte makes aqueous sodium-ion battery safe, green, and long-lasting. *Adv. Energy Mater*. **2017**, *7*, 1701189.

(79) Kuhnel, R. S.; Reber, D.; Battaglia, C. A high-voltage aqueous electrolyte for sodium-ion batteries. *ACS Energy Lett*. **2017**, *2*, 2005–2006.

(80) Luo, J. Y.; Cui, W. J.; He, P.; Xia, Y. Y. Raising the cycling stability of aqueous lithium-ion batteries by eliminating oxygen in the electrolyte. *Nat. Chem.* **2010**, *2*, 760–765.

(81) Wu, X. Y.; Cao, Y. L.; Ai, X. P.; Qian, J. F.; Yang, H. X. A low-cost and environmentally benign aqueous rechargeable sodium-ion battery based on $NaTi_2(PO_4)_3$–$Na_2NiFe(CN)_6$ intercalation chemistry. *Electrochem. Commun*. **2013**, *31*, 145–148.

(82) Kim, M. S.; Lee, W. J.; Paek, S. M.; Park, J. K. Covalent organic nanosheets as effective sodium-ion storage materials. *ACS Appl. Mater. Inter*. **2018**, *10*, 32102–32111.

(83) Wang, Y.; Wang, C. Y.; Wang, Y. J.; Liu, H. K.; Huang, Z. G. Superior sodium-ion storage performance of Co_3O_4@nitrogen-doped carbon: derived from a metal–organic framework. *J. Mater. Chem. A* **2016**, *4*, 5428–5435.

(84) Nie, P.; Shen, L. F.; Pang, G.; Zhu, Y. Y.; Xu, G. Y.; Qing, Y. H.; Dou, H.; Zhang, X. G. Flexible metal–organic frameworks as superior cathodes for rechargeable sodium-ion batteries. *J. Mater. Chem. A* **2015**, *3*, 16590–16597.

(85) Kresse, G.; Furthmuller, J. Efficiency of ab-initio total energy calculations for metals and semiconductors using a plane-wave basis set. *Comp. Mater. Sci*. **1996**, *6*, 15–50.

(86) Perdew, J. P.; Burke, K.; Ernzerhof, M. Generalized gradient approximation made simple. *Phys. Rev. Lett*. **1996**, *77*, 3865–3868.

(87) Lee, B. J.; Shim, J. H.; Baskes, M. I. Semiempirical atomic potentials for the fcc metals Cu, Ag, Au, Ni, Pd, Pt, Al, and Pb based on first and second nearest-neighbor modified embedded atom method. *Phys. Rev. B* **2003**, *68*, 144112.

(88) Blöchl, P. E. Projector augmented-wave method. *Phys. Rev. B* **1994**, *50*, 17953–17979.

[S1] Tevar, A. D.; Whitacre, J. F., Relating Synthesis Conditions and Electrochemical Performance for the Sodium Intercalation Compound Na4Mn9O18 in Aqueous Electrolyte. J. Electrochem. Soc. 2010, 157, (7), A870-A875.

[S2] Tian, D.; Zhang, H. Z.; Zhang, D. S.; Chang, Z.; Han, J.; Gao, X. P.; Bu, X. H. Li-ion storage and gas adsorption properties of porous polyimides (PIs). RCS Adv. 2014, 4, 7506–7510.

[S3] Wang, G.; Chandrasekhar, N.; Biswal, B. P.; Becker, D.; Paasch S.; Brunner, E.; Addicoat, M.; Yu M.; Berger, R.; Feng, X. A crystalline, 2D polyarylimide cathode for ultrastable and ultrafast Li storage. Adv. Mater. 2019, 31, 1901478.

[S4] Yang, J.; Wu, H.; Zhu, M.; Ren, W.; Lin, Y.; Chen, H.; Pan, F. Optimized mesopores enabling enhanced rate performance in novel ultrahigh surface area meso-/microporous carbon for supercapacitors. Nano Energy. 2017, 33, 453–461.

[S5] Song, Z. P.; Zhan, H.; Zhou, Y. H., Polyimides: Promising Energy-Storage Materials. Angew Chem Int Edit 2010, 49, (45), 8444-8448.

[S6] Yang, H.; Zhang, S. L.; Han, L. H.; Zhang, Z.; Xue, Z.; Gao, J.; Li, Y. J.; Huang, C. S.; Yi, Y. P.; Liu, H. B.; Li, Y. L., High Conductive Two-Dimensional Covalent Organic Framework for Lithium Storage with Large Capacity. Acs Appl Mater Inter, 2016, 8, (8), 5366-5375.

[S7] Yang, D. H.; Yao, Z. Q.; Wu, D. H.; Zhang, Y. H.; Zhou, Z.; Bu, X. H., Structure-modulated crystalline covalent organic frameworks as high-rate cathodes for Li-ion batteries. J Mater Chem A 2016, 4, (47), 18621-18627.

[S8] Xu, F.; Jin, S. B.; Zhong, H.; Wu, D. C.; Yang, X. Q.; Chen, X.; Wei, H.; Fu, R. W.; Jiang, D. L., Electrochemically active, crystalline, mesoporous covalent organic frameworks on carbon nanotubes for synergistic lithium-ion battery energy storage. Sci Rep-Uk, 2015, 5.

6

Layer-by-Layer Electrode Fabrication for Improved Performance of Porous Polyimide-Based Supercapacitors

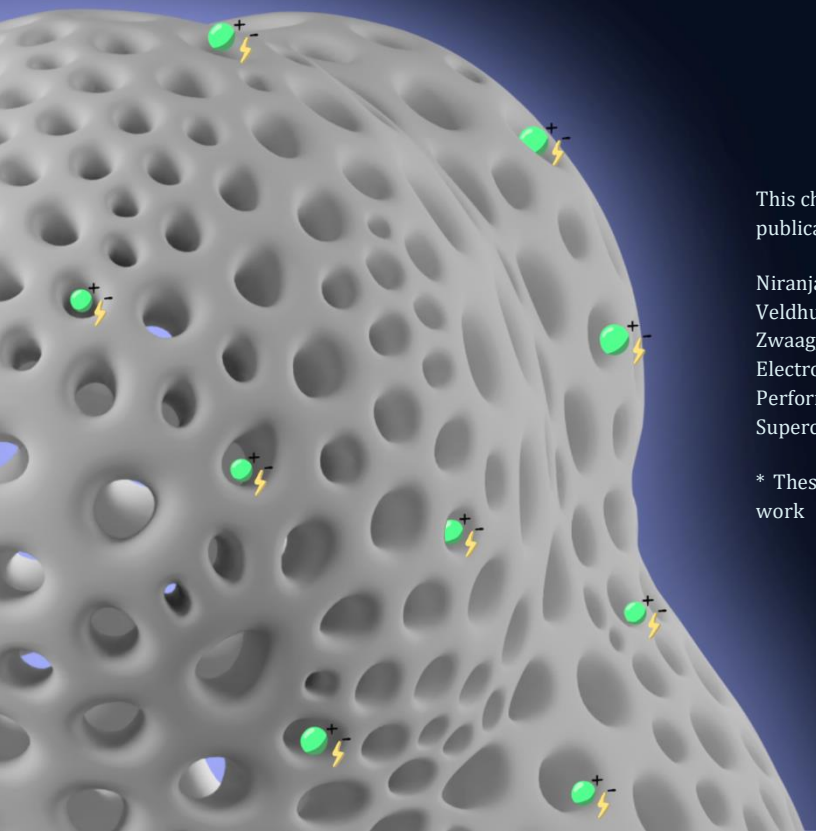

This chapter is based on the following publication:

Niranjala Fernando,* Hugo Veldhuizen,* Atsushi Nagai, Sybrand van der Zwaag, Amor Abdelkader. Layer-by-Layer Electrode Fabrication for Improved Performance of Porous Polyimide-Based Supercapacitors. *Materials* **2022**, *15*, 4.

* These authors contributed equally to this work

Abstract

Nanoporous polymers are becoming increasingly interesting materials for electrochemical applications, as their large surface areas with redox-active sites allow efficient adsorption and diffusion of ions. However, their limited electrical conductivity remains a major obstacle in practical applications. The conventional approach that alleviates this problem is the hybridisation of the polymer with carbon-based additives, but this directly prevents the utilisation of the maximum capacity of the polymers. Here, we report a layer-by-layer fabrication technique where we separated the active (porous polymer, top) layer and the conductive (carbon, bottom) layer and used these "layered" electrodes in a supercapacitor (SC). Through this approach, direct contact with the electrolyte and polymer material is greatly enhanced. With extensive electrochemical characterisation techniques, we show that the layered electrodes allowed a significant contribution of fast faradic surface reactions to the overall capacitance. The electrochemical performance of the layered-electrode SC outperformed other reported porous polymer-based devices with a specific gravimetric capacitance of 388 $F \cdot g^{-1}$ and an energy density of 65 $Wh \cdot kg^{-1}$ at a current density of 0.4 $A \cdot g^{-1}$. The device also showed good cyclability with 90% of capacitance retention after 5000 cycles at 1.6 $A \cdot g^{-1}$, comparable to the reported porous polymer-based SCs. Thus, the introduction of a layered electrode structure would pave the way for more effective utilisation of porous organic polymers in future energy storage/harvesting and sensing devices by exploiting their nanoporous architecture and limiting the negative effects of the carbon/binder matrix.

6.1 INTRODUCTION

The development of low cost, eco-friendly and high-performance energy storage devices is becoming crucial to meeting modern energy storage demand in various applications, including electric vehicles, portable electronics, and power grids. Among them, supercapacitors (SCs) gained significant attention as a promising energy storage device due to their outstanding energy density, power density and long cycle life [1,2]. There are two types of supercapacitor electrodes; one that uses the electric double layer phenomenon and one based on fast faradic surface reactions (pseudocapacitive SCs). High-performance electrode materials should have properties such as an electrical conductivity, a large specific surface area, and good wettability by the electrolyte in both cases. Several materials have been used to fabricate electrodes for supercapacitors, including carbon nanotubes [1,3], graphene [4,5], metal oxides nanoparticles [6–8], transition metal dichalcogenides [9], and carbon-based composites [10,11].

Next to these materials are conductive polymers, which have become increasingly popular alternatives as novel active materials for SCs [12–15]. Polymers as active materials for supercapacitors have several advantages over inorganic active materials, such as high theoretical specific capacitance, low cost and ease of large-scale production [16]. Furthermore, small molecular changes in the originating monomeric building blocks can yield a library of polymers with macroscopically different properties, meaning that polymers are highly tuneable. In the field of SCs, this tunability is reflected in the fact that redox-active segments can be implemented into the polymer-backbone, providing an additional pseudocapacitive energy storage feature. However, conductive polymers still experience limitations, such as poor cycle life and rate kinetics due to repeated swelling and shrinking of the polymer structure during the charge–discharge processes. Additionally, polymer particle aggregation makes it challenging to engineer electrodes that maintain the high theoretical specific capacitance [17].

Alternatively, nanoporous organic polymers emerged as an attractive replacement for linear conductive polymers. Their porous architecture circumvents problems such as low surface areas and aggregation of linear polymers. Thus, nanoporous polymers, in particular, allow the efficient diffusion of ions over an enormous surface area of active material, which significantly improves the capacity [18,19]. However, nanoporous polymers introduce the problem of not providing efficient conductive pathways. To alleviate the poor conductivity of these materials, the concept of hybridising them with conductive

materials (often carbon-based) has been suggested [20–22]. However, the addition of conductive materials, even when it contributes to the capacitance, reduces the specific capacity of the electrodes below the theoretical value of the nanoporous polymers. Moreover, complex techniques are often required to ensure good adhesion between the conductive agent and redox-active polymer, which hinders their practical applications. Therefore, it is desirable to engineer electrodes that can utilise the high surface area of the porous polymers without sacrificing the specific capacitance.

In the study presented here, we utilised a layer-by-layer electrode fabrication approach to produce bilayer conductive carbon/perylene diimide-based porous polymer electrodes as an alternative to the traditional casting of a pre-mixed paste of the active materials, binder and conductive agent (Figure 1). This electrode preparation approach allows us to prepare electrodes with maximum utilisation of the porous polymer as the active supercapacitive material by enhancing the exposure of active materials to the electrolyte, as has also been exploited by other research groups in the field of 1D polymers [23]. The formation of a layer-by-layer assembly can be explained through intermolecular interactions and is dependent on the chemical nature of the separate layers.

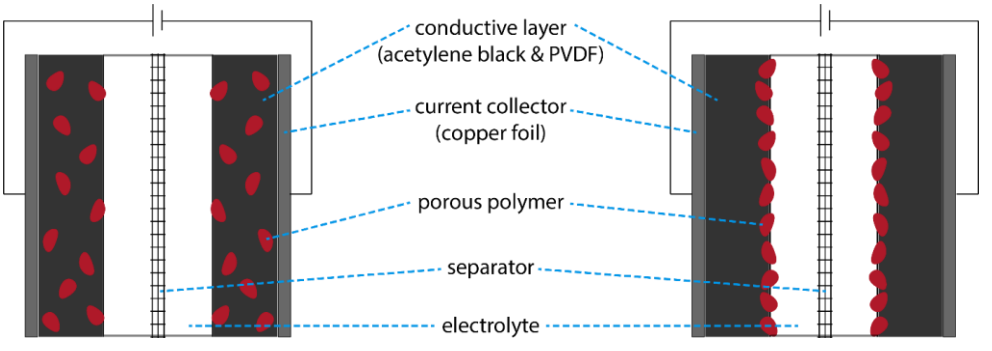

Figure 1. Schematic representation of SCs comprised of two identical electrodes prepared via the conventional mixing method (**left**) or the layer-by-layer method (**right**).

Polyimide porous polymers have been extensively used in gas storage and separation applications [24–27], but the investigation of their potential in the field of energy storage has been limited due to their poor conductivity [28–31]. However, the redox-active segments within their polymer backbone make them interesting to study, especially regarding energy storage applications. One-dimensional perylene diimide-based materials have been widely exploited in the field of photovoltaics and batteries. Often, high electron mobilities in such materials are observed as an effect of their favourable molecular π–π interactions

[32]. In addition, these aromatic polyimides are redox-active and their carbonyl groups can participate in reversible lithium complexation [33]. The combination of both of these properties, integrated within a porous framework, formed the idea that a porous perylene diimide-based polymer may exhibit good electrochemical performance in the application presented here.

6.2 EXPERIMENTAL

6.2.1 MATERIALS

All chemicals were commercially available and used without further treatment. Chemicals including; 3,4,9,10-perylenetetracarboxylic dianhydride (PTCDA); 1,3,5-tris(4-aminophenyl)benzene (≥93%, TAPB); isoquinoline; imidazole; *meta*-cresol and dimethyl carbonate were all purchased from TCI Europe N.V., Zwijndrecht, Belgium. In addition, 1-methyl-2-pyrrolidinone (NMP), poly(vinylidene fluoride) (PVDF) and 1.0 M LiPF6 in ethylene carbonate/ethyl methyl carbonate = 1/1 (*v*/*v*), battery grade were purchased from Sigma Aldrich, Gillingham, UK.

6.2.2 SYNTHESIS OF *PER-TAPB-PPI*

Scheme 1 shows the chemical structures of TAPB (204 mg, 0.58 mmol) and PTCDA (345 mg, 0.88 mmol), which were weighed and transferred to a 25 mL ampoule. An amount of 10 mL of a 1:1 (*v*/*v*) mixture of *meta*-cresol and imidazole was added to the ampoule, and the mixture was sonicated for five minutes. Then, 0.1 mL of isoquinoline was added, after which the ampoule was degassed via three freeze–pump–thaw cycles. Finally, the ampoule was flame-sealed, allowed to reach room temperature, and placed in an oven at 200 °C for 5 days. After polymerisation, the precipitate was washed with methanol (2 × 30 mL) and acetone (2 × 30 mL). The solid was dried in a vacuum oven (60 °C) and subsequently washed in a Soxhlet extractor using THF for 16 h. The resulting polymer, **Per-TAPB-PPI**, was finally dried overnight in a vacuum oven at 60 °C and obtained as a dark red powder with a yield of 91 %.

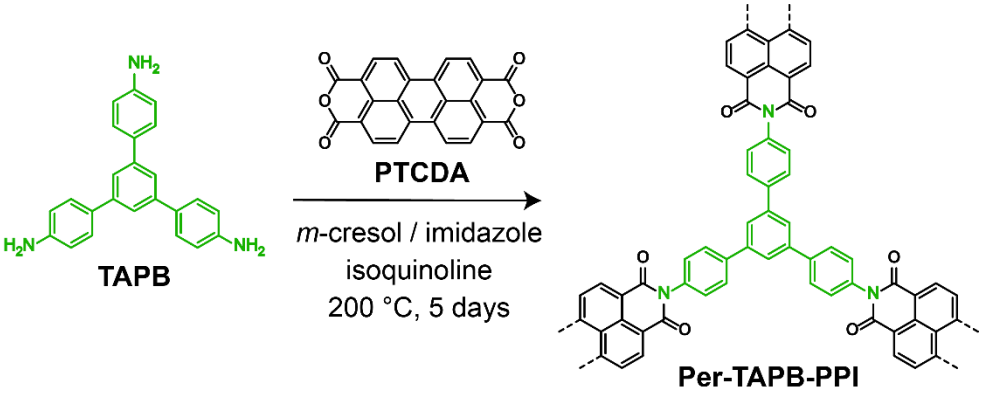

Scheme 1. Formation of porous perylene diimide-based polyimide (**Per-TAPB-PPI**) through a polycondensation of dianhydride PTCDA with triamine TAPB.

6.2.3 Molecular and Microstructural Characterisation

FT-IR spectra were recorded on a PerkinElmer Spectrum 100 FT-IR Spectrometer (Perkin Elmer, Bruxelles, Belgium) with the Universal ATR Accessory over a range of 4000 to 650 cm^{-1}. TGA analyses were performed from room temperature to 860 °C, under nitrogen atmosphere at a heating rate of 10 °C/min using a Perkin Elmer TGA 4000 (Perkin Elmer, Bruxelles, Belgium). Before the measurement, the samples were dried at 130 °C for one hour under a nitrogen atmosphere. The nitrogen sorption isotherms (at 77 K) were measured on a Tristar II 3020 Micromeritics instrument (Micromeritics B.V., Eindhoven, The Netherlands). The porous polymer was degassed before the measurement at 130 °C under vacuum for 16 h. Quenched-Solid Density Functional Theory (QSDFT) simulations based on the experimental nitrogen adsorption isotherms were performed to calculate the pore size distributions. The chosen model was the carbon, adsorption kernel, slit/cylindrical/spherical pore model, a standardised model in the VersaWin Gas Sorption Data Reduction Software (Quantachrome Instruments, Boynton Beach, FL, USA). Scanning electron microscopy (SEM) images were recorded with a JEOL JSM-840 SEM (JEOL Europe B.V., Nieuw-Vennep, The Netherlands): materials were deposited onto a sticky carbon surface on a flat sample holder, vacuum-degassed, and subjected to gold sputtering. PXRD data were collected on a Rigaku MiniFlex 600 powder diffractometer (Rigaku Innovative Technologies, Inc., Auburn Hills, MI, USA) using a Cu-Kα source (λ = 1.5418 Å) over the 2θ range of 5° to 40° with a scan rate of 1°/minute. Contact angle measurements were performed on a Kruss Contact Angle Measuring System G2 (Krüss GmbH, Hamburg, Germany). The solid

surfaces used for these measurements were dry-pressed Per-TAPB-PPI pellets (at 300 MPa for 10 s), and either water or dimethyl carbonate were used as liquids.

6.2.4 ELECTROCHEMICAL STUDY

6.2.4.1 Electrodes Prepared by the Traditional Mixing Method

The active material (**Per-TAPB-PPI**, 0.5 mg), acetylene black (2 mg) and PVDF binder were ground together using a small amount of NMP, and the resulting paste was loaded on a copper foil sheet using a doctor blade technique. PVDF act as an effective dispersion agent to connect the electrode species together, ensure the adhesion of materials to the current collectors and provide mechanical integrity for the electrode. The electrodes were dried under vacuum at 50 °C for around 24 h and pressed using a mechanical press with a pressure of 75 bar (Metaserv Automatic mounting press, Model C190, Surrey, England).

6.2.4.2 Electrodes Prepared by the Layer-by-Layer Method

Acetylene black (2 mg) and PVDF binder (0.1 mg) were ground using a small amount of NMP, and the resulting paste was loaded on a copper foil sheet using a doctor blade technique. Afterwards, the coated sheets were dried in a vacuum oven at 50 °C for 2 h to evaporate the excess NMP solvent. The active material (**Per-TAPB-PPI**) and PVDF binder (1%) were sonicated with NMP to form a homogenous slurry and dropwise added to the acetylene black/PVDF layer. The active material loading was ~0.28 mg·cm^{-2}. The electrodes were dried under vacuum at 50 °C for around 24 h and pressed using a mechanical press (pressure, 75 bar).

6.2.4.3 SC Fabrication

The symmetrical supercapacitors (SCs) were fabricated by sandwiching two identical working electrodes in a 2032 stainless steel coin cell in both scenarios. The electrolyte was 1 M LiPF6 in ethylene carbonate/ethyl methyl carbonate (EC/EMC) mixture (1:1, *v*/*v*) and a glass microfiber filter paper (GF/B, pore size: 1.0 µm) applied as the separator (see Figure 1). All the coin cells were assembled in a dry glove box filled with argon. The supercapacitor performances of as-built coin cells were evaluated on an Iviumstat Electrochemical Interface. Cyclic voltammetry (CV) and galvanostatic charge–discharge (GCD) assessments were applied within the potential range of 0.02–2.22 V and 0.2–1.8 V for the layered SC and traditional mixing SC, respectively. The electrochemical impedance spectroscopy (EIS) analysis was carried out by employing an amplitude of 5 mV

over the frequency range from 0.1 Hz to 400 kHz. The cycling stability of the SCs were evaluated over 5000 cycles.

6.3 Results and Discussion

6.3.1 Porous Polymer Characterisation

Imide-bond formation after the polymerisation was confirmed with FT-IR spectroscopy. The characteristic vibrations of the amine-containing monomer TAPB and the anhydride containing monomer PTCDA were not observed in the resulting polymer, while characteristic imide-bond vibrations appeared (see Figure S1, Supporting Information for detailed information). In addition, **Per-TAPB-PPI** showed excellent stability when exposed to heat, measured by TGA (Figure S2). A temperature of 546 °C was observed at 5% weight loss for Per-TAPB-PPI, which is on par with the current state-of-the-art porous polyimides [24,34], and it emphasises the advantage of using imide-linkages in porous polymers. Finally, while the specific use of the monomer TAPB was mainly to promote porous framework formation, it may have added benefits to the final material in terms of optoelectronic and mechanical properties [35].

Nitrogen sorption experiments were conducted to assess the porosity of the synthesised polymer (Figure 2a). The adsorption isotherm showed a steep increase in N_2 uptake at the low relative pressure region (<0.05 P/P_0), indicating the presence of micropores. Additionally, **Per-TAPB-PPI** exhibited a further (>0.05 P/P_0) slight increase in N_2 uptake, which indicates the presence of larger (meso)pores. Pore size distribution (PSD) was calculated by fitting the nitrogen adsorption isotherm to a DFT model (Figure 2b). Specifically, the quenched solid DFT (QSDFT) carbon model was chosen for the PSD calculations since it takes surface roughness into account [36]. Considering that this polymer is largely amorphous (discussed later), the pore geometries are expected to vary, meaning that slit-like, cylindrical, and spherical pores all were considered in the model. Next to the significant presence of micropores within the PSD of **Per-TAPB-PPI**, a distribution around the maximum population corresponding to a pore size of 2.5 nm was observed. It should be noted that such PSDs are still estimates based on models that are initially developed for carbon materials. The calculated surface area according to the Brunauer–Emmett–Teller (BET) theory for **Per-TAPB-PPI** was 411 $m^2 \cdot g^{-1}$ (Figure S3).

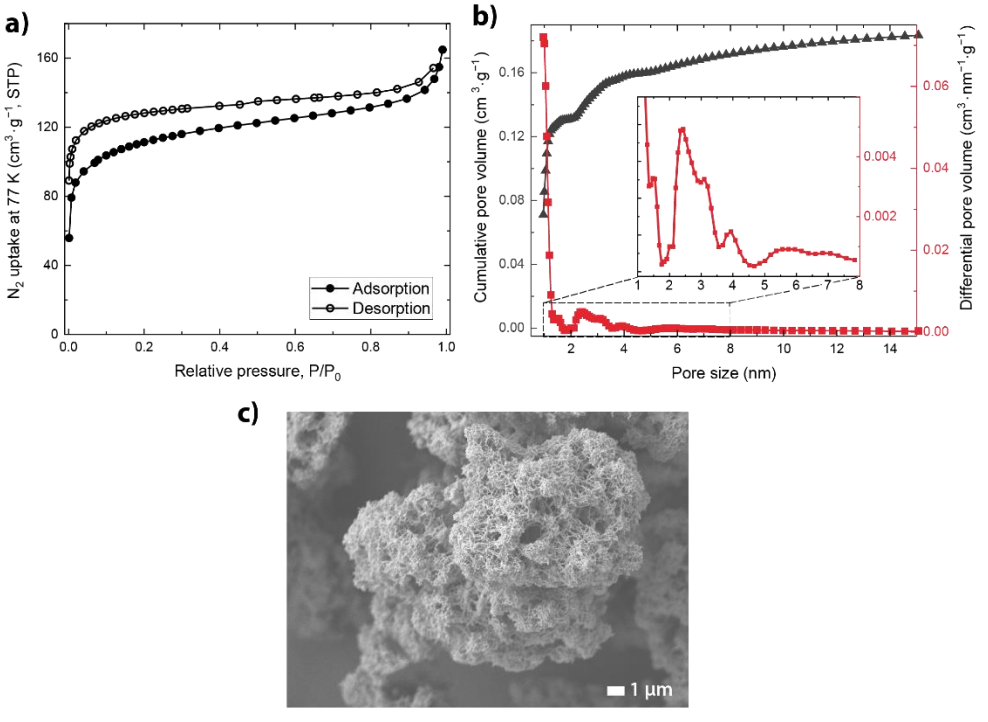

Figure 2. (**a**) Nitrogen adsorption and desorption isotherm of **Per-TAPB-PPI**. (**b**) Pore size distribution (i.e., pore size versus either cumulative pore volume (grey) or differential pore volume (red), including inset with zoom-in) of **Per-TAPB-PPI** calculated by a QSDFT model with the nitrogen adsorption isotherm input data. (**c**) SEM micrograph of **Per-TAPB-PPI**.

While the above results approximate a quantitative description of the nanoporous polymer, we conducted scanning electron microscopy (SEM) measurements to obtain a better qualitative picture of the microscopic porous morphology (Figure 2c). **Per-TAPB-PPI** exhibits large porous aggregate structures originating from interconnected plate-like and spindle-like substructures. In addition to the micro- and mesoporous structures discovered by nitrogen sorption studies described earlier, these SEM images also reveal the presence of larger macropores. This hierarchical porous structure (micro-, meso- and macroporosity) promises effective utilisation of the polymer's redox-active sites. The architecture of the polymer was further investigated by the use of powder X-ray diffraction (PXRD, Figure S4). The polymer exhibits a largely amorphous nature with no distinct crystalline domains, while increased diffuse intensity in the lower-angle regions of the PXRD pattern may indicate a short-ranged order of distances similar to the mesopore sizes observed in Figure 2b. Furthermore, the broad signal of **Per-TAPB-PPI** around 24° (corresponding to a distance of 3.7 Å) resembles the interlayer stacking signal often seen in covalent organic frameworks [37], which

may indicate a sheet-like character. Although **Per-TAPB-PPI** does not show long-range crystalline order, we do expect that, based on these results and similar patterns observed in the literature, the polymer structure exhibits local stacked regions of neighbouring planes. The porous polymer architecture may influence the wettability of the material, which was investigated next.

The electrolyte wettability of the **Per-TAPB-PPI** electrode is important for the electrochemical reactions at the electrolyte–electrode interface. We measured this property by performing swelling experiments through a contact angle measurement setup. Dry-pressed polymer pellets were used as solid surfaces. Unfortunately, a rough final surface is inherently linked to this sample preparation, which makes it difficult to obtain a defined contact angle from these measurements. However, the qualitative results that were obtained when comparing water or dimethyl carbonate on a **Per-TAPB-PPI** surface (Figure S5) exemplified the advantage of using carbonate esters as the electrolyte in the case of electrochemical applications. The referred figure shows the remarkable swelling behaviour of **Per-TAPB-PPI** when exposed to a droplet of dimethyl carbonate. On the other hand, water does not interact with the polymer in such a way and merely wets the polymer as a result of surface roughness. The hydrophobicity (extended aromatic structures) of the material is expected to be the main reason for this, which is strengthened by other research on vapour adsorption experiments of porous polyimides that show poor water uptake (compared to organic solvents such as benzene and hexane, with benzene / H_2O selectivity values of 13–28 reported by Li and Wang) [38,39]. Thus, these experiments not only illustrate a good wetting of the polymers with the organic electrolyte but even a pore-opening behaviour and consequently increased access to the polymer's active sites.

6.3.2 Supercapacitor Performance

The extensively characterised porous polymer **Per-TAPB-PPI** of the previous section has been implemented into two differently prepared electrodes in SCs: via a traditional mixing method and also via the layer-by-layer method. As indicated in the introduction, we expected significant compositional and morphological differences at the electrode's surface that is exposed to the electrolyte. In order to confirm this, SEM micrographs were taken of the surfaces of the two different electrodes (Figure S6a,b). The conventional electrode surface was comparatively smooth and displayed a slightly porous structure that originates from the conductive carbon network. In contrast, the layered electrode revealed the

presence of embedded aggregated porous polymer particles over the surface. To verify that this assumption, energy dispersive X-ray spectroscopy (EDX) was used to assess both different electrode surfaces (Figure S6c,d). The layer-by-layer-prepared electrodes contained a significantly higher amount of oxygen atoms at the surface, originating from the carbonyl groups of **Per-TAPB-PPI**. The larger availability of these redox-active carbonyl-groups is expected to improve the electrochemical performance of the layer-by-layer-prepared SCs when compared to the SC comprised of traditionally prepared electrodes.

The electrochemical performances of the SCs were studied using LiPF6 salt dissolved in a mixture of EC/EMC solvents as the electrolyte. Figure 3a,b show the CV curves for the **Per-TAPB-PPI**-based SCs prepared by the traditional mixing method and the layer-by-layer method, respectively, both at scan rates ranging from 10 to 200 $mV \cdot s^{-1}$. The CV curves of the SC fabricated from the traditional method show an electrical double layer capacitance (EDLC) with a minute pseudocapacitive contribution, which is apparent from the absence of clear redox peaks. In contrast, the layer-by-layer prepared **Per-TAPB-PPI** SC (Figure 3b) delivered EDLC, as well as a clear pseudocapacitance along with distinctive reversible redox humps at ~0.95 V for cathodic and ~1.20 and ~1.60 V for anodic peaks. First, the EDLC of both SCs can be attributed to the large surface area and nanoporous architecture of **Per-TAPB-PPI**, allowing the diffusion and adsorption of a high number of Li^+ ions. In addition, the contribution of acetylene black could be recognised in both scenarios in terms of EDLC, with a more prominent involvement expected in the traditional SC. Additionally, the presence of a sizeable π-conjugated system could further facilitate the electrical conductivity and hence increase the Li^+ ion adsorption to the active material [40,41]. Secondly, the pronounced pseudocapacitive contribution in the layered SC CVs indicates surface faradic redox reactions of Li^+ ions with carbonyl functionalities of the perylene diimide-based polymers (Scheme 2). This also explains the overall higher current compared to the traditional **Per-TAPB-PPI** SC. Furthermore, the minor faradic contribution in the conventional SC is likely caused by the hindrance of the acetylene black/PVDF matrix, limiting the availability of the active sites of the **Per-TAPB-PPI** polymer.

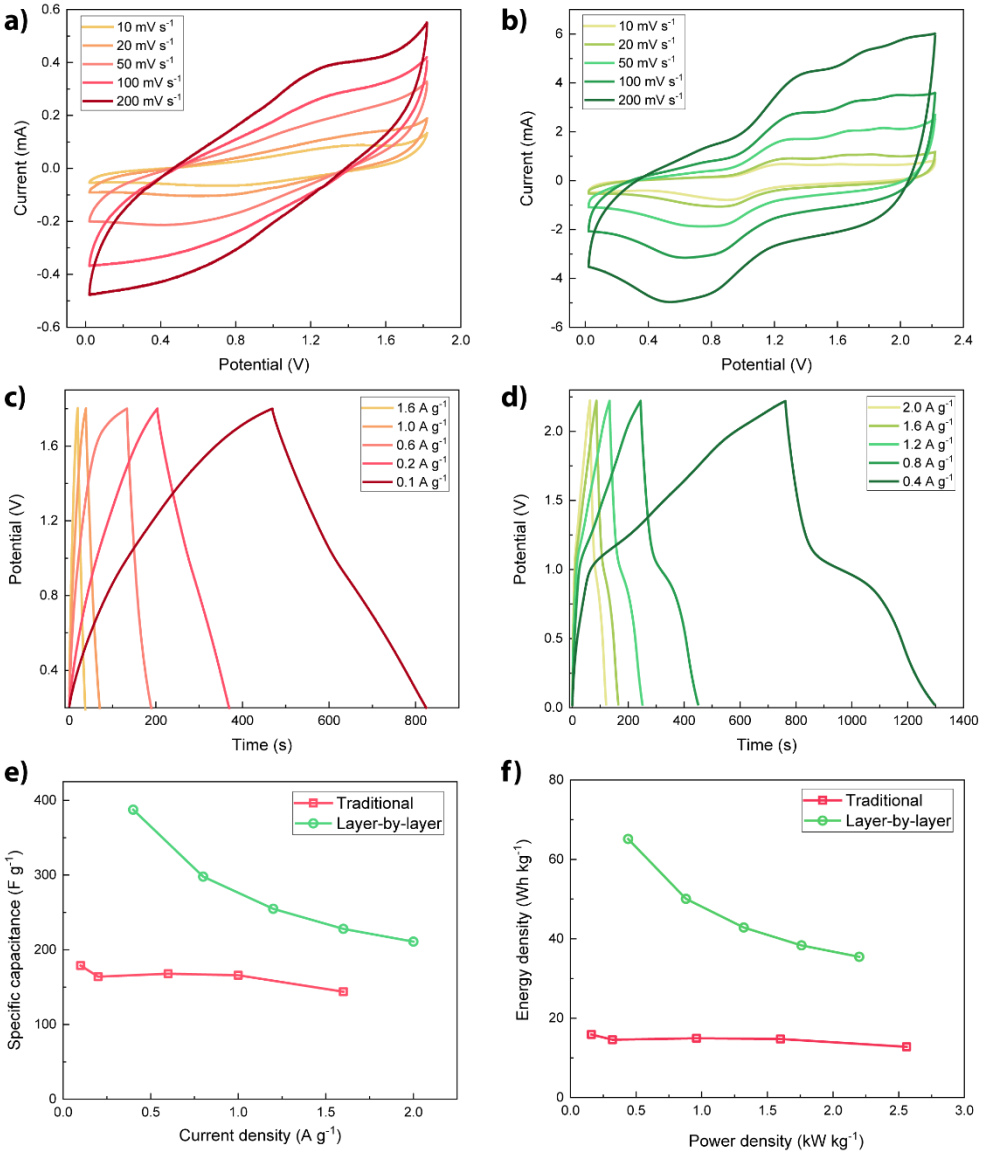

Figure 3. Cyclic voltammograms (scan rates 10 to 200 mV s^{-1}) of SCs composed of **Per-TAPB-PPI**-based electrodes prepared via (**a**) a traditional mixing method or (**b**) a layer-by-layer method. Galvanostatic charge–discharge profiles at different current densities of **Per-TAPB-PPI**-based electrodes prepared via (**c**) a traditional mixing method or (**d**) a layer-by-layer method. (**e**) Corresponding specific capacitance at different current densities. (**f**) Energy and power densities of SC devices.

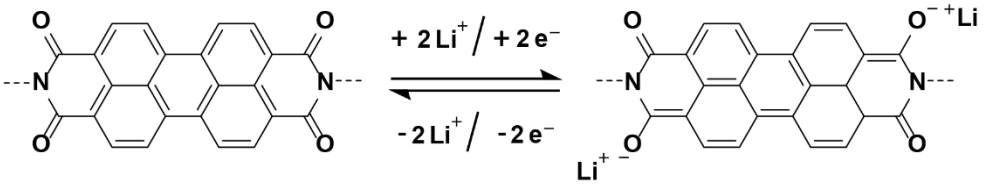

Scheme 2. Faradic reaction mechanism of perylene diimide-based porous polymers with Li-ions.

To further investigate the electrochemical performance of the **Per-TAPB-PPI** SCs, GCD measurements were carried out at various current densities (Figure 3c,d). For the traditional SC, a nearly perfect triangular-shaped profile was observed. Such a curved shape indicates a pure EDLC character, which reinforces the CV results. On the other hand, the GCD curves of the layered electrode displayed prominent nonlinear characteristics, confirming the pseudocapacitive contribution. Moreover, the layer-by-layer prepared SC exhibited longer discharge times at comparatively higher current densities than those of the traditional SC. Additionally, the layered SC's discharge curves show a rapid voltage decay at the early stage due to non-faradic electrostatic discharge (i.e., adsorption and diffusion processes) and a final slow potential drop due to the faradic discharge [42,43]. From these GCD plots, the specific capacitance C_s of both SCs was estimated using Equation (1) [1].

$$Cs = 4\frac{I}{m(dV/dt)} \qquad (1)$$

where I (A) is the constant discharge current, t (s) is the discharge time, V (V) is the potential window, and m (g) is the active material mass in both electrodes. Furthermore, the energy (E) and the power (P) densities for the SC cells were estimated using $E = 0.125\ C_s\ (\Delta V)^2/3.6$ and $P = 3600\ E/\Delta t$, respectively [44,45].

As presented in Figure 3e, the highest specific capacitance C_s of the traditional **Per-TAPB-PPI**-based SC was 178 $F \cdot g^{-1}$ at a current density of 0.1 $A \cdot g^{-1}$ while the layered SC exhibited an outstanding capacitance of 388 $F\ g^{-1}$ at a specific current density of 0.4 $A \cdot g^{-1}$. The resulting higher C_s of the layered SC follows directly from the observations in the CV and GCD plots, with the most prominent reason being the additional pseudocapacitive behaviour that this SC shows. The significant differences in C_s values between the differently prepared electrodes exemplify the electrode fabrication method greatly influences its electrochemical performance. In our case, **Per-TAPB-PPI** benefits from being in direct contact with the electrolyte (rather than being obstructed in the acetylene black/PVDF matrix), since the fast faradic surface reactions are then better exploited. Moreover, the

energy (E) and power (P) densities for the SC devices were evaluated and plotted in Figure 3f. As presented, the layer-by-layer prepared **Per-TAPB-PPI** SC device exhibited an excellent maximum energy density of 65 $Wh \cdot kg^{-1}$ at 0.4 $A \cdot g^{-1}$ and a high power density of 2.2 $kW \cdot kg^{-1}$ at 1.6 $A \cdot g^{-1}$. Similarly, the maximum energy density for the traditionally prepared **Per-TAPB-PPI**- SC device was only 16 $Wh \cdot kg^{-1}$ at a current density of 0.1 $A \cdot g^{-1}$ along with a power density of 2.6 $kW \cdot kg^{-1}$ at 1.6 $A \cdot g^{-1}$. According to the results, we demonstrated a substantial energy density improvement in the layer-by-layer prepared **Per-TAPB-PPI** SC device, confirming the enhanced electrochemical performance.

The cyclability test of the electrode prepared by the traditional and by the layer-by-layer methods are illustrated in Figure 4. Mass loadings of the electrodes were optimised for a balanced capacitance and cycle stability. During the cyclic test, the layered SC was first run at a current density of 0.8 $A \cdot g^{-1}$ over 5 cycles to activate the SC and a remarkable 90.6 % capacitance retention was observed after 5000 cycles at a current density of 1.6 $A \cdot g^{-1}$. Similarly, the traditional SC was activated at 0.4 $A \cdot g^{-1}$ over 5 cycles, and the 93.9 % capacitance retention was obtained after 5000 cycles at a current density of 0.8 $A \cdot g^{-1}$. The layered SC demonstrates the excellent electrochemical performance during cycling at a higher current density compared to the traditional electrode, which displays fast electrochemical kinetics that arise from the direct contact between the electrolyte and the porous polymer layer. The calculated cyclability of **Per-TAPB-PPI** are comparable with other COF-based electrodes prepared without any hybridisation with carbon materials as illustrated in Table S1 (supporting information), indicating the feasibility of our new materials and electrode fabrication method on improving the capacitance without sacrificing the cyclability of the electrode. A detailed post-mortem analysis of the electrode surface after cycling experiments, as has been studied by the group of Yoo [46], is able to provide additional insights in the effect of induced stress and strain to porous polymer materials. Our group is currently investigating this and aims to report this in future work.

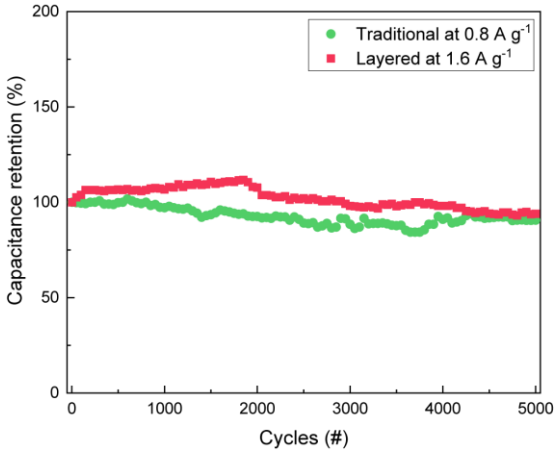

Figure 4. Cyclic stability of layered and traditional **Per-TAPB-PPI** supercapacitors.

A final characterisation method we used to elucidate the electrochemical performance of the differently prepared electrodes was electrochemical impedance spectroscopy (EIS), since it provides information on the equilibrated states of the SCs. The experiments were performed over a frequency range of 0.01–400 kHz, and the resulting impedance plots (Nyquist plots) are presented in Figure 5a,b. Overall, the near-vertical lines for the lower frequency range (Figure 5a) of both SCs indicate capacitive behaviour and efficient ion diffusion between the electrolyte and the electrode surface [47–51]. Furthermore, the higher frequencies in the Nyquist plots (Figure 5b) provide information about the serial (R_S) and charge transfer (R_{CT}) resistances in the electrodes. Here, the intersect with the Z' axis gives R_S, which originates from the internal resistance of the electrode materials. Both electrodes show relatively low internal resistances: 4.6 Ω for the layered and 6.2 Ω for the traditional electrode. These results suggest the presence of efficient conductive pathways between the polymer (π electrons) and conductive carbon. In addition, a slightly higher R_{CT} was observed for the layered electrode (3.0 Ω) compared to that of the traditional electrode (0.6 Ω). The lower charge transfer resistance in the traditional electrode is likely an effect of the large contribution by the highly conductive carbon matrix. Furthermore, the R_{CT} of both the layered and traditional **Per-TAPB-PPI** SCs were significantly lower than that of previously reported organic polymer electrodes including a hydroquinone-based COF TpPa-(OH) (37.5 Ω) [52], and a benzimidazole-based COF TpDAB (24.8 Ω) [53]. This contrast is likely an effect of molecular structure, rather than polymer architecture or device preparation procedure, since perylene diimide derivatives are among the most common acceptor units because of their high electron affinity and electron mobility. Finally, additional experiments on a range of related

polymers with perylene diimide units are required to link the promising performance of this polymer to its structure.

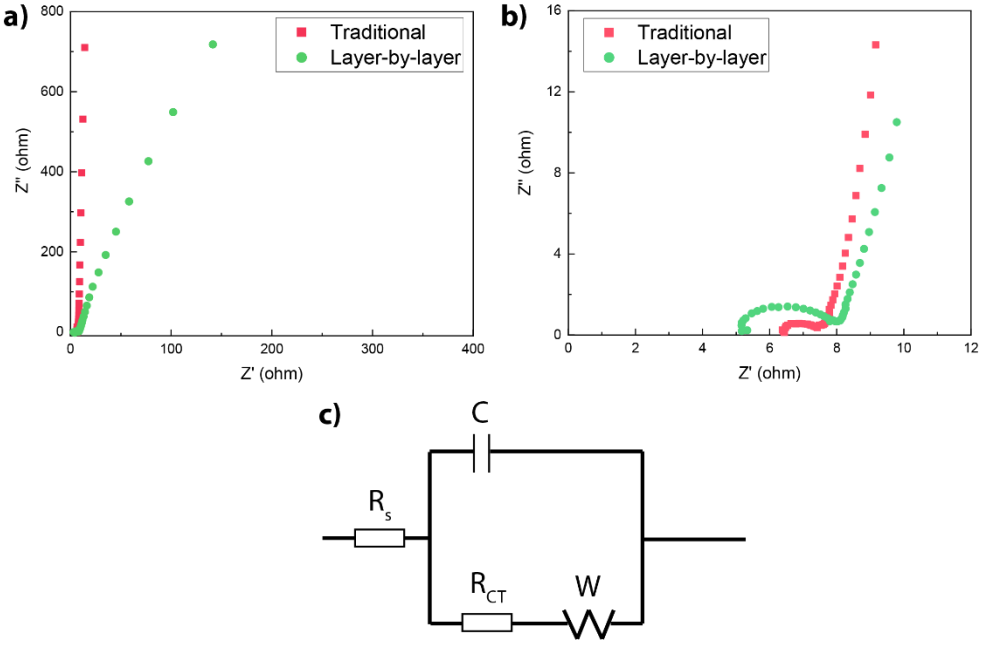

Figure 5. Electrochemical impedance spectra of SCs composed of **Per-TAPB-PPI**-based electrodes prepared via a conventional mixing or a layer-by-layer method. (**a**) Focused on the lower frequency measurements. (**b**) Focused on higher frequency measurements. (**c**) The equivalent circuit modelling of the EIS spectra.

6.4 CONCLUSIONS

In this research, we investigated the effects of a novel layer-by-layer electrode preparation method on the performance of a porous polymer-based supercapacitor. By physically separating the redox-active porous polymer layer and the electron-conducting carbon layer, we created better accessible pathways for ions to diffuse towards the electrodes. As a result, faradic surface reactions were contributing significantly to the overall supercapacitor performance. In addition, by exposing the polymer directly to the electrolyte, the advantages of a porous polyimide polymer (i.e., nanoporosity and redox-activity) were much more exploited. In planned future research, we aim to use a variety of porous polymers in layer-by-layer prepared electrodes to elucidate the correlation between polymer architecture and electrochemical performance. We expect that this electrode preparation method allows the observation of more apparent effects

originating from the polymer itself, which bridges the gap between molecular structure and electrochemical performance.

6.5 SUPPORTING INFORMATION

Imide-bond formation after the polymerisation was confirmed with FT-IR spectroscopy (Figure S1). The characteristic N-H stretching vibrations of the amine-containing monomer TAPB around 3400 cm^{-1} and the anhydride carbonyl vibrations of the PTCDA monomer (1730 and 1754 cm^{-1}) were not observed for **Per-TAPB-PPI**. Imide carbonyl vibrations were observed in the synthesised porous polymer: at 1665 and 1701 cm^{-1}. Lastly, the broad peak at 1344 cm^{-1} was attributed to imide C—N stretching. These results indicate the successful conversion of the monomers into the polyimide polymer.

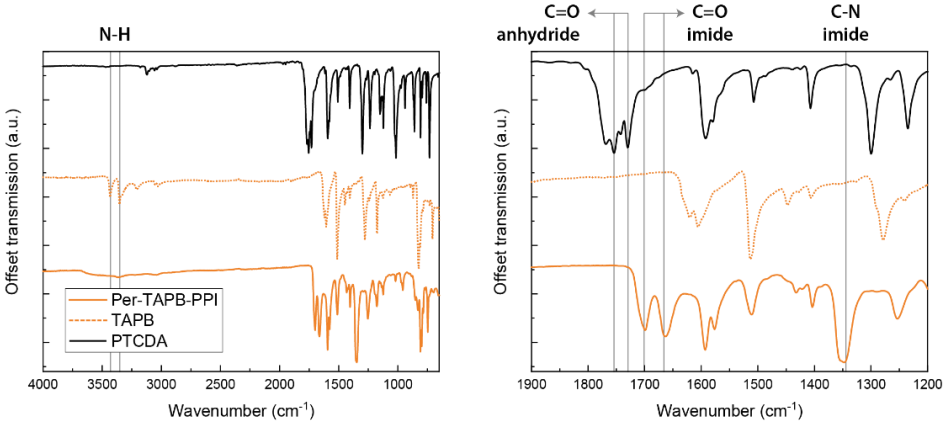

Figure S1 FT-IR spectra of **Per-TAPB-PPI** and its originating monomers PTCDA and TAPB.

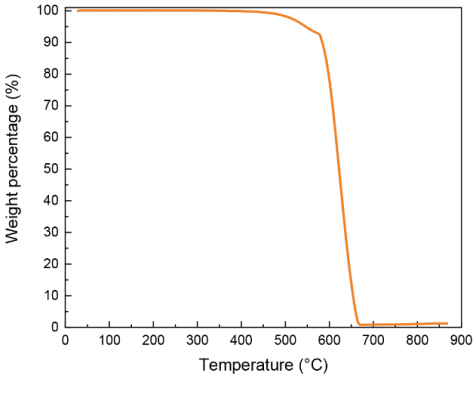

Figure S2 TGA profile of **Per-TAPB-PPI** heated from 30 to 860 °C at a rate of 10 °C / min under constant flow of nitrogen gas.

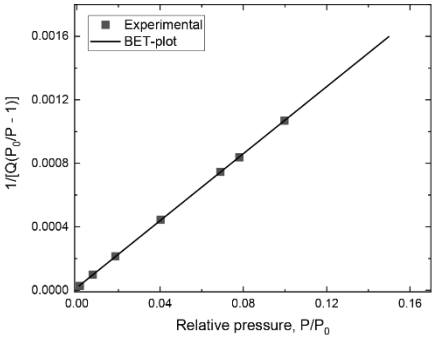

BET Report	
BET surface area:	411.5200 ± 1.3454 m²/g
Slope:	0.010561 ± 0.000035 g/cm³ STP
Y-intercept:	0.000016 ± 0.000002 g/cm³ STP
C:	663.972094
Qm:	94.5463 cm³/g STP
Correlation coefficient:	0.9999733
Molecular cross-sectional area:	0.1620 nm²

Figure S3 BET plot of **Per-TAPB-PPI**.

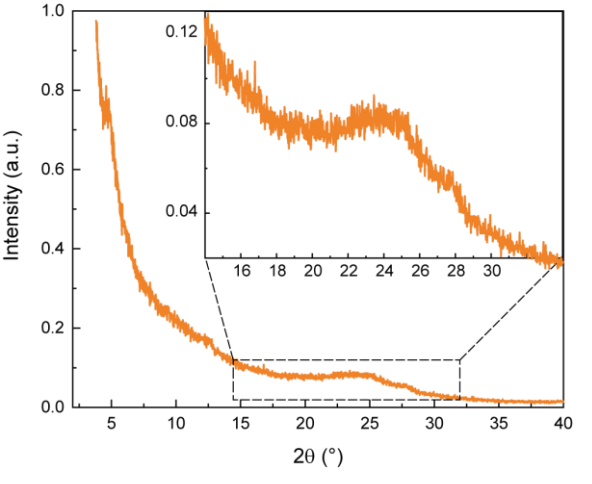

Figure S4 PXRD pattern of **Per-TAPB-PPI**.

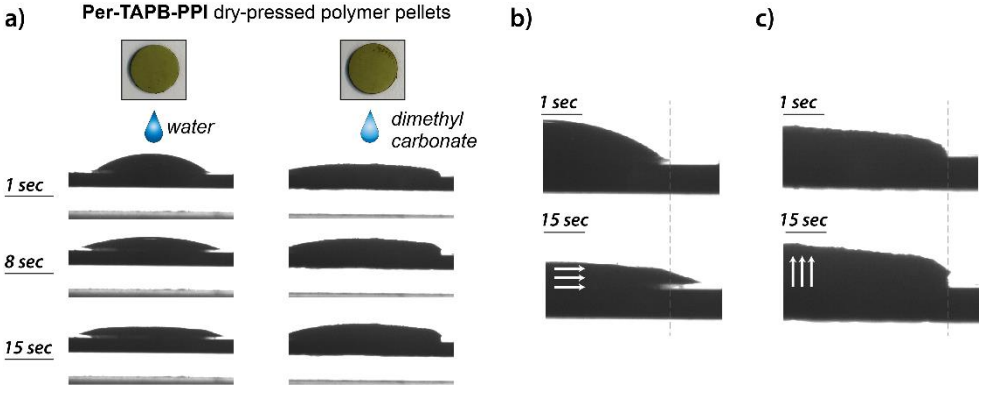

Figure S5 Contact angle measurements of dry-pressed **Per-TAPB-PPI** pellets with either dimethyl carbonate or water as liquid. Images were taken after 1, 8, and 15 seconds. **b)** Zoom-in of the 1 sec and 15 sec photographs regarding the water experiment showing droplet spreading.

c) Zoom-in of the 1 sec and 15 sec photographs regarding the dimethyl carbonate experiment showing swelling of the pellet.

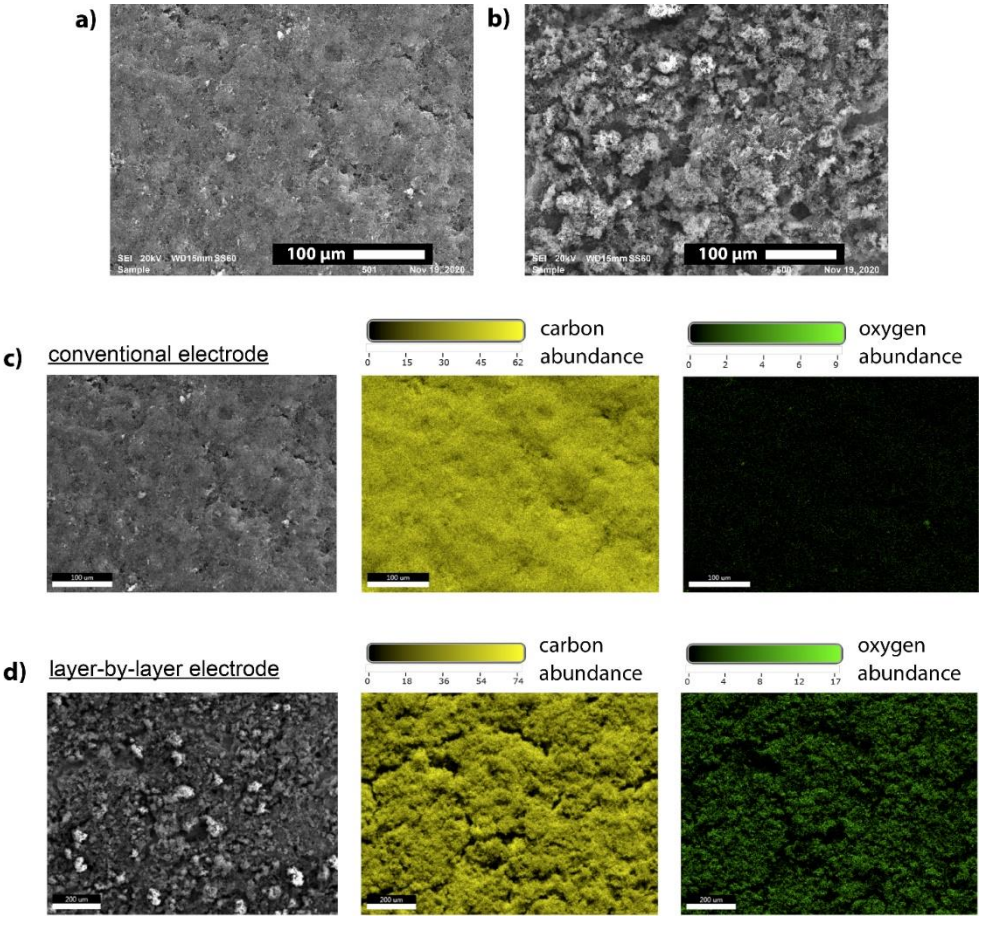

Figure S6 a) SEM micrograph of the surface of a Per-TAPB-PPI-based electrode prepared by a traditional mixing method. **b)** SEM micrograph of the surface of a Per-TAPB-PPI-based electrode prepared by a layer-by-layer method. **c)** SEM micrograph of the surface of a **Per-TAPB-PPI**-based electrode prepared by a traditional mixing method, including EDX mapping filtering for carbon and oxygen. **d)** SEM micrograph of the surface of a **Per-TAPB-PPI**-based electrode prepared by a layer-by-layer method, including EDX mapping filtering for carbon and oxygen.

Table S1 Comparison of our supercapacitor systems with previously reported COF based electrodes.

Electrode material	Electrolyte	Current density	Specific capacitance ($F\ g^{-1}$)	Capacitance retention %/ cycles	Refs.
TPDA-1	1 M H_2SO_4	1 A g^{-1}	348	95/1000	S1
DAAQ-TFP COF	1 M H_2SO_4	0.1 A g^{-1}	48±10	79/ 5000	S2
TFP-TPA COF	1 M KOH	2 A g^{-1}	291.1	91/ 5000	S3
TFP-TPP COF	1 M KOH	2 A g^{-1}	185.5	88.2/ 5000	S3
TFP-Car COF	1 M KOH	2 A g^{-1}	149.3	90.4/ 5000	S3
TaPa-Py COF	1 M H_2SO_4	0.5 A g^{-1}	209	92/ 6000	S4
DAB-TFP COF	1 M H_2SO_4	0.5 A g^{-1}	98	-	S4
BIBDZ	1 M H_3PO_4	0.5 A g^{-1}	88.4	93.61/ 5000	S5
NWNU-COF-1	6 M KOH	0.25 A g^{-1}	155.38	100/ 20000	S6
An-CPOP-2	1 M KOH	0.5 A g^{-1}	98.4	95.3/ 2000	S7
TPT-DAHQ	1 M KOH	0.5 A g^{-1}	256	98.8/ 1850	S8
Per-TAPB-PPI layered	1 M LiPF6	0.4 A g^{-1}	388	90.6 / 5000	This work
Per-TAPB-PPI traditional	1 M LiPF6	0.1 A g^{-1}	178	93.9 / 5000	This work

References

[1] Deng, L.; Young, R.J.; Kinloch, I.A.; Abdelkader, A.M.; Holmes, S.M.; De Haro-Del Rio, D.A.; Eichhorn, S.J. Supercapacitance from Cellulose and Carbon Nanotube Nanocomposite Fiber. *ACS Appl. Mater. Interfaces* **2013**, *5*, 9983–9990.

[2] Zhang, C.; Qiao, Y.; Xiong, P.; Ma, W.; Bai, P.; Wang, X.; Li, Q.; Zhao, J.; Xu, Y.; Chen, Y.; Zeng, J.H.; Wang, F.; Xu, Y.; Jiang, J.-X.; Conjugated Microporous Polymers with Tunable

Electronic Structure for High-Performance Potassium-Ion Batteries. *ACS Nano* **2019**, *13*, 745–754.

[3] Aval, L.F.; Ghoranneviss, M.; Pour, G.B. High-performance supercapacitors based on the carbon nanotubes, graphene and graphite nanoparticles electrodes. *Heliyon* **2018**, *4*, e00862.

[4] Zhang, L.L.; Zhou, R.; Zhao, X.S. Graphene-based materials as supercapacitor electrodes. *J. Mater. Chem.* **2010**, *20*, 5983–5992.

[5] Abdelkader, A.M. Electrochemical synthesis of highly corrugated graphene sheets for high performance supercapacitors. *J. Mater. Chem. A* **2015**, *3*, 8519–8525.

[6] Zhou, Y.; Lee, I.; Kim, D.; Han, S.; Kim, J.K.; Lee, D.; Ko, S.W.; Pyo, S.G.; Son, H.; Yoon, S. Direct Synthesis of Carbon Sheathed Tungsten Oxide Nanoparticles via Self-Assembly Route for High Performance Electrochemical Charge Storage Electrode. *J. Nanosci. Nanotechnol.* **2017**, *17*, 389–397.

[7] Sharma, V.; Singh, I.; Chandra, A. Hollow nanostructures of metal oxides as next generation electrode materials for supercapacitors. *Sci. Rep.* **2018**, *8*, 1307.

[8] Daneshvar, F.; Aziz, A.; Abdelkader, A.M.; Zhang, T.; Sue, H.J.; Welland, M.E. Porous SnO_2-Cu_xO nanocomposite thin film on carbon nanotubes as electrodes for high performance supercapacitors. *Nanotechnology* **2019**, *30*, 015401.

[9] Lin, L.W.; Lei, S.; Zhang, Y.; Liu, G.G.; Wallace, J.C. Two-dimensional transition metal dichalcogenides in supercapacitors and secondary batteries. *Energy Storage Mater.* **2019**, *19*, 408–423.

[10] Zheng, J.; Yang, T.; Chen, J.; Xu, J.; Jin, T.; Constructing Fe_3O_4/Nitrogen-doped Graphene Composites with Rich Pyrrolic Nitrogen for Excellent Supercapacitor Performance. *Int. J. Electrochem. Sci.* **2020**, *15*, 6207–6216.

[11] Sun, G.; Liu, J.; Zhang, X.; Wang, X.; Li, H.; Yu, Y.; Huang, W.; Zhang, H.; Chen, P. Fabrication of Ultralong Hybrid Microfibers from Nanosheets of Reduced Graphene Oxide and Transition-Metal Dichalcogenides and their Application as Supercapacitors. *Angew. Chem. Int. Ed.* **2014**, *53*, 12576–12580.

[12] Biswas, S.; Drzal, L.T. Multilayered Nanoarchitecture of Graphene Nanosheets and Polypyrrole Nanowires for High Performance Supercapacitor Electrodes. *Chem. Mater.* **2010**, *22*, 5667–5671.

[13] Wang, K.; Huang, J.; Wei, Z. Conducting Polyaniline Nanowire Arrays for High Performance Supercapacitors. *J. Phys. Chem. C* **2010**, *114*, 8062–8067.

[14] Sajedi-Moghaddam, A.; Saievar-Iranizad, E.; Pumera, M. Two-dimensional transition metal dichalcogenide/ conducting polymer composites: synthesis and applications. *Nanoscale* **2017**, *9*, 8052–8065.

[15] Qi, K.; Hou, R.; Zaman, S.; Qiu, Y.; Xia, B.Y.; Duan, H. Construction of Metal–Organic Framework/Conductive Polymer Hybrid for All-Solid-State Fabric Supercapacitor. *ACS Appl. Mater. Interfaces* **2018**, *10*, 18021–18028.

[16] Meng, Q.; Cai, K.; Chen, Y.; Chen, L. Research progress on conducting polymer based supercapacitor electrode materials. *Nano Energy* **2017**, *36*, 268–285.

[17] Snook, G.A.; Kao, P.; Best, A.S. Conducting-polymer-based supercapacitor devices and electrodes. *J. Power Sources* **2011**, *196*, 1–12.

[18] Buyukcakir, O.; Je, S.H.; Choi, D.S.; Talapaneni, S.N.; Seo, Y.; Jung, Y.; Polychronopoulou, K.; Coskun, A. Porous cationic polymers: the impact of counteranions and charges on CO_2 capture and conversion. *Chem. Commun.* **2016**, *52*, 934–937.

[19] Jagadesan, P.; Eder, G.; McGrier, P.L. The excited-state intramolecular proton transfer properties of three imine-linked two-dimensional porous organic polymers. *J. Mater. Chem. C* **2017**, *5*, 5676–5679.

[20] Sun, B.; Liu, J.; Cao, A.; Song, W.; Wang, D. Interfacial synthesis of ordered and stable covalent organic frameworks on aminofunctionalized carbon nanotubes with enhanced electrochemical performance. *Chem. Commun.* **2017**, *53*, 6303–6306.

[21] Jin, J.; Mu, H.; Wang, W.; Li, X.; Cheng, Q.; Wang, G. Long-life flexible supercapacitors based on nitrogen-doped porous graphene@π-conjugated polymer film electrodes and porous quasi-solid-state polymer electrolyte. *Electrochim. Acta* **2019**, *317*, 250–260.

[22] Tahir, M.; He, L.; Haider, W.A.; Yang, W.; Hong, X.; Guo, Y.; Pan, X.; Tang, H.; Li, Y.; Mai, L. Co-Electrodeposited porous PEDOT–CNT microelectrodes for integrated microsupercapacitors with high energy density, high rate capability, and long cycling life. *Nanoscale* **2019**, *11*, 7761–7770.

[23] Kulandaivalu, S.; Suhaimi, N.; Sulaiman, Y. Unveiling high specifc energy supercapacitor from layer-by-layer assembled polypyrrole/graphene oxide|polypyrrole/manganese oxide electrode material. *Sci. Rep.* **2019**, *9*, 4884.

[24] Rao, K.V.; Haldar, R.; Kulkarni, C.; Maji, T.K.; George, S.J. Perylene Based Porous Polyimides: Tunable, High Surface Area with Tetrahedral and Pyramidal Monomers. *Chem. Mater.* **2012**, *24*, 969–971.

[25] Jiang, L.; Tian, Y.; Sun, T.; Zhu, Y.; Ren, H.; Zou, X.; Ma, Y.; Meihaus, K.R.; Long, J.R.; Zhu, G. A Crystalline Polyimide Porous Organic Framework for Selective Adsorption of Acetylene over Ethylene . *J. Am. Chem. Soc.* **2018**, *140*, 15724–15730.

[26] Liebl, M.R.; Senker, J. Microporous Functionalized Triazine-Based Polyimides with High CO_2 Capture Capacity. *Chem. Mater.* **2013**, *25*, 970–980.

[27] Luo, Y.; Li, B.; Liang, L.; Tan, B. Synthesis of cost-effective porous polyimides and their gas storage properties. *Chem. Commun.* **2011**, *47*, 7704–7706.

[28] Tian, D.; Zhang, H.Z.; Zhang, D.S.; Chang, Z.; Han, J.; Gao, X.P.; Bu, X.H. Li-ion storage and gas adsorption properties of porous polyimides (PIs). *RSC Adv.* **2014**, *4*, 7506–7510.

[29] Xu, F.; Jin, S.; Zhong, H.; Wu, D.; Yang, X.; Chen, X.; Wei, H.; Fu, R.; Jiang, D. *In-situ* epitaxial growth of graphene/h-BN van der Waals heterostructures by molecular beam epitaxy. *Sci. Rep.* **2015**, *5*, 14760.

[30] Li, Z.; Zhou, J.; Xu, R.; Liu, S.; Wang, Y.; Li, P.; Wu, W.; Wu, M. Synthesis of three dimensional extended conjugated polyimide and application as sodium-ion battery anode. *Chem. Eng. J.* **2016**, *287*, 516–522.

[31] Van der Jagt, R.; Vasileiadis, A.; Veldhuizen, H.; Shao, P.; Feng, X.; Ganapathy, S.; Habisreutinger, N.C.; van der Veen, M.A.; Wang, C.; Wagemaker, M.; Van der Zwaag, S.; Nagai, A.. Synthesis and Structure–Property Relationships of Polyimide Covalent Organic Frameworks for Carbon Dioxide Capture and (Aqueous) Sodium-Ion Batteries. *Chem. Mater.* **2021**, *33*, 818–833.

[32] Venkateswararao, A.; Liu, S.W.; Wong, K.T. Organic polymeric and small molecular electron acceptors for organic solar cells. *Mater. Sci. Eng. R Rep.* **2018**, *124*, 1–57.

[33] Iordache, A.; Delhorbe, V.; Bardet, M.; Dubois, L.; Gutel, T.; Picard, L. Perylene-Based All-Organic Redox Battery with Excellent Cycling Stability. *ACS Appl. Mater. Interfaces* **2016**, *8*, 22762–22767.

[34] Fang, Q.; Wang, J.; Gu, S.; Kaspar, R.B.; Zhuang, Z.; Zheng, J.; Guo, H.; Qiu, S.; Yan, Y. 3D Porous Crystalline Polyimide Covalent Organic Frameworks for Drug Delivery. *J. Am. Chem. Soc.* **2015**, *137*, 8352–8355.

[35] Zhao, W.; Cao, X.; Huang, J.; Wen, J.; He, Y.; Zha, J.; Li, R.K.Y.; Wu, W. Construction of micro-branched crosslink fluorinated polyimide with ultra-low dielectric permittivity and enhanced mechanical properties. *Express Polym. Lett.* **2022**, *16*, 142–151.

[36] Neimark, A.V.; Lin, Y.; Ravikovitch, P.I.; Thommes, M. Quenched solid density functional theory and pore size analysis of micro-mesoporous carbons. *Carbon N. Y.* **2009**, *47*, 1617–1628.

[37] Spitler, E.L.; Koo, B.T.; Novotney, J.L.; Colson, J.W.; Uribe-Romo, F.J.; Gutierrez, G.D.; Clancy, P.; Dichtel, W.R. A 2D Covalent Organic Framework with 4.7-nm Pores and Insight into Its Interlayer Stacking. *J. Am. Chem. Soc.* **2011**, *133*, 19416–19421.

[38] Li, G.; Wang, Z. Microporous Polyimides with Uniform Pores for Adsorption and Separation of CO_2 Gas and Organic Vapors. *Macromolecules* **2013**, *46*, 3058–3066.

[39] Shen, C.; Bao, Y.; Wang, Z. Tetraphenyladamantane-based microporous polyimide for adsorption of carbon dioxide, hydrogen, organic and water vapors. *Chem. Commun.* **2013**, *49*, 3321–3323.

[40] Bhanja, P.; Das, S.K.; Bhunia, K.; Pradhan, D.; Hayashi, T.; Hijikata, Y.; Irle, S.; Bhaumik, A. A New Porous Polymer for Highly Efficient Capacitive Energy Storage. *ACS Sustain. Chem. Eng.* **2018**, *6*, 202–209.

[41] Vadiyar, M.M.; Liu, X.; Ye, Z. Macromolecular Polyethynylbenzonitrile Precursor-Based Porous Covalent Triazine Frameworks for Superior High-Rate High-Energy Supercapacitors. *ACS Appl. Mater. Interfaces* **2019**, *11*, 45805–45817.

[42] Wu, Y.; Yan, D.; Zhang, Z.; Matsushita, M.M.; Awaga, K. Electron Highways into Nanochannels of Covalent Organic Frameworks for High Electrical Conductivity and Energy Storage. *ACS Appl. Mater. Interfaces* **2019**, *11*, 7661–7665.

[43] Chang, I.C.; Chen, T.T.; Yang, M.H.; Chiu, H.T.; Lee, C.Y. Self-powered electrochemical deposition of Cu@Ni(OH)$_2$ nanobelts for high performance pseudocapacitors. *J. Mater. Chem. A* **2014**, *2*, 10370–10374.

[44] Fernando, N.; Chinnappan, A.; Aziz, A.; Abdelkader, A.; Ramakrishna, S.; Welland, M.E. Flexible free-standing Ni–Mn oxide antenna decorated CNT/nanofiber membrane for high-volumetric capacitance supercapacitors. *Nanoscale* **2021**, *13*, 19038–19048.

[45] Wang, H.; Yi, H.; Chen, X.; Wang, X. Asymmetric supercapacitors based on nano-architectured nickel oxide/graphene foam and hierarchical porous nitrogen-doped carbon nanotubes with ultrahigh-rate performance. *J. Mater. Chem. A* **2014**, *2*, 3223–3230.

[46] Ramakrishnan, S.; Velusamy, D.B.; Sengodan, S.; Nagaraju, G.; Kim, D.H.; Kim, A.R.; Yoo, D.J. Rational design of multifunctional electrocatalyst: An approach towards efficient overall water splitting and rechargeable flexible solid-state zinc–air battery. *Appl. Catal. B Environ.* **2022**, *300*, 120752.

[47] Basiricò, L.; Lanzara, G. Moving towards high-power, high-frequency and low-resistance CNT supercapacitors by tuning the CNT length, axial deformation and contact resistance. *Nanotechnology* **2012**, *23*, 305401.

[48] Gao, Y.; Zhi, C.; Cui, P.; Zhang, K.A.I.; Lv, L.P.; Wang, Y. Halogen-functionalized triazine-based organic frameworks towards high performance supercapacitors. *Chem. Eng. J.* **2020**, *400*, 125967.

[49] Li, K.B.; Shi, D.W.; Cai, Z.Y.; Zhang, G.L.; Huang, Q.A.; Liu, D.; Yang, C.P. Studies on the equivalent serial resistance of carbon supercapacitor. *Electrochim. Acta* **2015**, *174*, 596–600.

[50] Taberna, P.L.; Simon, P.; Fauvarque, J.F. Electrochemical Characteristics and Impedance Spectroscopy Studies of Carbon-Carbon Supercapacitors. *J. Electrochem. Soc.* **2003**, *150*, A292.

[51] Gao, Y.; Li, Y.; An, H.; Feng, Y.; Feng, W. Copolymers of aniline and 2-aminoterephthalic acid as a novel cathode material for hybrid supercapacitors. *RSC Adv.* **2017**, *7*, 8762–8770.

[52] Chandra, S.; Roy Chowdhury, D.; Addicoat, M.; Heine, T.; Paul, A.; Banerjee, R. Molecular Level Control of the Capacitance of Two-Dimensional Covalent Organic Frameworks: Role of Hydrogen Bonding in Energy Storage Materials. *Chem. Mater.* **2017**, *29*, 2074–2080.

[53] Patra, B.C.; Khilari, S.; Satyanarayana, L.; Pradhan, D.; Bhaumik, A. A new benzimidazole based covalent organic polymer having high energy storage capacity. *Chem. Commun.* **2016**, *52*, 7592–7595.

S1. P. Bhanja, S. K. Das, K. Bhunia, D. Pradhan, T. Hayashi, Y. Hijikata, S. Irle, A. Bhaumik, ACS Sustainable Chem. Eng. 2018, 6, 202–209.

S2. C.R. DeBlase, K.E. Silberstein, T.-.T. Truong, H.D. Abruña, W.R. Dichtel β-ketoenamine-linked covalent organic frameworks capable of pseudocapacitive energy storage, J. Am. Chem. Soc. 2013, 135, 45, 16821–16824.

S3. EL-Mahdy, A.F., Hung, Y.H., Mansoure, T.H., Yu, H.H., Hsu, Y.S., Wu, K.C. and Kuo, S.W., 2019. Synthesis of [3+ 3] β-ketoenamine-tethered covalent organic frameworks (COFs) for high-performance supercapacitance and CO2 storage. Journal of the Taiwan Institute of Chemical Engineers, 103, pp.199-208.

S4. Khattak, A.M., Ghazi, Z.A., Liang, B., Khan, N.A., Iqbal, A., Li, L. and Tang, Z., 2016. A redox-active 2D covalent organic framework with pyridine moieties capable of faradaic energy storage. Journal of Materials Chemistry A, 4(42), pp.16312-16317.

S5. Roy, A., Mondal, S., Halder, A., Banerjee, A., Ghoshal, D., Paul, A. and Malik, S., 2017. Benzimidazole linked arylimide based covalent organic framework as gas adsorbing and electrode materials for supercapacitor application. European Polymer Journal, 93, pp.448-457.

S6. Xue, R., Guo, H., Yue, L., Wang, T., Wang, M., Li, Q., Liu, H. and Yang, W., 2018. Preparation and energy storage application of a long-life and high rate performance pseudocapacitive COF material linked with–NH–bonds. New Journal of Chemistry, 42(16), pp.13726-13731.

S7. Mohamed, M.G., Zhang, X., Mansoure, T.H., El-Mahdy, A.F., Huang, C.F., Danko, M., Xin, Z. and Kuo, S.W., 2020. Hypercrosslinked porous organic polymers based on tetraphenylanthraquinone for CO2 uptake and high-performance supercapacitor. Polymer, 205, p.122857.

S8. El-Mahdy, A.F., Hung, Y.H., Mansoure, T.H., Yu, H.H., Chen, T. and Kuo, S.W., 2019. A Hollow Microtubular Triazine-and Benzobisoxazole-Based Covalent Organic Framework Presenting Sponge-Like Shells That Functions as a High-Performance Supercapacitor. Chemistry–An Asian Journal, 14(9), pp.1429-1435.

7

Combining Nickel- and Zinc-Porphyrin Sites via Covalent Organic Frameworks for Electrochemical CO_2 Reduction

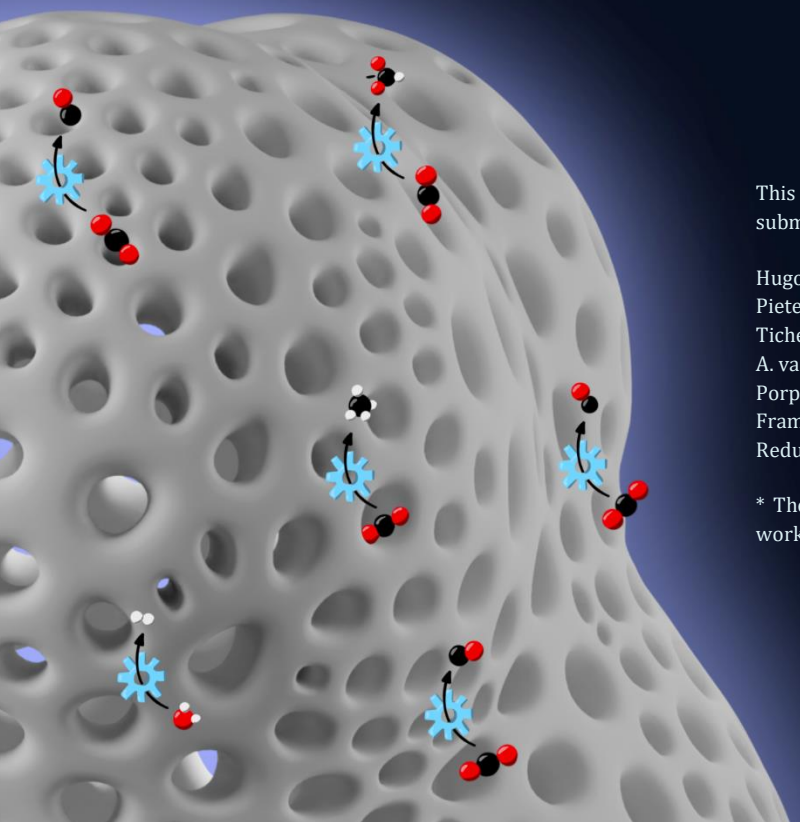

This chapter is based on the following submitted manuscript:

Hugo Veldhuizen,* Maryam Abdinejad,* Pieter J. Gilissen, Tom Burdyny, Frans D. Tichelaar, Sybrand van der Zwaag, Monique A. van der Veen. Combining Nickel- and Zinc-Porphyrin Sites in Covalent Organic Frameworks for Electrochemical CO_2 Reduction.

* These authors contributed equally to this work

Abstract

Covalent organic frameworks (COFs) are ideal platforms to spatially control the integration of multiple different molecular motifs throughout a single nanoporous framework. However, despite this design flexibility, COFs are generally synthesized via only two monomers. One bears the functional motif for the envisioned application, and the other is used as an inert connecting building block. Integrating more than one functional motif extends the functionality of COFs immensely, and is particularly useful in the case of COF catalysts for complex, multi-step reactions such as the electrochemical reduction of CO_2. Here, we synthesized five Ni(II)- and Zn(II)-porphyrin-based COFs, including the two pure component COFs and three mixed Ni/Zn-COFs with Ni:Zn ratios of 75:25, 50:50, and 25:75. In the co-synthesized metalloporphyrin COFs, nickel and zinc atoms are distributed relatively homogeneously throughout the framework, which generated greater quantities of formate and methane during electrochemical CO_2 reduction compared to the physical mixture of both pure components. The Ni_{50}/Zn_{50}-COF produced noteworthy quantities of formate and methane at Faradaic efficiencies of 43% and 14%, respectively, at 150 mA/cm^2, while the pure Ni- and Zn-COFs almost exclusively generated H_2 and CO. We discuss how the synergy between Ni- and Zn-porphyrins can lead to these results through a likely combination of the following: bifunctional catalysis, enhanced proton/electron transfer, and Ni-porphyrin-dependent stabilizing effects on the porous framework.

7.1 INTRODUCTION

Electrochemical carbon dioxide reduction reaction (CO_2RR) into C_1 products such as CO, formate, CH_4, and methanol using renewable electrical energy is a promising route towards fossil-fuel-free feedstock.[1] Since CO_2 is a highly thermodynamically stable molecule, catalysts are required to lower its reduction reaction energy barrier.[2] Well-studied materials for this purpose are transition metal particles and surfaces,[3,4] and molecular catalysts.[5] Continuous optimization of these catalysts is aimed at improving their stability, efficiency, and product selectivity. However, in terms of selectivity, steering the desired ratio of products through easily implementable chemical modifications of the catalyst is currently still difficult to achieve.

Covalent organic frameworks (COFs) and metal-organic frameworks (MOFs) are emerging alternative catalysts that have shown to present solutions to these issues. Careful selection of their originating monomers allows chemical and spatial control of the active sites: obtaining a high degree of control over product selectivity.[6,7] At the same time, their nanoporous networks makes the active sites highly accessible to CO_2 and product intermediates. COFs with strong polymer backbones such as 'locked' polyimines and polyimides, are receiving more attention due to their decent stability in aqueous electrolytes.[8,9] Widely used catalytically active units in these COFs are porphyrins and phthalocyanines.[10] These molecular motifs are highly tuneable, since the type of metal-ion that is coordinated to the porphyrin or phthalocyanine ligand has a large impact on specific electro- or photocatalytic reactions.[11,12] For example, in porphyrin-based COFs, the optimal metal-ion in the production of CO during electrochemical CO_2RR has been shown to be cobalt.[13,14] On the other hand, Ni- and Zn-porphyrin-based COFs outperform Co-porphyrin-COFs in the photocatalytic hydrogen evolution reaction.[15] Much of the catalytic activity of these materials depends on the electronic configuration of the coordination complex between the metal-ion and the porphyrin. This presents opportunities for the development of bi-functional (A-B) catalysts, where regulation of the ratio of A to B may provide control over the activity and selectivity during CO_2 electroreduction.

This strategy has been employed in phthalocyanine MOF systems, where control of both the metal node of the MOF backbone and the metal ion coordinated to the phthalocyanine allows the formation of a true A-B bifunctional catalyst. Zhong *et al.*[16] studied a system using either copper- or zinc-phthalocyanine linkers in MOFs structured by either copper- or zinc-bis(dihydroxy) nodes, totaling

4 different structures. Interestingly, the specific combination of a copper-phthalocyanine combined with a ZnO_4 backbone was able to produce the largest Faradaic efficiency (FE) of 88% CO and a current density (*j*) of 4 mA/cm^2 at -0.7 V vs RHE. This observation was attributed to metal hydrides that were generated during water electrolysis on the copper-phthalocyanine sites, being transported to the zinc-active sites where CO_2 could be efficiently converted into CO. In a similar system using copper-phthalocyanines and copper metal nodes, Chen and coworkers[17] demonstrated that C_2H_4 can be produced with FE: 50% and *j*: 7.3 mA/cm^2 at -1.2 V vs RHE. Their proposed mechanism for this conversion, verified by *in-situ* FT-IR, was: CO formation on both sites, followed by preferential CO desorption from the copper-node of the backbone, and CO diffusion towards the CO-copper-phthalocyanine active site, where C-C dimerization can occur. Thus, incorporation of multiple catalytically active units within one framework may provide cooperativity in terms of reaction mechanism.

In this work, nickel- and zinc-porphyrin units are implemented in covalent organic frameworks through the solvothermal synthesis of tetra-amino-functionalized metalloporphyrins with terephthaldehyde linkers. The molar ratios of nickel- to zinc-porphyrin units were varied: Ni_{100}/Zn_0, Ni_{75}/Zn_{25}, Ni_{50}/Zn_{50}, Ni_{25}/Zn_{75}, and Ni_0/Zn_{100}; totalling five different frameworks. After synthesis and thorough analysis of all five COFs' molecular and polymeric structure, they were utilised as catalysts in CO_2RR. The results demonstrate that the pure Ni_{100}/Zn_0 and Ni_0/Zn_{100} COFs favour the formation of H_2 and CO respectively. Remarkably, apart from H_2 and CO reaction products, the Ni_{50}/Zn_{50} COF catalyst generates significant quantities of formate (FE: 43%) and CH_4 (FE: 14%) at 150 mA/cm^2. A comparison of the Ni_{50}/Zn_{50} catalytic performance with that of a 1:1 (w/w) physical mixture of Ni_{100}/Zn_0 and Ni_0/Zn_{100} catalyst was vital to understand the underlying mechanism towards the formation of these different products.

7.2 EXPERIMENTAL

7.2.1 SYNTHESIS OF NI/ZN-PORPHYRIN COFS

Ni(II)-5,10,15,20-tetrakis(4-aminophenyl)porphyrin (Ni-TAPP) and Zn(II)-5,10,15,20-tetrakis(4-aminophenyl)porphyrin (Zn-TAPP) compounds were synthesized and analyzed, as detailed in the supplementary information. X % Ni-TAPP and (100 – X) % Zn-TAPP, combined totalling 0.04 mmol were added to a 20 mL prescorched borosilicate ampule. 6 mL of the solvent mixture (1:1 (v/v) mixture of *ortho*-dichlorobenzene and 1-butanol) was added to the ampule, after

which it was sonicated for 1 minute. Then, 0.08 mmol 2,5-dihydroxyterephthaldehyde was separately suspended in 1 mL acetic acid (6 M in water) and 2 mL solvent mixture, and subsequently dropwise added to the ampule. The mixture in the ampule was briefly homogenized and subjected to three freeze-pump-thaw cycles. Lastly, the ampule was flame-sealed and left in an oven at 120 °C for 3 days.

The workup of the COFs included washing with THF (~ 6 x 10 mL) until the washing solution was clear of colour and the COFs were subsequently washed with acetone (3 x 10 mL). Thereafter, the powders were dried at 60 °C in a vacuum oven for 16 hours. The yields of the COFs were: Ni_{100}/Zn_0 (34.0 mg, 86 %), Ni_{75}/Zn_{25} (37.1 mg, 93 %), Ni_{50}/Zn_{50} (33.1 mg, 84 %), Ni_{25}/Zn_{75} (32.7 mg, 82 %), Ni_0/Zn_{100} (33.6 mg, 84 %). All COFs appear as light fluffy powders, with colours ranging from: Ni_{100}/Zn_0 (deep red), Ni_{75}/Zn_{25} (dark red-brown), Ni_{50}/Zn_{50} (dark brown), Ni_{25}/Zn_{75} (dark brown-green), Ni_0/Zn_{100} (deep green). A complete overview of the analysis techniques and technique-specific sample preparations are detailed in the supporting information.

7.2.2 ELECTROREDUCTION EXPERIMENTS

7.2.2.1 Preparation of deposited COF complexes onto electrodes

The mixture of each COF compound (7 mg) in DMF (4 mL) with 5 wt.% Nafion was sonicated for 40 min to obtain a well-mixed suspension. Then, the mixture was stirred at room temperature overnight and subsequently drop-casted onto a gas diffusion electrode (GDE, Sigracet 38 BC, 5% PTFE applied non-woven carbon paper with a microporous layer; 2.5 cm x 2.5 cm) for the membrane electrode assembly (MEA) study. For the H-cell setup, 10 µL of the prepared suspension was drop-casted on the pre-prepared surface (d = 3.0 mm) of a standard glassy carbon electrode and let to dry for 24 hours. All potentials were reported versus the Ag/AgCl reference electrode. Potentials were changed from Ag/AgCl (3 M KCl) to the reversible hydrogen electrode (RHE, $E_{RHE}=E_{Ag/AgCl} + 0.059 \times pH + 0.210$).

7.2.2.2 Characterizations during electroreduction

The reduced products observed in the cathodic compartment were periodically collected from the reaction headspace and tested by gas chromatography (GC). The concentration of gaseous products (CO, CH_4, H_2) was obtained from GC, and the average of 4 injections was used to calculate their Faradaic efficiencies. The gas product from CO_2 electroreduction was analyzed using a chromatograph (InterScience PerkinElmer Clarus 680) coupled with two thermal conductivity

detectors (TCD) and a flame ionization detector (FID), while the liquid product was analyzed using HPLC (Infinity 1260 II LC, Agilent Technologies, Hi-Plex H column (at 50 °C) with VWD (at 210 nm and 280 nm) and RID (at 40 °C)) (Figures S12 and S13). ^{1}H NMR was measured using a Bruker 400 MHz setup and the data were processed in MestreNova. The chemical shifts (δ) are reported in ppm.

7.2.2.3 H-cell and membrane electrode assembly (MEA) experiments

To evaluate the electroactivity of the synthesized COF complexes, the electrochemical reduction of CO_2 was first studied with an H-cell using the Linear Sweep Voltammetry (LSV) technique. The two-compartment H-cell comprised of a three-electrode configuration, including the immobilized COF catalysts on a glassy carbon working electrode (GCE), a silver/silver chloride (Ag/AgCl) reference electrode, and a platinum (Pt) counter electrode in a CO_2-saturated 0.1 M $KHCO_3$ aqueous solution. Gas-phase products were collected from the reaction headspace and measured using gas chromatography (GC). For experiments with higher current densities, a membrane electrode assembly (MEA) electrolyzer consisting of an anode chamber (Ni-foam anode, Recemat BV) with a liquid phase anolyte (0.5 M KOH) and a cathode chamber (COF on GDE) with a gas phase inlet was employed (schematic shown at Figure S14). The membrane that separates these chambers is a Sustainion anion-exchange membrane (X37-50 Grade RT). In this design, gaseous CO_2 is delivered directly (at 40 ml min^{-1}, STP) to the active materials through an inlet located at the back side of the GDE.

7.3 Results

7.3.1 Metalloporphryin COF structure investigation

Nickel- and zinc-containing 5,10,15,20-tetra(4-aminophenyl)porphyrin monomers (Ni-TAPP and Zn-TAPP) were synthesized *via* a 3-step synthesis route using commercial building blocks and subsequently analysed (supplementary information, Figure S1). The polycondensation reactions of Ni- and/or Zn-TAPP with 2,5-dihydroxyterephthaldehyde (DHTA) in a solvothermal synthesis yielded COF structures with various ratios of nickel- and zinc-containing porphyrin segments (**Figure 1A**). FT-IR spectroscopy was used on COF powders to confirm the formation of the imine polymer backbone (C=N bonds at 1615 cm^{-1}) and the complete disappearance of the monomer functional groups (Figure S2). The presence of the thermally stable imine backbone was also confirmed with TGA analysis (Figure S3), where no significant differences in thermal stability were observed between the COFs. The nickel-to-zinc porphyrin ratio influenced the

spectroscopic properties, mainly in the fingerprint region of the FT-IR spectra. The rocking vibrational mode of the C-H groups within the pyrrole ring is significantly red-shifted from the Ni_{100}/Zn_0 COF (at 1003 cm^{-1}) to the Ni_0/Zn_{100} COF (at 997 cm^{-1}), as a result of the metal-ligand interaction. In addition, out-of-plane phenyl-ring blue shifts occur from 746 to 751 cm^{-1} and from 713 to 718 cm^{-1} for Ni_{100}/Zn_0 COF to the Ni_0/Zn_{100} COF. The synthesized frameworks that contain both Ni- and Zn-porphyrin units show gradual shifts expected based on their Ni:Zn ratios (Figure S4). Lastly, suspended COF particles were analysed with UV-vis spectroscopy, where metalloporphyrin-characteristic Q-bands were observed (Figure S5). The band at 545 nm is clearly visible for the Ni_{100}/Zn_0 COF but absent for the Ni_0/Zn_{100} COF, while the opposite is true for the band at 624 nm. However, both Q bands are visible for the co-synthesized metalloporphyrin COFs. In addition, the characteristic Soret band is located at 433 nm for the Ni_{100}/Zn_0 COF, while it is centred around 437 nm for all other COFs.

Although Ni/Zn-porphyrin COFs have different porosities depending on the ratio between originating Ni- and Zn-porphyrin monomers (**Figure 1B**, Figure S6), their nitrogen isotherm curve shapes remain similar: following typical curves representative of micro- and small mesoporosity. Interestingly, the Ni_{50}/Zn_{50} COF appears to have the largest absolute micro- and mesopore volume. To expand on this, pore size distributions (PSDs) were calculated using a quenched solid density functional theory (QSDFT) carbon model that considers slit- and cylindrical pores, with the adsorption branch of the isotherms as experimental input values (**Figure 1C,** Figure S7A). All COFs contain a significant micropore volume (0.17 – 0.25 $cm^3 \cdot g^{-1}$) and small mesopore volume (0.06 – 0.13 $cm^3 \cdot g^{-1}$, Figure S7-S8). Finally, surface areas based on BET theory were calculated, as well as the Gurvich total pore volume for all COFs, and these values are depicted in the diagram in **Figure 1D** as a function of the ratio of Ni- and Zn-porphyrin units. An apparent optimum for both of these properties is seen in the Ni_{50}/Zn_{50} COF, having a BET surface area of 1180 $m^2 \cdot g^{-1}$ and a total pore volume of 0.67 $cm^3 \cdot g^{-1}$.

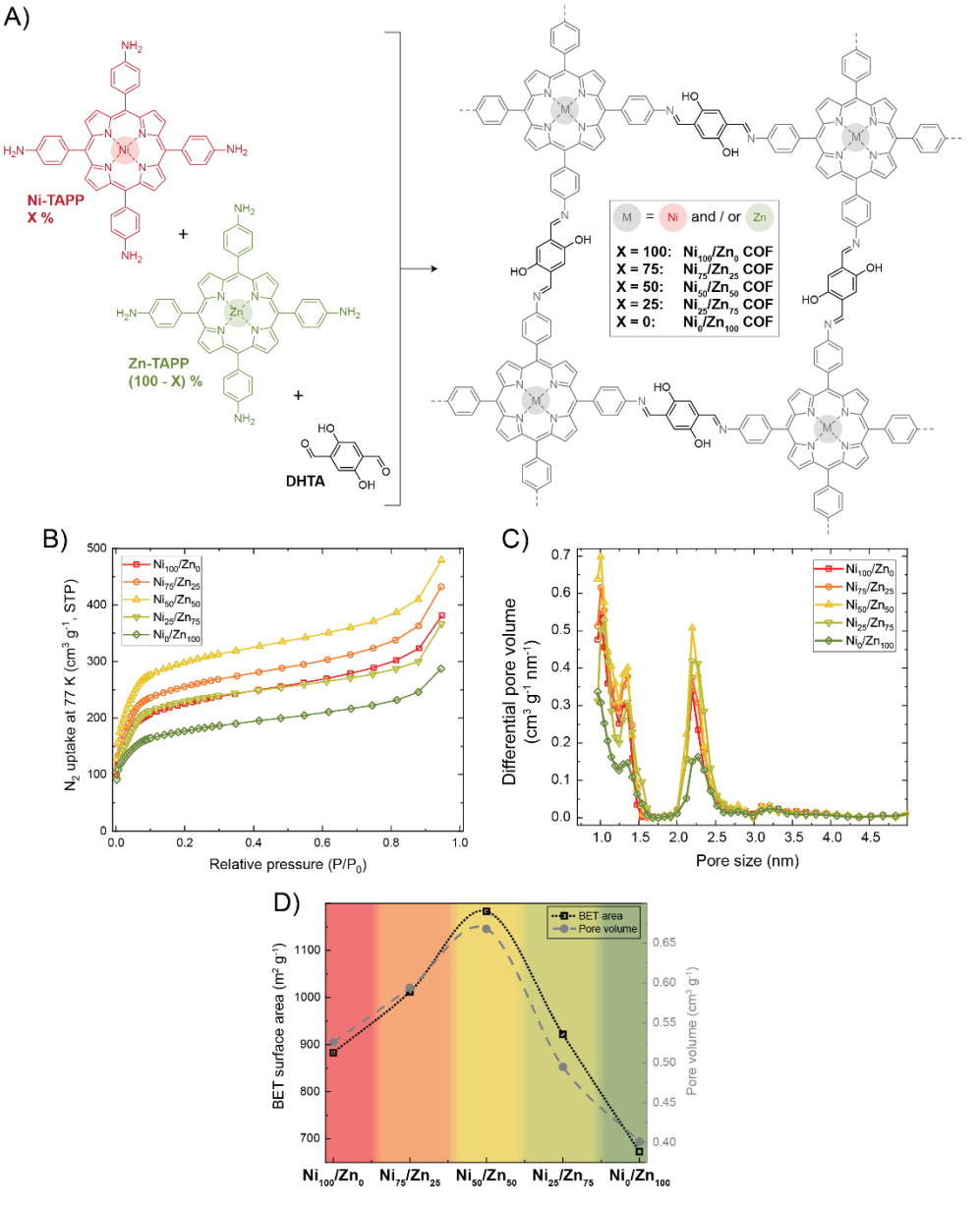

Figure 1. A) Chemical structure of Ni/Zn-porphyrin COFs and their monomers. **B)** Nitrogen adsorption isotherms of Ni/Zn-porphyrin COFs measured at 77 K. **C)** Pore size distributions of Ni/Zn-porphyrin COFs, calculated from experimental N_2 adsorption isotherm branches and based on a QSDFT carbon model with slit/cylindrical pore geometries. **D)** BET surface areas and Gurvich total pore volumes of Ni/Zn-porphyrin COFs, calculated from experimental N_2 adsorption isotherms.

X-ray photoelectron spectroscopy (XPS) was utilised to investigate the surface chemistry of the Ni/Zn-porphyrin COF powders (Figure S9), specifically focussing on the high-resolution C 1s, N 1s, O 1s, Ni 2p and Zn 2p spectra. The C 1s and O 1s spectra of all powders are highly similar: they all reveal four different carbon species on their surfaces and one distinct oxygen state originating from the DHTA monomer's hydroxyl groups. Two N 1s states are present for all COFs (at binding energies of ~ 398 eV and 399.5 eV) except for the Ni_0/Zn_{100} COF, which shows three N 1s states (397.2; 398.2; and 399.5 eV). In addition, since XPS spectra can be quantitatively analysed, atomic percentages of Ni and Zn based on these spectra were calculated (Table S1). The measured Ni:Zn ratios resemble the expected values based on the intended incorporation of Ni- and Zn-porphyrin units during COF synthesis, with slight deviations: 65:35, 40:60, and 29:71 for the Ni_{75}/Zn_{25}, Ni_{50}/Zn_{50}, Ni_{25}/Zn_{75} COFs respectively.

The polymer network was further investigated by powder X-ray diffraction (PXRD, Figure S10). All investigated COFs showed a prominent peak at 3.6 ° 2θ, corresponding to a distance of 2.45 nm. Secondary peaks and shoulder peaks were observed in the region of 6 – 10 ° 2θ, but they were not very well defined, which suggests positional order to be present only on a local length scale. Although no clear trend for the pure and mixed Ni/Zn-porphyrin COFs was observed, the Ni_0/Zn_{100} COF has the most prominent shoulder peak (~ 8.3 ° 2θ). Lastly, the diffuse signal centred around 22.5 ° 2θ – corresponding to an expected interplanar distance of 0.395 nm – observed for all COFs suggests a significant amount of stacking of the 2D COF sheets. The sheet-like character of the COFs was further inspected using high-resolution transmission electron microscopy (HR-TEM). The morphology of all COFs revealed interconnected/aggregated sheets with sizes in the range of 20 – 40 nm (Figure S11), of which a representative image (Ni_{50}/Zn_{50}) is shown in **Figure 2A**. The expected square-geometry of the repeating unit of ~ 2 nm is visible in these images. Closer inspection of the sheet-like structure of the Ni_{50}/Zn_{50} COF was performed using scanning transmission electron microscopy (STEM) with a high-angle annular dark field (HAADF) detector, in combination with energy-dispersive X-ray (EDX) spectroscopy (**Figure 2B**). Focussing on the elements Ni and Zn allowed us to obtain a 2D projection of the spatial distribution of these elements throughout the COF structure. Although no true atomic resolution can be reached (partly due to COF degradation under the beam after a prolonged time), the STEM-EDX map does indicate a relatively homogeneous distribution of Ni- and Zn-porphyrin units with no significant preference to form microdomains of the two metallic elements.

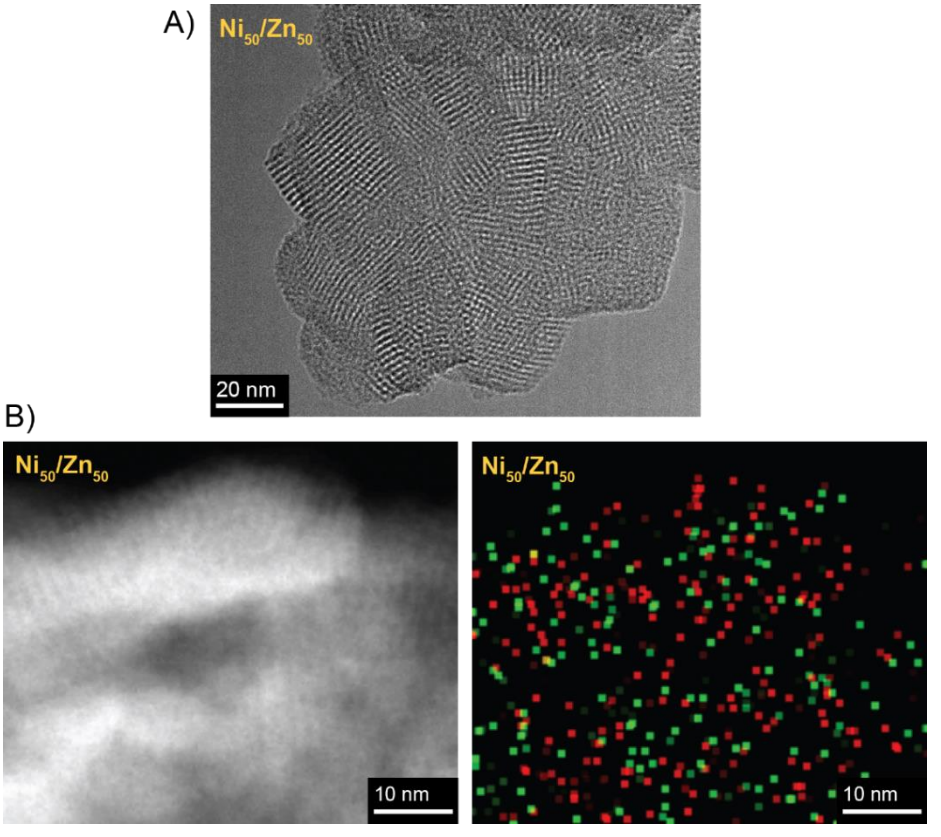

Figure 2. A) High-resolution TEM image of Ni_{50}/Zn_{50}-porphyrin COF. **B)** STEM-HAADF (left) and STEM-EDX mapping (right, red representing nickel and green representing zinc) images of Ni_{50}/Zn_{50} COF.

7.3.2 ELECTROCHEMICAL CO_2 REDUCTION PERFORMANCE

All five COF catalysts were studied by linear sweep voltammetry (LSV, Figure S15A). The largest increase in current density coupled with a noticeable positive shift to the lowest onset potential (~-0.5 V *vs* RHE) was observed in the case of the Ni_{50}/Zn_{50} COF. To get insight into the catalytic activities and selectivity of the synthesized catalysts, chronoamperometry was performed at several potentials of -0.4 to -0.8 V *vs* RHE (Figure S16). The optimal overpotential for Ni_0/Zn_{100} and Ni_{75}/Zn_{25} were found to be -0.7 V *vs.* RHE, while a less negative potential of -0.6 V vs RHE was observed in the case of Ni_{100}/Zn_0, Ni_{25}/Zn_{75} and Ni_{50}/Zn_{50} (Figure S15, Table 1). Aside from H_2, CO was the sole reduction product of Ni_0/Zn_{100}, Ni_{100}/Zn_0, and Ni_{75}/Zn_{25}, whereas formate was detected in addition to CO and H_2 in the case of Ni_{25}/Zn_{75} and Ni_{50}/Zn_{50}. Among the five modified electrodes, Ni_{50}/Zn_{50} exhibited the highest FE_{Tot} of 79% (FE_{CO}: 69% and $FE_{formate}$: 10%) followed by Ni_0/Zn_{100}

(FE_{CO}: 46%), Ni_{25}/Zn_{75} (FE_{CO}: 36% and $FE_{formate}$: 8%), Ni_{75}/Zn_{25} (FE_{CO}: 27%), and Ni_{100}/Zn_0 (FE_{CO}: 4.5%) at -0.6 V *vs* RHE.

Although H-cells are useful for studying the catalysts' behaviour, their performance is limited by: low solubility of CO_2 in an aqueous solution, dominant HER, and low current densities.[18,19] Maximizing the interaction between the electrolyte and the gas pathway via the catalytic scaffold allows flow cells to overcome mass transport limitations and suppresses the HER.[20] Therefore, the catalytic activity of the catalysts was investigated using a MEA cell through stepwise constant current densities ranging from 25 to 150 mA/cm^2 (**Figure 3A**). For all five catalysts, at higher applied current densities, higher cell voltages are measured. Specifically, a higher content of nickel (Ni_{100} to Ni_{50}) seems to be beneficial when high current densities (100 and 150 mA/cm^2) are applied, since these catalysts show both a stable signal, as well as relatively low cell voltages. In contrast, the cell voltages measured for Ni_{25}/Zn_{75} and Ni_0/Zn_{100} COFs are rather unstable at these higher current densities.

The selectivities obtained for the pure component catalysts in the MEA cells (especially at 150 mA/cm^2) reflect comparable results to the ones obtained in the H-cell setup: Ni_{100}/Zn_0 generating predominantly H_2 and Ni_0/Zn_{100} a combination of CO and H_2 (**Figure 3B** and **3F**). Generally, the COF catalysts in the MEA setup produce more CO than in the H-cell. Both pure component catalysts produce trace amounts of formate in MEA cells, of which the production is highest at 100 mA/cm^2. Although no formate was detected using Ni_{75}/Zn_{25} as a catalyst (**Figure 3C**), its product selectivity is largely a linear average of the pure components, taking into account the 75:25 Ni to Zn ratio. Interesting product selectivities are observed for the Ni_{50}/Zn_{50} and Ni_{25}/Zn_{75} catalysts (**Figure 3D** and **3E**), where a deviation from the linear average is evident in the relatively large production of formate and CH_4, especially in the case of Ni_{50}/Zn_{50}. The selectivity of this catalyst is $FE_{formate}$: 40% and FE_{CH4}: 11% at 100 mA/cm^2, and $FE_{formate}$: 43% and FE_{CH4}: 14% at 150 mA/cm^2. Larger amounts of formate and CH_4 are obtained at higher current densities, with a simultaneous decrease in the amount of CO produced. Finally, Ni_{50}/Zn_{50} and Ni_0/Zn_{100} catalysts were most effective in suppressing hydrogen evolution reaction (HER), both having a FE_{total} of 88% of the CO_2RR reduced products at 100 mA/cm^2.

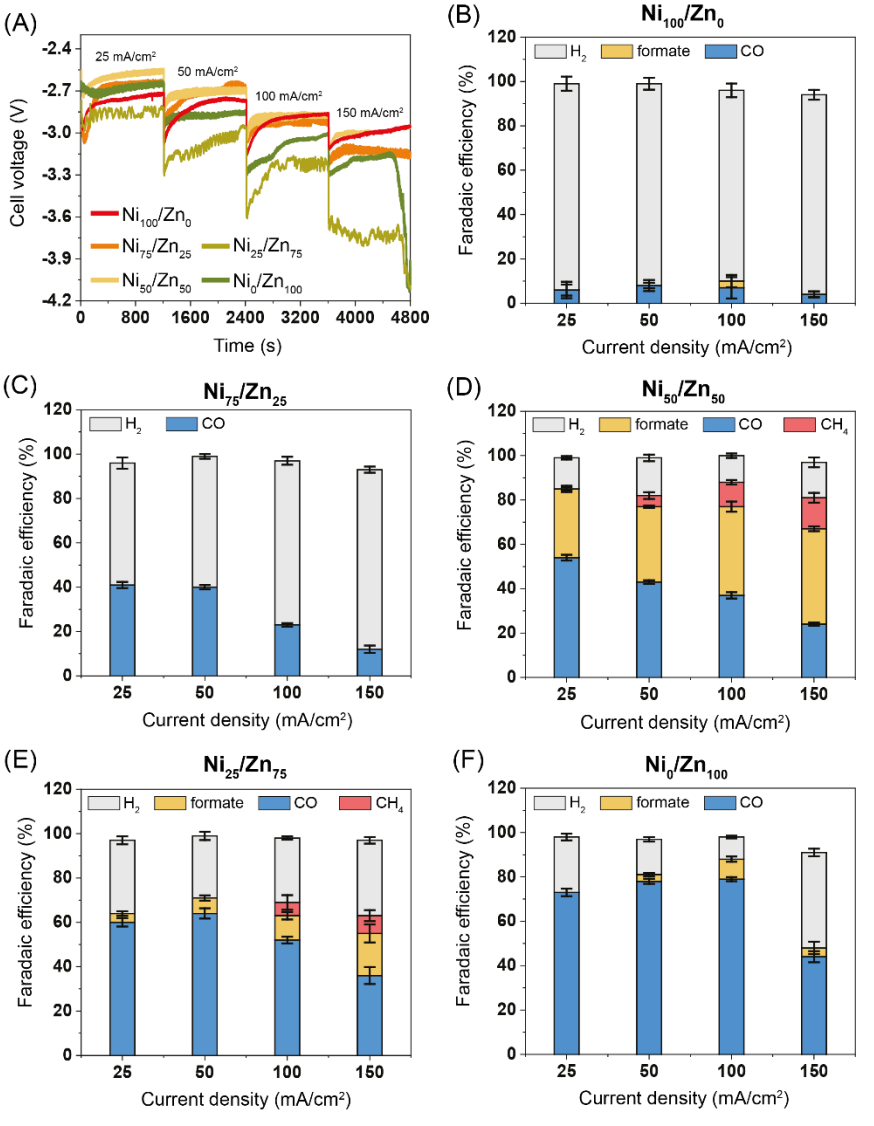

Figure 3. MEA-Cell results for the electrochemical reduction of CO_2. (**A**) Sketch graph of voltage against time at different current steps in the range of 25-150 mA/cm². Faradaic efficiency (FE) comparison of (**B**) Ni_0/Zn_{100}; (**C**) Ni_{100}/Zn_0; (**D**) Ni_{25}/Zn_{75}; (**E**) Ni_{50}/Zn_{50}; and (**F**) Ni_{75}/Zn_{25} at -0.4 to -0.8 V *vs* RHE in 0.5 M KOH.

The partial current densities for the reduced products differed significantly for the various Ni-Zn compositions (Figure S17). Considering the best performing catalyst ($Ni_{50}Zn_{50}$), the partial current density for CH_4 and formate increased at more negative voltage. Generally, the CO partial current density peaks decreased when cell voltages are lower than −3 V, while the partial current density

for H_2 production (j_{H2}) grows monotonously when the cell potential is more negative. Thus, at more negative cell voltages, the HER becomes dominant.

Since the reaction conditions during electroreduction in the MEA-cell are quite harsh (*i.e.* alkaline, relatively high current densities) and catalyst decomposition could take place during the electrochemical tests, we analysed the Ni_{50}/Zn_{50}-COF embedded GDE surface before and after catalysis. Scanning electron microscopy (SEM) was utilised to study morphological changes to the polymer particles at the surface (Figure S18). The COF particles are clearly visible on the GDE surface, both before and after catalysis. The effect of the electroreduction on these particles is noticeable in the form of unidentified matter partly covering and interpenetrating the COF particles. XPS was also used to assess chemical changes within the COF after catalytic reactions (Figure S19). A clear difference in the low binding energy region was observed, where peaks at 294.4 – 294.7 eV were only visible after catalysis. These peaks are characteristic for potassium K 2p3, which belongs to salt precipitation.[21] On the other hand, the deconvoluted peak for nitrogen into 397.5 – 397.8 eV and 398.7 – 399.3 eV is present at the electrodes both before and after catalysis, suggesting (at least partly) retention of stability of both the porphyrin-ring, as well as imine polymer backbone. Also, the signals for Ni 2p and Zn 2p are present before and after catalysis and show no clear changes. Lastly, FT-IR spectra of the electrode surfaces showed a prominent difference with peaks at 1618 an 1390 cm^{-1}, indicating characteristic vibrations of formate species, only visible after catalysis (Figure S20).

To further shed light on probable catalytic mechanisms using synthesized Ni/Zn COF catalysts, a 1:1 (w/w) physical mixture of Ni_{100}/Zn_0 and Ni_0/Zn_{100} COFs (named: Ni_{50} + Zn_{50}) was fabricated by mixing 3.5 mg of each of these COFs in 4 mL DMF through 40 min sonication. A GDE based on this mixture was prepared via the same method as the other COF catalysts and was tested as a control experiment using the same experimental MEA setup. As shown in **Figure 4A**, Ni_{50} + Zn_{50} exhibited more negative voltages compared to Ni_{50}/Zn_{50}. Ni_{50} + Zn_{50} produces higher quantities of H_2 and more comparable quantities of CO at all current densities compared to Ni_{50}/Zn_{50} (**Figure 4B** and **C**). Interestingly, Ni_{50} + Zn_{50} was also able to produce formate and even CH_4 ($FE_{formate}$: 18% and FE_{CH4}: 2.2% at 100 mA/cm^2), albeit at much lower Faradaic efficiencies than Ni_{50}/Zn_{50}. Apart from the slightly more pronounced formate production and the trace methane quantities, the catalytic activity of Ni_{50} + Zn_{50} resembles the linear average of the Ni_{100}/Zn_0 and Ni_0/Zn_{100} catalysts quite well.

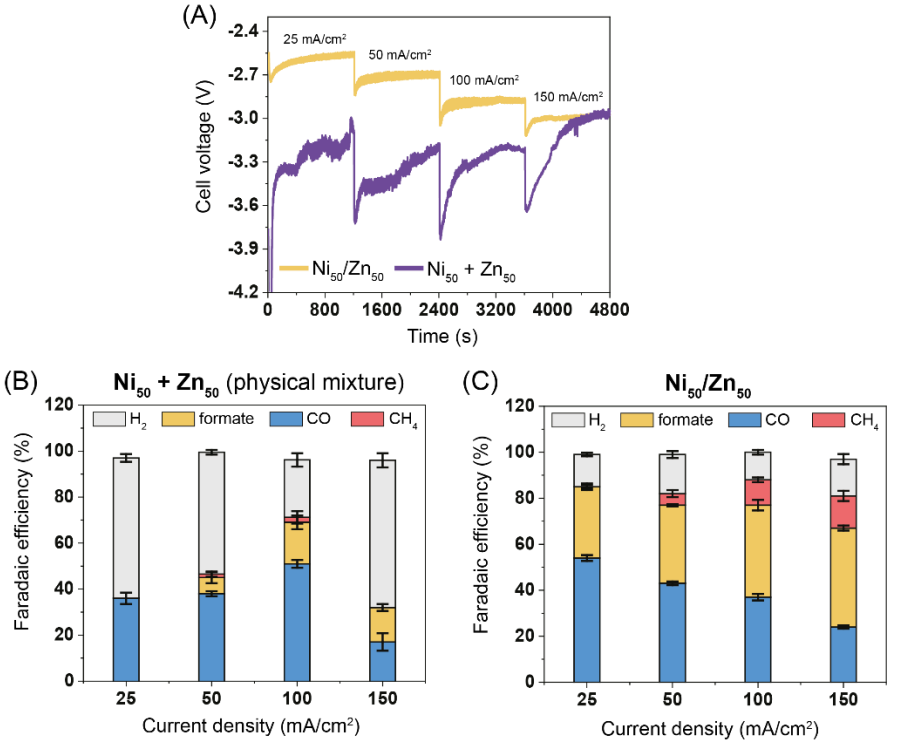

Figure 4. MEA-Cell results comparison of Ni_{50}/Zn_{50} COF and a 1:1 physical mixture of the Ni_{100}/Zn_0- and Ni_0/Zn_{100}-COFs (named Ni_{50} + Zn_{50}) for the electrochemical reduction of CO_2. (**A**) Sketch graph of voltage against time at different current steps in the range of 25-150 mA/cm²; Faradaic efficiency (FE) comparison of (**B**) Ni_{50} + Zn_{50} and (**C**) Ni_{50}/Zn_{50} in 0.5 M KOH.

7

7.4 DISCUSSION

7.4.1 STRUCTURAL SYNERGY IN MIXED NICKEL- AND ZINC-PORPHYRIN BASED COFS

Ni(II)- and Zn(II)-porphyrin units are chemically and geometrically different metal-ligand complexes. The former complex resembles a square-planar geometry, but the Zn(II)-porphyrin complex does not exactly, since the Zn-atom is often coordinated to the porphyrin nitrogens at a position slightly above the porphyrin-ring.[22] Thus, using these units as building blocks in a COF, one might expect differences in their molecular and polymeric structure, as well as in their catalytic activity.

The type of metal-ion inserted in the porphyrin ring does not have a noticeable impact on the reactivity of the amino groups to form polyimine frameworks, as was observed through FT-IR and TGA analysis of the final COFs. The chemical differences observed through spectroscopic techniques are mostly

related to porphyrin characteristic bonds. The metal ion-dependencies of the C-H pyrrole rocking vibration and the out-of-plane phenyl-ring vibrations as described for various metalloporphrins[22-24] are preserved in the porphyrin-based COF structures, and the mixed metalloporphyrin COFs display both Ni- and Zn-characteristic signals (Figure S4). This is also true for the Ni 2p and Zn 2p XPS spectra, as well as the porphyrin-specific Q-bands in the UV-vis spectra (Figure S5). The outlier in the UV spectra is the Soret band of the Ni_{100}/Zn_0 COF (at 433 nm instead of 437 nm). The red-shift of the Soret band is attributed to complexation of a porphyrin-coordinated metal with an organic ligand (in this case DMF solvent molecules) at the axial position. This phenomenon is known to occur for Zn(II)-porphyrin units, but not for Ni(II),[25] since the d^8 square-planar geometry of the Ni(II) ion coordinated to the porphyrin ligand is a highly stable conformation. The fact that solvent molecules are able to interact with the COF's active sites (at least with the zinc-ion), highlights the accessibility of these sites, which is promising for their catalytic performance.

The porous structure of 2D COFs is the result of a complex combination of variables, for example, the monomer geometry and reactivity, inter and out-of-plane defects and sheet stacking. As a result, it is not surprising that different porosities are obtained for the different metalloporphyrin COFs studied here. The small mesopore size of 2.2 nm is the expected pore size from geometry optimized crystal lattices of similar simulated COF structures.[12] The pore volume that arises from these specific pore sizes is lowest (both in absolute terms and as percentage of the total pore volume) in the Ni_0/Zn_{100} COF, which suggests the lowest amount of eclipsed stacking of crystalline domains in this framework. A brief discussion should also be dedicated to the Ni_{50}/Zn_{50} COF having the highest porosity overall, as it seems to be an effect of the Ni-TAPP: Zn-TAPP ratio (**Figure 1D**). Preventing monomer aggregation during COF synthesis is essential to allow the polycondensation reactions to occur effectively, which then allows the formation of a porous network. Yet, porphyrin units are known to aggregate through π-π stacking or metal-ligand interactions.[26] Seemingly, utilising a 1:1 ratio of metalloporphyrin monomers results in a high degree of monomer dispersion and prevents self-aggregation of the pure components. This is corroborated by the fact that STEM/EDX mapping did not indicate the presence of microdomains of the two elements (**Figure 2**). The observation of relatively homogeneous spatial distributions of Ni- and Zn-porphyrin units in the mixed metalloporphyrin COFs proves to be important in discussing the plausible mechanisms of reaction product formation during the CO_2RR experiments.

7.4.2 CATALYTIC SYNERGY IN NICKEL- AND ZINC-PORPHYRIN BASED COFS

The Ni_{50}/Zn_{50} COF catalyst was able to produce significant amounts of CH_4 during CO_2RR in the MEA cell. These results were unexpected, since single site nickel- and zinc catalysts are generally known for producing H_2 and CO respectively,[27,28] which has also been confirmed in this research. Additionally, the electrochemical conversion of CO_2 into CH_4 has a large energy barrier, and often requires high overpotentials to drive the reaction.[29] In this sense, it is valuable to hypothesize on catalytic mechanisms, taking into account that the two active sites Ni and Zn are in close (nanometer) proximity. Here, we propose three potential pathways of CH_4 production starting from CO, using the Ni_{50}/Zn_{50} COF catalyst (**Figure 5**). All pathways assume CO production from CO_2 on zinc sites, since the pure component Ni_0/Zn_{100} catalyst mostly produces CO, and the Ni_{100}/Zn_0 catalyst almost exclusively forms H_2. Additionally, all pathways consider the retention of framework structural stability under the experimental CO_2RR conditions, as has been indicated by XPS analysis (see section 7.3.2).

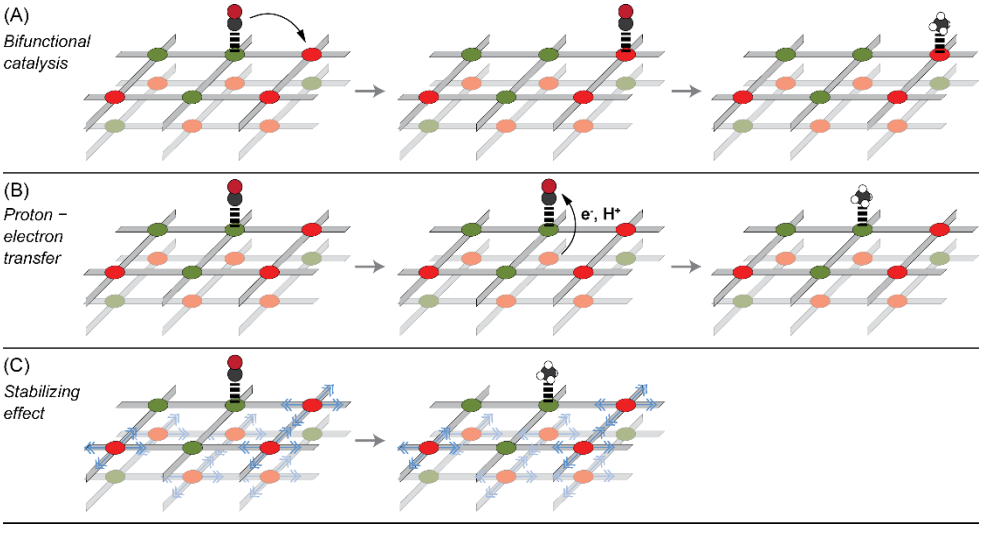

Figure 5. Schematic overview of possible simplified mechanisms behind the electrochemical conversion of CO into CH_4 using Ni_{50}/Zn_{50} COF catalysts, where nickel-sites are indicated in red and zinc-sites in green. (A): stepwise Zn–CO desorption, Ni–CO adsorption, and CO to CH_4 conversion on Ni active sites. (B): zinc active sites producing CH_4, supported by e-/H+ transfer through interlayer interactions. (C): nickel-porphyrin units providing structural stability.

Mechanism (A) illustrates the stepwise desorption of CO from zinc, followed by adsorption onto nickel, where it is converted into CH_4. This mechanism relies on differences in adsorption affinities of metal–CO complexes, of which it is known

that the interaction energy of Ni–CO (-53 kJ·mol^{-1}) is greater than the one of Zn–CO (-27 kJ·mol^{-1}).[30] The close proximity of Ni- and Zn-active sites in the Ni_{50}/Zn_{50} COF (average of ~ 0.5 – 2 nm based on **Figure 2B**) allows easily desorbed CO from Zn sites to strongly adsorb onto Ni sites where it can be converted further. Chen and coworkers have recently proposed a similar mechanism in the electroreduction of CO_2 using a Cu-phthalocyanine-based MOF,[17] where the formation of C_2H_4 relies on the preferred desorption of intermediate products from one of the two neighboring active sites. Mechanism (A) can still be valid in the case of the Ni_{50} + Zn_{50} physical mixture, which explains the trace amounts of CH_4 that this catalyst was able to form (**Figure 4**). In the case of Ni_{50} + Zn_{50}, however, the Ni-Zn average distance is more likely to approach the COF particle size range (10 – 100 µm, as estimated from Figure S18) and only likely to be in the nanometer-range at the interface of the separate COF particles.

The supply of electrons and protons from Ni active sites to the Zn–CO site is proposed to be the dominant pathway in mechanism (B). Ni_{100}/Zn_0 catalysts have been shown to produce a large amount of H_2 through water electrolysis. Abundant nickel hydride complexes are generated, allowing the possibility of hydrogen atom transfer towards the Zn–CO site, which are required for the conversion into CH_4. Since the Ni- and Zn-TAPP phenyl rings are oriented (close to) perpendicular with respect to the porphyrin ring, it is unlikely that proton/electron transfer occurs within one COF sheet because of the poor conjugation. However, efficient charge transfer is known to occur in stacked porphyrin units,[31] and has been proven in stacked porphyrin-based COF sheets.[32]

Mechanism (C) assumes that Ni-porphyrin units solely provide a stabilizing effect for Zn active sites to be able to convert CO into CH_4. The cell voltages during Ni_{25}/Zn_{75} and Ni_0/Zn_{100} MEA experiments at high current densities (**Figure 3A**) are indeed quite unstable compared to the COFs with higher nickel ratios. In addition, the porosity measurements of the powders showed that implementation of Ni-porphyrin units in Zn-porphyrin-based COFs creates a structural benefit (larger micro- and mesoporosity), resulting in more accessible zinc active sites. Xin and coworkers have proven that – given sufficient electrical conductance, microporosity, and stability – single-site Zn catalysts are able to produce CH_4 in high (FE 85 %) efficiencies.[29] Detailed *in-situ* IR studies utilizing, for example, a spectroelectrochemical H-cell, should be conducted in order to clarify which mechanisms of the ones proposed here are operational.

Lastly, this discussion has largely focussed on the formation of CH_4 on the Ni_{50}/Zn_{50} catalyst, as this is, in our view, the most unexpected yet most promising result. In addition, the relatively large quantities of formate (FE: 43% at 150 mA/cm^2) on the Ni_{50}/Zn_{50} catalyst are also worth discussing. A single definitive reaction pathway of CO_2 towards formate is not available, but a general consensus is that formate formation is a competing reaction with CO formation.[4,33] Cheng et al.[4] investigated competing CO and formate reaction mechanisms on a Cu(100) surface through quantum mechanics calculations with an explicit description of water. Here, they claim that direct reduction of CO_2 by metal hydrides leads to $HCOO^-$ formation. Comparing the Ni_{50}/Zn_{50} catalyst to the catalysts with higher nickel content, H_2 formation is inhibited to an even larger degree than expected based on the linear average. It is possible that the hydrides that are generated on the Ni-sites during water splitting are made available for subsequent formate formation reactions. Therefore, it is reasonable to suggest a similar pathway as mechanism (B) for formate formation on Zn-sites through hydride transfer from the neighbouring Ni-sites.

7.5 Conclusions

In conclusion, a novel synthetic strategy was developed by combining Ni- and Zn-porphyrin monomers to yield bifunctional COFs (Ni_{75}/Zn_{25}, Ni_{50}/Zn_{50}, and Ni_{25}/Zn_{75}), which were compared to the pure component Ni- and Zn-porphyrin COFs (Ni_{100} and Zn_{100}). Structural synergy was discovered as the Ni_{50}/Zn_{50} COF exhibited the highest micro- and mesoporosity. Additionally, synergy in CO_2RR catalytic activity between the two metal centres was apparent through the production of the relative largest amount of CH_4 using the Ni_{50}/Zn_{50} catalyst, compared to mostly H_2 and CO at the Ni_{100} and Zn_{100} catalysts respectively. As such, this material platform allowed tunable product selectivity through simple adjustment of the Ni- and Zn-porphyrin monomeric ratio. Considering the wide range of metalloporphyrins available, we anticipate this strategy will expand the library of bi- or even higher order-functional COF catalysts considerably, and that such catalysts are then utilized to tackle complex multi-step reactions as is shown here.

7.6 SUPPORTING INFORMATION

Reagents and analysis techniques

For synthetic procedures all reagents and solvents were of commercial reagent grade and were used without further purification unless stated otherwise. Pyrrole was purchased from TCI Europe N.V (Zwijndrecht, Belgium). Propionic acid (≥ 99 %), 4-nitrobenzaldehyde (98 %), tin(II) chloride dihydrate (98 %), acetic anhydride (≥ 98 %), nickel acetate tetrahydrate (98 %) and zinc acetate dihydrate (≥ 98 %) were purchased from Merck Sigma (Zwijndrecht, The Netherlands). 1-Butanol and pyridine (≥ 99 %) were purchased from Acros Organics B.V.B.A (Geel, Belgium). Ortho-dichlorobenzene was purchased from abcr GmbH (Karlsruhe, Germany). 2,5-Dihydroxyterephthaldehyde (98 %) was purchased from Fluorochem BV (Glossop, United Kingdom). Pyrrole was purified by filtration through a plug of alumina (Acros aluminium oxide, 0.050–0.200 mm, 60A).

NMR spectra were recorded at 298 K (unless stated otherwise) on an Agilent-400 MR DD2 spectrometer (400 MHz). ^{1}H NMR chemical shifts (δ) are given in parts per million (ppm) and were referenced to tetramethylsilane (0.00 ppm). Coupling constants are reported as *J* values in Hertz (Hz). Data for ^{1}H NMR spectra are reported as follows: chemical shift (multiplicity, coupling constant, integration). Multiplicities are abbreviated as s (singlet), d (doublet). FT-IR spectra were recorded on a PerkinElmer Spectrum 100 FT-IR Spectrometer with an universal ATR accessory over a range of 4000 to 650 cm^{-1}. TGA analyses were performed from 30 to 860 °C, under a nitrogen atmosphere at a heating rate of 10 °C·min^{-1} using a Perkin Elmer TGA 4000. Prior to the measurement, the samples were degassed at 130 °C for one hour under a nitrogen atmosphere. Liquid UV-vis spectra were recorded at 298 K on a PerkinElmer Lambda 35 UV-vis spectrometer (quartz cuvette) at a concentration of 5 µM in DMF. Prior to the measurements, the COF-DMF suspensions were sonicated for 30 minutes at room temperature. Nitrogen isotherms were measured on the NOVAtouch gas sorption analyzer from Quantachrome Instruments with high purity N2 (99.99%) at 77 K. Prior to the sorption measurements, all samples were degassed at 130 °C under vacuum for 16 h. The Quantachrome VersaWin software package was used for calculations of pore size distributions by fitting the nitrogen adsorption isotherms to the quenched solid density functional theory (QSDFT) carbon model (using slit/cylindrical/spherical pores). No smoothing factor was applied for the PSD calculation. X-ray photoemission spectroscopy (XPS) measurements were performed with a Thermo Scientific K-Alpha spectrometer using a monochromatic

Al Kα excitation source. The spectrometer was calibrated using the C 1s adventitious carbon with a binding energy of 284.8 eV. The base pressure at the analysis chamber was about 2×10^{-9} mbar. The spectra were recorded using a spot size of 400 µm at a pass energy of 50 eV and a step size of 0.1 eV. PXRD patterns were measured on a Rigaku MiniFlex 600 powder diffractometer using a Cu-Kα source (λ = 1.5418 Å) over the 2θ range of 2 ° to 40 ° with a scan rate of 1 °·minute^{-1}. For high-resolution transmission electron microscopy analysis, a FEI cubed Cs corrected Titan was used. HREM Lattice images are collected on a Thermo Scientific Ceta™ 16M. A low intensity on the camera was used to avoid beam damage. In scanning mode (STEM) ADF (Annular Dark Field) images are collected. In this mode, a sub nm beam is scanned on the electron transparent sample and for each beam position the diffracted electrons are collected on a ring shape detector. On heavy/thicker parts of the sample more diffracted electrons are collected and hence show up bright in the image. Elemental mapping in STEM mode was done, using the super-X in the ChemiSTEM™ configuration. The EDX spectrum is collected for each beam position in a STEM image. For TEM sample preparation, the COF powder was crushed in a mortar first without and then under some ethanol. The dispersion was ultrasonically shaken for 5 minutes. Using a pipette, the dispersion was drop casted onto a C foil supported with a Cu grid (holey Quantifoil TEM grid). After drying, the grid was ready for TEM inspection. Scanning electron microscopy (SEM) images were recorded with a JEOL JSM-840 SEM: materials were deposited onto a sticky carbon surface on a flat sample holder, vacuum-degassed, and sputtered with gold at a thickness of 15 nm.

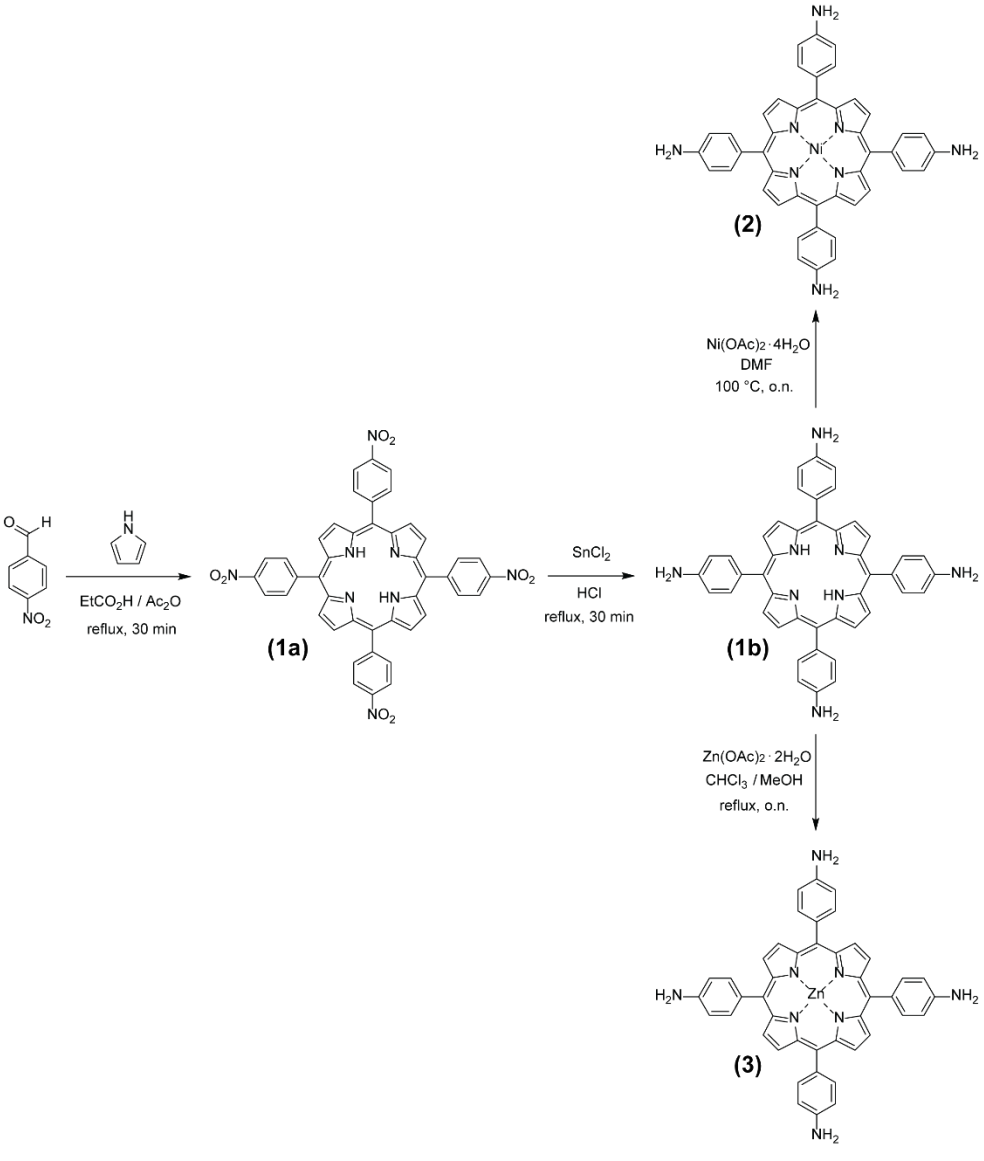

Scheme S1 Reaction scheme towards 5,10,15,20-tetrakis(4-nitrophenyl) porphyrin (**1a**); 2H-5,10,15,20-tetrakis(4-aminophenyl) porphyrin (**1b**); Ni(II)-5,10,15,20-tetrakis(4-aminophenyl) porphyrin (**2**); and Zn(II)-5,10,15,20-tetrakis(4-aminophenyl) porphyrin (**3**).

*Synthesis of H_2TNPP (**1a**)*

A solution of 4-nitrobenzaldehyde (18.9 g, 125 mmol, 4.0 equiv) in propionic acid (500 mL) and acetic anhydride (23.6 mL) was heated to 150 °C. Then, pyrrole (8.7 mL, 125 mmol, 4.0 equiv) was added dropwise and the resulting black mixture was refluxed for 30 minutes. Upon cooling, the precipitate was successively filtered off,

washed with water (200 mL), and dried under high vacuum. Pyridine (200 mL) was added to the black solid and the suspension was refluxed for 30 minutes. Upon cooling, the mixture was stored at 4 °C for 16–20 hours. The resulting precipitate was successively filtered off, washed with acetone (200 mL), and dried under high vacuum to afford TNPP (5.5 g, 22%) as a dark purple solid. Due to the poor solubility of H_2TNPP, it was immediately used in the next step without characterization.

*Synthesis of H_2TAPP (**1b**)*

H_2TNPP (5.5 g, 6.9 mmol, 1.0 equiv) was suspended in 37% hydrochloric acid (250 mL) and the resulting mixture was stirred at 20 °C for 30 minutes. Then, tin(II) chloride dihydrate (23.3 g, 103 mmol, 15 equiv) was added and the reaction mixture was stirred at 80 °C for 30 minutes. Upon cooling, the mixture was cooled further to 0 °C and carefully neutralized by the addition of ammonium hydroxide (300 mL). The resulting precipitate was filtered off, and air dried. The black solid was suspended in THF (50 mL) and stirred at 20 °C for 15 minutes and then it was filtered. Heptane (200 mL) was added to the filtrate to precipitate the product. Most THF was evaporated under reduced pressure and the resulting suspension was centrifuged. The supernatant was removed, the precipitate was washed with pentane (100 mL) and dried under high vacuum to afford H_2TAPP (1.5 g, 33 %) as a purple solid. ^{1}H NMR (400 MHz, $(CD_3)_2SO$) δ (ppm): -2.77 (s, 2H), 5.53 (s, 8H), 6.97 (d, *J* = 8.3 Hz, 8H), 7.81 (d, *J* = 8.3 Hz, 8H), 8.84 (s, 8H). Spectral data were in agreement with literature values.[3]

*Synthesis of Ni-TAPP (**2**)*

A solution of H_2TAPP (530 mg, 0.79 mmol, 1.0 equiv) and nickel acetate tetrahydrate (2.0 g, 7.9 mmol, 10 equiv) in DMF (100 mL) was heated at 100 °C for 16–20 hours. Upon cooling, water (300 mL) was added. The resulting precipitate was filtered off, and air dried. The residue was dissolved in THF and filtered through a plug of silica. The purified material was dissolved in minimal THF and precipitated by the addition of hexane. Most THF was evaporated under reduced pressure and the resulting suspension was centrifuged. The supernatant was removed, the precipitate was washed with hexane (100 mL) and dried under high vacuum to afford Ni-TAPP (298 mg, 52 %) as a red solid. ^{1}H NMR (400 MHz, $(CD_3)_2SO$) δ (ppm): 5.46 (s, 8H), 6.88 (d, *J* = 8.4 Hz, 8H), 7.60 (d, *J* = 8.3 Hz, 8H), 8.73 (s, 8H). Spectral data were in agreement with literature values.[3]

*Synthesis of Zn-TAPP (**3**)*

A solution of H_2TAPP (506 mg, 0.75 mmol, 1.0 equiv) and zinc acetate dihydrate (1.6 g, 7.5 mmol, 10 equiv) in chloroform/methanol (100 mL, 1:1, v/v) was refluxed for 16–20 hours. Upon cooling, triethylamine (2 mL) was added and the mixture was evaporated to dryness. The residue was dissolved in THF and filtered through a plug of silica. The purified material was dissolved in minimal THF and precipitated by the addition of hexane. Most THF was evaporated under reduced pressure and the resulting suspension was centrifuged. The supernatant was removed, the precipitate was washed with hexane (100 mL) and dried under high vacuum to afford ZnTAPP (347 mg, 63 %) as a green solid. ^{1}H NMR (400 MHz, $(CD_3)_2SO$) δ (ppm): 5.41 (s, 8H), 6.93 (d, J = 8.3 Hz, 8H), 7.77 (d, J = 8.3 Hz, 8H), 8.80 (s, 8H). Spectral data were in agreement with literature values.[3]

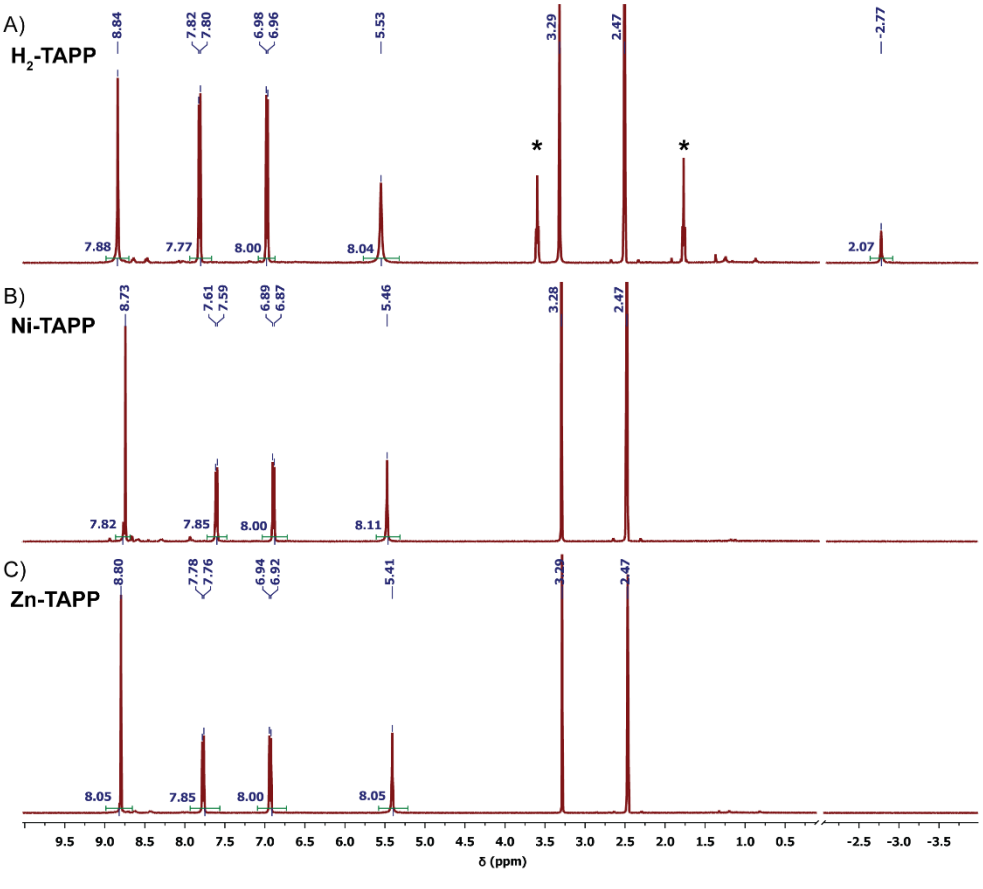

Figure S1 ^{1}H-NMR spectra of the porphyrin monomers: **A)** H_2TAPP (**1b**), **B)** Ni-TAPP (**2**), and **C)** Zn-TAPP (**3**). The asterisks indicate the presence of residual solvent (THF).

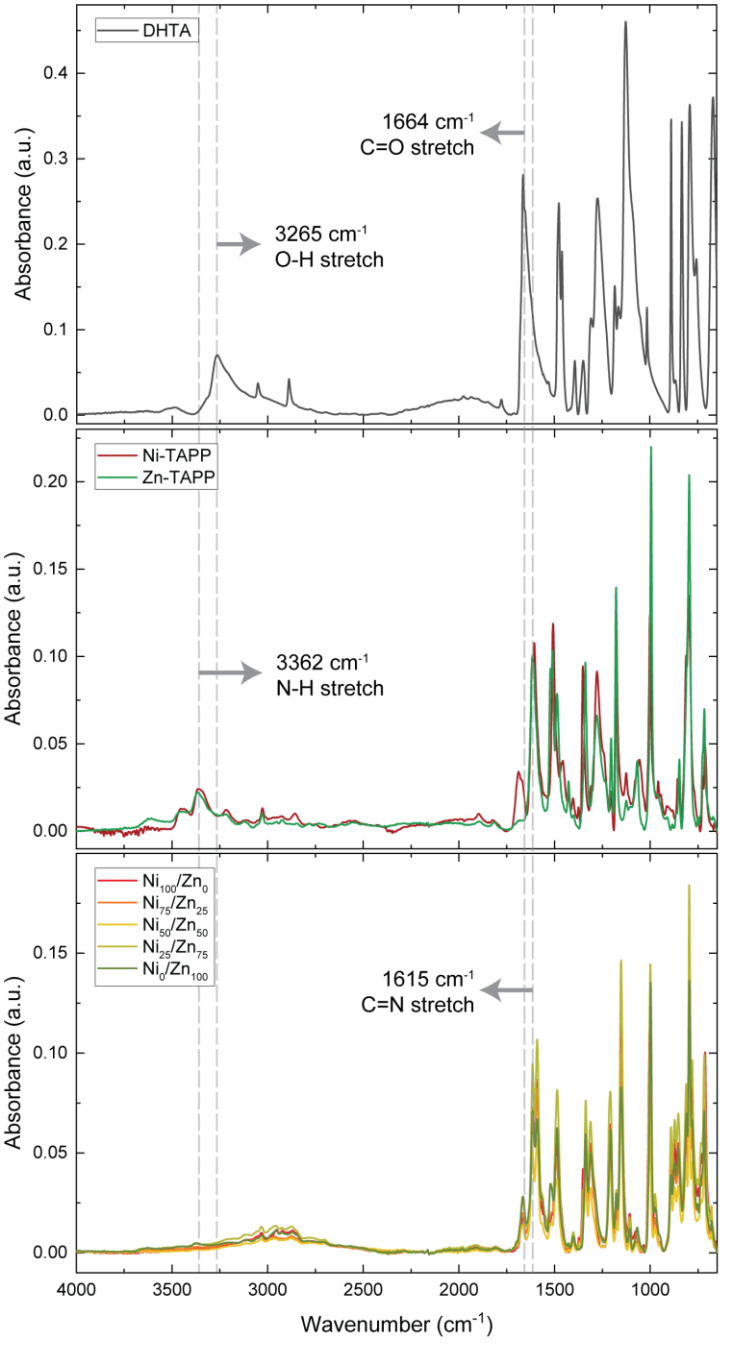

Figure S2 FT-IR spectra of 2,5-dihydroxyterephthaldehyde (DHTA, top), nickel- and zinc-inserted 5,10,15,20-tetrakis(4-aminophenyl)porphyrin (Ni-TAPP and Zn-TAPP, middle) and Ni/Zn-porphyrin COFs (bottom). Characteristic vibrations for each compound are indicated.

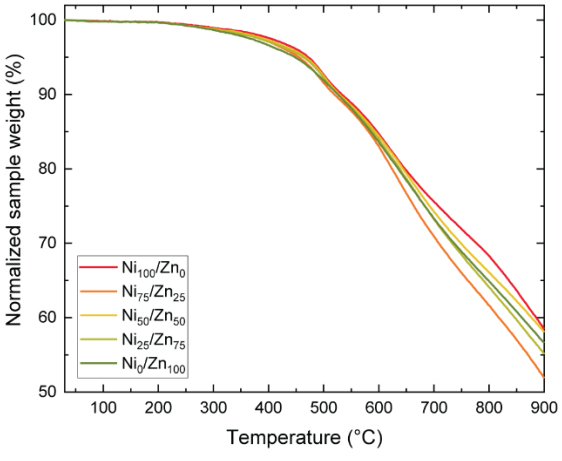

Figure S3 TGA curves of Ni/Zn-porphyrin COFs at a 10 °C/min heating rate and under a constant nitrogen flow of 20 mL/min.

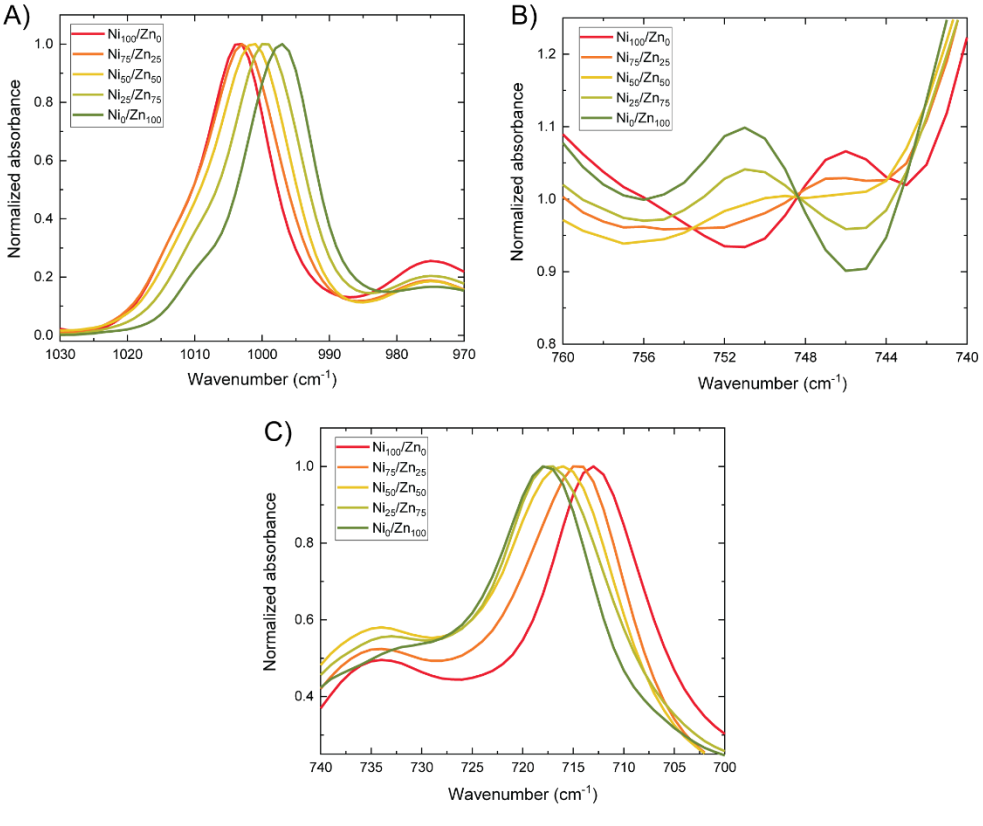

Figure S4 Normalized FT-IR spectra of Ni/Zn-porphyrin COFs, zoomed-in on the region of: **A)** pyrrole rocking vibrations and **B)** and **C)** out-of-plane phenyl- and porphyrin ring-vibrations.

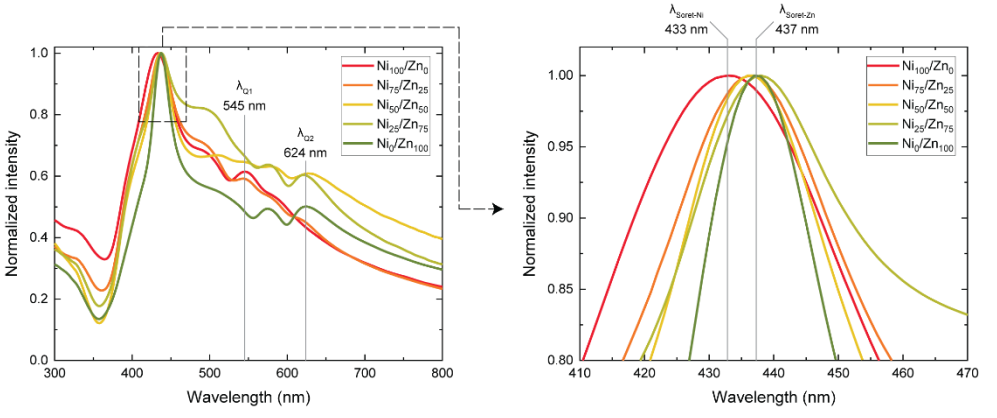

Figure S5 UV-vis spectra of Ni/Zn-porphyrin COF particles sonicated in DMF. The right graph is a zoom-in of the left. Ni- and Zn-porphyrin-characteristic Soret bands and Q bands are indicated.

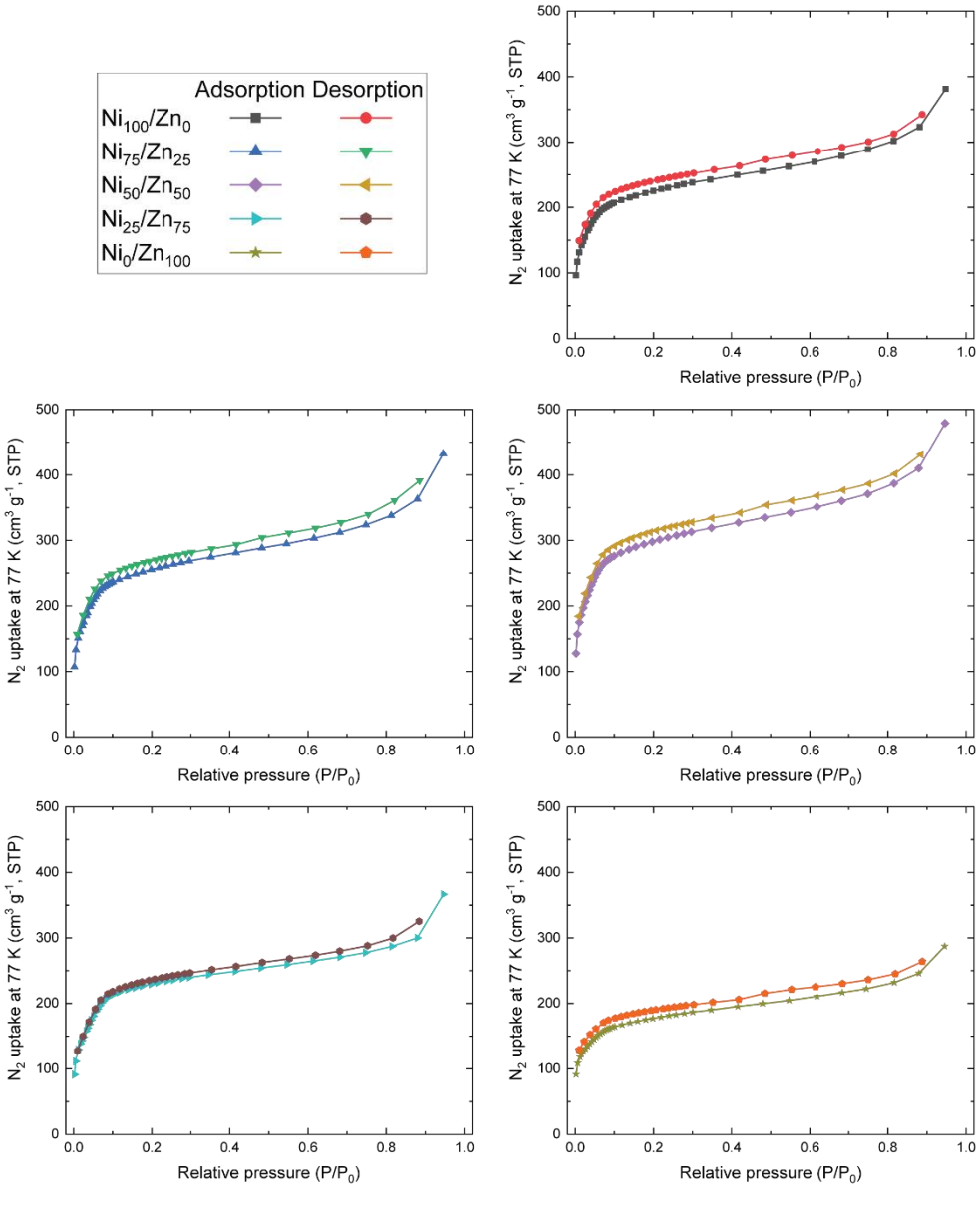

Figure S6 Nitrogen ad- and desorption isotherms of Ni/Zn-porphyrin COFs at 77 K.

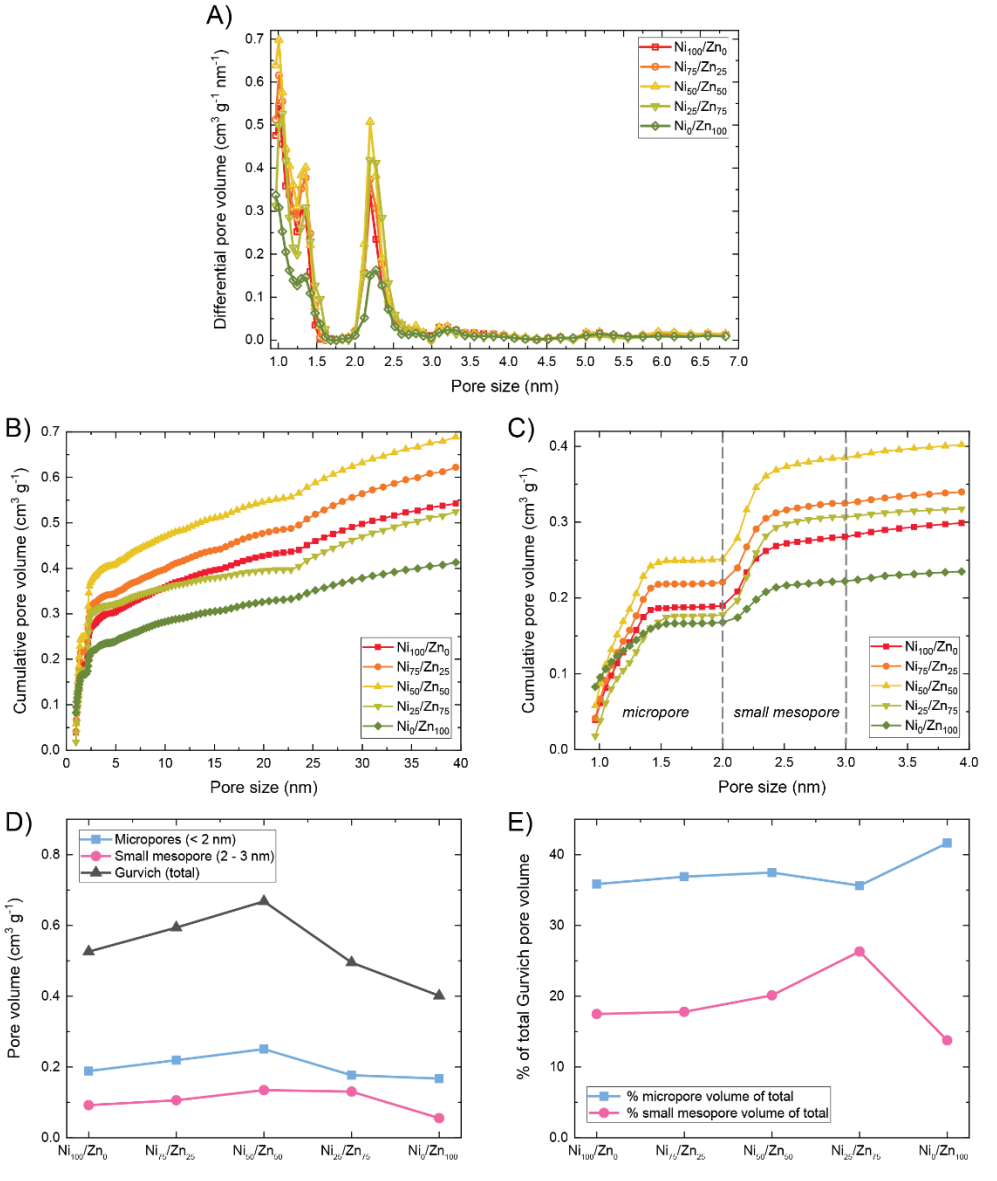

Figure S7 A) Complete pore size distributions and **B)** cumulative pore volume of Ni/Zn-porphyrin COFs, calculated from experimental N_2 adsorption isotherm branches and based on a QSDFT carbon model with slit/cylindrical pore geometries. **C)** Zoom-in of graph B), highlighting the regions where micropores and small mesopores are most dominant. **D)** Micro- and small mesopore volumes of Ni/Zn-porphyrin COFs estimated from the dotted lines represented in graph C), as well as their Gurvich pore volumes. **E)** Micro- and small mesopore volume as a percentage of the total Gurvich pore volume.

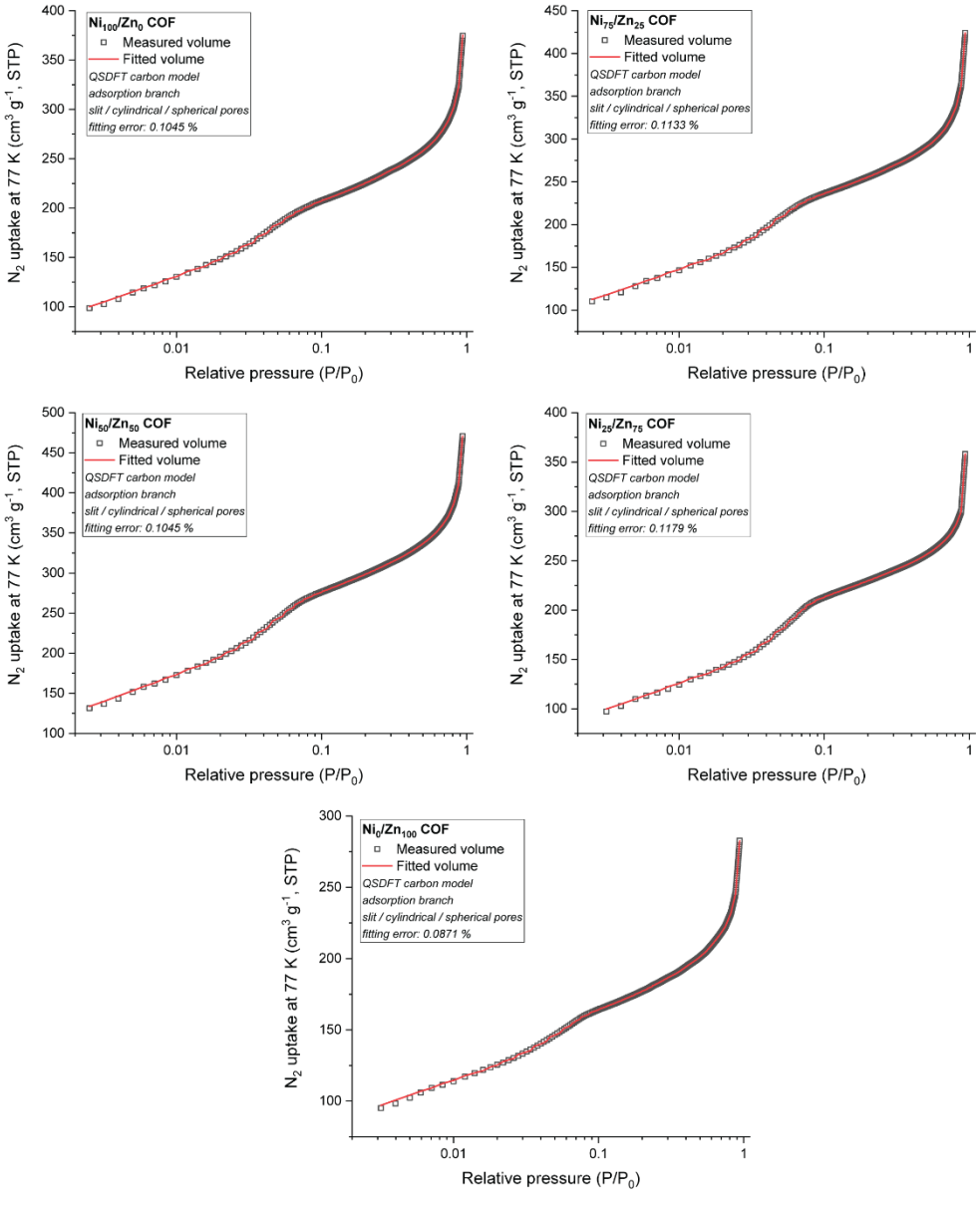

Figure S8 Fitting curves of the PSDs of Ni/Zn-porphyrin COFs, with indicated fitting errors.

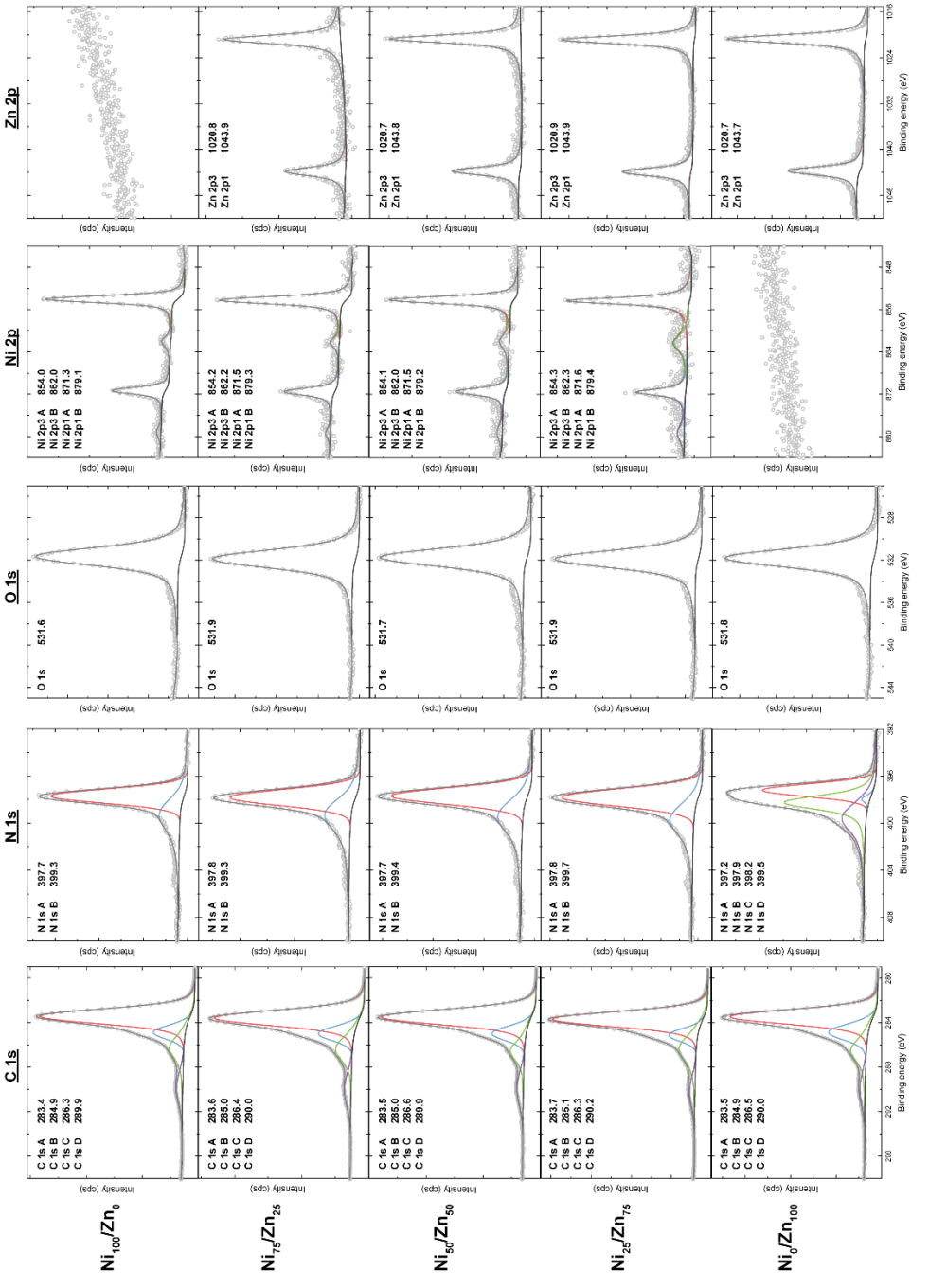

Figure S9 High-resolution N 1s, O 1s, Ni 2p, and Zn 2p XPS spectra of Ni/Zn-porphyrin COFs.

Table S1 XPS-derived atomic percentages of C, N, O, Ni, and Zn for Ni/Zn-porphyrin COFs.

	At. % C	At. % N	At. % O	At. % Ni	At. % Zn
Ni_{100}/Zn_0	80.21	10.48	8.26	1.05	0
Ni_{75}/Zn_{25}	79.31	10.58	8.73	0.9	0.49
Ni_{50}/Zn_{50}	79.81	10.64	7.98	0.63	0.93
Ni_{25}/Zn_{75}	79.44	10.42	8.57	0.45	1.12
Ni_0/Zn_{100}	80.47	10.4	7.62	0	1.51

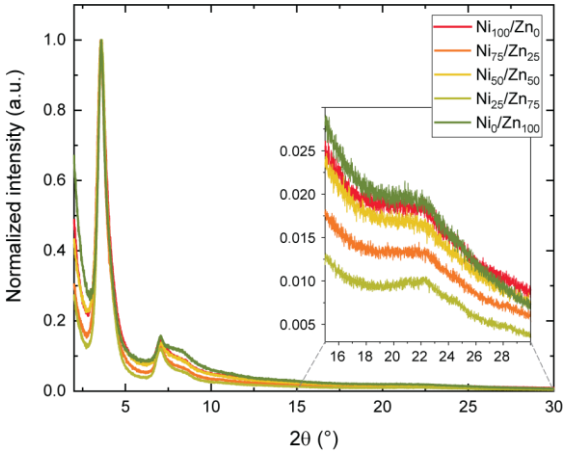

Figure S10 PXRD patterns of Ni/Zn-porphyrin COFs.

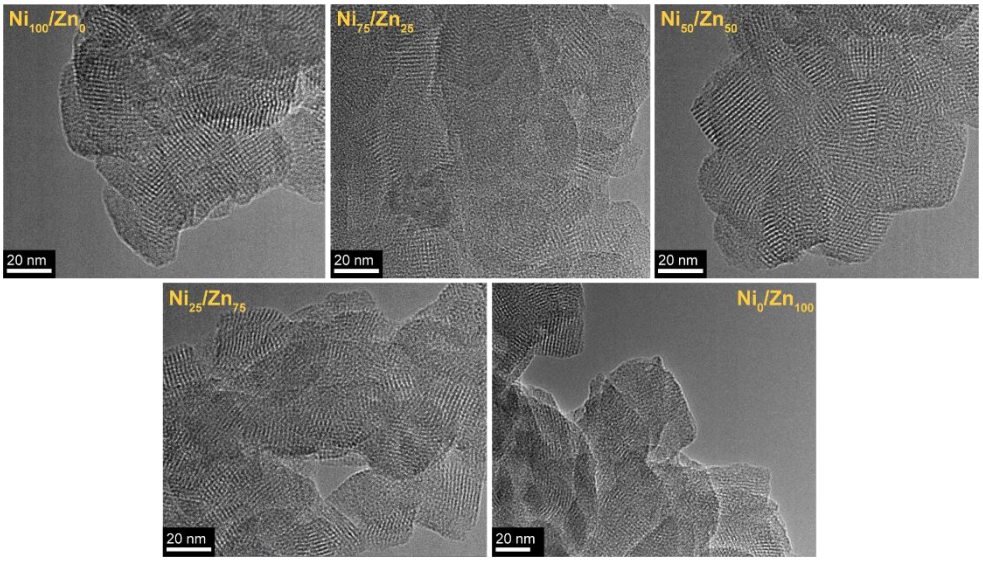

Figure S11 High-resolution TEM images of Ni/Zn-porphyrin COFs.

Faradaic efficiency calculation (for both H-cell and MEA):

Gas phase mole fractions were determined using GC injections periodically every 5 min during electrolysis. Liquid mole fractions were determined using NMR analysis. To estimate the Faradaic efficiency of gaseous products, the mole fractions of CO and H_2 were calculated from GC injections. Under constant pressure and temperature (ideal gas law), the volume fraction of the gas products (from GC) equals their corresponding mole fraction. The mole fraction of water vapour exiting the reactor was measured using a humidity sensor and found to be 78% (x_{H2O} = 0.023). Since the sum of mole fractions is equal to 1, the mole fraction of CO_2 exiting was calculated as Eq. S1.

Eq. S1:

$$x_{CO2,out} = 1 - (x_{CO} + x_{H2O} + x_{H2})$$

After calculating the mole fractions of all gaseous products, the volumetric flow rate at the reactor outlet (sccm units) was measured with the mass flow meter and used to calculate the moles of each product.

Eq. S2:

$$n_{CO} = \frac{P_{cal}}{RT_{cal}} \times \dot{V}_{outlet} \times x_{CO}$$

Eq. S3:

$$n_{H2} = \frac{P_{cal}}{RT_{cal}} \times \dot{V}_{outlet} \times x_{H2}$$

Eq. S4:

$$FE_{CO} = \frac{n_{CO} \times n^e \times F}{I} \times 100\ \%$$

e.g.: n_{CO} – moles/s of CO produced, n^e- number of electrons involved in CO_2RR (2 for CO), F- 96485 C/mol and I - applied current (in Amperes). P_{cal} and T_{cal} refer to the calibration T and P of the mass flow meters.

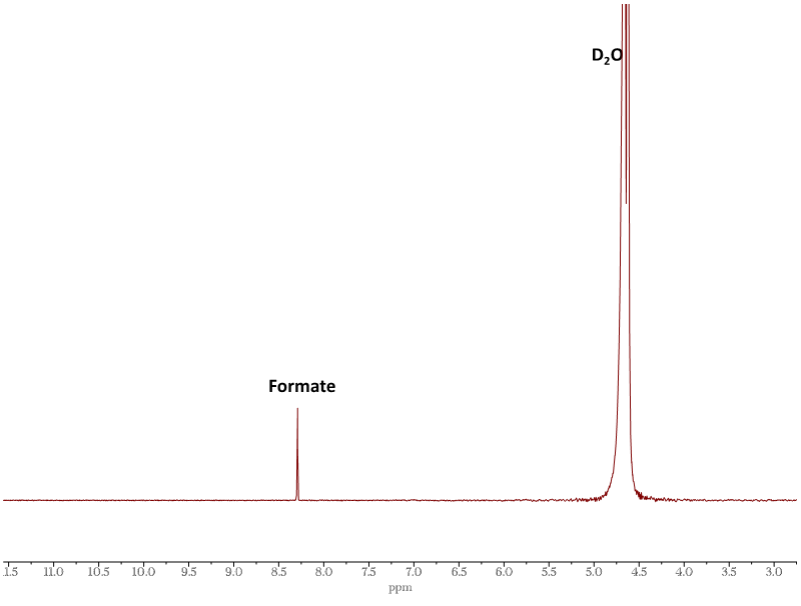

Figure S12 ^{1}H NMR spectrum example of formate obtained during CO_2 electroreduction.

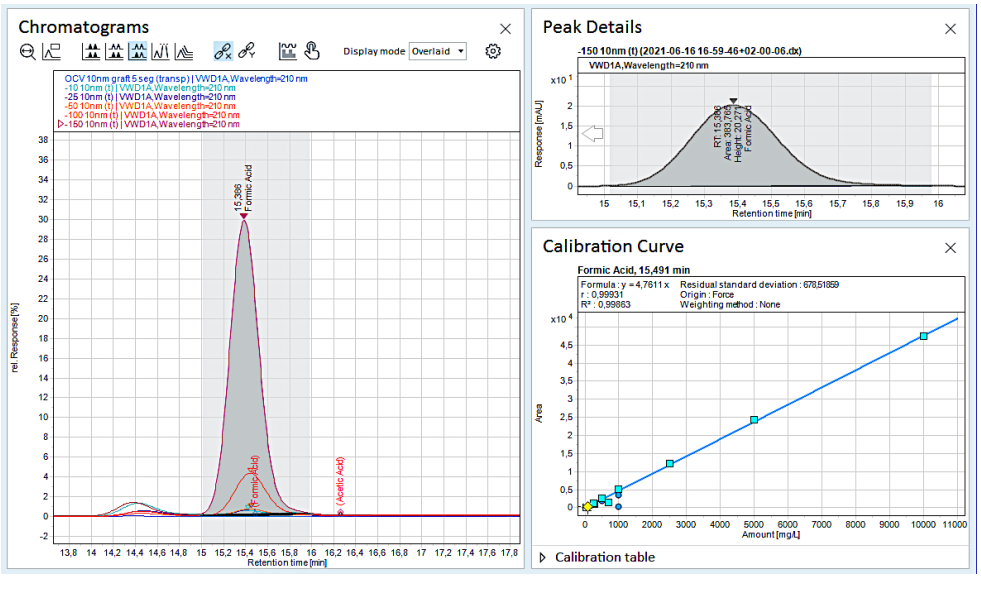

Figure S13 High-Performance Liquid Chromatography (HPLC) chromatogram example of formic acid obtained during CO_2 electroreduction.

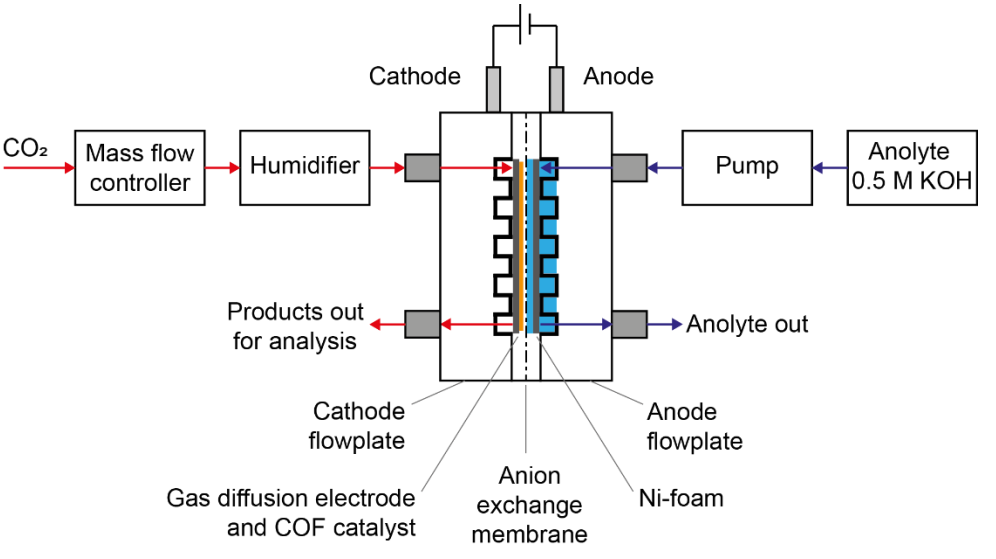

Figure S14 Schematic of MEA reactor.

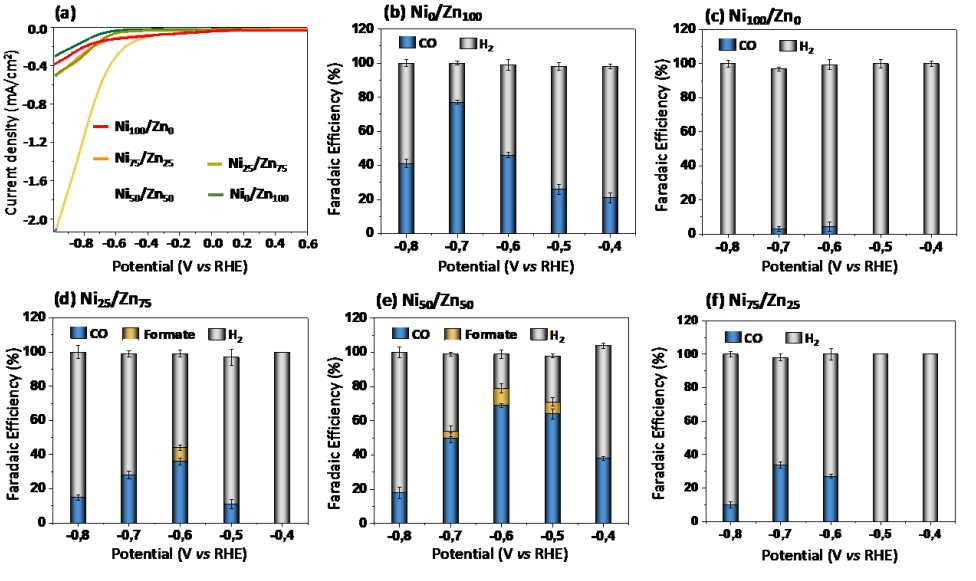

Figure S15 H-Cell results for the electrochemical reduction of CO_2. (a) Linear sweep voltammetry (LSV) comparison of heterogeneous COF complexes. Faradaic efficiency (FE) of (b) Ni_0/Zn_{100}; (c) Ni_{100}/Zn_0; (d) Ni_{25}/Zn_{75}; (e) Ni_{50}/Zn_{50}; and (f) Ni_{75}/Zn_{25} at -0.4 to -0.8 V *vs* RHE in 0.1 M $KHCO_3$.

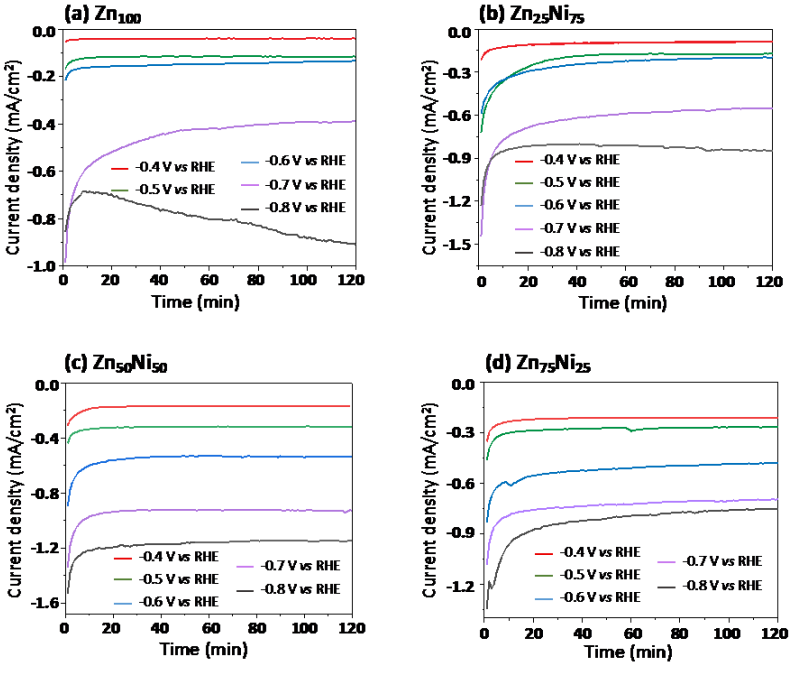

Figure S16 Chronoamperometry comparison of (a) Ni_0/Zn_{100}; (b) Ni_{75}/Zn_{25} (c) Ni_{50}/Zn_{50}; and (d) Ni_{25}/Zn_{75} at -0.4 to -0.8 V *vs* RHE in 0.1 M $KHCO_3$ H-cell.

Table S2 Product analysis of heterogeneous catalysts in a H-Cell using 0.1 M $KHCO_3$ electrolyte.

Compound	V vs RHE	*j* (mA/cm²)	FE% (CO)	FE% (formate)	FE% (CH_4)	FE% (H_2)
Ni100/Zn0	-0.4	-0.02	0	0	0	100±1.5
	-0.5	-0.048	0	0	0	100±2.3
	-0.6	-0.051	4.5±2.7	0	0	95±3
	-0.7	-0.21	3±1.5	0	0	94±1.1
	-0.8	-0.36	0	0	0	100±2
Ni0/Zn100	-0.4	-0.035	21±2.8	0	0	77±1.5
	-0.5	-0.06	26±3	0	0	72±2.3
	-0.6	-0.08	46±3.1	0	0	53±3
	-0.7	-0.34	77±1.2	0	0	23±1.1
	-0.8	-0.82	41±2.5	0	0	59±2.0
Ni75/Zn25	-0.4	-0.11	0	0	0	100
	-0.5	-0.15	0	0	0	100

Compound	V vs RHE	*j* (mA/cm²)	FE% (CO)	FE% (formate)	FE% (CH_4)	FE% (H_2)
Ni75/Zn25	-0.6	-0.28	27±1.1	0	0	73±3.4
	-0.7	-0.56	34±1.8	0	0	64±2
	-0.8	-0.73	10±2	0	0	80±1.5
Ni50/Zn50	-0.4	-0.21	38±1	0	0	66±1.5
	-0.5	-0.33	64±2.7	7±2.4	0	27±1.3
	-0.6	-0.49	69±1.2	10±2.8	0	20±2.4
	-0.7	-0.94	50±2.8	4±3.2	0	45±1.0
	-0.8	-1.1	18±3.4	0	0	82±3.1
Ni25/Zn75	-0.4	-0.18	0	0	0	100
	-0.5	-0.27	11±2.7	0	0	86±4.6
	-0.6	-0.46	36±2.0	8±1.4	0	55±2.0
	-0.7	-0.66	28±2.3	0	0	71±1.8
	-0.8	-0.7	15±1.5	0	0	85±3.7

Table S3 Product analysis of heterogeneous catalysts in a MEA Cell using 0.5 M KOH electrolyte.

Compound	V vs RHE	*j* (mA/cm²)	FE% (CO)	FE% (formate)	FE% (CH_4)	FE% (H_2)
Ni100/Zn0	-2,76	25	6±3.7	0	0	93±1.5
	-2,83	50	8±2.5	0	0	91±2.3
	-2,88	100	7±4.8	3±2.8	0	86±3
	-3,06	150	4±1.2	0	0	90±1.1
Ni0/Zn100	-2,7	25	73±1.7	0	0	25±1.7
	-2,86	50	78±1.1	3±0.8	0	16±1.0
	-3,13	100	79±0.9	9±1.2	0	10±0.6
	-3,19	150	44±2.5	4±2.8	0	43±0.7
Ni75/Zn25	-2,68	25	41±1.4	0	0	55±2.6
	-2,71	50	40± 1.0	0	0	59±1.1
	-2,91	100	23±0.8	0	0	74±1.8
	-3,14	150	12±0.8	0	0	76±1.4

Compound	V vs RHE	*j* (mA/cm²)	FE% (CO)	FE% (formate)	FE% (CH_4)	FE% (H_2)
Ni50/Zn50	-2,58	25	54±1.3	31±1.4	0	14±0.8
	-2,7	50	43±0.8	34±0.5	5±1.0	17±1.5
	-2,88	100	37±1.4	40± 2.1	11±2.3	12±1
	-3	150	24±0.7	43±1.0	14±1.1	16±2.2
Ni25/Zn75	-2,86	25	60±1.9	4±1.0	0	33±1.8
	-3,14	50	64±2.3	7±1.2	0	28±1.9
	-3,3	100	52±1.5	11±1.7	0	35±0.8
	-3,75	150	36±3.8	19±4.1	0	42±1.5

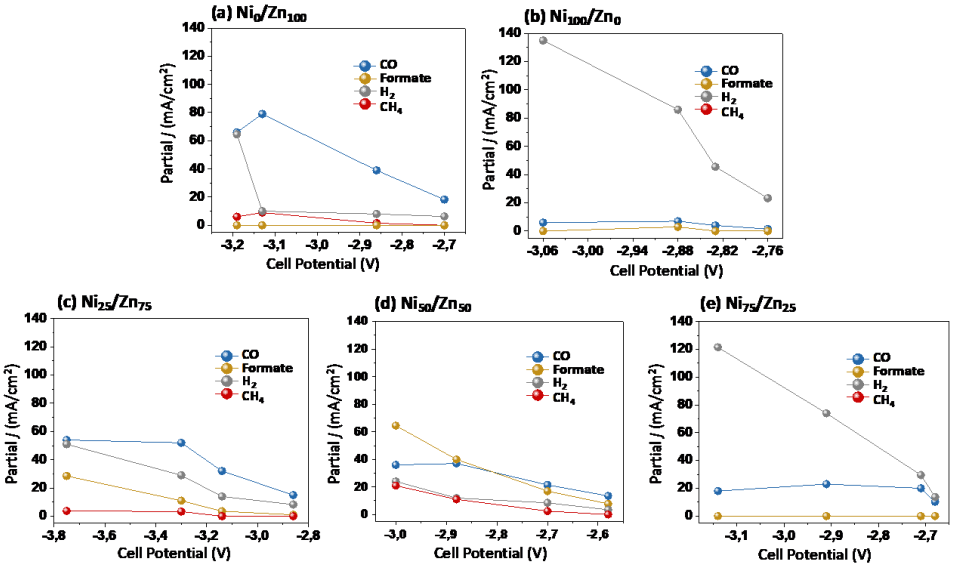

Figure S17 Partial current density comparison of (a) Ni_0/Zn_{100}; (b) Ni_{100}/Zn_0; (c) Ni_{25}/Zn_{75}; (d) Ni_{50}/Zn_{50}; and (e) Ni_{75}/Zn_{25} at -2.7 to -3.8 V in 0.5 M KOH.

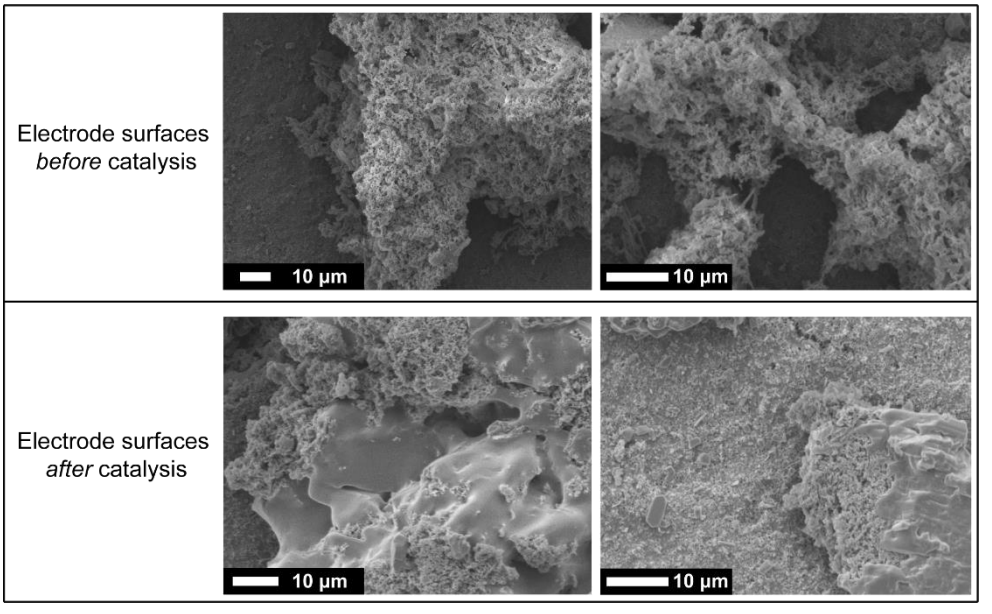

Figure S18 Scanning electron microscopy images of representative Ni_{50}/Zn_{50}-COF particles embedded onto the GDE surface: before (top) and after (bottom) CO_2 electroreduction experiments.

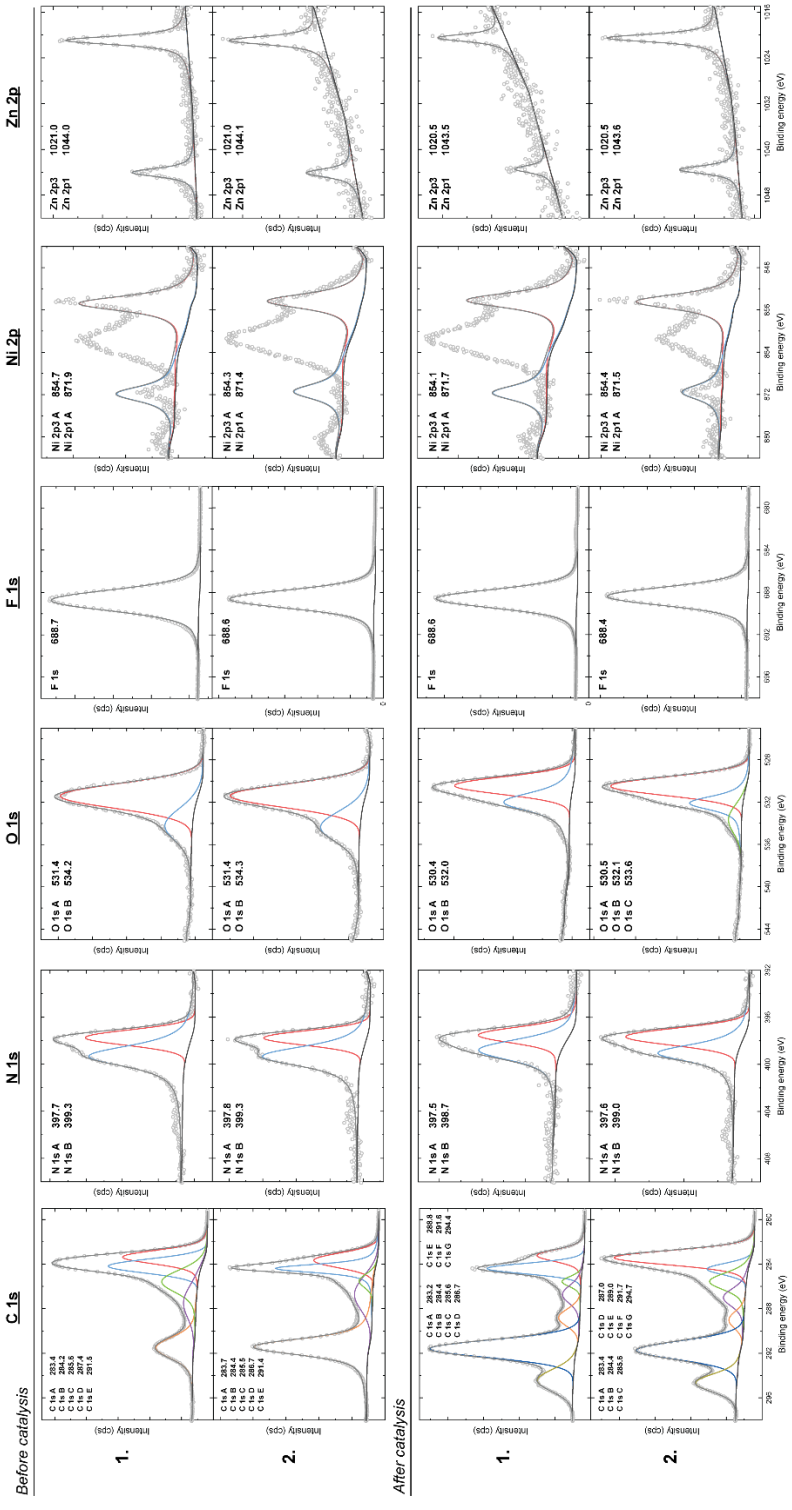
Before catalysis
After catalysis
C 1s
N 1s
O 1s
F 1s
Ni 2p
Zn 2p
1.
2.
Intensity (cps)
Binding energy (eV)

Figure S19 High-resolution N 1s, O 1s, Ni 2p, and Zn 2p XPS spectra of GDE surfaces with embedded Ni_{50}/Zn_{50}-COF particles, before (top 1. and 2.) and after (bottom 1. and 2.) CO_2 electroreduction experiments. "1." and "2." represent measurements at two different locations on the GDE surface.

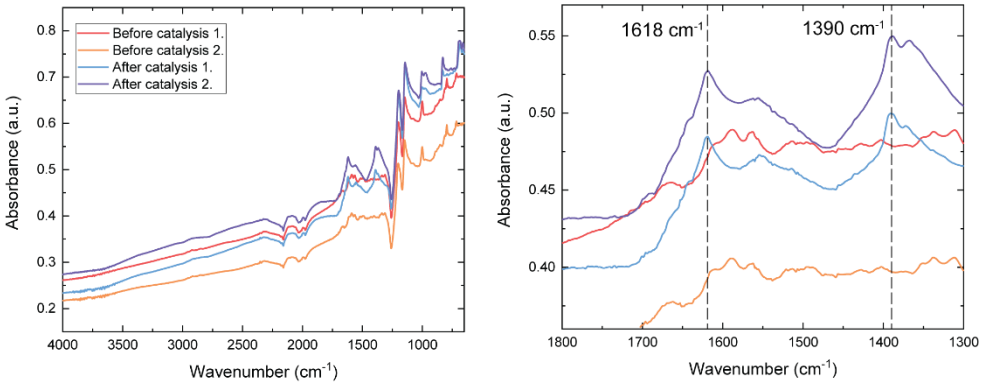

Figure S20 ATR FT-IR spectra of GDE surfaces with embedded Ni_{50}/Zn_{50}-COF particles; before and after CO_2 electroreduction experiments. "1." and "2." represent measurements at two different locations on the GDE surface.

REFERENCES

[1] Olah, G. A.; Prakash, G. K. S.; Goeppert, A. Anthropogenic Chemical Carbon Cycle for a Sustainable Future. *J. Am. Chem. Soc.* **2011**, *133*, 12881–12898.

[2] Qiao, J.; Liu, Y.; Hong, F.; Zhang, J. A Review of Catalysts for the Electroreduction of Carbon Dioxide to Produce Low-Carbon Fuels. *Chem. Soc. Rev.* **2014**, *43*, 631–675.

[3] Abdinejad, M.; Irtem, E.; Farzi, A.; Sassenburg, M.; Subramanian, S.; Iglesias van Montfort, H.-P.; Ripepi, D.; Li, M.; Middelkoop, J.; Seifitokaldani, A.; Burdyny, T. CO_2 Electrolysis via Surface-Engineering Electrografted Pyridines on Silver Catalysts. *ACS Catal.* **2022**, *12*, 7862–7876.

[4] Cheng, T.; Xiao, H.; Goddard, W. A. III Reaction mechanisms for the electrochemical reduction of CO_2 to CO and formate on the Cu (100) surface at 298 K from quantum mechanics free energy calculations with explicit water. *J. Am. Chem. Soc.* **2016**, *138*, 13802–13805.

[5] Abdinejad, M.; Tang, K.; Dao, C.; Saedy, S.; Burdyny, T. Immobilization Strategies for Porphyrin-Based Molecular Catalysts for the Electroreduction of CO_2. *J. Mater. Chem. A* **2022**, *10*, 7626– 7636.

[6] Diercks, C. S.; Liu, Y.; Cordova, K. E.; Yaghi, O. M. The role of reticular chemistry in the design of CO_2 reduction catalysts. *Nat. Mater.* **2018**, *17*, 301– 307.

[7] Zhan, T.; Zou, Y.; Yang, Y.; Ma, X.; Zhang, Z.; Xiang, S. Two-dimensional Metal-organic Frameworks for Electrochemical CO_2 Reduction Reaction. *ChemCatChem* **2022**, *14*, e20210145.

[8] Chen, X.; Addicoat, M.; Jin, E.; Zhai, L.; Xu, H.; Huang, N.; Guo, Z.; Liu, L.; Irle, S.; Jiang, D. Locking Covalent Organic Frameworks with Hydrogen Bonds: General and Remarkable Effects on Crystalline Structure, Physical Properties, and Photochemical Activity. *J. Am. Chem. Soc.* **2015**, *137*, 3241−3247.

[9] Yuan, J.; Chen, S.; Zhang, Y.; Li, R.; Zhang, J.; Peng, T. Structural Regulation of Coupled Phthalocyanine–Porphyrin Covalent Organic Frameworks to Highly Active and Selective Electrocatalytic CO_2 Reduction. *Adv. Mater.* **2022**, *34*, 2203139.

[10] Abdinejad, M.; Seifitokaldani, A.; Dao, C.; Sargent, E. H.; Zhang, X.-A.; Kraatz, H. B. Enhanced Electrochemical Reduction of CO_2 Catalyzed by Cobalt and Iron Amino Porphyrin Complexes. *ACS Appl. Energy Mater.* **2019**, *2*, 1330–1335.

[11] Gong, Y.-N.; Zhong, W.; Li, Y.; Qiu, Y.; Zheng, L.; Jiang, J.; Jiang, H.-L. Regulating Photocatalysis by Spin-State Manipulation of Cobalt in Covalent Organic Frameworks. *J. Am. Chem. Soc.* **2020**, *142*, 16723−16731.

[12] Qian, Y.; Li, D.; Han, Y.; Jiang, H.-L. Photocatalytic Molecular Oxygen Activation by Regulating Excitonic Effects in Covalent Organic Frameworks. *J. Am. Chem. Soc.* **2020**, *142*, 20763−20771.

[13] Lin, S.; Diercks, C. S.; Zhang, Y.-B.; Kornienko, N.; Nichols, E. M.; Zhao, Y.; Paris, A. R.; Kim, D.; Yang, P.; Yaghi, O. M.; Chang, C. J. Covalent organic frameworks comprising cobalt porphyrins for catalytic CO_2 reduction in water. *Science* **2015**, *349*, 1208–1213.

[14] Diercks, C. S.; Lin, S.; Kornienko, N.; Kapustin, E. A.; Nichols, E. M.; Zhu, C.; Zhao, Y.; Chang, C. J.; Yaghi, O. M. Reticular Electronic Tuning of Porphyrin Active Sites in Covalent Organic Frameworks for Electrocatalytic Carbon Dioxide Reduction. *J. Am. Chem. Soc.* **2018**, *140*, 1116−1122.

[15] Chen, R.; Wang, Y.; Ma, Y.; Mal, A.; Gao, X.-Y.; Gao, L.; Qiao, L.; Li, X.-B.; Wu, L.-Z.; Wang, C. Rational design of isostructural 2D porphyrin-based covalent organic frameworks for tunable photocatalytic hydrogen evolution. *Nat. Commun.* **2021**, *12*, 1354.

[16] Zhong, H.; Ghorbani-Asl, M.; Hoang Ly, K.; Zhang, J.; Ge, J.; Wang, M.; Liao, Z.; Makarov, D.; Zschech, E.; Brunner, E.; Weidinger, I. M.; Zhang, J.; Krasheninnikov, A. V.; Kaskel, S.; Dong, R.; Feng, X. Synergistic electroreduction of carbon dioxide to carbon monoxide on bimetallic layered conjugated metal-organic frameworks. *Nat. Commun.* **2020**, *11*, 1409.

[17] Qiu, X.-F.; Zhu, H.-L.; Huang, J.-R.; Liao, P.-Q.; Chen, X.-M. Highly Selective CO_2 Electroreduction to C_2H_4 Using a Metal−Organic Framework with Dual Active Sites. *J. Am. Chem. Soc.* **2021**, *143*, 7242−7246.

[18] Dinh, C. T.; Burdyny, T.; Kibria, G.; Seifitokaldani, A.; Gabardo, C. M.; Pelayo García De Arquer, F.; Kiani, A.; Edwards, J. P.; De Luna, P.; Bushuyev, O. S.; Zou, C.; Quintero-Bermudez, R.; Pang, Y.; Sinton, D.; Sargent, E. H. CO_2 electroreduction to Ethylene via

Hydroxide-Mediated Copper Catalysis at an Abrupt Interface. *Science* **2018**, *360*, 783–787.

[19] Pang, Y.; Burdyny, T.; Dinh, C.-T.; Kibria, M. G.; Fan, J. Z.; Liu, M.; Sargent, E. H.; Sinton, D. Joint Tuning of Nanostructured Cu-Oxide Morphology and Local Electrolyte Programs High-Rate CO_2 Reduction to C_2H_4. *Green Chem.* **2017**, *19*, 4023–4030.

[20] Lee, S.; Ju, H.; Machunda, R.; Uhm, S.; Lee, J. K.; Lee, H. J.; Lee, J. Sustainable Production of Formic Acid by Electrolytic Reduction of Gaseous Carbon Dioxide. *J. Mater. Chem. A* **2015**, *3*, 3029–3034.

[21] Subramanian, S.; Yang, K.; Li, M.; Sassenburg, M.; Abdinejad, M.; Irtem, E.; Middelkoop, J.; Burdyny, T. Geometric Catalyst Utilization in Zero-Gap CO_2 Electrolyzers. *ACS Energy Lett.* **2022**, *8*, 222–229.

[22] Thomas, D. W.; Martell, A. E. Metal Chelates of Tetraphenylporphine and of Some p-Substituted Derivatives. *J. Am. Chem. Soc.* **1959**, *81*, 5111–5119.

[23] Ogoshi, H.; Saito, Y.; Nakamoto, K. Infrared Spectra and Normal Coordinate Analysis of Metalloporphins. *J. Chem. Phys.* **1972**, *57*, 419–44202.

[24] Wölfle, T.; Görling, A.; Hieringer, W. Conformational flexibility of metalloporphyrins studied by density-functional calculations. *Phys. Chem. Chem. Phys.* **2008**, *10*, 5739–5742.

[25] Olsson, S.; Dahlstrand, C.; Gogoll, A. Design of oxophilic metalloporphyrins: an experimental and DFT study of methanol binding. *Dalton Trans.* **2018**, *47*, 11572–11585.

[26] Weyandt, E.; Leanza, L.; Capelli, R.; Pavan, G. M.; Vantomme, G.; Meijer, E. W. Controlling the length of porphyrin supramolecular polymers via coupled equilibria and dilution-induced supramolecular polymerization. *Nat. Commun.* **2022**, *13*, 248.

[27] Yuan, S.; Cui, L.; He, X.; Zhang, W.; Asefa, T. Nickel foam-supported Fe,Ni-Polyporphyrin microparticles: Efficient bifunctional catalysts for overall water splitting in alkaline media. *Int. J. Hydrog. Energy* **2020**, *45*, 28860–28869.

[28] Lashgari, A.; Williams, C. K.; Glover, J. L.; Wu, Y.; Chai, J.; Jiang, J. Enhanced Electrocatalytic Activity of a Zinc Porphyrin for CO_2 Reduction: Cooperative Effects of Triazole Units in the Second Coordination Sphere. *Chem. Eur. J.* **2020**, *26*, 16774–16781.

[29] Han, L.; Song, S.; Liu, M.; Yao, S.; Liang, Z.; Cheng, H.; Ren, Z.; Liu, W.; Lin, R.; Qi, G.; Liu, X.; Wu, Q.; Luo, J.; Xin, H. L. Stable and Efficient Single-Atom Zn Catalyst for CO_2 Reduction to CH_4. *J. Am. Chem. Soc.* **2020**, *142*, 12563–12567.

[30] Bloch, E. D.; Hudson, M. R.; Mason, J. A.; Chavan, S.; Crocellà, V.; Howe, J. D.; Lee, K.; Dzubak, A. L.; Queen, W. L.; Zadrozny, J. M.; Geier, S. J.; Lin, L.-C.; Gagliardi, L.; Smit, B.; Neaton, J. B.; Bordiga, S.; Brown, C. M.; Long, J. R. Reversible CO Binding Enables Tunable CO/H_2 and CO/N_2 Separations in Metal–Organic Frameworks with Exposed Divalent Metal Cations. *J. Am. Chem. Soc.* **2014**, *136*, 10752–10761.

[31] Verma, S.; Ghosh, H. N. Exciton Energy and Charge Transfer in Porphyrin Aggregate/Semiconductor (TiO_2) Composites. *J. Phys. Chem. Lett.* **2012**, *3*, 1877–1884.

[32] Feng, X.; Liu, L.; Honsho, Y.; Saeki, A.; Seki, S.; Irle, S.; Dong, Y.; Nagai, A.; Jiang, D. High-Rate Charge-Carrier Transport in Porphyrin Covalent Organic Frameworks: Switching from Hole to Electron to Ambipolar Conduction. *Angew. Chem. Int. Ed.* **2012**, *51*, 2618–2622.

[33] Peterson, A. A.; Abild-Pedersen, F.; Studt, F.; Rossmeisl, J.; Nørskov, J. K. How copper catalyzes the electroreduction of carbon dioxide into hydrocarbon fuels. *Energy Environ. Sci.* **2010**, *3*, 1311–1315.

SUMMARY

Covalent organic frameworks (COFs) are a subclass of hyper-crosslinked polymers that contain ordered nanoporosity within their polymer network. Control over pore size and shape, as well as structure regularity, is obtained through careful selection of the monomeric building blocks and the synthesis reaction conditions. This has led to a vast library of available COF structures that are each designed for a specific application, typically in the direction of controlled capture and release. The work presented in this thesis addresses challenges in the development of COFs as active materials in energy transition applications. The goal of this thesis was to draw structure-property relationships of novel COFs in order to establish COF design rules for applications such as: CO_2 capture, separation and conversion, as well as electrochemical energy storage.

In **Chapter 1**, a general introduction to the COF field is provided, with an emphasis on COF design and characterization. The current challenges in the COF field are laid out, focussing on the dilemma of crystallinity versus stability, challenges in the synthesis, and necessary improvements in order to make COF viable materials for their envisioned application.

In **Chapter 2**, the preparation of high-performance polyimide COFs for CO_2 capture through the imidization polymerization of mellitic trianhydride with two different triamines (1,3,5-tris(4-aminophenyl)benzene (TAPB) or 1,3,5-tris(4-aminophenyl)amine (TAPA)) is reported, yielding two novel polyimide COFs. The resulting porous polymers possess microporous structures (< 2 nm pore sizes), are thermally stable up to 548 K, and are stable in aqueous and acidic media. Moreover, these COFs show decent CO_2 capacities (at 1 bar and 273 K) of 1.7 and 2.1 mmol g^{-1} for TAPB- and TAPA-based COFs respectively. Computational structure optimizations revealed that the TAPA-based COF structure contains larger torsion angles in its polymer backbone than the TAPB-based COF, leading to differences in their inter-planar stacking distances. This observation, along with chemical differences between the two COFs, explain the trends in porosity and CO_2 uptake that were noticed here.

In **Chapter 3**, flow-induced disturbances were applied during the synthesis of a naphthalene diimide (NDI) COF in order to modify the COF structure by other means that conventional chemical modifications. Three situations were

assessed, where the reaction mixture was left: static, under mild stirring at 4.5 – 190 s^{-1}, or under high intensity stirring at 250 s^{-1}. COFs prepared via a static method display an outstretched, open polymer network, while a high intensity of stirring yields a COF polymer network that is more aggregated in micro- and nano-length scales. In addition, shear rates of 250 s^{-1} caused a large red-shift of the COF's absorbance of visible light, which is likely caused by a relatively higher contribution of intermolecular interactions between the NDI-segments.

In **Chapter 4**, the development of a water-stable polyimide COF is described, which is then used in $N_2/CO_2/H_2O$ breakthrough studies. The CO_2 separation performance is assessed under varying levels of relative humidity (RH). At limited RH, the competitive binding of H_2O over CO_2 (which is typically observed in literature) is replaced by cooperative adsorption. For some conditions, the CO_2 capacity showed a 25 % increase under humid versus dry conditions (*e.g.* at 333 K and 15 % RH). These results in combination with FT-IR studies on equilibrated COFs at controlled RH values, revealed that enhanced CO_2 adsorption is an effect of CO_2 being adsorbed on single-site adsorbed water. Once water cluster formation sets in, however, loss of CO_2 capacity is inevitable. The polyimide COF used in this research retained performance after a total exposure time of > 75 hours and temperatures up to 403 K.

In **Chapter 5**, four chemically similar polyimide COFs were developed, by combining two different dianhydrides with two different triamine building blocks. Here, the studied COFs are dual-functional: their imide-backbones and microporous architecture are beneficial for their use as resilient CO_2 adsorbents, and their redox-active imide motifs are useful for energy storage applications. Through density functional theory (DFT) calculations and powder X-ray diffraction it was revealed that the imide bonds prefer to form at an angle with one another, breaking the 2D symmetry, which shrinks the pore width and elongates the pore walls. The eclipsed 'perfect' stacking is preferable, while sliding of the COF sheets is energetically accessible in a relatively flat energy landscape with a few metastable regions. In the case of CO_2 adsorption, the two best performing COFs originated from the same triamine building block, similar to the effect observed in Chapter 2. On the other hand, the two most promising COF structures for energy storage have the dianhydride building block in common. These COFs provide a useful framework for Na-ion intercalation with retainable capacities and stable cycle life at a relatively high working potential (>1.5 V *vs* Na/Na^+). Although these capacities are low compared to conventional inorganic Li-ion materials, these COFs are, as a proof of principle, potentially promising for sustainable, safe, and stable

Na-aqueous batteries due to the combination of their working potentials and their insoluble nature in water.

In **Chapter 6**, a layer-by-layer electrode fabrication technique is presented for the preparation of nanoporous-based supercapacitors (SCs), where the active component (porous polymer) is layered on top of the conductive carbon layer. This is contrasted with a conventional mixing approach, where the polymer is mixed inside the conductive carbon matrix. Through the layered approach, direct contact with the electrolyte and polymer material is greatly enhanced. As a result, the layered electrodes allowed a significant contribution of fast faradic surface reactions to the overall capacitance, which boosted its performance significantly. The electrochemical performance of the layered-electrode SC outperformed other reported porous polymer-based devices with a specific gravimetric capacitance of 388 $F \cdot g^{-1}$ and an energy density of 65 $Wh \cdot kg^{-1}$ at a current density of 0.4 $A \cdot g^{-1}$. The device also showed good cyclability with 90% of capacitance retention after 5000 cycles at 1.6 $A \cdot g^{-1}$. Thus, the introduction of a layered electrode structure would pave the way for more effective utilisation of porous organic polymers in future energy storage/harvesting devices by exploiting their nanoporous architecture and limiting the negative effects of the carbon/binder matrix.

In **Chapter 7**, COFs with 2 different active sites are combined in a single framework, and could therefore be useful catalysts for multi-step reactions such as the electrochemical conversion of CO_2. This is accomplished through the synthesis of five Ni(II)- and Zn(II)-porphyrin-based polyimine COFs; being the pure phase COFs and co-synthesized Ni/Zn-COFs at Ni:Zn ratios of 75:25, 50:50, and 25:75. Nanoporous polyimine frameworks were formed in case of all the different Ni:Zn ratios. In terms of structural differences, the Ni_{50}/Zn_{50} COF showed the highest overall porosity. In the co-synthesized metalloporphyrin COFs, nickel and zinc atoms are distributed relatively homogeneously throughout the framework, as was confirmed by STEM/EDX studies. This led to significantly different catalytic activity during electrochemical CO_2 reduction compared to the physical mixture of both pure phases. The Ni_{50}/Zn_{50}-COF produced noteworthy quantities of formate and methane at Faradaic efficiencies of 43% and 14%, respectively, at 150 mA/cm^2, while the pure Ni- and Zn-COFs almost exclusively generate H_2 and CO. Synergy between Ni- and Zn-porphyrins can lead to these results through a likely combination of the following: bifunctional catalysis, enhanced proton/electron transfer, and Ni-porphyrin-dependent stabilizing effects on the porous framework.

Though the topics touched upon in this thesis are widespread and the various chapters dealing more with new concepts rather then detailed studies of a particular set of COFs and only one application field, the main goal of relating the molecular and polymeric structure of the newly developed COFs to their performance in energy transition applications has been achieved. Our approach towards achieving this goal was by addressing the challenges that are defined in the introduction chapter. First, the 'crystallinity versus stability' issue (1.3.1) has been addressed by designing and synthesizing COFs with thermally and hydrolytically stable backbones: polyimides (**Chapters 2 - 6**) and 'locked' polyimines (**Chapter 7**). Utilising such structures led to important insights on the retainment of stability and functionality when these COFs are exposed to typical chemical environments of their envisioned application. Second, the issue of COF synthesis under other than static conditions (1.3.2) has been investigated in **Chapter 3**, where physical pertubations during COF preparation revealed that novel COF structures can be obtained through the processing-side of synthesis rather than through its chemistry. Finally, the shortage of reported structure-property relationships in the COF field (1.3.3) has been addressed in **Chapters 4 – 7**, allowing us to establish COF-design rules for applications where COFs show a real promise: greenhouse gas capture and conversion, and energy storage.

One might ask "What's next?", although it is a difficult question to answer concisely for a thesis with such a broad range of topics. Also, the COF field is relavtively young (the discovery of the first COFs being reported in 2005), making it seem scientists have only scratched the surface of the potential of COFs. Nevertheless, looking at the two key features of the title of this thesis "*Novel Covalent Organic Frameworks for the Energy Transition*", I envision two important directions in which the COF field should be heading.

(I) Starting with *the Energy Transition*. For COFs to become viable functional materials in this transition, there needs to be more cross-communication between the fields of material science and engineering. A pure COF powder may have exceptional CO_2 capacity when exposed to only CO_2 gas, but the CO_2 separation performance of the material may be drastically different once: the powder is pelletized, the production is scaled-up, and the material is exposed to industrial flue gas mixtures. **Chapter 4** took first steps into this unknown territory and showed that simply the addition of water vapor to the system changes the performance significantly. Thus, more communication between process

engineers and material chemists may yield better testing under relevant conditions (*i.e.* relevant process streams) and better stability assessments under these and realistic regeneration conditions. Subsequently, this should be followed by techno-econmic assessments comparing COFs to convential technologies (*e.g.* amine scrubbers), after which acceleration of COF implementation on an industrial scale would be possible.

(II) The other key feature of this thesis title - *Novel Covalent Organic Frameworks* - makes it clear that the librabry of different COF structures is forever expanding. Machine learning alogrithms are assisting organic chemists more and more in identifying optimal COF structures for specific properties, and are a great tool to diminnish the trial-and-error of synthetic optimization. Parralel to this continuous development, innovation in the COF field for novel structures can come from unexpected experimental angles. For example, **Chapter 3** showed how the photophysical properties of COFs with the same chemical backbone can be altered through different means than just chemistry. Similar to the argument made in (I), further exploration of these directions requires more cross-communication with engineers (*e.g.* fluid mechanics experts in collaboration with chemists to fundamentally understand how a specific flow regime can lead to a specific microstructure). On the other hand, as chemists are achieving more control on both the nano- and microstructural level, the complexity of novel COF structures continues to increase. As has been shown in **Chapter 7**, going from a two-component system (pure phase Ni- or Zn-porphyrin COFs with inert linkers) to a three-component system (combined Ni_{50}/Zn_{50}-COF) revealed unexpected results in terms of structure, as well as functionality. Multifunctionality within a single framework to catalyze multi-step reactions (*e.g.* CO_2 reduction) will be a unique advantage of COFs compared to conventional materials. In order to push that field forward, fundamental understanding of the topology and spatial distribution of the reactive entities in COF structures needs to be expanded. Subnanometer characterization (*e.g.* atom probe tomography) can, for example, be implemented to better study the spatial distribution of COF monomers. In addition, utilizing operando spectroscopic techniques to study such novel COF

catalysts will gain deeper insights into unknown reaction mechanisms.

Notwithstanding all these obstacles and the long journey ahead, I trust that this thesis serves as an example of the promise of this exciting material class in such a broad range of research fields. More specifically, both in fundamental chemistry, in the continuously improving spatial control of molecular and atomic building blocks by organic chemists, as well as more generally, in the innovation in material science to solve relevant societal challenges.

SAMENVATTING

Covalent-organische roosters (Engels: covalent organic frameworks, COFs) zijn hypervernette (Engels: cross-linked) polymeren met geordende nanoporositeit. De grootte en vorm van de nanoporiën, alsmede de regelmatigheid van de structuur van het netwerk, worden beïnvloed door de gebruikte monomeren of bouwstenen en de procesparameters van de synthese. Er is een uitgebreide 'bibliotheek' beschikbaar van COF-structuren die elk zijn ontworpen voor een specifieke toepassing, vaak op het gebied van het gecontroleerd afvangen van kleine moleculen en gassen. Het werk dat in dit proefschrift wordt gepresenteerd gaat in op de uitdagingen bij de ontwikkeling van COFs als functionele materialen die relevant zijn voor de energietransitie. Het doel van dit onderzoek is om structuur-eigenschap relaties van nieuwe COFs te ontrafelen om zo richtlijnen op te stellen voor het ontwerp van COFs voor specifieke toepassingen zoals: CO_2-afvang, -scheiding en -conversie, evenals elektrochemische energieopslag.

In **Hoofdstuk 1** wordt een algemene inleiding van het COF-veld gegeven, met de nadruk op COF-ontwerp en karakterisering. De huidige uitdagingen worden uiteengezet, met de nadruk op: (1) het dilemma van kristalliniteit versus stabiliteit, (2) uitdagingen in de synthese, en (3) verbeteringen die noodzakelijk zijn om COFs geschikt te maken voor hun beoogde toepassing.

In **Hoofdstuk 2** wordt de synthese van twee nieuwe hoogwaardige polyimide COFs voor het afvangen van CO_2 beschreven. Deze polymeren zijn gesynthetiseerd door de imidisatiepolymerisatie tussen mellitinezuuranhydride en twee verschillende triaminen: 1,3,5-tris(4-aminofenyl)benzeen (TAPB) of 1,3,5-tris(4-aminofenyl)amine (TAPA). Beide hebben microporeuze structuren (poriegrootte van < 2 nm), zijn thermisch stabiel tot 548 K en zijn stabiel in waterige en zure omstandigheden. Bovendien vertonen ze een significante CO_2-opvang capaciteit (bij 1 bar en 273 K) van 1,7 en 2,1 mmol g^{-1} voor respectievelijk TAPB- en TAPA-gebaseerde COFs. Analyse van de berekende ketenstructuren onthult dat de TAPA-COF-structuur grotere torsiehoeken in de polymeerketen bevat dan de TAPB-COF, wat leidt tot verschillen in de afstand tussen de gestapelde 2D polymeerlagen. Deze waarneming, samen met de chemische verschillen tussen de twee COFs, verklaren de verschillen in porositeit en CO_2-opname.

In **Hoofdstuk 3** wordt beschreven hoe agitatie van het reactiemengsel tijdens de synthese van een naftaleendiimide (NDI) COF de uiteindelijke structuur beïnvloedt. Er zijn drie agitatieniveaus te onderscheiden: statisch (stroomsnelheid 0 s^{-1}), mild roeren (stroomsnelheid 4,5 – 190 s^{-1}), en intensief roeren (stroomsnelheid 250 s^{-1}). COFs die gesynthetiseerd zijn onder statische condities vertonen een uitgestrekt, open polymeernetwerk, terwijl intensief roeren een COF-polymeernetwerk oplevert dat op micro- en nanolengteschalen meer geaggregeerd is. Door de verschillen in pakking treedt een grote roodverschuiving in de absorptie van zichtbaar licht op door de COF die is gesynthetiseerd onder intensief roeren. Dit wijst waarschijnlijk op een relatief grotere bijdrage van intermoleculaire interacties tussen de NDI-segmenten.

In **Hoofdstuk 4** wordt de synthese van een waterstabiele polyimide COF beschreven, die vervolgens wordt gebruikt in $N_2/CO_2/H_2O$-doorbraakstudies. De CO_2-scheidingsprestatie is beoordeeld bij verschillende relatieve luchtvochtigheid (RL). Bij een hoge RL wordt competitieve adsorptie waargenomen, waar H_2O beter adsorbeert dan CO_2 (van welke de adsorptie afneemt, wat doorgaans ook in de literatuur wordt waargenomen), maar bij beperkte RL wordt dit gedrag vervangen door coöperatieve adsorptie, waarbij de CO_2-capaciteit juist toeneemt. Voor specifieke omstandigheden vertoonde de CO_2-capaciteit een toename van 25% onder vochtige omstandigheden in vergelijking met de droge situatie (bijv. bij 333 K en 15% RL). Deze resultaten, in combinatie met FT-IR-metingen aan geëquilibreerde COFs bij gecontroleerde RL-waarden, tonen aan dat de verbeterde CO_2-capaciteit het gevolg is van CO_2-adsorptie aan water enkelvoudig gebonden aan een adsorptiesite van de COF. Echter, zodra de vorming van waterclusters begint, is verlies van CO_2-capaciteit onvermijdelijk. De polyimide COF die in dit onderzoek werd gebruikt, behield zijn opmerkelijke scheidingsprestaties zelfs na een totale blootstellingstijd van meer dan 75 uur en temperaturen tot 403 K.

In het werk beschreven in **Hoofdstuk 5** zijn vier polyimide COFs ontwikkeld uitgaande van twee verschillende dianhydride- en twee triamine-monomeren of bouwstenen. Deze COFs zijn interessant voor CO_2 adsorptie vanwege hun microporeuze structuur, en voor (elektrische) energieopslag vanwege hun redox-actieve imide-segmenten. Dichtheidsfunctionaaltheorie (DFT) en poeder Röntgen diffractie zijn toegepast om de structuren te bestuderen, waardoor de conclusie kan worden getrokken dat de imide-verbindingen zich preferentieel onder een relatief grote (~ 30°) torsiehoek vormen. Hierdoor wordt de poriegrootte verkleind en de porielengte vergroot. Deze combinatie van technieken laat inzien dat een ‘perfecte’ parallelle stapeling van de 2D COF-lagen

het meest energie-gunstig is, maar dat er ook enkele metastabiele gebieden zijn waarin de COF-lagen ten opzichte van elkaar verschoven zijn. Voor wat betreft de toepassing als CO_2 adsorpbens, de twee best-presterende COFs bevatten dezelfde triamine bouwsteen, die ook al in de COFs van **Hoofdstuk 2** gebruikt is (*i.e.* TAPA). De twee meest-belovende COF structuren voor de toepassing van de opslag van elektrische energie hebben de dianhydride-bouwsteen gemeen. Bij deze laatste COFs kan efficiënte Na-ion intercalatie plaatsvinden, en ze behouden hun elektrische capaciteit onder een relatief hoog werkpotentiaal (>1,5 V *vs* Na/Na^+

standaard potentiaal). Hoewel de capaciteit relatief laag is ten opzichte van conventionele Li-ion materialen, zijn deze COFs veelbelovend voor Na-ion batterijen met een waterig elektrolyt ten gevolge van hun hoge werkpotentiaal en onoplosbaarheid in water.

In **Hoofdstuk 6** wordt een laag-voor-laag techniek voor de fabricage van elektroden beschreven met als toepassingsgebied nanoporeuze supercondensatoren (SCs). Hierbij is de actieve component (*i.e.* de microporeuze polyimide) als niet geleidende laag aangebracht op de geleidende koolstoflaag, om zo direct contact tussen het elektrolyt en de polymere scheidingslaag te bewerkstelligen. Deze methode wordt vergeleken met een conventionele methode voor het bereiden van elektrodes, waarbij de actieve component ongecontroleerd in de geleidende koolstofmatrix wordt gemengd. Het gedrag van de gelaagde elektrode is beter dan dat van de conventionele elektrode (ongeveer een verdubbelde specifieke elektrische capaciteit), wat voor een groot deel is te wijten aan snellere Faraday-oppervlaktereacties. Met een specifieke gravimetrische capaciteit van 388 $F \cdot g^{-1}$, een energiedichtheid van 65 $Wh \cdot kg^{-1}$ (bij een stroomdichtheid van 0,4 $A \cdot g^{-1}$) en een goede bestendigheid tegen meervoudig op- en ontladen (90% capaciteitsbehoud na 5000 cycli bij 1,6 $A \cdot g^{-1}$) presteerde dit poreuze polymeer via de gelaagde techniek beter dan andere gerapporteerde poreuze polymeer-gebaseerde SCs. De verbetering is vrijwel zeker niet exclusief voor deze nieuwe COF. We verwachten dat ook andere poreuze polymeren door deze laag-voor-laag fabricage techniek beter kunnen presteren in elektrochemische toepassingen, aangezien de nanoporeuze structuur beter wordt benut en de negatieve effecten van de koolstofmatrix worden verminderd.

In **Hoofdstuk 7** wordt gefocust op COFs die als katalysatoren voor CO_2-reductie kunnen dienen. Anders dan eerder onderzoek naar monometallische porfyrine COFs onderzochten we hier het effect van het gebruik van twee metaal atomen in de synthese. De synthese van vijf op Ni(II)- en Zn(II)-porfyrine gebaseerde nanoporeuze polyimine COFs wordt beschreven, waaronder de COFs

met enkel Ni(II)- of Zn(II)-porfyrines, en de COFs gesynthetiseerd met zowel het Ni(II)- als Zn(II)-porfyrines met Ni:Zn verhoudingen van 75:25, 50:50 en 25:75. STEM/EDX metingen tonen aan dat in alle gevallen de nikkel- en zinkatomen relatief homogeen verdeeld zijn over de roosters in het geval van de Ni/Zn COFs. De verhouding van nikkel- en zinkatomen heeft een groot effect op de katalytische activiteit tijdens de elektrochemische CO_2-reductie. De Ni_{50}/Zn_{50} COF, met een hogere porositeit dan de andere systemen, produceerde significante hoeveelheden formiaat en methaan onder Faraday rendementen van respectievelijk 43% en 14% bij 150 mA/cm^2, terwijl de pure Ni- en Zn-COFs bijna uitsluitend H_2 en CO (en nauwelijks formiaat of methaan) produceren. De waargenomen synergie is waarschijnlijk afkomstig van de volgende effecten: bifunctionele katalyse, verbeterde protonen-/elektronenoverdracht en stabiliserende effecten op het poreuze rooster afkomstig van de Ni-porfyrines.

Tot slot: de onderwerpen van deze thesis zijn breed van opzet. Er is meer aandacht besteed aan nieuwe concepten dan gedetailleerde studies van een specifieke COF in een specifieke toepassing. Desalniettemin is het doel om de moleculaire en polymere structuur van de nieuwe COFs te relateren aan hun prestatie in het energietransitie toepassingenbereik. Het plan van aanpak daarbij is geweest om ons te richten op de uitdagingen rondom het COF onderzoeksveld zoals beschreven in **Hoofdstuk 1** van dit proefschrift. Ten eerste: de uitdaging rondom 'kristalliniteit versus stabiliteit' (1.3.1) is aangepakt door COFs met thermisch en hydrolytisch stabiele polymeerketens te ontwerpen en synthetiseren, namelijk: polyimides (**Hoofdstukken 2 – 6**) en 'vergrendelde' polyimines (**Hoofdstuk 7**). Het gebruik van deze structuren heeft geleid tot belangrijke inzichten in de relevantie van het behoud van stabiliteit en functionaliteit wanneer deze COFs worden blootgesteld aan omgevingen die typisch zijn voor hun beoogde toepassing. Ten tweede: de voorheen nauwelijks onderzochte optie van COF synthese onder niet-statische omstandigheden om andere configuraties en betere eigenschappen te verkrijgen is onderzocht in **Hoofdstuk 3**. Door agitatie van het reactiemengsel toe te passen tijdens de synthese, werden nieuwe COF-structuren verkregen die waarschijnlijk niet te bereiken zijn door aanpassing van de keuze van de chemische constituenten. Ten slotte is het gebrek aan structuur-eigenschapsrelaties in het onderzoeksveld aangepakt in **Hoofdstukken 4 – 7**, wat ons dichterbij bij het opstellen van duidelijke richtlijnen brengt voor COF ontwerp, afhankelijk van de beoogde toepassing.

Het is niet eenvoudig om een beknopt antwoord te geven op de vraag "What's next?", gezien het brede scala aan onderwerpen besproken in dit

proefschrift. Daarbij komt ook het feit dat het COF onderzoeksveld relatief jong is (de eerste COFs zijn ontdekt in 2005) en het mogelijk is dat onderzoekers alleen het topje van de ijsberg van de potentie van COFs hebben gezien. Kijkend naar de twee hoofdkenmerken van de titel van dit proefschrift "*Novel Covalent Organic Frameworks for the Energy Transition*", zie ik twee belangrijke richtingen waar het COF-veld zich naar zou moeten bewegen:

(III) Ik begin met de woorden *Energy Transition*. Om COFs marktrelevante materialen voor de energietransitie te laten worden, moet er meer communicatie komen tussen de onderzoeksvelden van materiaalkunde en procestechnologie. Een zuiver COF poeder kan exceptionele CO_2 capaciteit hebben wanneer het wordt blootgesteld aan zuiver CO_2 gas, maar de CO_2 scheidingsprestatie kan drastisch veranderen onder meer realistische procesomstandigheden zoals wanneer het poeder wordt gepelletiseerd en het materiaal wordt blootgesteld aan industrieel rookgas. In **Hoofdstuk 4** zijn de eerste stappen hiertoe genomen door aan te tonen dat simpelweg door de toevoeging van waterdamp aan het systeem de scheidingsprestatie significant wordt beïnvloed. Meer communicatie tussen procestechnologen en materiaal chemici kan dus leiden tot relevantere testcondities (*i.e.* relevante gas processtromen) en betere stabiliteitsbeoordelingen onder dergelijke condities. Vervolgens zijn techno-economische evaluaties nodig waarbij COFs worden vergeleken met conventionele technologieën (bijvoorbeeld aminescrubbers), waarna versnelling van COF-implementatie op industriële schaal mogelijk is. Ook het onderzoek naar het effect van de stromingscondities tijdens de synthese toonde aan dat grootschalige industriële synthese condities kunnen leiden tot andere structuren en eigenschappen dan verkregen onder kleinschalige laboratorium condities.

(IV) Het andere hoofdkenmerk van de titel van dit proefschrift – *Novel Covalent Organic Frameworks* – laat zien dat de bestaande 'bibliotheek' van nieuwe COF structuren niet compleet is maar dat er nog veel nieuwe varianten moeten bestaan. Machine learning algoritmen kunnen organisch chemici meer en meer helpen bij het identificeren van mogelijk optimale COF structuren voor specifieke toepassingen, en zijn handige hulpmiddelen om de inefficiëntie van de huidige *trial-and-error* benadering van

synthetische optimalisatie te verminderen. Parallel aan deze gestructureerde ontwikkeling loopt de continue innovatie in de ontwikkeling van nieuwe COF structuren die uit onverwachte experimentele hoeken kan komen. **Hoofdstuk 3** laat bijvoorbeeld zien dat de fotofysische eigenschappen van COFs met exact dezelfde chemie kunnen worden gestuurd via andere manieren dan enkel de chemie. Passend bij het argument dat bij punt (I) gemaakt is, zou dit beter uitgezocht kunnen worden door communicatie tussen diverse technologische experts te bevorderen (*e.g.* vloeistofmechanica experts samenwerkend met polymeersynthese experts om zo in detail uit te zoeken welke parameters nodig zijn om specifieke COF microstructuren te genereren). Aan de andere kant, naarmate chemici meer controle krijgen over de nano- en microstructuren van COFs, zal de complexiteit van deze structuren toenemen. **Hoofdstuk 7** laat onder anderen zien dat de transitie van een twee-componenten systeem (enkel Ni- of Zn-porfyrine COFs met een inerte derde linker) naar een drie-componenten systeem (Ni_{50}/Zn_{50}-COF) onverwachte gevolgen kan hebben voor de structuur en de functionaliteit van een COF. Multifunctionaliteit binnen een enkel COF rooster om meerstapsreacties te katalyseren (bv. CO_2 reductie) zal een uniek voordeel van COFs zijn in vergelijking met conventionele nanoporeuze materialen. Om innovatie in dit onderzoeksveld te stimuleren moet de kennis rondom de topologie en ruimtelijke verdeling van reactieve segmenten in COF structuren worden uitgebreid. Subnanometerkarakterisering (met behulp van bijvoorbeeld atomaire tomografie) kan een beter inzicht geven in de precieze ruimtelijke verdeling van voormalige COF monomeren in een COF. Gekoppeld daaraan kunnen operando spectroscopische technieken worden ingezet om de werking van nieuwe COF katalysatoren te onderzoeken om zo diepere inzichten in de optredende reacties te verkrijgen.

Ondanks het aantal en de complexiteit van bovengenoemde obstakels die overbrugd moeten worden, ben ik ervan overtuigd dat dit proefschrift als een voorbeeld kan dienen voor gestructureerd onderzoek naar de mogelijkheden van deze veelbelovende materiaalklasse voor een breed scala aan onderzoeksvelden. Dit betreft zowel de fundamentele chemische aspecten van een continue verbetering van het ruimtelijk controleren van moleculaire/atomaire bouwstenen,

als meer in het algemeen de innovatie binnen het vakgebied van de technische materiaalkunde om relevante maatschappelijke uitdagingen op te lossen.

Acknowledgements

Although it can sometimes feel like it, a PhD is never a solo-mission. In this section I would like to acknowledge and sincerely thank all the people who have contributed to my PhD in one way or another. It is a section I have thought about a lot, since – despite the love for science and the joy of diving deep into unknown scientific territory – it has been truly the people around me that make me want to continue to do work that I do.

First and foremost, I would like to thank Sybrand van der Zwaag. You have been my promotor from the start of my PhD trajectory, but our work relationship changed somewhat after the departure of my daily supervisor Atsushi Nagai from the TU Delft. Working more closely together, it became even more clear to me what makes you such an accomplished scientist and mentor. You have a constant drive for excellence and quality research, no matter the outcome. The creative new directions that you were able to give to research projects is something that I will continue to aspire to. The scientific and professional growth that I see in myself could not have reached this level without your mentorship. Organizing your retirement party together with Gawel, Shanta and Vincent was an honour, and will forever be fondly in my memories.

I owe a great deal of gratitude to Monique van der Veen, for stepping up as my second promotor and daily supervisor from my second PhD year and onwards. The transition of supervisors went very smooth and you immediately invited me to join your groupmeetings, where I feel I really got the opportunity to grow as a critical scientist under the company of others working on similar projects. Thank you for all the expertise and guidance that you brought, bringing our projects to a higher level.

Atsushi Nagai, here I would like to thank you as well, for introducing me to the wondrous world of COFs. Your COF synthesis knowledge is unlimited and working side by side together in the lab on optimisations of synthesis conditions was the perfect start for my PhD. Learning from you in my first year at TU Delft was both fun and inspiring, and your level of lab-involvement is something I want to strive for to maintain in my later career as well.

Whether it was for supporting my research, collaborating, or simply sharing ideas, I am thankful to the following PhD's, postdocs, professors, and

technical staff: Alexandros Vasileiadis, Amor Adbdelkader, Atsushi Urakawa, Bahiya Ibrahim, Bart Boshuizen, Durga Mainali, Ed Roessen, Ferdinand Grozema, Frans Tichelaar, Freek Kapteijn, Hugo Perrin, José Palomo Jiménez, Maryam Abdinejad, Mohammed Jafar, Nera Fernando, Lorenzo Botto, Luis Cutz, Remco van der Jagt, Rob van der List, Stephen Eustace. A special thanks should definitely go to Bart van der Linden and Willy Rook, both for your excellent quality of support, and for being very welcoming and friendly to this stranger from the aerospace faculty (as well as for my students).

Speaking of, I was lucky to work together with many students on the projects that are presented in this thesis. Jeffrey, you were already there when I arrived, so really you were more of a supervisor for me. Thank you for showing me all the intricate COF synthesis techniques. Jennifer, we started around the same time and it helped a lot to have someone in the lab that understands the sometimes exhausting trial-and-error of COF synthesis optimizations. Luc, you reinforced the Brabantse gezelligheid in the group, as well as bringing the football skills to make us not end last place in the ASM tourney. Tim, I am still impressed that you finished a purely theoretical bachelor thesis perfectly on time, all from your desk at home (due to covid restrictions). I can only hope to, one day, achieve your level of discipline. Bart, although you had a hybrid theory–experimental project, luckily we still had a period to work on some synthesis in the lab, using all kinds of exotic new COF linkers. Annemiek, together with Bart van der Linden, we resurrected the breakthrough setup and your first experiments grew out to be the start of one of my most proud chapters. Marie-Claire, I remember giving you instructions to the gas sorption analyzer while being at the beach, being a supervisor was never so sunny and easy. Lara, we learned together that mellitic anhydride is a tricky compound to work with, all the while enjoying your positive attitude and dry sense of humour. Saira, you brought a lot of curiosity to the breakthrough project and you were doing independent research almost straight from the start. I enjoyed working together with you and giving a speeach at your master ceremony. My aim for all of you has been to do quality research, but in a way that is fun and energy-gaining, instead of energy-demanding. I think I still have a lot to learn in that aspect, but I do hope that I have been making steps in the right directions.

Looking back, I was in a similar position as you and it seems right to thank my previous supervisors during studies as well, since their guidance and mentorships contributed immensely to my interest for science in general. Many thanks to Loai Abdelmohsen, David Williams, Sjoerd Postma, Wilhelm Huck, Pim van der Asdonk and Paul Kouwer.

The statements in the first paragraph of this acknowledgements chapter definitely ring true with the whole NovAM group in mind. It has been a joy to see (not only for me, I know for a lot of other members as well) how quickly the word 'colleague' can be interchanged by the word 'friend' in this group; sharing coffees over stories of science and beers over stories of life. Vincenzo, as I arrived and we found out that we share the same birthday, being office-mates felt nothing less than destined. The Mediterranean warmth that you brought to the office every day (despite the Dutch weather), will always be unmatched. Attending your wedding in Napoli with our crazy Greek friend Dimos and Paul (obligatory: "eeuuuujjj"), was an honour and an absolute highlight of the PhD period. NovAM has also managed to keep my boardgame passion going: having spent many bandit- and ooze-slaying sessions with Anton, Vincent and Tadhg, which often helped almost therapeutically to deal with ongoing frustrations of failed experiments. Tinashe, it was a joy having you in the office for the final part of my PhD period; your kindness (with a dash of chaos) will always be fondly in my memory. Other NovAM members, old and new, you have kept the spirit of this big, ever-changing family going and I am thankful to all of you: Adrià, Elif, Gawel, Hao, Jingjing, Johan, Marlies, Marlon, Miisa, Nan, Lakshmi, Pim, Ricardo, Santiago, Satya, Yifan, Yinglu, and many more of the early generation. Secretly at the head of this all – or should we say: 'the real boss' – is Shanta. Thank you for always being there for us, be it for work- or life-related issues.

I got the privilege to work in two research groups at the same time, so here I would also like to thank all the members of the Catalysis Engineering group for the group discussions and the many social activities. Among those, some extra words of gratitude for the subgroup of Monique: Adrian, Begüm, Chunyu, Davide, Han, Jelco, Jintao, Srinidhi, Sven, Usman, Vitalii. Despite being most of the time in my other office at LR at the far, far (actually not so far) end of the street, you always made me feel welcome during our weekly meetings, conferences, and axe throwing activities.

Een constante support vanaf het eerste studiejaar op de uni tot en met het heden zijn mijn vrienden uit Nijmegen: Casper, Cedric, Jeroen, Joost, Luke, Miguel, Pieter, Roel, Tuur. Als 18-jarige jongvolwassenen (met vooral *niet* de nadruk op volwassen) hebben we elkaar leren kennen, en ik prijs me gelukkig dat we nog steeds lief en leed met elkaar delen. De borrel- en bordspelweekendjes blijven een erg dankbare mentale reset tussen de werkdrukte door, en ik hoop dat we die er nog lang kunnen inhouden. Verder terugblikkend op de middelbare school, ben ik zeker ook Bas, Emmanuel, Floris, Jesse, Robin, Ted dankbaar. Hoewel we elkaar

een stuk minder zien dan voorheen, de kerst-/zomerborrels halen toch altijd geweldige herinneringen naar boven en jullie constante interesse in mijn onderzoek waardeer ik zeer.

Dan rest me nog mijn (schoon)-familie te bedanken. Bernadette, Erik, Lara, Eva, Sebas, Xi, jullie support voor mij en Nanda wordt altijd gevoeld: zowel tijdens het wonen in het 'verre' Leiden, als sinds kort weer een stuk dichterbij. Pepijn en Louise, we go way back, en dit is een goed moment om terug te kijken en met oprechtheid te zeggen dat ik trots op ons drieën ben, met wat we allemaal voor elkaar hebben geschopt. Jullie staan altijd voor me klaar, van huwelijksaanzoek advies tot aan advies over de beste PC specificaties, en van koopwoning advies tot aan advies over de beste Bossche koffietentjes. Mama en papa, de onvoorwaardelijke support en vrijheid die jullie ons gegeven hebben waardeer ik enorm. Als wetenschapper kan ik nu zonder enige 'bias' en met 100% objectiviteit zeggen dat jullie de beste ouders ter wereld zijn.

Nanda, zij aan zij streden we in ons eerste jaar op de universiteit (zo'n 10 jaar geleden) tijdens onze hertentamens biomoleculen en statistiek, en zij aan zij streden we tijdens onze PhD. Strijden klinkt alsof het erg was, maar dat viel eigenlijk wel mee, want thuiskomend bij jou tovert altijd weer een glimlach op mijn gezicht, ongeacht wat voor een dag het was. Jij leert me de mooie momenten te vieren en de verdrietige momenten te verlichten, en ik kan nog wel een thesis volschrijven met dingen waarvoor ik je dankbaar bent. Maar ik zal het kort houden. Ik hou van je. Opdat we zij en zij nog tientallen jaren mogen strijden.

CURRICULUM VITÆ

Hugo Veldhuizen was born in 's-Hertogenbosch (the Netherlands) on the 18th of September in 1994, and lived for most of his youth in a nearby village called Vlijmen. He obtained his bachelor's degree in chemistry at the Radboud University in Nijmegen and continued his master's there as well. In early 2018 he obtained his master's degree in chemistry *cum laude* and his master thesis was performed in the Physical Organic Chemistry department, with the thesis title "A Dynamic, Stress-Relaxing Hydrogel Through Continuous Thiol-Disulfide Exchange". His master's internship on UV-gel ink formulation was done at Canon Production Printing in Venlo (The Netherlands), formerly known as Océ. After his master's, Hugo continued to work for Canon for another 3 months, after which he started his PhD at the TU Delft in September 2018, with the aim of becoming a more well-rounded researcher.

His PhD research on the topic of synthesis and structure-property relationships of covalent organic frameworks (COFs) was initially supervised by Dr. Atsushi Nagai and Prof. Dr. Sybrand van der Zwaag. After 1.5 years, Dr. Nagai made the decision to pursue his career outside TU Delft and Dr. Monique van der Veen (TU Delft, Applied Sciences) stepped up as a co-supervisor. Hugo's research combined design, synthesis and application of various novel COF structures, where the applications were aimed at areas within the energy transition (*e.g.* CO_2 capture, CO_2 conversion, electrochemical devices). He published several peer-reviewed papers in international journals and presented his research (posters and oral) at international conferences. He obtained the title of Registered Polymer Scientist (RPK) from the Dutch national postgraduate research school Polymeer Technologie Nederland (Polymer Technology Netherlands).

On August 2023, Hugo started working for Tremco CPG Netherlands B.V. in Arkel as a R&D scientist on polyurethane foams for construction applications.

List of Publications

1. Hugo Veldhuizen, Alexandros Vasileiadis, Marnix Wagemaker, Tadhg Mahon, Durga P. Mainali, Lishuai Zong, Sybrand van der Zwaag, Atsushi Nagai. Synthesis, Characterization, and CO_2 Uptake of Mellitic Triimide-Based Covalent Organic Frameworks. *J. Polym. Sci. Part A Polym. Chem.* **2019**, *57*, 2373–2377.
2. Hugo Veldhuizen, Luc van den Elzen, Tadhg Mahon, Ruben Abellon, Atsushi Nagai. Charge-Transfer-Complexed Conjugated Microporous Polymers (CT-CMPs). *Macromol. Chem. Phys.* **2020**, *221*, 1900415.
3. Remco van der Jagt,* Alexandros Vasileiadis,* Hugo Veldhuizen,* Pengpeng Shao, Xiao Feng, Swapna Ganapathy, Nicolas C. Habisreutinger, Monique A. van der Veen, Chao Wang, Marnix Wagemaker, Sybrand van der Zwaag, Atsushi Nagai. Synthesis and Structure–Property Relationships of Polyimide Covalent Organic Frameworks for Carbon Dioxide Capture and (Aqueous) Sodium-Ion Batteries. *Chem. Mater.* **2021**, *33*, 818–833.
4. Niranjala Fernando,* Hugo Veldhuizen,* Atsushi Nagai, Sybrand van der Zwaag, Amor Abdelkader. Layer-by-Layer Electrode Fabrication for Improved Performance of Porous Polyimide-Based Supercapacitors. *Materials* **2022**, *15*, 4.
5. Hugo Veldhuizen, Sybrand van der Zwaag, Monique A. van der Veen. Impact of flow-induced disturbances during synthesis on the photophysical properties of naphthalene diimide covalent organic frameworks. *Microporous Mesoporous Mater.* **2022**, *343*, 112122.
6. Hugo Veldhuizen, Saira Alam Butt, Annemiek van Leuken, Bart van der Linden, Willy Rook, Sybrand van der Zwaag, Monique A. van der Veen. Competitive and Cooperative CO_2–H_2O Adsorption through Humidity Control in a Polyimide Covalent Organic Framework. *ACS Appl. Mater. Interfaces* **2023**, *15*, 29186–29194.
7. Hugo Veldhuizen, Maryam Abdinejad, Pieter J. Gilissen, Tom Burdyny, Frans D. Tichelaar, Sybrand van der Zwaag, Monique A. van der Veen. Combining Nickel- and Zinc-Porphyrin Sites in Covalent Organic Frameworks for Electrochemical CO_2 Reduction. *Submitted*